THERMAL PERFORMANCE AND HEAT TRANSFER ENHANCEMENT OF PARABOLIC TROUGH RECEIVERS – NUMERICAL INVESTIGATION, THERMODYNAMIC AND MULTI-OBJECTIVE OPTIMISATION

by

Aggrey Mwesigye

Submitted in partial fulfilment of the requirements for the degree

PHILOSOPHIAE DOCTOR in Mechanical Engineering

in the

Department of Mechanical and Aeronautical Engineering

Faculty of Engineering, Built Environment and Information Technology

University of Pretoria

Pretoria

Supervisor: Prof. Tunde Bello-Ochende

Co-Supervisor: Prof. Josua P. Meyer

2015

ABSTRACT

TITLE: **THERMAL PERFORMANCE AND HEAT TRANSFER ENHANCEMENT OF PARABOLIC TROUGH RECEIVERS – NUMERICAL INVESTIGATION, THERMODYNAMIC AND MULTI-OBJECTIVE OPTIMISATION**

AUTHOR: **A. Mwesigye**

SUPERVISOR **Prof. T. Bello-Ochende**

CO-SUPERVISOR: **Prof. J. P. Meyer**

DEPARTMENT: **Mechanical and Aeronautical Engineering**

DEGREE: **Philosophiae Doctor (Mechanical Engineering)**

Parabolic trough systems are one of the most commercially and technically developed technologies for concentrated solar power. With the current research and development efforts, the cost of electricity from these systems is approaching the cost of electricity from medium-sized coal-fired power plants. Some of the cost-cutting options for parabolic trough systems include: (i) increasing the sizes of the concentrators to improve the system's concentration ratio and to reduce the number of drives and controls and (ii) improving the system's optical efficiency. However, the increase in the concentration ratios of these systems requires improved performance of receiver tubes to minimise the absorber tube circumferential temperature difference, receiver thermal loss and entropy generation rates in the receiver. As such, the prediction of the absorber tube's circumferential temperature difference, receiver thermal performance and entropy generation rates in parabolic trough receivers therefore, becomes very important as concentration ratios increase.

Abstract

In this study, the thermal and thermodynamic performance of parabolic trough receivers at different Reynolds numbers, inlet temperatures and rim angles as concentration ratios increase are investigated. The potential for improved receiver thermal and thermodynamic performance with heat transfer enhancement using wall-detached twisted tape inserts, perforated plate inserts and perforated conical inserts is also evaluated.

In this work, the heat transfer, fluid flow and thermodynamic performance of a parabolic trough receiver were analysed numerically by solving the governing equations using a general purpose computational fluid dynamics code. SolTrace, an optical modelling tool that uses Monte-Carlo ray tracing techniques was used to obtain the heat flux profiles on the receiver's absorber tube. These heat flux profiles were then coupled to the CFD code by means of user-defined functions for the subsequent analysis of the thermal and thermodynamic performance of the receiver. With this approach, actual non-uniform heat flux profiles and actual non-uniform temperature distribution in the receiver different from constant heat flux profiles and constant temperature distribution often used in other studies were obtained.

Both thermodynamic and multi-objective optimisation approaches were used to obtain optimal configurations of the proposed heat transfer enhancement techniques. For thermodynamic optimisation, the entropy generation minimisation method was used. Whereas, the multi-objective optimisation approach was implemented in ANSYS DesignXplorer to obtain Pareto solutions for maximum heat transfer and minimum fluid friction for each of the heat transfer enhancement techniques.

Results showed that rim angles lower than 60^{o} gave high absorber tube circumferential temperature differences, higher receiver thermal loss and higher entropy generation rates, especially for flow rates lower than 43 m^3/h. The entropy generation rates reduced as the inlet temperature increased, increased as the rim angles reduced and as concentration ratios increased. Existence of an optimal Reynolds number at which entropy generation is a minimum for any given inlet temperature, rim angle and concentration ratio is demonstrated. In addition, for the heat transfer enhancement techniques considered, correlations for the Nusselt number and fluid friction were obtained and presented. With heat transfer enhancement, the thermal efficiency of the receiver increased in the range 5% – 10%,

3% – 8% and 1.2% – 8% with twisted tape inserts, perforated conical inserts and perforated plate inserts respectively. Results also show that with heat transfer enhancement, the absorber tube's circumferential temperature differences reduce in the range 4% – 68%, 3.4 – 56% and up to 67% with twisted tape inserts, perforated conical inserts and perforated plate inserts respectively. Furthermore, the entropy generation rates were reduced by up to 59%, 45% and 53% with twisted tape inserts, perforated conical inserts and perforated plate inserts respectively. Moreover, using multi-objective optimisation, Pareto optimal solutions were obtained and presented for each heat transfer enhancement technique.

In summary, results from this study demonstrate that for a parabolic trough system, rim angles, concentration ratios, flow rates and inlet temperatures have a strong influence on the thermal and thermodynamic performance of the parabolic trough receiver. The potential for improved receiver thermal and thermodynamic performance with heat transfer enhancement has also been demonstrated. Overall, this study provides useful knowledge for improved design and efficient operation of parabolic trough systems.

Key words: Absorber tube; Computational fluid dynamics; Concentration ratio; Entropy generation rate; Heat transfer enhancement; Monte-Carlo ray tracing; Multi-Objective optimisation; Parabolic trough receiver; Perforated plate inserts; Perforated conical inserts; Rim angle, Twisted tape inserts.

DEDICATION

This thesis is dedicated to:

my dear wife,

Charity Ashimwe Mwesigye

and my children,

Michelle Atukunda Johanna and Joel Arinda Matthew.

ACKNOWLEDGEMENTS

First, I would like to thank Almighty God for the gift of life, provision and protection. Without Him, I would not have come this far.

I would like to express my heartfelt gratitude to my supervisor, Prof. Tunde Bello-Ochende, for his invaluable guidance and counsel throughout my studies, and the directions he provided during the course of this investigation. You have been a true mentor.

I am grateful to my co-supervisor, Prof. Josua Petrus Meyer, for the constant guidance, inspiration and for all his efforts in reviewing my write-ups and ensuring that they are of the required standard. Your support and encouragement will always be remembered.

Special thanks to my family for all the support and encouragement you provided throughout my studies. To my dear wife Charity Ashimwe Mwesigye, you have been a source of support and comfort. You provided a shoulder to lean on, when times were tough. To my children, Michelle Atukunda Johanna, Joel Arinda Matthew, you gave me many reasons to smile and work hard. To my parents, Mr Mugume Wilson Kamukama and Mrs Kellen Kamukama, my in-laws Dr and Mrs Mfitundinda, I am so grateful for your staunch support, love and prayers.

My gratitude goes to all the academic staff of the Thermofluids research group, and the Department of Mechanical and Aeronautical Engineering, University of Pretoria. You created an enabling environment for me to complete my studies successfully. Also gratefully acknowledged are the encouragement and friendliness of Prof. Ken Craig, Prof. Johan Slabber, Dr Jaco Dirker, Mr Logan Page, Mr Johnathan Vadaz, Mr Stephan Roux, Ms Barbara Huyssen, Ms Lelanie Smith and Ms Nicola Kotze.

The support of the administrative staff of the department is duly acknowledged. Thanks to Ms Tersia Evans, Ms Elzabe Pieterse and Ms Ntsindy Mnyamana for making my stay in the department comfortable and rewarding.

I would like to express my gratitude to colleagues and fellow students in the thermofluids research group, Department of Mechanical Engineering, University of Pretoria: Lloyd Ngo, Jeffrey Baloyi, Mostafa Mahdavi, Saheed Adia, Mehdi Mehrabi, Louw Coetzee, Adewumi Yinka, Noah Olugbenga, Okafor Francis, Saheed Adio, Rupert, Metemba, Ntumba, Eugene,

Henriette, Stefan, Ewan Huisamen, to mention but a few. Thank you for your consistent help and encouragement throughout my studies.

All the support received from Annecke Janse van Rensburg, chairman of the Unidia body corporate is deeply appreciated. You have been like a mother to me and my family, may the Lord richly bless you.

Finally, the funding received from the NRF, TESP and Stellenbosch University/University of Pretoria, SANERI/SANEDI, CSIR, EEDSM Hub and NAC is gratefully acknowledged and appreciated.

PUBLICATIONS IN JOURNALS AND CONFERENCES

The following articles and conference papers were produced in the course of study:

Articles in refereed journals

1. Mwesigye A., Bello-Ochende T. and Meyer J. P. Numerical investigation of entropy generation in a parabolic trough receiver at different concentration ratios. **Energy 53 (2013), 114-127**.

2. Mwesigye A., Bello-Ochende T. and Meyer J. P. Thermodynamic performance of a parabolic trough receiver with centrally placed perforated plate inserts. **Appl Energy 136 (2014), 989 – 1003.**

3. Mwesigye A., Bello-Ochende T. and Meyer J. P. Minimum entropy generation due to heat transfer and fluid friction in a parabolic trough receiver with non-uniform heat flux at different rim angles and concentration ratios. **Energy 73 (2014), 606-617.**

4. Mwesigye A., Bello-Ochende T. and Meyer J. P. Multi-objective and thermodynamic optimisation of a parabolic trough receiver with perforated plate inserts. **Appl Therm Eng 77 (2015), 42-56**

Papers presented at refereed conferences

1. Mwesigye A., Bello-Ochende T. and Meyer J. P., Thermal performance of a parabolic trough receiver with perforated conical inserts for heat transfer enhancement. *In Conference Proceedings of ASME 2014 International Mechanical Engineering Congress and Exposition*, IMECE2014, Nov 14-20, 2014, Montreal, Quebec, Canada, Paper ID: IMECE2014-39849.

2. Mwesigye A., le Roux W.G., Bello-Ochende T. and Meyer J. P., Thermal and thermodynamic analysis of a parabolic trough receiver at different concentration ratios and rim angles. *In Conference Proceedings of the 10th International Conference on Heat Transfer, Fluid Mechanics and Thermodynamics,* HEFAT2014, 14 – 26 July 2014, Orlando, Florida.

3. Mwesigye A., Bello-Ochende T. and Meyer J. P., Heat transfer enhancement in a parabolic trough receiver using perforated conical inserts. *In Conference Proceedings of the 15th International Heat Transfer Conference*, IHTC-15, August 10-15, 2014, Kyoto, Japan. Paper I.D. IHTC15-9150.

4. Mwesigye A., Bello-Ochende T. and Meyer J. P., Determination of heat flux and temperature distribution in a parabolic trough receiver at different rim angles and concentration ratios, *In Conference Proceedings of the 2nd Southern African Solar Energy Conference*, SASEC 2014, January 27-29, 2014, Pine Lodge Resort, Nelson Mandela Bay, South Africa. Paper ID. 27.

5. Mwesigye A., Bello-Ochende T. and Meyer J. P. Heat transfer enhancement in a parabolic trough receiver using wall detached twisted tape inserts. *In Conference Proceedings of the ASME 2013 International Mechanical Engineering Congress and Exposition*, IMECE2013, Nov 15-21, 2013, San Diego CA, USA. Paper ID: IMECE2013-62745.

6. Mwesigye A., Bello-Ochende T. and Meyer J. P. Thermodynamic performance of a parabolic trough receiver with centrally placed perforated plate inserts. *In Conference Proceedings of the 5th International Conference on Applied Energy*, ICAE2013, Jul 1-4, 2013, Pretoria, South Africa. Paper ID: ICAE2013-258.

7. Mwesigye A., Bello-Ochende T. and Meyer J. P., Numerical analysis of thermal performance of an externally longitudinally finned receiver for parabolic trough solar collector, *In Conference Proceedings of the 9th International conference on Heat Transfer, Fluid Mechanics and Thermodynamics*, HEFAT 2012, pp. 159 – 168, Malta, 16-18th July 2012.

CONTENTS

LIST OF FIGURES

LIST OF TABLES

ACRONYMS

AZTRAK	AZimuthal TRAcKing
EES	Engineering equation solver
EGM	Entropy generation minimisation method
CFD	Computational fluid dynamics
CSP	Concentrating solar power
DOE	Design of experiments
HCE	Heat collection element
HTF	Heat transfer fluid
IEA	International Energy Agency
IPCC	Intergovernmental Panel on Climate Change
LFR	Linear Fresnel Reflector
MENA	Middle East and North Africa
PEC	Performance evaluation criteria
PV	Photovoltaic
RANS	Reynolds Averaged Navier-Stokes
RSM	Response surface methodology
RNG	Re-Normalisation Group
SEGS	Solar electricity generating systems
TPES	Total primary energy supply
TREC	Trans-Mediterranean Renewable Energy Cooperation

NOMENCLATURE

A_a	Collector's projected aperture area (m^2)
A_c	Absorber tube's cross-section area (m^2)
A_f	Collector geometrical factor $=A_l/A_a$ (-)
A_{gc}	Area of the glass cover (m^2)
A_l	Lost aperture area (m^2)
A_r	Absorber tube's projected area (m^2)
A_o, A_s	Realisable k-ε model constants (-)
$C_{1\varepsilon}, C_2, C_\mu$	Realisable k-ε model constants (-)
C_{2p}	Perforated insert inertial resistance factor (m^{-1})
c_p	Specific heat capacity (J kg^{-1} K^{-1})
C_R	Geometric concentration ratio (-)
D	Receiver diameter (m)
d	Perforated plate diameter (m)
DNI	Direct Normal Irradiance (W/m^2)
d_{gi}	Receiver's glass cover inner diameter (m)
d_{go}	Receiver's glass cover outer diameter (m)
d_{ri}	Absorber tube's inner diameter (m)
d_{ro}	Absorber tube's outer diameter (m)
E_D	Exergy destroyed (W)
E_{in}	Exergy in (W)
E_{out}	Exergy out (W)
f	Darcy friction factor (-)
f_p	Parabola focal distance (m)

G	Mass flux (kg $s^{-1}m^{-2}$)
G_k	Generation of turbulence kinetic energy due to mean velocity gradients (kg $m^{-1}s^{-3}$)
h	Heat transfer coefficient (W $m^{-2}K^{-1}$)
h_c	Conduction heat loss coefficient (W $m^{-2}K^{-1}$)
h_p	Parabola height (m)
h_r	Linearised radiation heat loss coefficient (W $m^{-2}K^{-1}$)
h_w	Heat loss coefficient due to wind effects (W $m^{-2}K^{-1}$)
I_b	Direct solar radiation (W m^{-2})
k	Turbulent kinetic energy (m^2 s^{-2})
k_p	Turbulent kinetic energy at the near-wall node, p (m^2 s^{-2})
L	Length (m)
N_s	Non-dimensional entropy generation number (-)
$N_{s,en}$	Enhancement entropy generation number = $S_{gen}/(S_{gen})_p$
Nu	Nusselt number (-)
Nu_p	Plain absorber tube Nusselt number (-)
Nu_{en}	Enhanced absorber tube Nusselt number (-)
P	Pressure (Pa)
p	Perforated plate spacing (m)
Pr	Prandtl number (-)
$\dot{q}$	Heat transfer rate (W)
Q	Heat transfer to the collector (W)
Q^*	Heat transfer from the sun to the collector (W)
Q_o	Collector heat loss = Q^* - Q (W)

q'_u	Useful energy/heat gain/ (W/m)
q''	Heat flux (W m^{-2})
r	Radial position, rim radius (m)
r_p	Perforated plate radius = $d/2$ (m)
r_r	Collector's rim radius (m)
Ra	Rayleigh number (-)
Re	Reynolds number (-)
Re_p	Plain absorber tube's Reynolds number (-)
Re_{en}	Enhanced absorber tube's Reynolds number (-)
S	Modulus of the mean rate-of-strain tensor (s^{-1})
S_{ij}	Rate of linear deformation tensor (s^{-1})
S_{gen}	Entropy generation rate (W/K)
S'_{gen}	Entropy generation rate per unit length (W/m K)
$(S_{gen})_H$	Entropy generation rate due to heat transfer (W/ K)
$(S_{gen})_F$	Entropy generation rate due to fluid friction (W/ K)
$(S'_{gen})_H$	Entropy generation rate due to heat transfer per unit length (W/ m K)
$(S'_{gen})_F$	Entropy generation rate due to fluid friction per unit length (W/ m K)
S'''_{gen}	Volumetric entropy generation rate (W $m^{-3}K^{-1}$)
$(S'''_{gen})_F$	Volumetric entropy generation rate due to fluid friction (W $m^{-3}K^{-1}$)
$(S'''_{gen})_H$	Volumetric entropy generation rate due to heat transfer (W $m^{-3}K^{-1}$)
$S'''_{PROD,VD}$	Entropy production by direct dissipation (W $m^{-3}K^{-1}$)
$S'''_{PROD,TD}$	Entropy production by turbulent dissipation (W $m^{-3}K^{-1}$)
$S'''_{PROD,T}$	Entropy production by heat transfer with mean temperatures (W $m^{-3}K^{-1}$)
$S'''_{PROD,TG}$	Entropy production by heat transfer with fluctuating temperatures (W $m^{-3}K^{-1}$)
S_m	Momentum source term (kg ms^{-1})

T	Temperature (K)
T_g	Glass cover inner-wall temperature (K)
T_o	Ambient temperature (K)
T_r	Absorber tube outer-wall temperature (K)
T_s	Apparent black body temperature of the sun (K)
T_*	Apparent temperature of the sun as an energy source = ¾ T_s (K)
u	Velocity (m s^{-1})
U_∞	Mean flow velocity (m s^{-1})
U_L	Overall heat transfer coefficient (W/m^2 K)
u_i, u_j	Averaged velocity components (m s^{-1})
u_i', u_j'	Velocity fluctuations (m s^{-1})
u', v', w'	Velocity fluctuations (m s^{-1})
u_τ	Friction velocity (m s^{-1})
u^+	Dimensionless velocity (-)
U^*	Dimensionless velocity (-)
U_p	Mean velocity of the fluid at the near-wall node p (m/s)
V	Volume (m^3)
$\dot{V}$	Volumetric flow rate (m^3/h)
$\dot{W}_p$	Pumping power, W
W_a	Collector's aperture width (m)
x_i, x_j	Spatial coordinates (m)
x, y, z	Cartesian co-ordinates (m)
y_p	Distance from the near wall node p to the wall
y^+	Dimensionless wall coordinate (-)

y^*	Dimensionless distance from the wall (-)
$-\rho\overline{u_i' u_j'}$	Reynolds stresses (Nm^{-2})
∇p	Pressure drop (Pa)
Δm	Perforated plate thickness (m)
ΔT	Receiver temperature gain (^oC)

Greek symbols

α	Thermal diffusivity ($m^2\ s^{-1}$)
α_{abs}	Absorber tube absorptivity
α_t	Turbulent thermal diffusivity ($m^2\ s^{-1}$)
α_p	Permeability of the perforated plate (m^2)
β	Perforated insert orientation angle (degrees)
δ_{ij}	Kronecker delta
ε	Turbulent dissipation rate ($m^2\ s^{-3}$)
ε_g	Glass cover emissivity
ε_r	Absorber tube emissivity
γ	Intercept factor
λ	Fluid thermal conductivity ($Wm^{-1}\ K^{-1}$)
λ_{abs}	Absorber tube thermal conductivity ($Wm^{-1}\ K^{-1}$)
λ_{air}	Air thermal conductivity ($Wm^{-1}\ K^{-1}$)
$\lambda_{air,eff}$	Effective air thermal conductivity ($Wm^{-1}\ K^{-1}$)
λ_{eff}	Effective fluid thermal conductivity ($Wm^{-1}K^{-1}$)
λ_g	Glass cover thermal conductivity ($Wm^{-1}\ K^{-1}$)
κ	von Kármán constant (= 0.4187)

η	Turbulence model parameter = Sk/ε (-)
η_0	Optical efficiency (%)
η_{th}	Collector thermal efficiency
ϕ	Absorber tube temperature gradient or difference (°C)
φ_r	Collector rim angle (degrees)
ρ	Fluid density (kg m^{-3})
ρ_c	Concentrator mirror reflectivity
α_t	Turbulent thermal diffusivity (m^2 s^{-1})
σ	Stefan Boltzmann constant (W m^{-2} K^{-4})
σ_ε	Turbulent Prandtl number for ε (-)
$\sigma_{h.t}$	Turbulent Prandtl number for energy (-)
σ_k	Turbulent Prandtl number for k (-)
τ_g	Glass cover transmissivity
τ_w	Wall shear stress (N/m^2)
θ	Receiver circumferential angle, angle of incidence (degrees)
θ_m	Half acceptance angle (degrees)
μ	Viscosity (Pa s)
μ_t	Turbulent viscosity (Pa s)
μ_τ	Friction velocity (m/s)
μ_{eff}	Effective viscosity (Pa s)
ν	Kinematic viscosity (m^2 s^{-1})
Ω_{ij}	Rotation tensor
ω_k	Angular velocity (rad/s)

Subscripts

a	Ambient
abs-lw	Absorber tube lower wall
abs-up	Absorber tube upper wall
amb	Ambient state
c	Receiver's glass cover, perforated conical insert
inlet	Absorber tube inlet
i, j, k	General spatial indices
t	Turbulent
w	Wall
p	Plain absorber tube (no inserts)
outlet	Absorber tube outlet
b	Bulk fluid state
gi	Receiver glass cover inner diameter
go	Receiver glass cover outer diameter
max	Maximum value
r	Absorber tube
ro	Absorber tube outer wall
ri	Absorber tube inner wall

Superscripts

‾	Mean value
~	Dimensionless value
'	Fluctuation from mean value/per unit metre

CHAPTER ONE

CHAPTER ONE: INTRODUCTION

1.1 BACKGROUND

Access to modern energy services is still a challenge to the world today, especially in developing countries. It is generally accepted that modern energy services are essential to the wellbeing of humankind and to the development of any country [1]. The provision of clean water, sanitation and health care, reliable and efficient lighting, heating and cooling, cooking, mechanical power, transport and telecommunication services depends on the availability of modern energy services [1]. According to the World Energy Outlook 2012 [1], millions of people gained access to modern energy services in the past two decades, most of them in India and China [1]. However, more than 1.3 billion people are still without access to much-needed electricity, and 2.6 billion people still rely on traditional biomass to meet their fuel needs for cooking [1]. About 95% of those without access to modern energy services are in developing countries in Asia and sub-Saharan Africa.

A secure and reliable supply of energy is essential for the growth and development of any economy. There is therefore a correlation between a country's level of development and access to modern energy services. Figure 1.1 shows the World total primary energy supply by region [2], where most (61.4%) of the world's primary energy supply is in the member countries of the Organisation for Economic Co-operation and Development (OECD). They include most of the developed nations such as the USA, Japan, the UK, Canada, Australia and the Netherlands. It is also clear that the demand for energy and therefore the primary energy supply is continuously increasing. The increase in the world's population, increasing rates of urbanisation and industrialisation are partly responsible for the increase in the demand for energy.

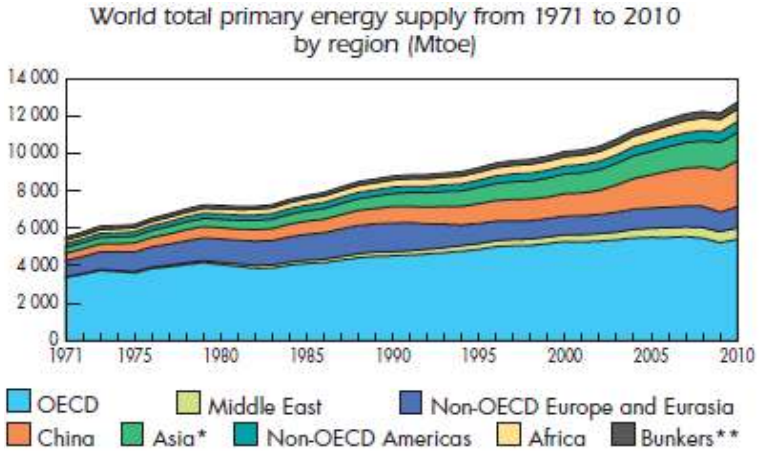

(a)

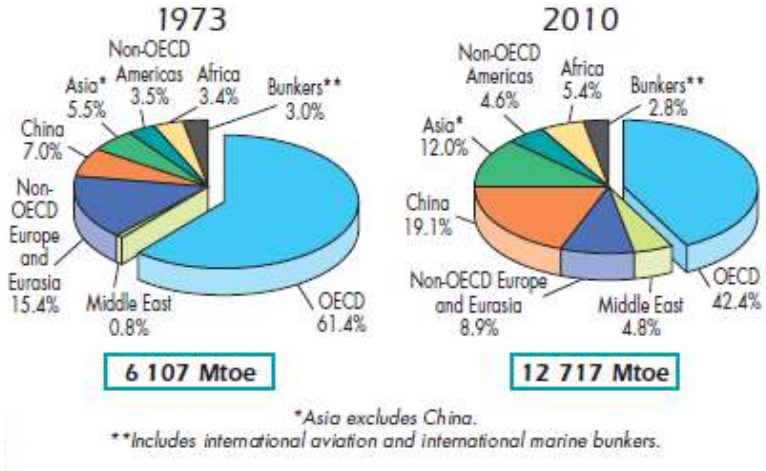

(b)

Fig. 1.1: Total primary energy supply by region: (a) world total primary energy supply from 1971 to 2010 by region (Mtoe) (b) 1973 and 2010 regional shares of total primary energy supply [2].

The world's primary energy supply mix is predominantly based on fossil fuels, as shown in Fig. 1.2. The continued dependence on fossil fuels for meeting humankind's energy needs has increased the emission of harmful substances and greenhouse gases into the atmosphere. The impacts of energy use on the environment are presented in detail by Dincer and by Dincer and Rosen [3,4]. The resulting emissions include carbon dioxide (CO_2), methane (CH_4), nitrogen oxides (NO_x), halocarbons and others. CO_2 is believed to be the most important anthropogenic greenhouse gas. The annual emissions of CO_2 are estimated to have increased by 80% between 1970 and 2004 from 21 to 38 Gt [5]. The overall anthropogenic greenhouse

gas emissions have also increased overall since pre-industrial times: the increase was about 70% between 1970 and 2004 [2,5]. Though the largest increase in greenhouse gas emissions has come from the energy supply [5], fossil fuels will continue to be the primary source of energy for some time. The demand for coal, oil and gas is expected to grow until 2035 [6]. The global energy demand will also continue to increase. The global energy demand is expected to go up by one-third by 2035. With the increase in demand for fossil fuels and energy, energy-related emissions are predicted to increase from 31.2 Gt in 2011 to 37 Gt in 2035 [6].

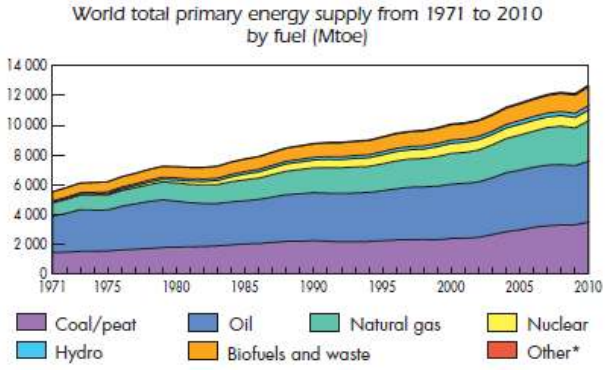

(a)

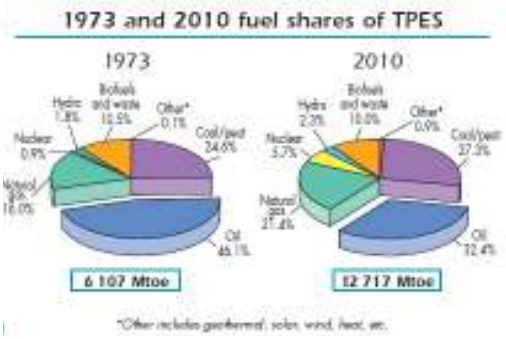

(b)

Fig. 1.2: Total primary energy supply by fuel: (a) world total primary energy supply from 1971 to 2010 by fuel (Mtoe) and (b) 1973 and 2010 fuel shares of total primary energy supply [2].

The increased emission of greenhouse gases has significantly accelerated global warming and the resulting effects of climate change. The increase in the global average temperature, the rise in sea levels, flooding and loss of ice mass are some of the indications and the effects of

the changing climate. According to the IPCC [5,7], climate change is predicted to have severe impacts on systems and sectors. The impacts on the ecosystem will range from floods, wildfires, droughts, over-exploitation of natural resources, extinction of plant and animal species and negative consequences for biodiversity and ecosystem goods [5]. Additional impacts of climate change include a decrease in crop production, effects on industry, settlements and society due to floods and extreme weather conditions, higher incidence of disease, death and injury due to extreme weather conditions and pollution, and impacts on the availability and quality of water [5].

Consequently, the need to meet the ever-increasing energy demand, to ensure and improve access to modern energy services and to minimise the emission of greenhouse gases have led to increased research into, and the development of sustainable, clean and renewable energy technologies. The declaration by the United Nations of the year 2012 as the year of sustainable energy for all further underlines the importance of access to sustainable energy [1].

Renewable energy resources, compared to non-renewable energy resources, are those that are replenished naturally. They are not finite when compared to non-renewable resources such as oil, coal or natural gas, which occur in finite amounts. Renewable energy resources include solar, wind, hydropower, biomass and geothermal sources. Renewable energy sources have several benefits when compared to fossil-based resources, such as little or no emissions, wide availability, the potential for use in the distributed generation of electricity [8] and lower costs of operation. According to the International Energy Agency [9], there has been a steady increase in hydropower generation, and solar and wind energy have been rapidly expanding. Predictions indicate that, by 2015, renewable energy will be the second-largest source of electricity and by 2035, it will approach coal as the primary source of global energy [9]. The decrease in technology cost, increase in fossil fuel prices, carbon pricing, continued subsidies [9], research and development of efficient and optimised power plant components [4] and provision of a secure supply of energy are some of the driving forces behind the rapid increase in renewable energy deployment.

The solar energy resource is one of the renewable energy resources. It is the world's most abundant and clean source of energy with the potential to meet a significant portion of the

global energy requirement. Even with a tiny part of the sun's energy received on earth's surface (about 1.7 x 10^{14} kW), it was estimated that only 84 minutes of solar radiation was equivalent to the world's energy demand for one year of about 900 EJ in 2009 [10]. Furthermore, the potential of the solar resource is demonstrated by the DESERTEC concept developed by Trans-the Mediterranean Renewable Energy Cooperation (TREC). It shows that by using solar thermal technology in less than 1% of the Middle East and North African (MENA) deserts, sufficient electricity could be generated to meet the energy needs of Europe, the Middle East and North Africa (EU-MENA) [11]. Despite this enormous potential of the solar energy resource, there are still technical, economic and institutional challenges to its full exploitation [12]. As such, significant research and development efforts are still needed to overcome these challenges. Research and development focus at improving the existing or developing new, efficient and low-cost technologies so that the operation costs and capital costs can both be reduced.

Concentrating solar power (CSP) technologies and solar photovoltaic technologies (PV) are the two main methods for converting solar radiation into electricity. Compared to solar photovoltaic technologies, the potential of CSPs to store thermal energy for later use makes them favourable for large-scale electricity generation. Besides electricity generation, CSP technologies have the potential to produce solar fuels and other energy carriers such as hydrogen [13], to provide energy for heating and cooling, and provide process heat and water desalination [14]. As such, CSPs are deemed to have great potential for mitigating climate change [13,15] and to provide reliable electricity [11,13]. With the reduction in the cost of generating electricity using concentrated solar power technologies [11,13,15-18], CSPs are becoming competitive with electricity from other alternative forms of energy and even becoming competitive with electricity from oil for sites with good solar radiation [11,19]. The estimated cost of electricity from solar thermal will be between 4-6 ¢/kWh by 2015. The cost at which it is competitive with fossil fuel alternatives was 5¢/kWh based on the 2002 oil prices [18]. Therefore, concentrated solar power will play a significant role in meeting the world's energy needs. It will contribute about 7% of the world's energy supply by 2030 and 25% by 2050 for the advanced industry and high efficiency scenario, according to the global CSP outlook 2009 [17].

CSP technologies use the direct solar radiation component of solar radiation [13,15,17]. Accordingly, they are usually deployed in regions with low atmospheric humidity, low dust and low fumes [13,17]. For these reasons, sites with direct normal irradiance of at least 2 000 kWh/m^2 are deemed suitable and the best sites are those with direct normal irradiance of more than 2 800 kWh/m^2 per annum. Figure 1.3 shows a worldwide map of areas with potential for CSP deployment [20]. It can be seen from Fig. 1.3 that most sites with a high potential for CSP use are located in Northern Africa, Southern Africa, the Middle East, India, Australia, North America and South America [20].

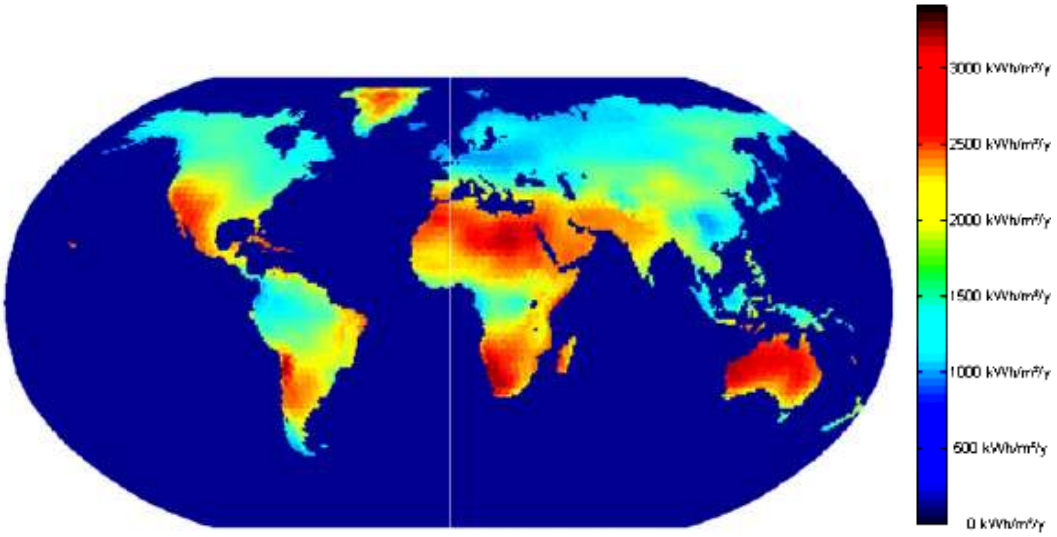

Fig. 1.3: Map showing the worldwide annual direct normal irradiation in kWh/m^2/y for potential CSP sites [20].

Most CSP plants work in the same way as conventional power plants; they use steam or gas to drive turbines. Unlike conventional power plants that rely on fossil fuels, CSP plants use solar radiation from the sun. The sun's energy is converted to high temperature steam or gas that is used to drive turbines and generate power. In general, CSP plants have four main components: the collector in the form of a concentrator, the receiver, transport media or storage media and power conversion devices [17]. The type and arrangement of these components are what differentiates the CSP technologies from other technologies. The collectors or concentrating systems can be linear or point-focusing. Linear systems concentrate up to 212 times (theoretical maximum limit), achieving temperatures of up to

550 °C, whereas point-focusing systems can concentrate up to more than 1 000 times, achieving working temperatures of the order of 1 000 °C and more [17].

The main commercial technologies for CSP include parabolic trough systems, linear Fresnel systems, central receivers or solar towers and parabolic dishes. The output for each of these plants as of 2009 is shown in Table 1.1. As can be seen, most of the installed plants, plants under construction and proposed solar thermal power plants use the parabolic trough technology followed by the solar tower and then parabolic dishes.

Table 1.1: Solar thermal output for each technology as of 2009 [17].

Technology type	Installed capacity 2009 [MW]	Electricity produced up to 2009 [GWh]	Approximate capacity under construction and proposed [MW]
Parabolic trough	500	>16 000	>10 000
Solar tower	40	80	3 000
Fresnel	5	8	500
Dish	0.5	3	1 000

As shown in Table 1.1, the parabolic trough technology is the most commercially established CSP technology today [10,17,21,22] and will continue to provide a significant portion of CSP electricity [15,17]. The successful operation experience of the first plants; the Luz Solar Electric Generating Systems (SEGS) in California's Mojave Desert, is one of the factors that made the parabolic trough technology very successful. The SEGS plants were constructed in the period 1984-1990 in sizes between 14 MW – 80 MW, with an installed capacity of 354 MW, covering more than 2 000 000 m^2 of collector area [10,13,15,17,21]. They have been in continuous operation since then.

The parabolic trough technology includes large fields of parabolic trough concentrator collectors; made of a parabolic linear reflecting surface (concentrator) and a linear receiver or heat collection element (HCE) at the collector's focus, onto which the sun's rays are focused. The receiver consists of an absorber, an evacuated glass envelope to reduce the heat loss and supporting structures. A heat transfer fluid flows through the receiver's absorber tube where it is heated to high temperatures by concentrated solar radiation. The heated heat transfer

fluid then exchanges heat with the working fluid of a power cycle in the power block (usually water) to generate high-pressure superheated steam, which expands in the turbine, producing mechanical power that the generator converts into electrical power.

Even though the parabolic trough receiver technology represents the most mature CSP technology available, it is believed that further improvements are possible [14,17,18,21]. The road map for the development of the parabolic trough technology highlights the research and development efforts needed to reduce the cost and improve the reliability and performance of the parabolic trough technology [23]. Research and development focus on all the components of the parabolic trough technology, ranging from improving the designs of the concentrators, trough receivers and reflectors, and the development of thermal storage systems, to advances in power cycle integration [21,23]. The SunShot initiative by the US department of energy represents one of the several research and development efforts to assess and improve the performance, increase the longevity and reduce the costs of CSP technologies [24].

Increasing the size of the collectors of parabolic trough systems has the potential for cost reduction. Increased collector size would lead to a reduction in collector interconnections, drives, electronics and controls, and would therefore reduce costs [18,21]. The concentrator can be increased either lengthwise or aperturewise. With the availability of lightweight materials, concentrators are now longer than the ones previously used in the SEGS plants [18,21]. The EuroTrough, a European-developed parabolic trough concentrator, represents about a 14% reduction in solar field cost due to the reduction in weight and an extension of the collector to 150 m [25,26]. The other notable major development in concentrator technology is the SkyTrough®DSP, a novel parabolic trough system being developed by SkyFuel [27]. The entire programme works to achieve an optimised trough working at base load and temperatures of 100 ^{o}C above the state-of-the art systems. With these high temperatures, concentration ratios of 40%-90% greater than the prior state of-the-art and optical accuracies of 30% – 75% over the prior state of-the-art are anticipated [27]. Currently, the developed SkyTrough®DSP parabolic trough system has a 25% increase in concentration ratio, a 40% increase in aperture width and a 50% increase in length, compared to today's troughs [27].

There is still a potential for an increase in parabolic trough concentration ratios. The maximum theoretical achievable geometrical concentration ratio for parabolic trough linear reflectors is about 212. Lower concentration ratios of about 61-82 are today's state-of-the-art for most of the installed commercial parabolic trough systems [10,16,18,21,25,28]. High concentration ratios would require highly accurate tracking mechanisms and improved receiver designs to overcome some of the limitations on operating at high temperatures. The performance limitations of the current receivers at high temperatures include the degradation of absorber tube selective coatings at high temperatures, the degradation of most heat transfer fluids beyond 400 ^{o}C [29], higher absorber tube selective coating emissivity at elevated absorber tube temperatures [30,31] and an increase in the circumferential temperature gradients of absorber tube [32-35]. Research to overcome these limitations and the development of improved receivers have been continuing and are still ongoing [21]. Further research efforts are being undertaken, such as research and development initiatives under the SunShot initiative [24].

As absorber tube coatings that can withstand high temperatures and as heat transfer fluids that can operate at higher temperatures are developed, the use of higher concentration ratios will become an attractive option. Already, the use of higher concentration ratios has been demonstrated for the SkyTrough®DSP parabolic trough [27]. With the increase in concentration ratios, the resulting high heat fluxes and the possible higher absorber tube circumferential temperature difference will necessitate high heat removal capacities from the receiver's absorber tube. The circumferential temperature differences in the receiver's absorber tubes are one of the causes of failure of receivers (glass cover breakages) [32,36]. For this reason, the reduction of these temperature gradients is paramount for increasing the life span of the receiver. Moreover, high heat fluxes on the receiver's absorber tube will increase the heat transfer irreversibilities due to the high finite temperature difference. Minimising these irreversibilities is also essential to improve the thermodynamic performance of the entire collector system.

Most studies on parabolic trough receivers focus mainly on the performance assessment, absorber tube selective coating, vacuum reliability, improved glass cover transmittance and improved absorber tube absorptance, with few or limited studies on enhancing the

thermodynamic performance and heat transfer. Some studies have considered the potential of heat transfer enhancement in the receiver's absorber tube, with a view to improving the performance of the receiver. Muñoz and Abánades [32] have demonstrated the potential of heat transfer enhancement for reducing the absorber tube's circumferential temperature difference. Enhancement of heat transfer in the receiver's absorber tube is not only essential for reducing the absorber tube's circumferential temperature difference, but also for improving the thermal and thermodynamic performance of the receiver. The improved thermal performance is achieved through a reduction in the receiver's heat loss, thus increasing the heat transfer rate from the absorber tube to the heat transfer fluid. These all lead to improved thermodynamic performance through a reduction of heat transfer irreversibilities, especially at a high concentration ratio.

Therefore, this work investigated the thermal and thermodynamic performance of the parabolic trough receiver at different rim angles, concentration ratios, inlet temperatures and Reynolds numbers. Also investigated were the potential of different heat transfer enhancement techniques for reducing the absorber tube's circumferential temperature difference, improving heat transfer performance and minimising entropy generation due to heat transfer and fluid flow processes in the receiver's absorber tube.

1.2 REVIEW OF RELATED LITERATURE

The research and development efforts in parabolic trough systems are broad, covering almost every component of the parabolic trough system [23,24]. In this research, the focus is on the thermal performance of the receiver as well as heat transfer enhancement in the receiver's absorber tube. As the receiver is responsible for converting highly concentrated solar radiation into thermal energy, it is one of the crucial components in parabolic trough systems [21,36,37]. It is one of the reasons for the high efficiencies achievable in the current parabolic trough systems [21,23]. It is also the most critical part as far as the reliability of the entire parabolic trough system is concerned. Experience in the operation of the SEGS plants shows that the failure of the receiver tubes is one of the largest contributors to the operational costs of the plants [18,21,36]. At SEGS plants the cost of replacing a failed receiver tube has a payback period of 1 – 5 years [21]. This is why one of ways of further bringing down the cost

of electricity from parabolic trough systems is by improving the thermal performance and reliability of the receiver.

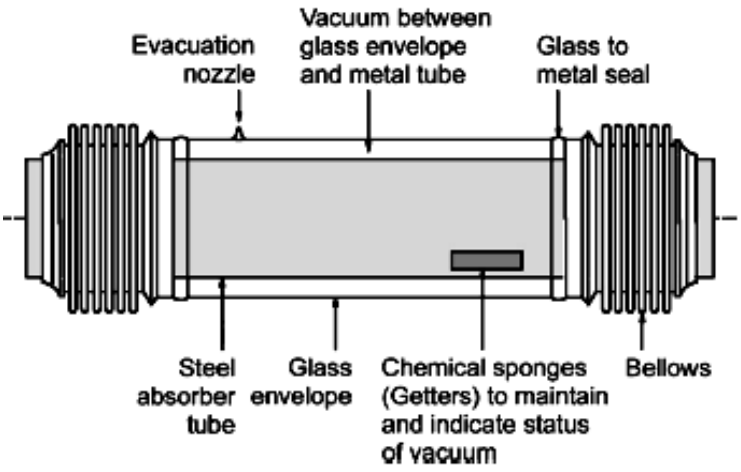

Fig. 1.4: Schematic diagram of a parabolic trough receiver tube [21].

The conventional receivers in use today consist of an absorber tube with a selective coating to minimise the radiation heat loss. The absorber tube is enclosed in an anti-reflective evacuated glass envelope to minimise the convection heat loss. The glass-to-metal seals and metal bellows are used to ensure a vacuum condition in the space between the absorber tube and the glass cover and to accommodate the difference in thermal expansion between the steel and the glass cover. Figure 1.4 shows a conventional receiver tube [21].

Several options for improving the reliability of receivers have been developed and other efforts are still continuing. These efforts have developed and tested receivers that differ from the Luz types designed for the SEGS plants. They include the Solel UVAC receiver [21] and the SCHOTTs receiver [30]. Other low-cost receivers for use in low-temperature parabolic trough systems have also been developed and their performance assessed [38,39]. As discussed above, heat transfer enhancement in the receiver's absorber tube will play a significant role in improving performance and in ensuring the receiver's reliability, especially when using higher concentration ratios. However, studies on the use of heat transfer enhancement techniques on the performance of receiver tubes are still limited.

The next sections present a review of the literature related to the thermal performance and heat transfer enhancement of parabolic trough receivers.

1.2.1 THERMAL PERFORMANCE OF PARABOLIC TROUGH RECEIVERS

The receiver's thermal performance greatly affects the thermal efficiency of the collector and the efficiency of the entire power plant. Accordingly, several studies dedicated to the assessment of the thermal performance of the receiver tube have been conducted. Most important, thermal performance analysis is used to assess the performance of different receiver configurations and different operating conditions. Studies on receiver thermal performance include experiments under actual operating conditions, steady-state laboratory investigations and recently, numerical analysis using computational fluid dynamics tools.

Dudley *et al.* [40] carried out thermal testing of the LS-2 collector and provided information on the efficiency and thermal losses of the collector under various operating conditions. A full collector module including the concentrator, the receiver, support structure was investigated using the AZTRAK rotating platform at the SANDIA National Laboratories. Two receivers with different coatings were used: cermet and black chrome in three configurations, i.e. one with a glass envelope and vacuum, another with a glass envelope filled with air and the third with a bare absorber tube. The cermet coated receiver had a performance superior to that of black chrome, given its lower emissivity. The evacuated receiver also showed better performance than the one with air in the annulus and the other with no glass envelope at all.

In a similar study, Dudley *et al.* [40] investigated the thermal performance of an Industrial Solar Technology collector [41]. The tests showed an improved optical efficiency of 77% because of the silver-film reflectors, the black nickel selective coating and the solgel anti-reflective glass receiver envelope used. An experimental facility for parabolic trough collectors was also built to assess the thermal performance of the collector in the Tongzhou district in Beijing [42]. The variables were the mass flow rate of the heat transfer fluid and the solar radiation heat flux. The efficiency achieved was in the range 40% – 60%.

Almanza *et al.* [35] experimentally studied the behaviour of receivers under direct steam generation. They concluded that, to avoid the thermal stresses from the presence of the

circumferential temperature difference in the receiver's absorber tube, steel tubes should be replaced by copper tubes. Using steel absorber tubes (thermal conductivity = 54 W $m^{-1}K^{-1}$) the temperature difference was about 60 ^oC causing a deflection of about 6.5 cm that broke the glass cover. When using copper absorber tubes (thermal conductivity = 389 $Wm^{-1}K^{-1}$), a temperature difference of 10 ^oC was observed with a deflection of 2 mm.

Concerning steady-state laboratory tests, the receiver is tested for thermal performance under uniform heat flux conditions. The electrical power needed to maintain the temperature constant is the receiver heat loss at that temperature. Burkholder and Kutscher [31] used this method to investigate heat loss in two Solel UVAC3 receivers in the range of absorber tube temperatures of 300 ^oC to 400 ^oC. The heat loss was presented as a function of the difference between the average absorber tube temperature and ambient temperatures. In a similar study, Burkholder and Kutscher [30] studied the heat loss for SCHOTT's new receiver (PTR®70). The heat loss was found to be a strong function of the average absorber tube temperature. The emissivity of the absorber tube also depended on the temperature of the absorber tube.

Lüpfert *et al.* [43] presented a study on the experimental analysis of the thermal performance of trough receivers. They used steady-state equilibrium, quasi-steady-state and surface measurement tests, all without solar irradiation, to determine the receiver's heat loss. Some deviations in the measurements were reported due to the different testing conditions. The assumed evenness of the absorber tube temperature for laboratory testing also represents a source of deviations in the measured heat loss. Nevertheless, these authors report the same trend of increasing heat loss with absorber tube temperature.

Price e*t al.* [44] reported the results obtained by using an infrared camera for evaluating the in- situ performance of parabolic trough receivers. They observed temperatures of up to over 170 ^oC in the glass cover, depending on the design of the receiver, the life of the receiver and whether the receiver incorporated hydrogen removers or had getters. Hydrogen build-up in the annulus space is one of the causes of the observed high receiver tube temperatures due to the increase in heat loss as hydrogen is formed in the vacuum space [45].

Forristall [45] developed and validated a heat transfer model for the parabolic trough receiver implemented in EES. The model accounts for all the heat transfer modes in the conventional

receivers with or without vacuum, as well as a receiver without a glass envelope, different absorber tube selective coatings, different gases in the annulus space and different wind speeds. Similar to the previous heat loss tests, the heat loss is expressed as function of the average absorber tube temperature above the ambient temperature. The heat loss increased as this temperature difference increased. In addition, the wind speed is shown to have a strong effect on the collector's thermal efficiency for the case of a bare absorber tube. The accumulation of hydrogen in the annulus space is shown to increase significantly the thermal losses when compared to the evacuated receiver tube and one with air in the annulus space. The author recommends a study of the possible use of heat transfer enhancement in the absorber tube to improve the receiver's thermal performance.

The presence of a circumferential temperature difference in parabolic trough receivers is a cause for concern and significantly affects their reliability [35]. Several studies have reported the existence of temperature gradients/differences in the circumference of the receiver's absorber tube [32-35,46]. These temperature gradients induce thermal stresses that can generate some bending moments in the receiver and therefore cause eventual failure, especially in high-performance applications such as direct steam generation [35,46]. Lüpfert *et al.* [46] experimentally produced temperature maps using an infrared camera with a highly spectral filter. They report uneven temperature distribution in the longitudinal direction as well as around the absorber tube circumference. He *et al.* [34] used a Monte-Carlo ray trace procedure coupled with a finite volume method to solve the heat transfer mechanism in the parabolic solar collector system. Their analysis also shows the existence of a circumferential temperature difference in the absorber tube. In an absorber tube of a fixed size, an increase in the geometric concentration ratio reduced the non-uniformity in the heat flux on the absorber tube surface. The studies by He *et al*. [34] and Cheng *et al*. [33] both demonstrate the use of a Monte-Carlo ray trace to represent the non-uniform solar flux on the receiver.

With the increased computational power of the available computers as well as advances in computational fluid dynamics, the complex heat transfer mechanisms underlying the thermal performance of a parabolic trough receivers can now be studied [33,34,47]. This has enabled several investigators to build numerical models to assess the thermal performance of various receiver configurations. He *et al.* [34] and Cheng *et al*. [33] demonstrate the use of numerical

methods that combine Monte-Carlo ray tracing and computational fluid dynamics so that the actual performance of parabolic trough collector system can be accurately represented.

Several other configurations of the receiver tube have been investigated. Roesle *et al.* [47] used computational fluid dynamics and Monte-Carlo ray tracing to study the performance of a parabolic trough receiver with an active vacuum system. They show that the temperature of the glass cover, the absorber tube temperatures and heat loss increase as the absorber tube temperature and heat transfer fluid temperature rise. Al-Ansary and Zeitoun [39] present the results of an investigation into an insulated air-filled annuli receiver tube for low temperature applications. The use of insulation significantly reduced the receiver's heat loss. A uniform heat transfer coefficient and a constant bulk fluid temperature were used as the boundary conditions on the absorber tube. The effect of the absorber tube's angle of orientation on heat loss was investigated and shown to be small. In another study on modified receivers for low temperature applications, Daniel *et al*. [38] showed that a receiver with an outer vacuum shell performed better than a non-evacuated receiver tube. The receiver also showed better performance than the evacuated receiver at a higher value of emissivity and that wind speed had a negligible effect on its performance. In their study, a uniform heat flux was assumed on the absorber tube circumference. The effect of the receiver's angle of orientation on thermal performance and glass cover temperature was not investigated.

In summary, a significant amount of research has been carried out to assess and improve the thermal performance of parabolic trough receiver tubes. All these investigations have shown that the thermal performance of the receiver is reduced as the absorber tube temperatures increase. Other studies showed the existence of non-uniform absorber tube circumferential temperatures, which are likely to induce stresses and cause receiver failures. Still other investigators showed the potential for modifying the receiver for low temperature applications, using air in the annulus space between the absorber tube and the glass cover. This would give a low-cost and reliable receiver by avoiding the use of the glass-to-metal seals found in conventional evacuated receivers. Most of the above studies are limited to the thermal analysis of the receiver, and none of the studies examines the thermodynamic performance of the receiver. Moreover, most of these studies do not present the effect of the rim angle and concentration ratio on both the thermal and thermodynamic performance and

use a uniform heat flux on the receiver's absorber tube. Thermodynamic performance analysis becomes important in parabolic trough systems, especially as the concentration ratios and heat fluxes on the receiver's absorber tube increase, resulting in higher entropy generation rates due to the greater difference in finite temperature.

1.2.2 HEAT TRANSFER ENHANCEMENT

As in other engineering applications, heat transfer enhancement in parabolic trough receivers has the potential to improve the receivers' performance significantly. In the literature review of the receiver's thermal performance presented above, it is shown that a receiver's heat loss mainly depends on the temperature of the absorber tube [30,31,43]. Therefore, improved receiver performance due to heat transfer enhancement can be achieved through a reduction in the absorber tube's average temperatures and an increased heat transfer rate from the absorber tube to the heat transfer fluid. Furthermore, the reduction in the absorber tube's circumferential temperature difference due to heat transfer enhancement [32] is another benefit of heat transfer enhancement, especially at low flow rates. This will be essential for improving the reliability of the receiver, especially as the use of higher concentration ratios becomes feasible [24,27]. As the absorber tube's average temperatures reduce, the radiation heat loss will also reduce, further improving the receiver's thermal performance. Further improvement in thermal performance due to a reduction in the radiation heat loss will result from the lower emissivity of the absorber tube's selective coating as the absorber tube's temperatures reduce. Moreover, a reduction of entropy generation at higher concentrations and higher heat flux is worth investigating as it could be another likely benefit of heat transfer enhancement in parabolic trough receivers.

Given the above benefits, considerable attention is being given to heat transfer enhancement in parabolic trough receivers. Studies on various techniques for heat transfer enhancement in parabolic trough receivers are recommended [45]. The role of computational fluid dynamics in studying heat transfer enhancement in parabolic trough receivers under actual conditions or approximate conditions cannot be under-estimated. Recent studies have used computational fluid dynamics tools to represent the complex heat transfer mechanisms involved in parabolic trough receivers.

Reddy *et al.* [48] used porous fins to study heat transfer enhancement in parabolic trough receivers. They used a commercial computational fluid dynamics code (FLUENT) in their analysis and used the RNG k-ε model for turbulent closure. The performance of the porous fins was compared with that of a solid fin and found to be significantly better. They presented a correlation for the Nusselt number and used a comparative study to obtain optimal porous fin geometries. The optimum fin geometry was found to be 4 mm for the considered receiver tube with a spacing of 49.5 mm between the consecutive porous fins.

Kumar and Reddy [49] report on an investigation on heat transfer enhancement in a parabolic trough receiver with wall-mounted porous discs. Different orientations, heights and distance between the discs were considered and their influence on the receiver's thermal performance investigated. They achieved optimum thermal performance with a top-mounted half-porous disc receiver with a height $H = 0.5d_i$, spacing $w=d_i$ and angle of orientation $\theta = 30^o$. At the optimal configuration, the Nusselt number increased by about 64% and the pressure drop penalty of 457 Pa against a tubular receiver was obtained.

Recently Muñoz and Abánades [32] used CFD tools to investigate the use of internal helical fins on the performance of a parabolic trough receiver. The emphasis of the study was on reducing the temperature gradients in the receiver's absorber tube. The temperature difference of about 176.5 ^{o}C in the absorber tube for non-enhanced receiver was obtained for the low flow rates used. The authors show that using internally helically finned absorber tubes, the temperature difference can be reduced by up to 41.6% depending on the configuration of the helical fins.

Another recent study by Cheng *et al.* [50] showed an improvement in the heat transfer enhancement of the receiver tube using longitudinal vortex generators. They studied the effects of Reynolds numbers, heat transfer fluid inlet temperature, incident solar radiation and geometrical parameters of the vortex generators. These authors show that for a smooth tube, the increase in Reynolds number reduces both the heat loss and the absorber wall temperatures. The performance evaluation in heat transfer enhancement based on equal pumping power is shown to increase with an increase in the temperature of the heat transfer fluid. The thermal loss for the enhanced receiver is reduced by 1.35% – 12.10% for the range of parameters studied. Larger Reynolds numbers provided a comprehensive heat transfer

performance. The average Nusselt number and average fluid friction increased with the geometrical parameters while the wall temperature and thermal losses decreased with an increase in the geometrical parameters considered.

Despite the limited studies on heat transfer enhancement in parabolic trough receivers, the field of heat transfer enhancement has been greatly developed and various heat transfer enhancement techniques have been developed and investigated. The review on heat transfer enhancement by Bergles [51,52], Webb [53] and Manglik [54] indicates the importance of heat transfer enhancement and the enormous database of technical literature available.

The enhancement techniques are broadly classified as passive – those requiring no direct external power input, and active – those requiring direct external power input [53]. The effectiveness of either of the two methods strongly depends on the application under consideration and whether it is used for single-phase or multi-phase heat transfer [52]. Since these techniques involve no direct external power supply and usually have fewer complications, passive enhancement techniques tend to be used more in most applications and have been widely investigated [53]. Their enhancement capabilities for a given application can be determined using different criteria as given by Bergles and by Webb [52,53].

The available passive techniques for heat transfer enhancement include [52] the following:

- Treated surfaces – involving the fine-scale alteration of surface finish or coating.
- Rough surfaces – ranging from random sand grain-type rough surfaces to discrete protuberances.
- Extended surface – including the use of fins, interrupted surfaces and ribbed surfaces.
- Displaced enhancement devices – these are inserted into the flow channel to indirectly improve energy transport at the heated surface. Flow is displaced from the core of the flowing fluid to the surface being cooled.
- Swirl flow devices – including geometrically varied flow arrangements, duct modification and tube inserts. They promote heat transfer through fluid agitation and mixing induced by the generated secondary circulation from the helical fluid motion. They include twisted tapes, axial cores with screw-type windings, helical vane inserts, static mixers, inlet swirl vanes and helically twisted tubes.

- Coiled tubes – generating secondary flow, leading to higher single-phase coefficients.
- Surface tension devices – consisting of wicking or grooved surfaces to direct the flow.
- Additives for liquids and additives for gases.

Two or more of the above techniques may be used together to provide better heat transfer enhancement.

Among the passive enhancement techniques mentioned above, tube inserts appear attractive for heat transfer enhancement in parabolic trough receivers. Given the high temperatures and high heat fluxes that can be achieved and the likely thermal stresses due to modification of the absorber tube surface, the absorber tube surface should essentially be left intact and heat transfer enhancement achieved through fluid agitation, mixing or displacement. Furthermore, it is paramount to avoid formation of temperature hot spots that are likely in areas of low heat transfer, as is the case with enhancement techniques involving re-circulation and re-attachment. With the current heat transfer fluids, the decomposition of the heat transfer fluid is accelerated with temperatures higher than 400 ^{o}C [29,55] and the hydrogen formed significantly increases the heat loss [45,46].

Several inserts are available as displaced enhancement devices or as swirl flow devices. Among the swirl flow devices, twisted tape inserts are the most widely used devices in many industrial applications for transfer enhancement [56]. They provide very high heat transfer enhancement with a relatively low pressure drop and are easy to install [52,54,56]. Regarding displaced enhancement devices, the heated surface is left intact and fluid flow near the surface is altered by the insert. Displaced enhancement devices include metallic mesh, static mixer elements, rings, disks or balls. They provide significant heat transfer enhancement but have a high pressure drop. In view of this, a method for heat transfer enhancement in the core flow along the tube was developed by Liu *et al.*[57,58]. They propose temperature uniformity in the core flow of the tube as a way of forming a thin thermal boundary layer near the wall and a high temperature gradient and these have high heat transfer enhancement effect. The essentials and further consideration of the proposed mechanism include: (a) strengthening the temperature uniformity in the core flow; (b) avoiding an increase in velocity gradients in the core; (c) reducing the disturbance to the hydrodynamic boundary layer inside the tube; and (d) reducing the surface area of the heat transfer component in the core flow to minimise

surface friction [57]. The use of porous media inserts is considered to satisfy the above requirements, especially for ensuring temperature uniformity [57-59]. The additional benefits of the use of porous media in heat transfer enhancement are better stiffness and a light weight, higher surface area to volume ratio and reduced local thermal stresses [60].

Therefore, twisted tape inserts and displacement enhancement devices have the potential to enhance heat transfer in parabolic trough receivers. In the present research, an investigation of heat transfer enhancement in parabolic trough receivers using twisted tape inserts and perforated inserts is considered numerically. The perforated inserts investigated are perforated plate inserts and perforated conical inserts.

Heat transfer enhancement results in increased fluid friction irreversibility and reduced heat transfer irreversibility. Thermodynamic optimisation requires that the generated entropy due to heat transfer enhancement should be less than that of a non-enhanced device or, better still, should be a minimum [61]. This is because the generation of entropy is directly proportional to the destruction of the available work according to the Gouy-Stodola theorem [61]. Higher entropy generation rates result in greater destruction of the available work. The entropy generation minimisation method (EGM) that is synonymous with thermodynamic optimisation, second law analysis, etc. and first introduced by Bejan [62], provides a means of determining the irreversibilities in engineering systems through the second law of thermodynamics. The EGM method combines the fundamental principles of fluid mechanics, heat transfer and thermodynamics for establishing the irreversibility in a system or system components. In heat transfer, the EGM method finds applications in both internal and external flows, heat exchanger design as well as in heat transfer enhancement [61]. Therefore, for each heat transfer enhancement technique, the resulting entropy generation rates will be analysed and compared to those in plain absorber tubes.

Furthermore, in addition to heat transfer enhancement, most heat transfer enhancement techniques result in increased pressure drops. For applications where maximizing the heat transfer and minimizing the pressure drop are equally important, the heat transfer technique should be optimised so that sufficient heat transfer enhancement is achieved with the minimum pressure drop or fluid friction. This presents a multi-objective optimisation problem. There is no single solution which satisfies both objectives for such a problem.

Instead, a set of solutions called non-dominated solutions is sought, in which an increase in the quality of one objective sacrifices the quality of the other [63]. Therefore, the designer has a choice among a set of trade-off solutions. Multi-objective genetic algorithms are suited to such problems [63,64] and have been used for the analysis of engineering problems involving more than one objective [65-72] as well as in the optimisation of heat exchangers and heat transfer devices [73-80].

In summary, heat transfer enhancement in parabolic trough receivers provides a means of improving performance and reducing temperature gradients in the receiver's absorber tube. Despite the significant amount of research on heat transfer enhancement in many engineering applications, there has been little research on heat transfer enhancement in parabolic trough receivers. Moreover, studies are not widespread on heat transfer enhancement in parabolic trough receivers with the realistic non-uniform heat flux boundary condition on the receiver's absorber tube. Most studies on heat transfer enhancement, as provided in reviews by Webb [53], Manglik [54] and Bergles [51,52,56], use constant heat flux or constant temperature boundary conditions on the tube's surfaces, yet parabolic trough receivers present a non-uniform heat flux distribution on the absorber tube's surface. Furthermore, the studies presented in the above reviews provide significant information on heat transfer and fluid friction and correlations are presented in most cases. However, studies are not widespread on finding optimum configurations based on multi-objective optimisation techniques and thermodynamic optimisation through entropy generation minimisation.

1.3 NEED FOR THE STUDY

The increased need for reducing the cost of electricity from concentrated solar power systems is one of the drivers of the current research on and development of concentrated solar power technologies. Improving the performance of the receiver and increasing the concentrator sizes (concentration ratios) are some of the cost reduction options for parabolic trough technology.

The use of higher concentration ratios in parabolic trough collectors provides an opportunity to reduce system costs. However, high concentration ratios give rise to high heat fluxes and result in high absorber tube circumferential temperature gradients and high heat transfer irreversibilities in parabolic trough receivers. With these, heat transfer enhancement appears an attractive option for improving receiver's thermal performance.

Despite the enormous number of investigations on heat transfer enhancement and the several heat transfer enhancement techniques developed, heat transfer enhancement in parabolic trough receivers has not been widely investigated. Moreover, entropy generation in the receiver at different concentration ratios, rim angles, inlet temperatures and Reynolds numbers and the analysis of entropy generation of several heat transfer enhancement techniques used in parabolic trough receivers, have not been investigated. In addition, most of the studies available in the literature on the thermal performance of parabolic trough receivers assume a constant heat flux around the circumference of the receiver's absorber tube, yet the actual realistic heat flux profile is non-uniform.

Therefore, in this work an appropriate thermal model of a parabolic trough receiver is developed and used to investigate the thermal and thermodynamic performance of a parabolic trough receiver with and without inserts for heat transfer enhancement. Unlike, other models that assume constant heat flux on the reeciver's absorber tube, this model uses the actual heat flux profile which provides a means for determining actual circumferential temperature gradients in the receiver's absorber tube.

1.4 RESEARCH OBJECTIVES

1.4.1 GENERAL OBJECTIVE

The overall objective of this work was to develop thermal and thermodynamic models for investigating the performance of a parabolic trough receiver and to investigate the potential for improvement in receiver thermo-hydraulic and thermodynamic performance with several heat transfer enhancement techniques.

1.4.2 SPECIFIC OBJECTIVES

In order, to achieve the general objective, the following specific objectives were defined:

- To develop and validate a numerical model to predict the thermal performance of parabolic trough receivers with a realistic non-uniform heat flux profile.
- To investigate the entropy generation due to heat transfer and fluid flow irreversibilities in parabolic trough receivers at different operating conditions.
- To investigate the heat transfer enhancement potential of twisted tape inserts, perforated plate inserts and perforated conical inserts in parabolic trough receivers: develop

relevant correlations for heat transfer and fluid friction, determine the potential absorber tube circumferential temperature reductions and determine the resulting entropy generation rates.

- To determine optimal configurations and conditions of the considered heat transfer enhancement techniques for maximum heat transfer rate, minimum fluid friction and minimum entropy generation.

1.5 RESEARCH APPROACH

The developments in electronics have made high power and fast computers available. This, together with availability of general-purpose CFD codes, has made it possible to solve complex heat transfer and fluid flow problems with complex boundary conditions, complex geometries as well as complex multi-physics. The present research used a general-purpose commercial CFD code to study the thermal performance and heat transfer enhancement in parabolic trough receivers. A numerical model was developed and validated to predict the performance of a parabolic trough receiver. The developed model was then used to evaluate the receiver's thermal and thermodynamic performance.

Several techniques for heat transfer enhancement in the receiver's absorber tube have been suggested and analysed numerically. The heat transfer enhancement techniques include the use of wall-detached twisted tape inserts, perforated plate inserts and perforated conical inserts. The potential of these enhancement techniques in providing maximum heat transfer enhancement at minimum pressure drop with low levels of entropy generation was also investigated through the simultaneous use of multi-objective optimisation and entropy generation minimisation.

For all the numerical investigations, validation was achieved by conducting mesh dependence tests and comparing the numerical results with the experimental data or numerical data reported in related studies available in the literature.

1.6 ORGANISATION OF THE THESIS

This thesis is organised in eight chapters. For better organisation and ease of understanding, Chapters four, five, six, and seven are written as semi-autonomous chapters, detailing the solution procedure, validation of the numerical models, results and discussions and

conclusions. Chapters five, six and seven have been written with stand-alone introduction sections for a better work flow. Chapter three gives the detailed explanation of the numerical modelling framework and optimisation. A detailed explanation of each chapter of the thesis is given below.

- **Chapter One** provides a general background to the study, presents a brief review of the related literature on parabolic trough receiver thermal performance and heat transfer enhancement. The need for the study, objective of the study and research approach are also presented in this chapter.
- **Chapter Two** gives a review of the fundamentals of concentrated solar power systems, with specific emphasis on parabolic trough receivers. An in-depth presentation of the theoretical aspects of the thermal and thermodynamic performance of the parabolic trough receivers is given in this chapter.
- **Chapter Three** presents the numerical modelling used in this study. The governing equations and turbulence modelling procedure are discussed in detail. This chapter also presents the fundamental aspects of the method for minimising entropy generation for heat transfer problems. Finally, the chapter discusses the multi-objective optimisation method. The optimisation procedure used in the present work is presented in detail with a discussion of the relevant steps involved.
- **Chapter Four** presents the development and validation of the numerical model for the thermal performance of a parabolic trough receiver. This chapter demonstrates the non-uniformity of heat flux on the receiver and the presence of circumferential temperature difference in the receiver's absorber tube. The thermal performance of the receiver with non-uniform heat flux at different rim angles and concentration ratios is discussed in this chapter.
- **Chapter Five** provides an analysis of the entropy generation in parabolic trough receivers at different conditions. This chapter gives a detailed analysis of entropy generation in a parabolic trough receiver with a plain absorber tube at different inlet temperatures, concentration ratios, rim angles and Reynolds numbers. The entropy generation due to heat transfer and fluid flow irreversibilities are investigated

numerically. The chapter also compares the entropy generation due to heat transfer and fluid flow with the entropy generation for the entire collector system.

- **Chapter Six** describes a detailed numerical investigation of heat transfer enhancement in a parabolic trough receiver, using twisted tape inserts. Different twist ratios and width ratios of the twisted tape are considered and an analysis given of the potential of the twisted tape inserts for improving heat transfer and the thermal performance of the receiver, reducing the absorber tube's circumferential temperature difference and minimising entropy generation. Correlations for Nusselt numbers and the friction factor obtained are also presented. The chapter further presents the results from the multi-objective optimisation approach.
- **Chapter Seven** presents a detailed numerical investigation of heat transfer enhancement in a parabolic trough receiver, using perforated inserts. Two types of inserts are considered, i.e. perforated plate inserts and perforated conical inserts. For different variables of the two inserts, the potential is investigated for enhancing heat transfer, reducing the absorber tube's circumferential temperature difference and minimising entropy generation using each insert. Correlations for Nusselt numbers and the fluid friction are developed and presented. The chapter also presents the results of a multi-objective optimisation approach to maximise heat transfer and minimise fluid friction for each of the inserts considered.
- **Chapter Eight** provides the general conclusions drawn from this study and makes recommendations on possible future work.

CHAPTER TWO

CHAPTER TWO: CONCENTRATED SOLAR POWER FUNDAMENTALS

2.1 INTRODUCTION

This chapter serves to lay a foundation for an understanding of concentrated solar power. It begins with a description of the commonly used concentrated solar power technologies, the advantages and disadvantages of each and then gives a more detailed theoretical background to parabolic trough technology.

2.2 CONCENTRATED SOLAR POWER TECHNOLOGIES

In the past decade, the concentrated solar power (CSP) industry has grown rapidly and is expected to continue growing in the next years. CSP installations generated about 436 MW of the world's electricity by 2008, the projects under construction in 2009 were expected to add another 1 000 MW by 2011 and other planned projects are expected to add another 10 000 MW by 2017 [17]. The installed capacity was about 3.6 GW by the end of 2013 according to the IEA 2014 technology roadmap for solar thermal electricity [81]. This shows the rapid growth of the CSP industry sector. The cost of CSP electricity is decreasing and it is deemed that it will continue decreasing and become competitive with thermal generation from medium sized coal plants [17,19]. The cost of CSP electricity is mainly affected by the solar resource, grid connectivity, local infrastructure, project development costs and type of technology. Cost reductions can be achieved by scaling-up plant sizes, advances in research and development, greater market competition and the increased production volume of components, and government actions through good legislation, preferential financing and tax or investment incentives [17].

The concept of concentrating solar radiation to achieve higher temperatures was first demonstrated by Archimedes around 212 B.C., when he devised a concave metallic mirror from hundreds of polished shields to burn an attacking Roman fleet [16]. Since then, many

attempts have been made to convert solar energy into other forms [16]. The commercial exploitation of concentrated solar power was demonstrated in the mid-1980s, when the first large-scale solar electricity generation plants were built in California's Mojave Desert [13,16,21]. Given the vast renewable resource it uses (the sun) and very few shortcomings, CSP has since demonstrated huge technical and economic promise [17] and many technologies have been developed and others are still in the research and development phase.

Most technologies for concentrating solar power and its consequent conversion into electricity use the same principle. The main components required for all CSP technologies include a concentrator, a receiver, heat transport media or storage, and a power conversion unit. The variation in the shape and configuration of these components is what differentiates one technology from another. The four major CSP technologies for electricity generation are the parabolic trough, the parabolic dish, the central receiver (also called solar tower) and the linear Fresnel reflector.

2.1.1 PARABOLIC TROUGH

In this type of technology, parabolic trough shaped mirrors reflect the sun's direct solar radiation onto a linear receiver, also called the heat collection element, placed at the trough's focal line as shown in Fig. 2.1. The parabolic trough collectors have the property that all rays parallel to the axis of the parabola are reflected to a single point, the focal point of the parabola, and for cylindrical collectors the rays are reflected to a focal plane. Parabolic trough systems for high temperature delivery fall in the category of sun-tracking imaging collectors where the system continually follows the motion of the sun. Figure 2.1 shows an arrangement of a parabolic trough collector system.

Usually single-axis tracking is sufficient, making it possible to use long collector modules [16] Geometrical concentration ratios up to 212 are theoretically achievable. The heat transfer fluid circulating through the receiver is heated (up to about 400 ^{o}C) and pumped through a series of heat exchangers to produce superheated steam. The superheated steam is then used for electricity generation in a cycle similar to the conventional steam cycle or integrated into a combined steam and gas cycle or an organic Rankine cycle [15].

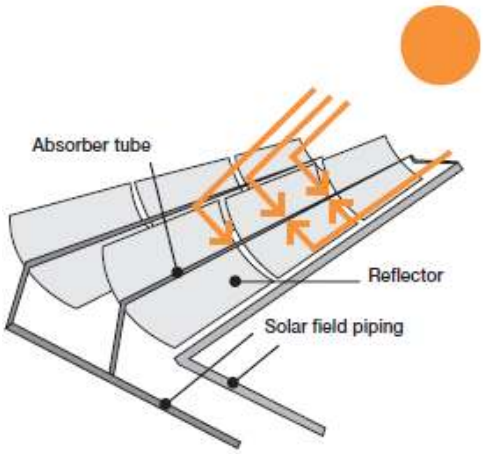

Fig. 2.1: Schematic diagram of a parabolic trough solar collector assembly [15].

2.1.2 CENTRAL RECEIVER/SOLAR TOWER

These make use of a circular array of heliostats (larger individually tracking mirrors) to concentrate the sun's direct solar radiation onto a central receiver. The highly concentrated radiation is then absorbed in the central receiver by an absorber and converted into thermal energy that is used for the generation of superheated steam. The heat transfer fluids mainly used include water/steam, molten salts, liquid sodium and air [15]. The high heat flux intercepted by the receiver results in temperatures higher than 1 500 ^{o}C [16]. Figure 2.2 shows an arrangement of a central receiver.

2.1.3 PARABOLIC DISH

This concentrates direct solar radiation onto a receiver at its focal point. The schematic representation of the dish system is shown in Fig. 2.3 [15]. The dish must track the sun fully to reflect direct radiation onto the receiver. These receivers can achieve temperatures above 1 500 ^{o}C, concentration ratios between 600 – 2 000 and are the most efficient of all the CSP technologies [16].

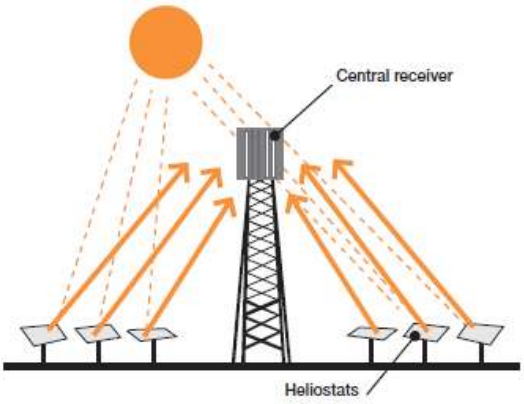

Fig. 2.2: Schematic diagram of a solar thermal collector system with heliostats and a central receiver [15].

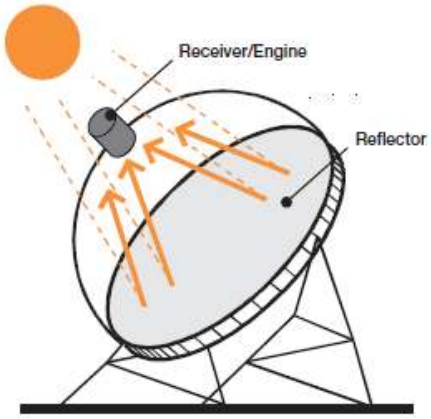

Fig. 2.3: Schematic diagram of a parabolic dish solar thermal system [15].

2.1.4 LINEAR FRESNEL REFLECTOR (LFR)

These make use of near-flat reflector arrays to concentrate solar radiation onto elevated inverted linear receivers. Similar to parabolic trough systems, they are also linear focusing systems. They have the advantages of low cost for structural supports and reflectors, fixed fluid joints, receivers separated from the reflector system and long focal length allowing the use of flat mirrors [17].

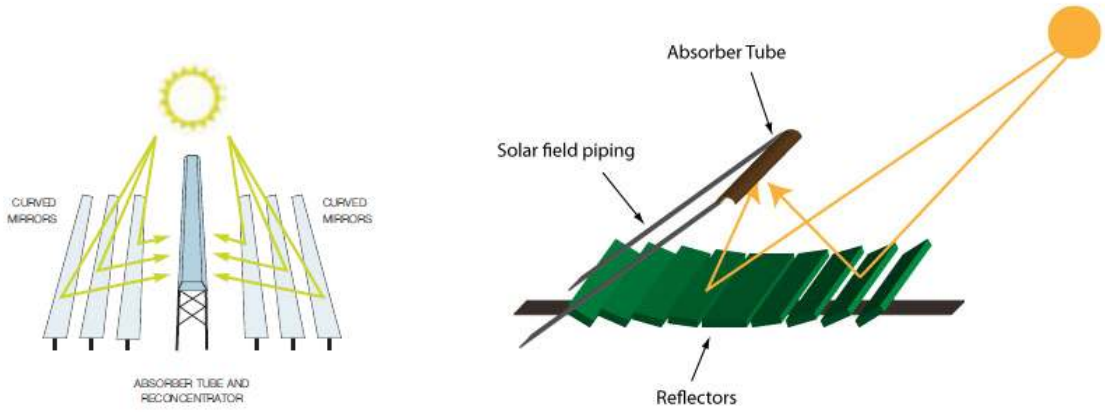

Fig. 2.4: Schematic diagrams of linear Fresnel solar thermal systems [17].

Parabolic trough technology represents the most mature solar thermal technology, both commercially and technically [15,17,21]. With research and development, the other technologies also have significant potential for concentrated solar power. Table 2.1 shows a summary of the application, advantages and disadvantages of each technology.

Table 2.1: Comparison of the main types of concentrated solar thermal technologies.

	Parabolic trough	**Central receiver**	**Parabolic dish**	**Fresnel linear reflector**
Applications	- Grid-connected plants, mid to high-process heat. - Highest single unit solar capacity to date: 80 MWe. - Total capacity built: over 500 MW and more than 10 GW under construction or proposed.	- Grid-connected plants, high temperature process heat. - Highest single unit capacity to date: 20 MWe under construction. - Total capacity – 50 MW with at least 100 MW under development.	- Stand-alone, small off-grid power system or clustered to large-scale grid-connected dish parks. - Highest single unit capacity to date: 100 kWe, proposal for 100 MW and 500 MW in Australia and US.	- Grid connected, or steam generation. - Highest single unit to date: 5 MW, with 177 MW of installation and under development.
Advantages	- Commercially Available. - Commercially proven annual net efficiency of 14% (solar radiation to electric output).	- Good mid-term prospects for high conversion efficiencies, operating temperature potential beyond 1 000 ^{o}C.	- Very high conversion efficiencies – peak solar to net electric conversion efficiency of over 30%. - Modularity. - Most effectively	- Readily available. - Flat mirrors can be purchased and bent on site leading

	- Commercially proven investment and operation costs. - Modularity - Good land-use factor - Lowest material demand. - Hybrid concept proven. - Storage capability.	- Storage at high temperatures. - Hybrid systems operational. - Better suited to dry cooling concepts. - Better options to use non-flat sites.	integrated thermal storage for a large plant. - Operation experience of first demonstration projects. - Easily manufactured and mass-produced from available parts. - No water requirements for cooling the cycle.	to lower manufacturing costs. - Hybrid operation possible. - Very high space efficiency around solar noon.
Disadvantages	- The use of oil-based heat transfer media restricts operating temperatures today to 400 °C, resulting in only moderate quality steam.	- Projected annual performance values, investment and operating costs need wide-scale proof in commercial operation.	- No large-scale commercial examples. - Project cost goals of mass production still to be proven. - Lower dispatchability potential for grid integration. - Hybrid receivers still an R&D goal.	- Recent market entrant, only small projects operating.

Source: Adopted from Richter *et al.* [17].

Despite being the most technically and commercially proven of the CSP technology, research and development of parabolic trough system components is still ongoing. The recent developments include [15]: (i) advanced structural design to improve optical accuracy to reduce weight and costs; (ii) increasing collector sizes to reduce end losses, reduce on-drive systems and controls as well as connection piping; (iii) Next-generation receiver tubes to reduce thermal losses and increase reliability; (iv) improvements in the heat transfer medium operating temperature and performance; and (v) low-cost thermal bulk storage to increase annual operating hours and reduce generation costs. With the use of high concentration ratios, the absorber tube's circumferential temperature difference and heat transfer irreversibility are expected to increase. Therefore, heat transfer enhancement will prove crucial to reducing the absorber tube's circumferential temperature difference and minimising the heat transfer irreversibility. The present research has been done on the thermal performance and heat

transfer enhancement of the parabolic trough receiver. The following sections discuss the theoretical analysis of parabolic trough collectors as well as the thermal performance of the receiver.

2.3 PARABOLIC TROUGH COLLECTORS

Parabolic trough collectors are sun-tracking as well as concentrating collectors. For energy delivery at high temperatures, solar radiation is usually concentrated onto a small collection area by interposing an optical device between the sun and the heat collection surface [16]. Because of this, concentrating collectors collect very little diffuse radiation and some form of tracking is essential to ensure that the collector follows the sun. Figure 2.5 shows the installed EuroTrough collector system in operation.

Fig. 2.5: Photograph of an installed EuroTrough parabolic trough system [26].

When pointed towards the sun, parallel rays from the sun are reflected onto a linear receiver, as such single-axis tracking is sufficient. Collectors are usually oriented along the east-west axis, tracking the sun from north to south or along the north-south axis, tracking the sun from east to west depending on the demand for the produced energy. The east-west oriented trough collectors with north-south tracking require less adjustment through the day and the full aperture always faces the sun at noon. But their performance in the early and late hours is strongly affected by large incidence angles. The north-south oriented trough collectors have high cosine losses at noon and the lowest losses during the mornings and evenings when the sun is due east or due west [16].

The main components of the parabolic trough collector system include the concentrator, the receiver, the tracking mechanism and the supporting structure. The concentrator is made by bending a sheet of reflective material into a parabolic shape [10,16]. The high-quality of the glass material used has a high reflectivity – over 0.98. The receiver or heat collection element is the part of the collector system where the absorbed radiation is converted into heat and transferred to a heat transfer fluid. It consists of a linear metallic tube, called the absorber tube that is placed along the focal line of the trough and surrounded by a glass envelope that is evacuated to suppress convection loss. The size of the absorber is determined by the size of the reflected image of the sun and the tolerances during the manufacture of the trough [16]. Various forms of tracking the sun are available from very simple to very complex. Tracking mechanisms can be categorised as mechanical and electrical or electronic systems. The electronic systems give greater reliability and tracking accuracy; they include mechanisms employing motors controlled electronically through sensors that detect the magnitude of solar radiation and mechanisms using computer-controlled motors that provide feedback by measuring the solar heat flux on the receiver [16]. Several structural concepts have been proposed, such as the steel framework structures with central torque tubes or double V-trusses or fibreglass [10]. Recently, the design and manufacture of the Euro trough collector with advanced light-weight structures has significantly reduced the cost of electricity from parabolic trough receivers [25,26]. Advances in the research and development of parabolic trough technology and several achievements in terms of efficiency and cost reduction are presented by Price *et al.* [21].

2.3.1 PARABOLIC TROUGH GEOMETRY

The geometry of the collector plays a significant role in the performance of the entire collector system. The optical efficiency and how much of the reflected rays are intercepted by the receiver are significantly influenced by the accuracy with which the concentrator is made.

The geometry of the cross-section making up the parabolic trough concentrator is shown in Fig. 2.6 [10]. The important factors to consider in designing the collector include: the rim angle, φ_r; the rim radius, r_r; the focal distance, f_p; half acceptance angle, θ_m; and the receiver diameter to intercept the entire solar image, D.

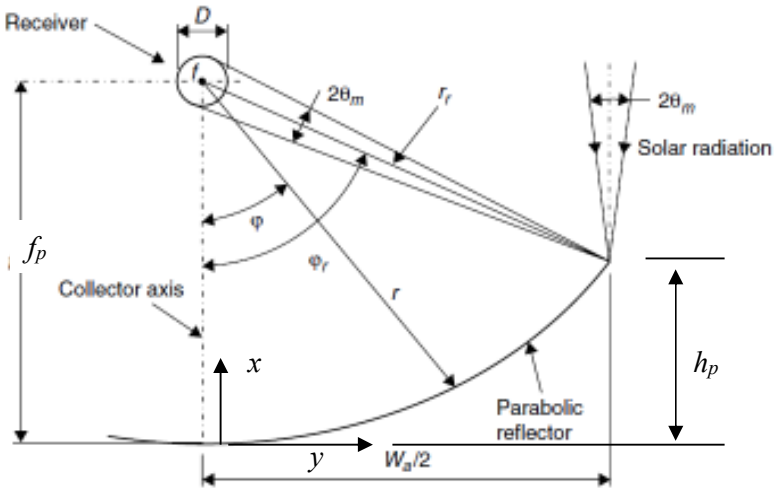

Fig. 2.6: Schematic diagram showing parabolic trough collector geometry and reflection of rays from the mirror.

The equations for determining these parameters are presented by Kalogirou, Duffie and Beckman and Stine *et al*. [10,28,82] respectively.

The parabolic shape forming the concentrator is defined by the equation:

$$y^2 = 4 f_p x \tag{2.1}$$

For specular reflectors, and considering perfect alignment, there is a size of a circular receiver for which all of the incident solar image will be intercepted. Trigonometrically, the size D to intercept the entire solar image is given as [10]

$$D = 2 r_r \sin(\theta_m) = \frac{W_a \sin(\theta_m)}{\sin \varphi_r} \tag{2.2}$$

The half acceptance angle, θ_m, is determined by the accuracy of the tracking mechanism and the irregularities appearing in the reflector surface [10]. A small effect of these two gives θ_m close to the sun disc angle of about 16' and thus a smaller image and higher concentration. By contrast, a large effect of the error in tracking and reflector surface will result in image spread and less concentration.

The rim radius is given accordingly as

$$r = \frac{2f_p}{1+\cos\varphi} \tag{2.3}$$

where φ is the angle between the collector axis and a reflected beam at the focus, so that the rim radius (r_r) is a maximum at the rim of the collector and is determined from Eq. (2.3) when $\varphi = \varphi_r$.

The collector's aperture W_a is also given from Fig. 2.6 as

$$W_a = 2r_r \sin\varphi_r \tag{2.4}$$

Combining Eq. (2.3) and Eq. (2.4) gives

$$W_a = \frac{4f_p \sin(\varphi_r)}{1+\cos(\varphi_r)} = 4f_p \tan\left(\frac{\varphi_r}{2}\right) \tag{2.5}$$

The equations given above define a parabola of an infinite extent. For a truncated portion usually employed for actual collectors, the extent of the parabola depends on the ratio of the focal length to the aperture's width [82]. The size of the truncated curve can then be specified for a given aperture in terms of either f_p or W_a as shown in Fig. 2.7 [82].

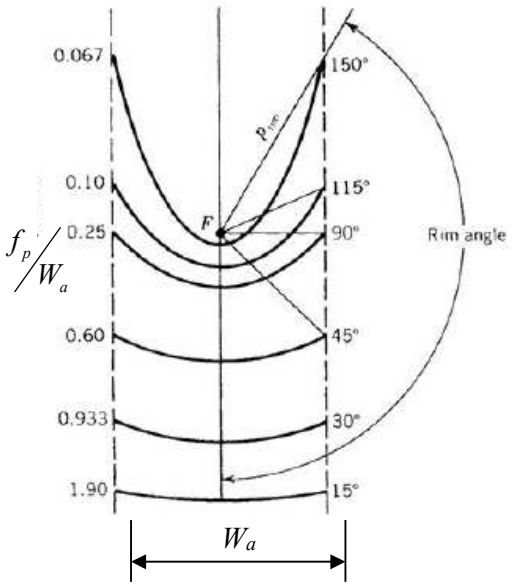

Fig. 2.7: Focal length to aperture width ratio *(f_a/W_a)* as a function of rim angle at a given aperture width [82].

Once a specific curve has been selected, the height of the parabola, h_p, shown in Fig. 2.6 is given by

$$h_p = \frac{W_a}{16 f_p} \tag{2.6}$$

The rim angle is given by

$$\varphi_{rim} = \tan^{-1}\left[\frac{8\left(f_p/W_a\right)}{16\left(f_p/W_a\right)^2 - 1}\right] = 2\tan^{-1}\left[\frac{1}{4\left(f_p/W_a\right)}\right] = \sin^{-1}\left(\frac{W_a}{2r_r}\right) \tag{2.7}$$

Figure 2.7 shows that it is possible to use different rim angles for the same aperture. The mean focus-to-reflector distance is minimised as the rim angles increase but the material usage increases. With minimum focus-to-reflector distance, the beam spread is minimised because such tracking errors and slope errors are less pronounced [10]. However, a trade-off has to be made concerning the sacrifice in optical efficiency achievable at high rim angles and the material savings achievable at low rim angles.

For a tubular receiver, the geometric concentration ratio, C_R, is defined as the ratio of the projected aperture area to the projected area of the receiver as

$$C_R = \frac{W_a \times L}{D \times L} \tag{2.8}$$

where L is the span-wise length of the collector and receiver.

Substituting Eq. (2.2) and Eq. (2.4) in Eq. (2.8) gives

$$C_R = \frac{\sin(\varphi_r)}{\sin(\theta_m)} \tag{2.9}$$

According to Eq. (2.9), maximum geometric concentration ratio will occur when $\varphi_r = 90^o$ and is given as $(C_R)_{max} = 215$ for a half angle of 16'. Low concentration ratios are generally used,

currently up to 82 [21]. Higher concentration ratios are possible [24,27] but the tracking mechanisms should be as accurate as possible [16].

2.3.2 OPTICAL EFFICIENCY

The collector's optical efficiency determines how much of the incident solar radiation will be absorbed by the receiver. Several factors determine the collector's optical efficiency and these include: the optical properties of the materials used, the geometry of the collector and various imperfections arising from the collector during manufacture and assembly. Other errors are due to the fact that the sun's rays are not truly parallel. Many variations exist in the expressions for determining the collector's optical efficiency; the widely used and acceptable definition is given by Kalogirou [10] as

$$\eta_o = \rho_c \tau_g \alpha_{abs} \gamma \left[(1 - A_f \tan\theta) \cos\theta \right] \qquad 2.10$$

where ρ_c – is the reflectivity of the concentrator mirror, τ_g – the transmissivity of the glass envelope, α_{abs} – the absorptivity of the absorber tube, θ – the angle of incidence of the solar rays. A_f is the geometric factor defined from the geometry of the collector, measuring the effective reduction of the aperture area due to abnormal incidence effects including: blockages, shadows and loss of radiation reflected from the mirror beyond the end of the receiver [10]. The parameter γ is the intercept factor defined as the ratio of energy intercepted by the receiver to the energy reflected by the collector.

The suggested value of A_f was given by Jeters in 1983 [10] as the ratio of the lost area to the aperture area. The lost area A_l is given as [10]

$$A_l = \frac{2}{3} W_a h_p + f_p W_a \left[1 + \frac{W_a^{\,2}}{48 f_p^{\,2}} \right] \qquad 2.11$$

where W_a is the aperture diameter, h_p – the height of the parabola, f_p – the focal length and A_f is

$$A_f = \frac{A_l}{A_a} \qquad 2.12$$

The angle of incidence varies according to the declination of the sun, the hour angle, the latitude, zenith angle and the number of days. The detailed definition and determination of these angles is presented in [16,28].

The determination of the intercept factor involves determining the energy reflected from the concentrator and that incident on the receiver. As discussed above, the intercept factor depends on the size of the receiver, the surface angle errors inherent in the mirror and the solar beam spread. An optimally sized receiver will intercept between 90% – 95% of the incident solar radiation [28].

2.3.3 THERMAL ANALYSIS OF PARABOLIC TROUGH RECEIVERS

The thermal analysis of the parabolic trough system centres mostly on the receiver system. The receiver is a central component to the performance of the entire trough system. It is the reason for the high efficiency of the current plants [21]. The performance of the receiver has been the subject of many investigations [21,30,31,37,39,83] and any new receiver that is developed must be tested to assess its thermal performance.

The receiver or the heat collection element (as shown in Fig. 2.8) consists of a steel absorber tube enclosed in a glass jacket that is evacuated to suppress convection heat loss. The glass cover and absorber tube are sealed by bellows at the receiver end to keep the receiver evacuated and allow for thermal expansion between the glass envelope and the absorber tube. Getter material is provided to absorb any hydrogen that infiltrates from the heat transfer fluid. Radiation loss is minimised by using selective coating on the absorber tubes with high absorptivity to the incoming radiation low emissivity for infrared radiation [21].

The gas in the annulus space significantly influences the thermal performance of the receiver. Heat loss is significantly higher with increased amounts of hydrogen in the annulus space compared to the loss when there is air [45]. Hydrogen in the receiver's annulus is formed when the temperatures of the heat transfer fluid reaches about 400 ^{o}C. At these temperatures and higher, the current heat transfer fluids begin to decompose [29,55]. A cross-section of the receiver tube is shown in Fig. 2.9.

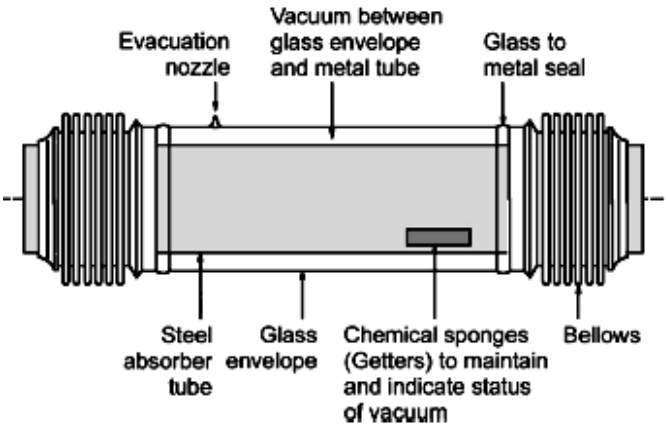

Fig. 2.8: Schematic diagram of a parabolic trough receiver tube [21].

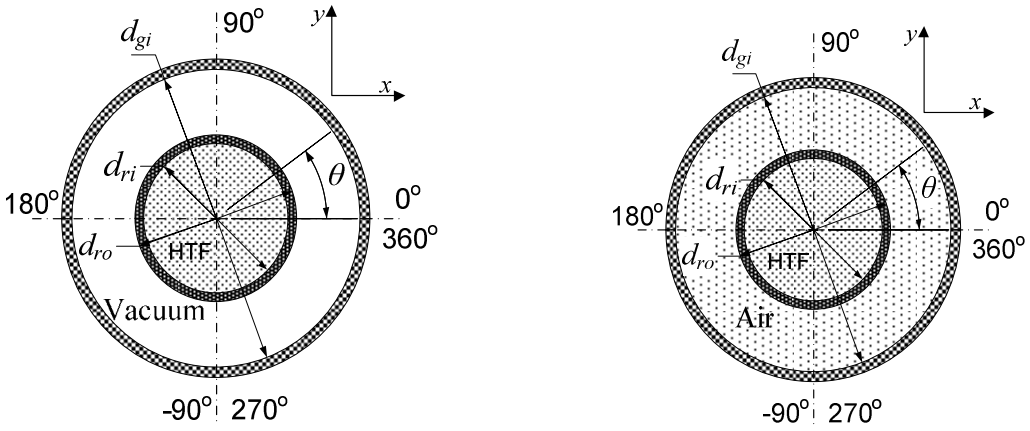

(a) Evacuated receiver (b) Non-evacuated receiver

Fig. 2.9: Schematic diagrams showing cross-section views of evacuated and non-evacuated parabolic trough receiver tubes, respectively.

The instantaneous efficiency of the collector is determined from the receiver's energy balance. For a receiver of length L and area A_r, the useful energy is given as [10,16,28]

$$q_u' = I_b \eta_o \frac{A_a}{L} - \frac{A_r U_L}{L}(T_r - T_a) \qquad 2.13$$

The useful energy is equivalent to the energy transferred by conduction to the heat transfer fluid inside the absorber tube. When the local fluid temperature is T_f, the useful energy per unit length can also be given by

$$q'_u = \frac{\left(\frac{A_r}{L}\right)\left(T_r - T_f\right)}{\frac{d_{ro}}{h_{fi}d_{ri}} + \frac{d_{ro}}{2\lambda_{abs}}\ln\frac{d_{ro}}{d_{ri}}} \qquad 2.14$$

Where h_{fi} is the heat transfer coefficient on the inner wall of the absorber tube and λ_{abs} is the absorber tube's thermal conductivity. For cases where analytical methods are used and T_r is not known, the elimination of T_r by combining Eq. (2.14) and Eq. (2.13) yields an appropriate equation relating useful heat to the overall heat transfer coefficient, ambient temperature, heat transfer fluid temperature, incident solar radiation and concentration ratio.

The energy carried by the heat transfer fluid is

$$q_u = \dot{m}c_p(T_{outlet} - T_{inlet}) \qquad 2.15$$

The value of the overall heat transfer coefficient in Eq. (2.13) depends on the state of the receiver: whether it is bare, with air in the annulus or evacuated.

For a bare receiver tube, assuming no temperature difference in the receiver, the overall heat transfer coefficient includes: convection and radiation from the surface as well as conduction through the supports [10]. It is therefore given as

$$U_L = h_w + h_r + h_c \qquad 2.16$$

where h_w is the heat transfer coefficient due to wind effects. It is related to the Reynolds number according to Kalogirou [10].

$$Nu = 0.4 + 0.54Re^{0.52} \qquad 2.17$$

for $0.1 < Re < 1\,000$

$$Nu = 0.3Re^{0.6} \qquad 2.18$$

for $1\,000 < Re < 50\,000$

Burkholder and Kutscher [30] propose a simpler relation that gives an approximate value of the wind loss coefficient. It is given as

$$h_w = 4.9 + 4.9v_w - 0.18v_w^2 \qquad 2.19$$

The linearised radiation heat transfer coefficient is given as [28]

$$h_r = \varepsilon\sigma\left(\frac{T_r^4 - T^4_{sky}}{T_r - T_a}\right) \qquad 2.20$$

The conduction heat loss coefficient (h_c) is estimated based on knowledge of the construction of the collector and how it is supported [10].

For an evacuated receiver in which the convection heat loss between the absorber tube and the glass cover are negligible, the overall heat transfer coefficient is given by Kalogirou [10] as

$$U_L = \left[\frac{A_r}{(h_w + h_{r,c-a})A_{gc}} + \frac{1}{h_{r,r-c}}\right] \qquad 2.21$$

$h_{r,c\text{-}a}$ – is the linearised radiation coefficient from the cover to ambient temperature, as estimated by Eq. (2.20) (W/m^2 K), A_{gc} – is the area of the glass cover (m^2), $h_{r,r\text{-}c}$ – is the linearised radiation coefficient from the absorber tube to the glass cover, given by

$$h_{r,r-c} = \frac{\sigma\left(T_r^2 + T_c^2\right)(T_r + T_c)}{\frac{1}{\varepsilon_r} + \frac{A_r}{A_c}\left(\frac{1}{\varepsilon_c} - 1\right)} \qquad 2.22$$

The convective heat transfer coefficient inside the absorber tube (h_{fi}) appearing in Eq. (2.14) can be determined from the existing correlations for Nusselt numbers commonly used for internal forced convection. A modern correlation by Gnielinski [84] covering lower Reynolds numbers as well as larger Reynolds numbers and a wider range of Prandtl numbers is generally used and is given as [84]

$$Nu = \frac{\left(f/8\right)\left(Re-1000\right)\mathrm{Pr}}{1+12.7\left(f/8\right)^{0.5}\left(\mathrm{Pr}^{2/3}-1\right)} \quad \text{for } 0.5 \le Pr \le 2\,000 \qquad 2.23$$

$$3\times10^{3} \le Re \le 5\times10^{6}$$

The friction factor in Eq. (2.23) is the Darcy friction factor, which can be determined for smooth tubes according to Petkuhov's first equation as [84]

$$f = \left(0.790\ln Re - 1.64\right)^{-2} \qquad 2.24$$

The absorber tube's thermal conductivity λ_{abs}, in Eq. (2.14) is also determined based on knowledge of the material used in the construction of the absorber tube. For stainless steel, a temperature-dependent thermal conductivity is given by [45]

$$\lambda_{abs} = 14.8 + 0.0153T_r \qquad 2.25$$

The solution of the above equations will give the thermal performance of the parabolic trough receiver. Unknown parameters in the above equations are determined through an energy balance applied to the receiver. Accordingly, the energy that is lost from the absorber tube by radiation and convection is equal to the energy conducted through the glass and is equal to the energy lost from the surface of the glass envelope to the environment by convection and radiation.

For a receiver of length L surrounded by a glass cover, the heat transfer from the absorber tube at T_{ro} to the inside glass cover at T_{gi}, through the glass cover to the outside of the glass cover at T_{go} and then to the surroundings is given by Duffie and Beckman as given in Eq. (2.26) [28].

$$Q_{loss} = \frac{2\pi\lambda_{eff}L}{\ln\frac{d_{gi}}{d_{ro}}}\left(T_{ro}-T_{gi}\right) + \frac{\pi d_{ro}L\sigma\left(T_{go}^{4}-T_{gi}^{4}\right)}{\frac{1}{\varepsilon_r}+\frac{1-\varepsilon_g}{\varepsilon_g}\left(\frac{d_{ro}}{d_{gi}}\right)} = \frac{2\pi\lambda_g\left(T_{gi}-T_{go}\right)}{\ln\left(\frac{d_{go}}{d_{gi}}\right)} \qquad 2.26$$

or

$$Q_{loss} = \pi d_{go} L h_w \left(T_{go} - T_a\right) + \varepsilon_g \pi d_{go} L \sigma \left(T_{go}^4 - T_{sky}^4\right) \qquad 2.27$$

The subscript *ro* – represents the absorber tube outer wall, *gi* – represents the glass cover inner wall, *go* – represents the glass cover outer wall, *g* – represents the glass cover and *r* – represents the absorber tube, whereas σ is the Stefan Boltzman constant, where $\sigma = 5.670373\times10^{-8}$ W m^{-2} K^{-4} and λ_g is the glass cover's thermal conductivity.

The effective thermal conductivity of air, $\lambda_{air,eff}$ depends on the state of the annulus space between the glass cover and the absorber tube and is determined according to the correlation given by Raithby and Hollands [84]

$$\frac{\lambda_{air,eff}}{\lambda_{air}} = max\left[1,\ 0.386\left(\frac{Pr \times Ra^*}{0.861 + Pr}\right)^{1/4}\right] \qquad 2.28$$

Valid for $Ra^* \leq 10^7$

where

$$Ra^* = \frac{\left(ln\left(d_{gi}/d_{ro}\right)\right)^4}{L_c^3\left(d_{ro}^{-3/5} + d_{gi}^{-3/5}\right)^5} Ra_L \qquad 2.29$$

The characteristic Rayleigh number, Ra_L is based on the space between the absorber tube and the glass cover, $L_c = (d_{gi} - d_{ro})/2$ according to:

$$Ra = \frac{g\beta(T_{ro} - T_{gi})L_c^3}{\nu^2} \qquad 2.30$$

For $Ra^* \leq 100$, Eq. (2.28) gives $\lambda_{air,eff} = \lambda_{air}$ and convection currents become so negligible that heat is lost due to free molecular conduction. The reduction of annulus pressures to lower levels reduces the conductivity of air so much that at very low vacuum pressures, $\lambda_{air,eff} \approx 0$ and only the radiation heat transfer term in Eq. (2.26) between the glass cover and the absorber tube is considered. As the pressure reduces, the thermal conductivity of air varies with pressure according to Potkay and Sacks [85]

$$\lambda_{air} = \lambda_{air,o} \frac{1}{1 + \frac{7.6x10^{-5}}{P L_c / T}} \qquad 2.31$$

Where the characteristic length, $L_c = (d_{gi} - d_{ro})/2$. And $\lambda_{air,o}$ is the thermal conductivity of air determined at standard temperature and pressure conditions

The value of the sky temperature in these equations is approximated according to García-Valladares and Velázquez [86]

$$T_{sky} = 0.0552 T_{amb}^{1.5} \qquad 2.32$$

The emissivity of the absorber tube varies with the temperature, depending on the selective coating used. For a cement-coated receiver, the emissivity is given by Kalogirou [83] as:

$$\xi_{abs} = 0.000327(T+273.15) - 0.065971 \qquad 2.33$$

The equations presented in section 2.3.2 and 2.3.3 provide a way of characterising the optical and thermal performance of parabolic trough systems, respectively. The thermal analysis presented in section 2.3.3 assumes that there is a uniform temperature distribution on the absorber tube, which is not the case in an actual trough system. Accordingly, experimental methods [46] or numerical procedures should be used [33,34,47] to account for the non-uniform temperature distribution in the receiver's absorber tube.

2.3.4 SECOND LAW ANALYSIS OF SOLAR COLLECTORS

The use of the second law of thermodynamics for the analysis of engineering systems and components provides a basis for evaluating the quality and quantity of energy in these systems. The second law of thermodynamics provides a basis of determining the irreversibility in engineering systems and components. An engineer's main interest is to have reversible systems and reversible components, since reversible energy-producing systems and components will produce more work, whereas reversible energy-consuming systems and components will consume less energy.

Based on Bejan's work on entropy generation minimisation in solar collectors [61], Kalogirou [10] adapted the analysis to concentrating collectors. For a collector with an

aperture area A_a, receiving solar radiation at the rate Q^* from the sun with q_o as the energy absorbed by the receiver, $q_o = \eta_o Q^*/A$ as shown in Fig. 2.10.

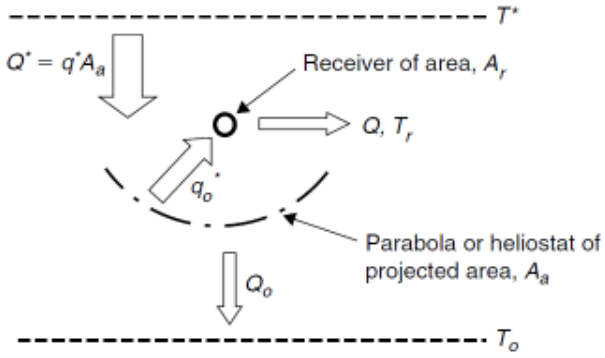

Fig. 2.10: Representation of energy flow for concentrating collectors [10].

Some of the radiation incident on the collector is not delivered to the power cycle. The difference between what the collector receives and what is delivered to the power cycle represents the ambient heat loss Qo.

$$Q_o = Q^* - Q \qquad 2.34$$

The second law analysis, also known as the entropy generation minimisation method, seeks to minimise the destruction of available work thus maximising the power output. The entropy generation is related to the energy destroyed through the Gouy-Stodola theorem [61] as:

$$T_o S_{gen} = E_{in} - E_{out} = \text{Exergy destroyed} \qquad 2.35$$

The exergy flow diagram for the collector processes is shown in Fig. 2.11 [10], for a collector of area A_a, receiving solar radiation at a rate Q^* from the sun. Q^* is proportional to the area of the collector and the direct normal irradiance, I_b. The incident solar radiation is partly delivered to the user as heat transfer Q at the receiver temperature T_r, the remaining fraction, Q_o is lost to the ambient.

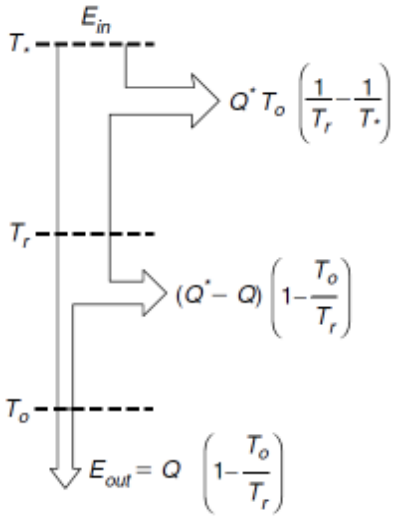

Fig. 2.11: Schematic representation of exergy analysis for concentrating solar collectors [10].

where T_* is the apparent temperature of the sun as an energy source approximately equal to $¾T_s$ [10], T_s is the apparent blackbody temperature of the sun, T_o is the ambient temperature.

$$E_{in} = Q^* \left(1 - \frac{T_o}{T_*}\right) \tag{2.36}$$

and

$$E_{out} = Q \left(1 - \frac{T_o}{T_r}\right) \tag{2.37}$$

Such that on combining Eqs. (2.35) – (2.37), the entropy generation rate becomes

$$S_{gen} = \frac{Q_o}{T_o} + \frac{Q}{T_r} - \frac{Q^*}{T_*} \tag{2.38}$$

For a non-isothermal collector, the entropy generation due to these processes, without considering the pressure drop between the inlet and outlet, is given as [10,61]

$$S_{gen} = \dot{m} c_p \ln \frac{T_{out}}{T_{inlet}} - \frac{Q^*}{T_*} + \frac{Q_o}{T_o} \tag{2.39}$$

From Eqs. (2.34) – (2-39) several combinations of collector parameters and operating conditions can be determined for which the entropy generation is minimum and therefore power output is maximum. The determination of entropy generation can also be realised through consideration of the local entropy generation rates due to heat transfer and fluid flow in the absorber tube [61] such that combinations of flow rates, concentration ratios are also achieved for which the entropy generation rate is minimum. This method is essential when heat transfer enhancement is under consideration. This method is considered in detail in Chapter 5 to lay a foundation for the thermodynamic comparison of enhanced and non-enhanced receiver tubes.

2.4 CONCLUDING REMARKS

In this chapter, a brief background on concentrated solar power is presented. The different concentrated solar power technologies have been described and the advantages and disadvantages of each technology discussed. The parabolic trough technology is shown to be the most commercially and technically developed concentrated solar power technology.

An overview of the parabolic trough technology has also been provided to lay a foundation for work in the next chapters of this thesis. Equations for the parabolic trough geometry, optical analysis of the collector and thermal analysis of the receiver tube as well as for the second law analysis of concentrating collectors are discussed briefly.

CHAPTER THREE

CHAPTER THREE: NUMERICAL MODELLING AND OPTIMISATION PROCEDURE

3.1 INTRODUCTION

Chapter two introduced the equations for the thermal analysis of parabolic trough receivers. The analytical solutions of these equations yield typical solutions that characterise the performance of parabolic trough receivers. The main shortcoming of this analytical method is the assumption of a uniform temperature on the absorber tube's circumference. An accurate prediction of the receiver's thermal performance can be obtained through experimentation under actual operating conditions or through numerical modelling. Numerical modelling using computational fluid dynamics provides an alternative to experimentation for determining the performance of the receiver with realistic boundary conditions so that the circumferential temperature differences in the receiver's absorber tube are accounted for. This also reduces the time, cost and effort that would be required for equivalent experimental investigations. Furthermore, the availability of optimisation tools coupled with tools for computational fluid dynamics enables designers to determine optimal configurations, significantly reducing the time for product design. Computational fluid dynamics modelling can be a valuable tool, but only if the designer knows the specific limitations, assumptions, solution techniques and mathematical modelling capabilities so that the problem under consideration is accurately described and the physics involved are solved in as detailed a manner as possible. Therefore, this chapter presents a general overview of the numerical modelling and optimisation framework used in the present work. The specific solution procedure used for each of the cases considered in Chapters 4 to 7 are presented in those chapters.

3.2 NUMERICAL MODELLING

Computational fluid dynamics has grown and become an essential tool for the analysis and investigation of fluid flow, heat transfer and associated phenomena in engineering systems ranging from simple to complex. The Navier-Stokes equations that represent fluid flow are so highly coupled and non-linear that obtaining an analytical solution is not feasible for most flows. For some flows where an analytical solution is possible, well-defined boundary conditions and additional simplifying assumptions must be provided. Accordingly, most heat transfer and fluid flow problems in many engineering applications involving complex geometries, complex flow interactions and complex multi-physics require numerical approaches to obtain acceptable solutions.

With the advances in computational fluid dynamics in the past few decades, the availability of general-purpose solvers has increased mainly because of the availability of affordable high-performance computer hardware [87]. The general-purpose solver is now widely used in industry and academia. Using general-purpose solvers eliminates the repetition of programming so that the same code can be used for a diverse number of problems and the researcher/designer can focus on the problem instead of programming. The present research used a computational fluid dynamics code (CFD), ANSYS FLUENT [88,89].

All CFD codes work in almost the same way: they include a user interface to input the problem parameters and examine the results obtained [87]. The basic steps involved in the CFD analysis are [87] as follows:

- Pre-Processing: consists of defining the problem and geometry under consideration – the computational domain; generation of the grid – subdividing the domain into smaller non-overlapping subdomains; selecting the physical and chemical phenomena to be modelled; defining the fluid properties; and specifying the appropriate boundary conditions.

- Solver Execution: all the governing equations are integrated over the computational domain; then the resulting integral equations are converted into a system of algebraic equations; the resulting algebraic equations are solved iteratively.

- Post-Processing: involves examining the results obtained and validating them with existing data or models.

All of the above steps were implemented in a commercial code ANSYS® release 13, 14 and 14.5. The problem geometries were modelled in ANSYS design modeller; the grid generation was done in ANSYS meshing; the problem solutions and post-processing were done in ANSYS FLUENT with further post-processing done in ANSYS CFD post. For any results of a numerical investigation to credible and of acceptable standard, several guidelines have been proposed. In this work, the guidelines of the editorial policy statement on numerical accuracy by the ASME Journal of Heat Transfer [90] were followed.

3.2.1 GOVERNING EQUATIONS

The flow of a fluid is described in terms of mass, momentum and energy transfer by a set of non-linear partial differential equations called the Navier-Stokes equations. When the flow is turbulent, the small-scale fluctuations cannot be resolved by using the Navier-Stokes equations, instead the Navier-Stokes equations are averaged to give the Reynolds Averaged Navier-Stokes (RANS) equations [87,91]. As the averaging of the Navier-Stokes equations presents a closure problem, they require additional equations to achieve a numerical solution. The additional equations are provided through turbulence modelling with a variety of turbulence closure models that are discussed later.

In parabolic trough receivers, laminar and turbulent flows are both possible, depending on the condition of the glass envelope. In the annulus space between the absorber tube and the glass cover, laminar natural convection co-exists with radiation when the space is not evacuated. Inside the absorber tube, higher flow rates are generally required to provide better heat transfer and to reduce the absorber tube's circumferential temperature differences; accordingly the flow is turbulent forced convection.

Other equations may be solved depending on the physics being considered. In this research, radiation heat transfer between the absorber tube and the glass cover of the receiver is accounted for by solving the radiative heat transfer (RTE) equation [87]. The solution to the radiative heat transfer equation is obtained by using the discrete ordinates model with air or vacuum in the annulus space radiatively non-participating [88].

The governing equations are presented in detail in later sections of this chapter.

3.2.2 SOLUTION ALGORITHMS AND DISCRETISATION SCHEMES

The problems associated with the non-linearities as well as the pressure-velocity linkage in the Navier-Stokes equations require appropriate solution algorithms. The algorithm used depends largely on the type of flow under consideration. The most common algorithms are the 'Semi-Implicit Method for Pressure Linked Equations' or SIMPLE algorithm of Patankar [87,92] and the "Pressure-Implicit with Splitting of Operators" of Issa [87]. Other variations of the SIMPLE algorithm are also available [88,89]. The algorithm used does not affect the results in most cases, but can affect the simulation run time or memory usage. The SIMPLE algorithm is widely used for steady-state problems and was used for this work; each governing equation is segregated from other equations while being solved and is memory efficient [88,89]. The steps followed are shown in Fig. 3.1 [88].

The choice of the discretisation scheme can affect the solution. In CFD codes, the flow variable values are stored at the cell centres, yet the solution algorithm requires values at the cell faces. Therefore the solution variables must be interpolated from the cell centre values [88]. Upwinding is commonly used for this purpose, so that face values are derived from quantities in the cell upstream relative to the direction of normal velocity [88]. Second-order discretisation schemes are recommended for accurate results, especially for complex flows and in cases where flow is not aligned with the mesh [89]. For this reason, the second-order upwind scheme was adopted for all our simulations in the present research.

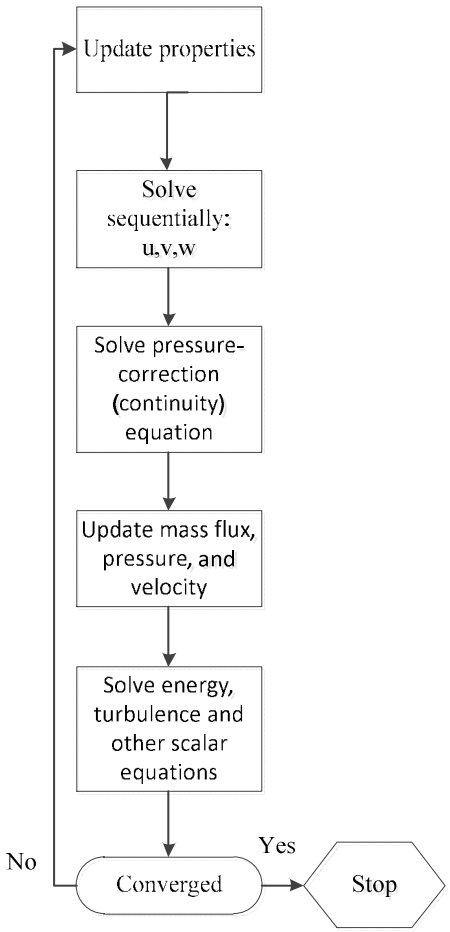

Fig. 3.1: Flow diagram of the solution procedure based on the SIMPLE algorithm [88].

3.3 TURBULENCE MODELLING

Most flows present in nature as well as in most engineering applications are turbulent. Several efforts have therefore been directed to modelling and understanding the turbulent flow phenomena. A flow is said to become turbulent when the inertial forces in the fluid dominate the viscous forces. The transition from a laminar to a turbulent flow regime depends on whether flow is an internal or external forced convection or a natural convection. For internal flows the transition takes place at Reynolds numbers of about 2 300 [84,91]. Turbulent flows are characterised by rapid and irregular fluctuations in the flow field variables promoting mixing in a fluid and therefore have higher heat transfer rates than

laminar flows. As discussed above, the Reynolds Averaged Navier Stokes equations are used for modelling turbulent flows.

3.3.1 REYNOLDS AVERAGED NAVIER-STOKES EQUATIONS

The Navier-Stokes equations describe fully both laminar and turbulent flows, but because in turbulent flows the fluctuations can be too small and of a high frequency, they are usually computationally expensive to resolve numerically. Accordingly, the basic governing equations are time-averaged so that small-scale variations are removed, resulting in a set of equations that is less computationally expensive and known as the Reynolds Averaged Navier-Stokes equations (RANS).

The averaging process that yields the RANS equations results in additional unknown terms, causing a closure problem. The process of obtaining these additional terms is called turbulence modelling. The steady-state RANS equations obtained after averaging are given after time averaging the Navier-stokes equations [88].

The instantaneous field is defined as the sum of the mean and fluctuating components. For pressure and velocity, it is given as

$$P = \bar{P} + P' \quad and \quad u_i = \bar{u}_i + u_i' \tag{3.1}$$

By averaging the Navier-Stokes equations, the Reynolds averaged Navier-Stokes equations become [88]:

Mass conservation

$$\frac{\partial\left(\rho\bar{u}_i\right)}{\partial x_i} = 0 \tag{3.2}$$

Conservation of momentum

$$\frac{\partial}{\partial x_j}\left(\rho\bar{u}_i\bar{u}_j\right) = -\frac{\partial\bar{P}}{\partial x_i} + \frac{\partial}{\partial x_j}\left[\mu\left(\frac{\partial\bar{u}_i}{\partial x_j} + \frac{\partial\bar{u}_j}{\partial x_i}\right) - \frac{2}{3}\mu\frac{\partial\bar{u}_i}{\partial x_i}\delta_{ij} - \rho\overline{u_i'u_j'}\right] \tag{3.3}$$

Conservation of energy

$$\frac{\partial}{\partial x_j}\left(\rho \bar{u}_j c_p \bar{T}\right) = \frac{\partial}{\partial x_j}\left(\lambda \frac{\partial \bar{T}}{\partial x_j} + \frac{\mu_t}{\sigma_{h,t}} \frac{\partial\left(c_p \bar{T}\right)}{\partial x_j}\right) + \bar{u}_j \frac{\partial \bar{P}}{\partial x_j} + \left[\mu\left(\frac{\partial \bar{u}_i}{\partial x_j} + \frac{\partial \bar{u}_j}{\partial x_i}\right) - \frac{2}{3}\mu \frac{\partial \bar{u}_i}{\partial x_i}\delta_{ij} - \rho\overline{u_i' u_j'}\right]\frac{\partial \bar{u}_i}{\partial x_j} \quad 3.4$$

The additional terms appearing in the governing equations result from the averaging process and represent the effects of turbulence. Where $-\rho\overline{u_i' u_j'}$ are the Reynolds stresses, $\bar{u}_i$ and $\bar{u}_j$ are the time-averaged velocity components in the *i*- and *j*-directions respectively, $\bar{T}$ is the time-averaged temperature, $\bar{P}$ is the time-averaged pressure and λ is the fluid thermal conductivity. The Reynolds stress tensor ($-\rho\overline{u_i' u_j'}$) introduces six new unknowns in a 3-D analysis that can only be obtained when the turbulent structure is known. This turbulent structure is not known beforehand so the effects of small-scale fluctuations are given through turbulent modelling instead of calculating the turbulent inertia tensor.

RANS models fall into two categories, depending on how the Reynolds stresses $-\rho\overline{u_i' u_j'}$ are calculated. These categories are the Eddy viscosity models (EVM) and Reynolds stress models (RSM). The eddy viscosity models assume the stress is proportional to strain, so that closure is achieved by using the Boussinesq approach in which Reynolds stresses are taken to be homogenous and represented by [88]

$$-\rho\overline{u_i' u_j'} = \mu_t\left(\frac{\partial \bar{u}_i}{\partial x_j} + \frac{\partial \bar{u}_j}{\partial x_i}\right) - \frac{2}{3}\left(\rho k + \mu_t \frac{\partial \bar{u}_k}{\partial x_k}\right)\delta_{ij} \quad 3.5$$

where *k* is the turbulent kinetic energy per unit of mass, given by

$$k = \frac{1}{2}\left(\overline{u'^2} + \overline{v'^2} + \overline{w'^2}\right) \quad 3.6$$

Various models based on the Boussinesq approach have been developed; they include the *k*-ε models, the standard and SST *k*-ω models, the *k*-*kl*-ω model and the $\overline{v^2} - f$ model. Interested readers are referred to the ANSYS FLUENT theory guide [88] for details of these models and their use in FLUENT. The *k*-ε models are the most widely used and validated turbulence models for most engineering applications [87,88]. Due to the strengths and weaknesses of the

original version of these models, the standard *k-ε*, modifications to improve its performance were introduced, including the RNG *k-ε* model and the realisable *k-ε* model. It is not clear yet under what circumstances the realisable *k-ε* outperforms the RNG *k-ε* but initial studies have shown that it has a far superior performance than all *k-ε* for separated flows and flows with complex secondary features [88]. The realisable *k-ε* model was used throughout this research study and solves two additional equations for turbulent kinetic energy *(k)* and turbulent dissipation rate *(ε,)* given as:

For kinetic energy *(k)*

$$\frac{\partial}{\partial x_j}\left(\rho k\bar{u}_j\right)=\frac{\partial}{\partial x_j}\left[\left(\mu+\frac{\mu_t}{\sigma_k}\right)\frac{\partial k}{\partial x_j}\right]+G_k-\rho\varepsilon \tag{3.7}$$

For dissipation rate *(ε)*

$$\frac{\partial}{\partial x_j}\left(\rho\varepsilon\bar{u}_j\right)=\frac{\partial}{\partial x_j}\left[\left(\mu+\frac{\mu_t}{\sigma_\varepsilon}\right)\frac{\partial \varepsilon}{\partial x_j}\right]+\rho C_{1\varepsilon}S\varepsilon-\rho C_2\frac{\varepsilon^2}{k+\sqrt{\nu\varepsilon}} \tag{3.8}$$

G_k represents the turbulent generation of kinetic energy due to mean velocity gradients

$$G_k=\mu_t S^2 \tag{3.9}$$

The eddy viscosity is given by

$$\mu_t=\rho C_\mu\frac{k^2}{\varepsilon} \tag{3.10}$$

Unlike the standard *k-ε*, the value of C_μ is not constant in the realisable *k-ε* model and is given as

$$C_\mu=\frac{1}{A_o+A_s\dfrac{kU^*}{\varepsilon}} \tag{3.11}$$

where

$$U^*=\sqrt{S_{ij}S_{ij}+\tilde{\Omega}_{ij}\tilde{\Omega}_{ij}} \tag{3.12}$$

and

$$\tilde{\Omega}_{ij} = \Omega_{ij} - 2\varepsilon_{ijk}\omega_k$$
$$\Omega_{ij} = \bar{\Omega}_{ij} - \varepsilon_{ijk}\omega_k \qquad 3.13$$

$\bar{\Omega}_{ij}$ is the mean rate of rotation tensor viewed in a moving reference frame with angular velocity ω_k. The model constants A_o and A_s are given as $A_o = 4.04$, $A_s = \sqrt{6}\cos\phi$

where

$$\phi = \frac{1}{3}\cos^{-1}(\sqrt{6}W_r),\ W_r = \frac{S_{ij}S_{jk}S_{ki}}{\tilde{S}^3},\ \tilde{S} = \sqrt{S_{ij}S_{ij}} \text{ and } S_{ij} = \frac{1}{2}\left(\frac{\partial u_j}{\partial x_i} + \frac{\partial u_i}{\partial x_j}\right) \qquad 3.14$$

The other model constants for the realisable k-ε are

$$C_{1\varepsilon} = 1.44,\ C_2 = 1,\ \sigma_k = 1.0 \text{ and } \sigma_\varepsilon = 1.2 \qquad 3.15$$

In the Reynolds stress model (RSM), equations are derived for each stress term in Eq. (3.3) and Eq. (3.4), yielding a set of six equations in the 3-dimensional space. The additional equations are solved with the additional equation for the dissipation rate. The assumption of isotropy of the Reynolds stresses is removed so that the magnitude of u' varies in different directions. The model is complex, but may be crucial in some flows where the anisotropic nature of turbulence is of importance. In many cases the eddy viscosity models may perform so well that the additional computational expense of the Reynolds stress model is not warranted [88]. The use of RSM is recommended for cases where turbulence is highly anisotropic and affects the mean flow, such as highly swirling flows, and stress-driven secondary flows in ducts, such as cyclone flows, rotating flows in flow passages and highly swirling flows in combustors [88].

3.3.2 NEAR-WALL TREATMENT

The turbulent models discussed above do not resolve the near-wall phenomena. In particular, the models based on k-ε are derived for the bulk flow region and are invalid in regions near the walls. Solution variables in the near-wall region have large gradients and momentum, and other scalar transport occurs most vigorously. Therefore, for wall-bounded flows, the flow near the wall should be represented accurately to obtain acceptable results.

The near-wall region can be subdivided into three layers: the innermost layer called the viscous sublayer where flow is almost laminar and momentum and heat transfer are mainly due to molecular viscosity, the outer layer which is a fully turbulent layer and the region between the viscous sublayer and the fully turbulent layer where molecular viscosity and turbulence are of equal importance. Figure 3.2 shows these regions plotted on a graph of dimensionless velocity and y^+.

Where $y^+ \equiv \rho u_\tau y/\mu$ and μ_τ is the friction velocity defined as $\mu_\tau = \sqrt{\frac{\tau_w}{\rho}}$, and $u^+ = u/u_\tau$

The near-wall region is usually modelled using two approaches. In one approach, semi-empirical formulas called "wall functions" are used to bridge the viscous-affected region and the fully turbulent region; in this case, the viscous affected inner region is not resolved. In the other approach, turbulent models are modified to enable the resolution of the viscous affected region with a mesh all the way to the wall, including the viscous sublayer [88].

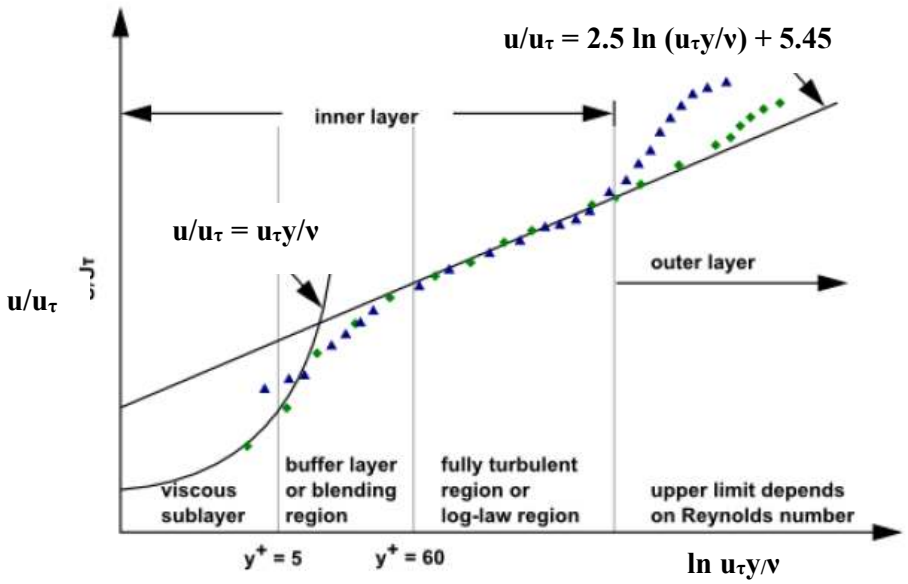

Fig. 3.2: Graph showing the subdivisions of the near-wall region for turbulent flows [88].

The standard wall functions implemented in ANSYS FLUENT are based on the work of Launder and Spalding (1972) and are given as [88]

$$U^* = \frac{1}{\kappa}\ln(Ey^*) \tag{3.16}$$

where U^* is the dimensionless velocity given by

$$U^* = \frac{U_P C_\mu^{1/4} k_P^{1/2}}{\tau_w / \rho} \tag{3.17}$$

y^* is the dimensionless distance from the wall given by

$$y^* = \frac{\rho C_\mu^{1/4} k_p^{1/2} y_p}{\mu} \tag{3.18}$$

κ is the von Kármán constant (= 0.4187), E is an empirical constant (= 9.793), U_p is the mean velocity of the fluid at the near-wall node p, k_p is the turbulent kinetic energy at the near-wall node p, y_p is the distance from point p to the wall; and μ is the dynamic viscosity of the fluid.

The temperature wall function is given by

$$T^* \equiv \frac{(T_w - T_p)\rho c_p C_\mu^{1/4} k_p}{\dot{q}} \tag{3.19}$$

c_p is the specific heat capacity of the fluid, $\dot{q}$ is the wall heat flux, T_w is the wall temperature, T_p is the temperature of the first near-wall node p.

The use of standard wall function leads to unbounded errors in the wall shear stress and heat transfer when the grid is refined in a wall-normal direction, leading to a deterioration of numerical results. This is why advanced wall formulations allowing for the refinement of the mesh without a deterioration of results are implemented in ANSYS FLUENT and are recommended for use with most turbulence models. This is achieved using the enhanced wall treatment, which combines the two-layer model with the so-called enhanced wall function and allows the refinement of the mesh so that the viscous sublayer ($y^+ \approx 1$) is resolved [88].

In the two-layer model for enhanced wall treatment, the entire domain is divided into a viscous-affected region and a fully turbulent region. The demarcation of these regions is given by the wall-distance-based turbulent Reynolds number, Re_y defined as

$$Re_y = \frac{\rho y \sqrt{k}}{\mu} \tag{3.20}$$

y is the wall-normal distance calculated at the cell centres, interpreted as the distance to the nearest wall; and k is the turbulent kinetic energy. In the fully turbulent region ($Re_y > Re_y^*$; $Re_y^* = 200$), the k-ε model and Reynolds stress models are used [88]. In the viscosity-dominated region ($Re_y < Re_y^*$), the one-equation model of Wolfestein [88] is used. In this one-equation model, the momentum and k equations are defined similarly to those used in the k-ε and Reynolds stress models but the turbulent viscosity is given as [88]

$$\mu_{t,2layer} = \rho C_\mu l_\mu \sqrt{k} \tag{3.21}$$

The length scale l_μ is given as

$$l_\mu = y C_l^* (1 - e^{-\mathrm{Re}_y / A_\mu}) \tag{3.22}$$

The turbulent viscosity for the two-layer formulation described above is used as part of the enhanced wall treatment, in which smooth blending of the two-layer formulation with high Reynolds number μ_t definition from the outer region as proposed by Jongen (1992) as given in Ref. [88] as

$$\mu_{t,enh} = \lambda_\varepsilon \mu_t + (1 - \lambda_\varepsilon) \mu_{t,2layer} \tag{3.23}$$

where μ_t is the high Reynolds number definition given in the k-ε models, λ_ε is a blending function defined such that it is unity away from the walls and zero in the vicinity of the wall. It has the form [88].

$$\lambda_\varepsilon = \frac{1}{2}\left[1 + \tanh\left(\frac{Re_y - Re_y^*}{A}\right)\right] \tag{3.24}$$

The constant A, determines the width of the blending function. For λ_ε to be within 1% of its far-field value, given a variation of $\Delta \mathrm{Re}_y$, then

$$A = \frac{\left|\Delta Re_y\right|}{\operatorname{artanh}(0.98)} \tag{3.25}$$

The typical value of ΔRe_y is between 5% and 20% of Re_y^* [88]. The ε field in the viscous - affected region is computed from

$$\varepsilon = \frac{k^{3/2}}{l_\varepsilon} \tag{3.26}$$

The length scale l_ε is computed in the same way as l_μ according to Eqn. (3.22) such that

$$l_\varepsilon = yC_l^*(1 - e^{-\mathrm{Re}_y/A_\varepsilon}) \tag{3.27}$$

The constants appearing in the above equations are given as

$$C_l^* = \kappa C_\mu^{-3/4},\ A_\mu = 70,\ A_\varepsilon = 2C_l^* \tag{3.28}$$

In the enhanced-wall treatment, the law of the wall is formulated so that it is applicable throughout the near-wall region (viscous sublayer, buffer region and fully turbulent outer region) as a single wall law for the entire wall region [88]. In ANSYS FLUENT this is achieved by a blending function suggested by Kader (1981) as given by Ref. [88] for the linear (laminar) and logarithmic (turbulent) laws of the wall as

$$u^+ = e^{\Gamma} u_{lam}^+ + e^{\frac{1}{\Gamma}} u_{turb}^+ \tag{3.29}$$

The blending function Γ is given as

$$\Gamma = -\frac{a(y^+)^4}{1 + b\, y^+} \tag{3.30}$$

where a = 0.01 and b = 5 and the general derivative is given as

$$\frac{du^+}{dy^+} = e^{\Gamma}\frac{du^+_{lam}}{dy^+} + e^{\frac{1}{\Gamma}}\frac{du^+_{turb}}{dy^+} \qquad 3.31$$

With this approach, the fully turbulent law can be easily modified and extended to take into account variable fluid properties and other effects including pressure gradients. The correct asymptotic behaviour for large and small y^+ is guaranteed as well as a reasonable representation of velocity profiles when y^+ is within the wall buffer region ($3 < y^+ < 10$) [88]. In most parts of the present work, the enhanced-wall treatment was used and the $y^+ \approx 1$ ensured.

3.4 OPTIMISATION

The optimisation used in this work is based on the entropy generation minimisation method and multi-objective optimisation. The two methods are briefly discussed in this section.

3.4.1 ENTROPY GENERATION MINIMISATION

The entropy generation method is used for modelling and optimisation and combines the second law of thermodynamics, heat transfer and fluid mechanics to obtain an optimum design, namely the one with the lowest entropy generation. The second law of thermodynamics is the basis of any entropy analysis. It relates the entropy change in an irreversible process with the heat transfer rate and entropy generation as

$$S_2 - S_1 = \int_1^2 \frac{\partial Q}{T} + S_{gen} \qquad 3.32$$

The entropy generation S_{gen} is a measure of irreversibility accompanying the process 1 to 2. For all engineering systems, S_{gen} is undesirable and should be reduced. Two methods are generally used in thermal design and optimisation to minimise entropy generation. They are: (1). exergy analysis, which relies on thermodynamics alone and relates the exergy destruction to entropy generation according to the Gouy-Stodola theorem [61]. According to the Gouy-Stodola theorem, the exergy destroyed (E_D) is directly proportional to the entropy generated according to:

$$E_D = T_o S_{gen} \qquad 3.33$$

and (2) the entropy generation minimisation method which combines fundamental principles of fluid mechanics, heat transfer and thermodynamics to establish the level of irreversibility in a system and its components. The entropy generation minimisation method does not necessarily rely on the concept of exergy [61]: it is a new method combining thermodynamics, heat transfer and fluid mechanics. Since its introduction by Bejan in 1979 [62], it has become widely used in the design and optimisation of thermal systems. It finds applications in the optimisation of cryogenics, heat transfer devices (such as heat exchangers, ducts and fins), storage systems, power plants, solar energy conversion systems, etc. The entropy generation minimisation method has been used in the present work.

The application of the entropy generation method to solar collectors is discussed in section 2.3.4. This section discusses the application of the entropy generation minimisation method to heat transfer and more specifically for assessing heat transfer enhancement techniques.

For the flow of a single phase fluid through a heat exchanger tube, the entropy generation rate per unit of tube length, as derived from the second law of thermodynamics in combination with heat transfer and fluid mechanics, is given in terms of the contribution from heat transfer and fluid friction according to [61]

$$S'_{gen} = \frac{q'^2}{\pi\lambda T_{bulk}{}^2 Nu} + \frac{32\dot{m}^3 c_f}{\pi^2 \rho^2 T_{bulk} D^5} \qquad 3.34$$

Where $\dot{m}$ is the stream flow rate, D is the tube diameter, q' is the heat transfer rate per unit length, $Nu = hD/\lambda$ with $h = q''/(T_w - T_{bulk})$, $c_f = (-dp/dx)\rho D/2G^2$, with $G = 4\dot{m}/\pi D^2$ and T_{bulk} is the bulk fluid temperature $(T_{inlet} + T_{outlet})/2$.

Equation (3.34) is applicable to a tube subjected to a constant heat flux and without any modifications or any inserts. As conditions vary from these assumptions, Eq. (3.34) can no longer be relied on to determine the entropy generation rates accurately [93]. Kock and Herwig [93] demonstrate the performance of Eq. (3.34) for a tube with a twisted tape insert and show that large errors occur, compared with methods considering local entropy generation using numerical methods. The advantages of evaluating entropy generation in a local sense lies in the ability of the method to be used with complex geometries and complex

boundary conditions. Accordingly, the analysis of local entropy generation rates and its use in general-purpose computational fluid dynamics codes have been recommended [61,94].

Kock and Herwig [94], using the equation for the transport of entropy for a single phase and incompressible fluid, together with the time-averaging approach applied in the RANS equations, derived useful relations for predicting the local entropy generation rates. Similar to Eq. (3.34), the derived set of equations gives the entropy generation in terms of entropy generation due to heat transfer irreversibility and fluid friction/fluid flow irreversibility. According to Kock and Herwig [94], the local entropy generation is given by [94]

$$S'''_{gen} = (S'''_{gen})_F + (S'''_{gen})_H \tag{3.35}$$

The entropy generation due to fluid friction $(S'''_{gen})_F$ is given as

$$(S'''_{gen})_F = S'''_{PROD,VD} + S'''_{PROD,TD} \tag{3.36}$$

where

$$S'''_{PROD,VD} = \frac{\mu}{\overline{T}}\left(\frac{\partial \overline{u}_i}{\partial x_j} + \frac{\partial \overline{u}_j}{\partial x_i}\right)\frac{\partial \overline{u}_i}{\partial x_j} \tag{3.37}$$

is the entropy generation by direct dissipation

and

$$S'''_{PROD,TD} = \frac{\rho\varepsilon}{\overline{T}} \tag{3.38}$$

is the entropy production by indirect (turbulent) dissipation.

The entropy generation due to heat transfer irreversibility $(S'''_{gen})_H$, is given as

$$(S'''_{gen})_H = S'''_{PROD,T} + S'''_{PROD,TG} \tag{3.39}$$

where

$$S'''_{PROD,T} = \frac{\lambda}{\overline{T}^2}(\nabla \overline{T})^2 \qquad 3.40$$

is the entropy production by heat transfer due with mean temperatures and

$$S'''_{PROD,TG} = \frac{\alpha_t}{\alpha}\frac{\lambda}{\overline{T}^2}(\nabla \overline{T})^2 \qquad 3.41$$

is the entropy production with fluctuating temperatures, λ is the fluid thermal conductivity, α and α_t are the thermal diffusivities.

This method has been validated against the analytical expression for entropy generation in a tube with a constant heat flux boundary condition given by Eq. (3.34). The results obtained were found to be in agreement [94]. For complex geometries, the method predicts the same trend, but gives large errors when compared with the results given by Eq. (3.34) [94]. For this reason, the direct method, which uses Eqs. (3.35) – (3.41) in determining entropy generation rates in heat transfer and fluid flow problems is recommended when flow deviates from simple tube flow with constant heat flux boundary conditions. The direct method was utilised in the present work to determine the local entropy generation in parabolic trough receivers of different configuration as well as to assess the thermodynamic performance of enhanced receivers whose absorber tubes are enhanced.

3.4.2 MULTI-OBJECTIVE OPTIMISATION IN HEAT TRANSFER ENHANCEMENT

Optimisation is the process of determining a set of solutions for a vector of design variables so that there is an optimum value for an objective. Calculus-based methods for single-objective constrained or unconstrained optimisation using the gradient-based approach to search for optimal solutions are widely used and well documented [95]. Optimisation algorithms using the direct search and gradient-based methods are associated with some difficulties, such as the dependence of the converged solution on the initial solution guess, failure to locate the global optimal solution by getting stuck on the local optimal solution, failure in handling problems with discrete search spaces and the lack of a general-purpose

algorithm [63,72]. These difficulties have inspired the use of heuristic optimisation methods such as Genetic algorithms (GAs) in the past two decades [72].

Genetic algorithms borrow their name from the field of genetics. They use fundamental ideas of genetics to construct search algorithms that are robust and require minimum problem information [63]. Interested readers are referred to [63,64] for details on genetic algorithms and their application to multi-objective optimisation problems. Genetic algorithms generally work with a population rather than a single point in the search space. This is why they are not trapped in local optima [72], provided that the diversity of the population is preserved.

Many engineering problems have multiple objectives. These objectives are generally conflicting and require simultaneous optimisation. The objectives might include maximising performance, minimising cost or maximising reliability. For a given system, an improvement in performance will require modification or additional components which increase the cost. In heat transfer enhancement problems, the objective is usually to improve the heat transfer performance. However, the improvement in heat transfer performance is usually associated with an increase in pressure drop, which should be minimised, giving another objective for the optimisation problem.

GAs are well suited to multi-objective optimisation problems since they use a population-based approach. Several multi-objective genetic algorithms have since been developed and are widely used in multi-objective optimisation problems. Konak *et al.* [64] provide a list of well-known multi-objective genetic algorithms, their advantages and disadvantages, and how they work. Deb [63] gives a detailed explanation of both non-elitist and elitist multi-objective genetic algorithms. A comparison of different genetic algorithms shows that the strength of the Pareto evolutionary algorithm (SPEA) and the non-dominated sorting genetic algorithm (NGSA) have superior performance compared to other algorithms [96]. In the same study, elitism is also shown to be an important factor in evolutionary multi-objective optimisation [96]. The concept of elitism involves the use of an elite-preserving operator such that the elites of a population are directly carried over to the next generation. Once introduced, elitism ensures that the fitness of the population-best solution does not deteriorate. Accordingly, a good solution found earlier on in the simulation will never be lost unless a better solution is found [63].

The non-dominated sorting genetic algorithm II (NSGA II) proposed by Deb *et al.* [97,98] as an improvement of the NSGA algorithm to solve the inherent issues of NSGA, which include: the high computational complexity of non-dominated sorting, lack of elitism and the need for specifying a sharing parameter [98]. The variant algorithm NSGA II was found to give better results than the SPEA and other contemporary algorithms, with better convergence towards a global optimal front, maintaining the diversity of the population on the Pareto-optimal front as well presenting less computational complexity than other multi-objective evolutionary algorithms. The NSGA II has become widely used in many multi-objective optimisation problems and is implemented in the ANSYS design exploration toolbox. For these reasons, the NSGA II was used in this work for the multi-objective optimisation of the suggested heat transfer enhancement techniques. Detailed information about the NSGA II algorithm is given by several sources [63,97,98].

3.4.2.1 Multi-objective optimisation problem

In its general form, a multi-objective optimisation problem can be written as [63]:

$$\begin{aligned} &\text{Minimise/maximise} && f_m(\mathbf{x}), && m = 1, 2, \ldots\ldots, M; \\ &\text{Subject to} && g_j(\mathbf{x}) \geq 0 && j = 1, 2, \ldots\ldots\ldots, J; \\ & && h_k(\mathbf{x}) = 0 && k = 1, 2, \ldots\ldots\ldots, K; \\ & && x_i^{(L)} \leq x_i \leq x_i^{(U)} && i = 1, 2, \ldots\ldots\ldots, n. \end{aligned} \qquad 3.42$$

where $f_m(\mathbf{x})$ is the objective function and M is the number of functions to be optimised. A solution $\mathbf{x}$ is a vector of n decision variables such that $\mathbf{x} = (x_1, x_2, \ldots, x_n)^T$. The functions $g_j(\mathbf{x})$ and $h_k(\mathbf{x})$ are constraint functions with J representing the inequality constraints and K the equality constraints. The last set represents the variable bounds, where each variable takes a value within the specified lower limit $x_i^{(L)}$ and upper limit $x_i^{(U)}$.

For multi-objective optimisation problems, no single solution is possible that satisfies all the objectives, especially when the objectives are conflicting. In such a case, a set of best solutions often called non-dominated solutions or Pareto optimal solutions [63,99] is sought, such that selecting any one solution in place of another sacrifices the quality of one of the objectives while improving the other objective. With higher-level information, a designer can then choose among the Pareto optimal solutions [63]. The concept of domination is commonly used to obtain such a set of solutions.

3.4.2.2 Concept of domination

Determination of the set of solutions that are non-dominated with respect to one another is the main objective of multi-objective optimisation. The NSGA II algorithm and most other genetic algorithms used for multi-objective optimisation use the concept of domination between two solutions to obtain a set of solutions that are not dominated with respect to one another.

A solution $\mathbf{x}^{(1)}$ is said to dominate solution $\mathbf{x}^{(2)}$ if these two conditions are true [63].

- The solution $\mathbf{x}^{(1)}$ is no worse than $\mathbf{x}^{(2)}$ in all objectives
- The solution $\mathbf{x}^{(1)}$ is strictly better than $\mathbf{x}^{(2)}$ in at least one objective

The non-dominated set of solutions, also called the Pareto-optimal solutions, can then be defined as [63]: given a set of solutions P, the non-dominated set of solutions P' are those that are not dominated by any member of the set P. A set of these non-dominated solutions represents the "best" solutions in the sense of multi-objective optimisation.

3.5 DESIGN OF EXPERIMENTS

Meta-modelling-based optimisation involves the use of experimental or simulation data and then constructing meta-models to which the optimisation algorithm is applied. For the effective representation of the design space, design of experiments (DOE) is used to determine the location of sampling points in such a way that the space of random input variables is explored in the most efficient way and the required information is obtained with a minimum number of sampling points. Five types of DOE are available in ANSYS, i.e. Central Composite Design, Box-Behnken Design, Optimal Space-filling Design, Custom, Custom and Sampling and Sparse Grid Initialisation [99].

For non-random and deterministic computer experiments, “space filling” designs are considered efficient since they treat the design space equally [99,100]. They also support the use of higher-order meta-models including Kriging meta-models [99]. Therefore, the optimal space-filling DOE type [99] was used in this work.

3.6 META-MODELLING

Meta-modelling, also called surrogate modelling or response surface methodology is an engineering method used when an outcome of interest cannot be easily or directly measured, so that a model of the outcome is used. In many real-world engineering problems, experiments or simulations are required to evaluate design objectives and constraint functions as the functions of design variables. These experiments or simulations may take minutes, hours or days to complete. This method of query and response often leads a designer to a trial-and-error approach, where the designer may never appreciate the functional relationship between the independent variables and the output and best settings for the independent variables might never be identified.

As a way of alleviating the above concerns, statistical techniques such as meta-modelling that mimic the behaviour of the simulation model as closely as possible while being computationally cheaper, are widely used in engineering design [100]. They give an insight into the functional relationship among the independent variables, and the output and best settings can be easily identified.

In meta-modelling-based optimisation, an initial meta-model is built, using the available experimental or simulation data to which an optimisation algorithm is applied. The accuracy of the model can then be improved, using higher-order meta-models.

For most real engineering problems, second-order models usually suffice [101]; these are based on regression analysis to estimate the relationship between two or more independent variables and a dependent variable.

Meta-modelling involves the use of a collection of statistical tools and mathematical techniques to develop, improve and optimise processes and products [101]. It provides a way to better understand functional relationships among design variables or inputs and responses or outputs. For a design involving a response y which is usually not known and perhaps complicated, as it depends on controllable input variables $x_1, x_2 \ldots\ldots x_k$. We can write a true response y as $y = f(x_1, x_2, \ldots\ldots, x_k)$. Meta-modelling uses the results from experiments or from a numerical analysis of design points to build responses using empirical models. The responses from these empirical models are usually approximations of the true response. For k

independent variables and n observations where $n > k$, a second-order model which includes all two-factor interactions is given by

$$y = \beta_0 + \sum_{j=1}^{k} \beta_j x_j + \sum_{j=1}^{k} \beta_{jj} x_j^{\,2} + \sum \sum_{i<j=2}^{k} \beta_{ij} x_i x_j + \varepsilon_i \qquad \text{for } i = 1, 2, 3 \ldots n \qquad 3.43$$

where ε_i is the error in fitting the model.

Equation (3.43) is a multiple linear regression model with k regressors (independent variables, or predictor variables); the parameters β_j, β_{jj} , β_{ij} for $j = 0, 1, \ldots k$ and $i = 1, 2, 3, \ldots n$ are called regression coefficients. The parameters β_j , β_{jj} , β_{ij} represent the expected change in response y per unit change in x_i, x_j when all the remaining independent variables x_i $(i \neq j)$ are held constant.

The method involves statistical analysis and is fully explained by several sources [101-103]. The linear and quadratic terms in Eq. (3.43) are treated in the same way. After linearisation, the model can be written as

$$y = X\beta + \varepsilon \qquad 3.44$$

where

$$y = \begin{bmatrix} y_1 \\ y_2 \\ . \\ . \\ . \\ y_n \end{bmatrix}, \quad X = \begin{bmatrix} 1 & x_{11} & x_{12} & \ldots & x_{1k} \\ 1 & x_{21} & x_{22} & \ldots & x_{2k} \\ 1 & . & . & \ldots & . \\ 1 & . & . & \ldots & . \\ 1 & . & . & \ldots & . \\ 1 & x_{n1} & x_{2n} & \ldots & x_{nk} \end{bmatrix}, \beta = \begin{bmatrix} \beta_0 \\ \beta_1 \\ . \\ . \\ . \\ \beta_k \end{bmatrix} \qquad 3.45$$

where x_{ij} is the i_{th} observation or level of variable x_j, ε is an n × 1 vector of random errors, n is the number of experiments or numerical investigations and k is the number of polynomial terms or independent variables.

The regression coefficients in the multiple linear regression models are estimated by using the method of least squares. The estimators of the response, also called least-squares

estimators, are determined by regression analysis through the minimisation of the sum of the squares of the resulting errors. This is similar to minimising the function, L [101]

$$L = \sum_{i=1}^{n} \varepsilon_i^{\,2} \tag{3.46}$$

such that

$$\hat{\beta} = (X^T X)^{-1} X^T y \tag{3.47}$$

The fitted regression model is

$$\hat{y} = X\hat{\beta} \tag{3.48}$$

Several metrics are used to measure the accuracy or goodness of fit of the response surface model. The methods most often used include the following:

Root mean square error (RMSE): this is the square root of the average square of residuals e, where e = y_i - $\hat{y}_i$. The best value should be zero for the predicted response to accurately represent the observed values.

$$RMSE = \sqrt{\frac{\sum_{i=1}^{n} (y_i - \hat{y}_i)^2}{n}} \tag{3.49}$$

Maximum relative residual *(MRR)*: this is the maximum distance of all the generated values from the calculated response surface to each generated value. Should be zero or close to zero for better accuracy, it is mathematically represented as

$$MRR = \underset{i=1:n}{\text{Max}} \left(Abs \left(\frac{y_i - \hat{y}_i}{\bar{y}} \right) \right) \tag{3.50}$$

Relative average absolute error (*RAAE*): this is the absolute maximum residual value relative to the standard deviation of the actual output data modified by the number of samples. It should be close to zero for better accuracy of the response surface.

$$RAAE = \frac{1}{\sigma_y}\frac{1}{n}\sum_{i=n}^{n} Abs(y_i - \hat{y}_i) \qquad 3.51$$

Coefficient of determination (R^2): gives the percentage of the variation of the output parameter that can be explained by the response surface regression equation. It measures the amount of reduction in the variability of y obtained by using the regression model. R^2 should be as close to 1 as possible for the regression model to accurately represent the actual response.

$$R^2 = 1 - \frac{\sum_i (y_i - \hat{y}_i)^2}{\sum_i (y_i - \bar{y}_i)^2} \qquad 3.52$$

Because R^2 always increases when additional terms are added to the model, the adjusted R^2_{adj} is sometimes used and gives a good measure of variability, taking into consideration the number of samples. R^2_{adj} is defined as [101].

$$R^2_{adj} = 1 - \frac{n-1}{n-p}\left(1 - R^2\right) \qquad 3.53$$

y_i is the output parameter at the i-th sampling point, $\hat{y}$ is the value of the regression model at the i-th sampling point, $\bar{y}$ is the arithmetic mean of the values y_i, n is the number of samples, p is the number of polynomial terms for a quadratic response surface ($p=k+1$) and σ_y is the standard deviation of the values y_i.

Since R^2_{adj} takes the sample size into consideration, it is usually more reliable for small samples (n < 30) [99].

The accuracy of the response surface can be improved by using higher-order models; in ANSYS design exploration, the Kriging meta-model is provided [99]. It is an interpolating meta-modelling technique for improving the accuracy of the response surfaces. The Kriging meta-model in ANSYS® 14 [99] has an automated refinement procedure. It determines where more design points are needed in a response surface in order to improve its accuracy. The refinement terminates when the number of specified refinement points is reached or

when the predicted relative error has been achieved. The use of the Kriging meta-model is recommended for deterministic and highly non-linear functions with factors less than 50 [100].

Kriging suggests a combination of a polynomial model and a departure of the form [99,100,104]

$$y(x) = f(x) + Z(x) \tag{3.54}$$

y(x) is the unknown function of interest, *f(x)* is a polynomial of *x*, and *Z(x)* is the realisation of a normally distributed Gaussian random process with mean zero and variance σ^2, and a non-zero covariance. In this case, *f(x)* is similar to the polynomial model, providing a global model of the design space while *Z(x)* creates localised variations so that the Kriging model interpolates the n sample data points.

3.7 OPTIMISATION PROCEDURE

The multi-objective optimisation was carried out using the design exploration toolbox available in ANSYS® release14 and 14.5 [99]. The flow chart illustrating the optimisation procedure is shown in Fig. 3.3.

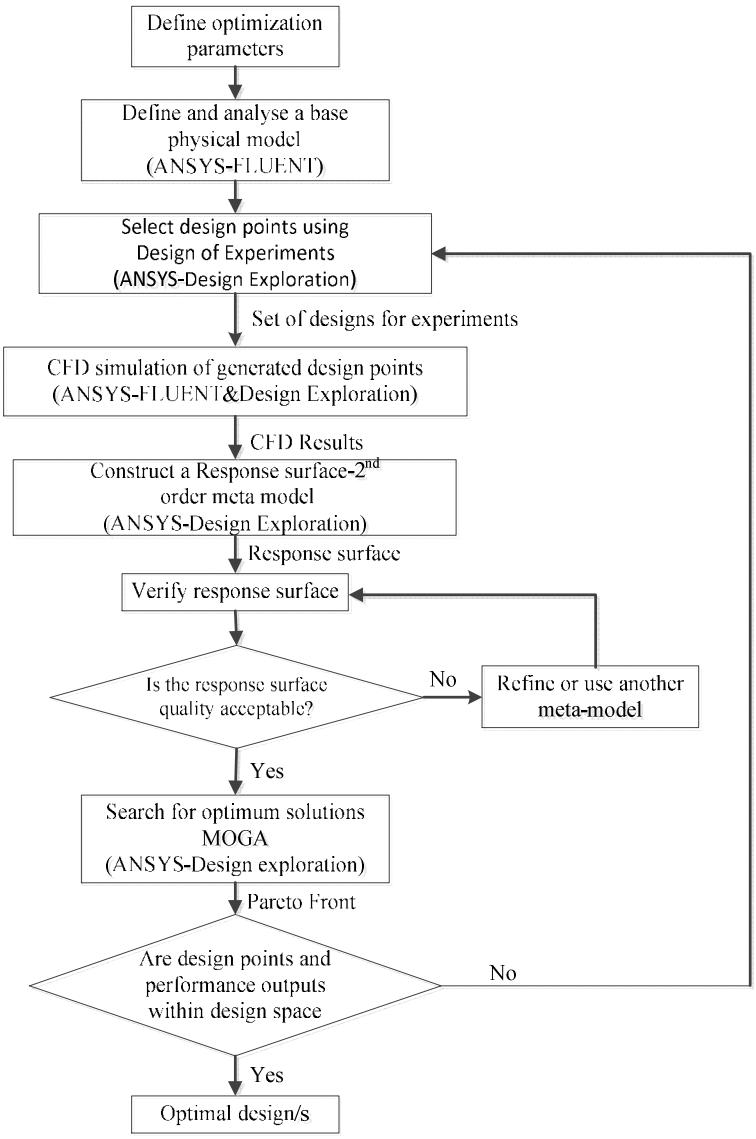

Fig. 3.3: Flow chart of the multi-objective optimisation procedure using ANSYS design exploration toolbox.

The optimisation process starts by building an accurate physical model of the problem using the numerical procedure discussed above. Then the design parameters and their ranges of variation are selected as well as the specification of performance parameters. After the physical model, the design variables as well as performance parameters are defined and an initial solution is obtained and used as a base case for the optimisation process. Using Design

of Experiments (DOE), a set of design points was generated, based on the selected DOE type. The design points correspond to different geometrical configurations of the physical model. "Space filling" designs are considered efficient for deterministic computer experiments, since they treat the design space equally [99,100]. "Space filling" also supports the use of higher-order meta-models including the Kriging meta-models also used in the present study [99]. Therefore, the optimal space-filling DOE type in the ANSYS® release 14 design exploration toolbox [99] was used in the present work. The optimisation requires the specification of a number of design points, which represent different combinations of independent variables. The configurations given by the chosen design points are then evaluated using ANSYS FLUENT® a commercial computational fluid dynamics code, following the same procedure described in the numerical modelling procedure to obtain the defined performance parameters.

Once all the design points have been updated, the next step is building response surfaces or a meta-model to relate the performance parameters to the design parameters. The accuracy of the response surface is essential for the remaining steps. The detailed method for building standard response surfaces and metrics used for determining the response surface accuracy is detailed in Myers and Montgomery [101]. A brief discussion of the meta-modelling procedure appears in section 3.6 above.

3.8 DECISION SUPPORT PROCESS

Most multi-objective optimisation problems require a decision support tool to help the designer come to a single design. If higher-level information concerning the objectives is available (such as whether heat transfer enhancement is more important than fluid friction or if the minimisation of fluid friction is more important than heat transfer enhancement or if all have the same level of importance), a design can be arrived at by using some decision support procedure. A decision support process provided in ANSYS® release 14 was adopted for this study. The decision support process used is a goal-based, weighted, aggregation-based technique that ranks the design candidates according to the order of importance of the objectives [99].

For n input parameters and m output parameters and their individual lower and upper bounds, the objectives are combined into one weighted objective function Φ [99]. The candidates are then ranked in ascending orders of magnitudes of the values of Φ.

$$\Phi \equiv \sum_{i=1}^{n} w_i N_i + \sum_{j=1}^{m} w_j M_j \qquad 3.55$$

w_i, w_j are weights defined as [99]

$$w_i = w_j = \begin{cases} 1.000 & \text{if the importance is higher} \\ 0.666 & \text{if the importance is default} \\ 0.333 & \text{if the importance is lower} \end{cases} \qquad 3.56$$

N_i and Mj are normalised objectives for input and output parameters, respectively [99]

$$N_i = \left(\frac{|x_t - x|}{x_u - x_l} \right)_l \qquad 3.57$$

$$M_j = \left(\frac{|y_t - y|}{y_{\max} - y_{\min}} \right)_l \qquad 3.58$$

where x = current value of input parameter i, x_t, y_t = corresponding "target values", y = current value for output parameter j, x_l and x_u are lower and upper bounds, respectively, for input parameters i, y_{min} and y_{max} correspond to the lower and upper bounds respectively for out parameter j.

For continuous input parameters, the targets will give the desired values of the parameter according to ANSYS® [99].

$$x_t = \begin{cases} x & \text{if objective is "No Objective"} \\ x_l & \text{if objective is "Minimise"} \\ \tfrac{1}{2}(x_l + x_u) & \text{if objective is "Seek Midpoint"} \\ x_u & \text{if objective is "Maximise"} \end{cases} \qquad 3.59$$

$$y_t = \begin{cases} y, & \text{if objective is "No Objective"} \\ y_{\min}, & \text{if objective is "Minimise" and a "Target" value is not defined} \\ y_t^*, & \text{if objective is "Values < = Target" and "Target is defined and } y \geq y_t^* \\ y, & \text{if objective is "Values < = Target" and "Target is defined and } y \leq y_t^* \\ y_t^*, & \text{if objective is "Seek Target" or "Values = Target"} \\ y, & \text{if objective is "Values > = Target" and "Target is defined and } y \geq y_t^* \\ y_t^*, & \text{if objective is "Values > = Target" and "Target is defined and } y \leq y_t^* \\ y_{\max}, & \text{if objective is "Maximise" and a "Target" value is not defined} \end{cases} \quad 3.60$$

where y_t^* = user-specified target value .

3.9 CONCLUDING REMARKS

This chapter describes the numerical modelling essentials and procedure used in the entire work. The numerical modelling procedure used in this work together with the governing equations, turbulence modelling procedure and near-wall treatment is presented in detail. For accurate prediction of temperature and velocity fields from which the entropy generation rates are determined, the need to maintain the dimensionless wall coordinate about 1 ($y^+ \approx 1$) is emphasised. Also provided is a review of the two optimisation methods used in the present work, i.e. the entropy generation minimisation method and multi-objective optimisation.

Furthermore, the concepts of design of experiments and meta-modelling are introduced since they are needed for goal-driven optimisation in ANSYS design exploration. For multi-objective optimisation, it has been shown that the non-dominated sorting genetic algorithms (NSGA) provide better results than the other genetic algorithms. Accordingly, the non-dominated sorting genetic algorithm II (NSGA II) an improvement of the ordinary NSGA algorithm was chosen for multi-objective optimisation studies in this work.

CHAPTER FOUR

CHAPTER FOUR: DEVELOPMENT AND VALIDATION OF THE PARABOLIC TROUGH RECEIVER THERMAL MODEL

4.1 INTRODUCTION

This section presents the development and validation of the parabolic trough receiver thermal model. The developed thermal model was thoroughly validated against experimental data from Sandia National Laboratories by Dudley *et al.* [40] for temperature gain and collector efficiency and against experimental data from Burkholder and Kutscher [31] for the receiver's heat loss. The forced convection heat transfer in the receiver's absorber tube was validated by Gnielski correlation (Eq. 2.23) as obtained from Cengel [84]. The fluid friction was compared with Petukhov's first equation for friction factors (Eq. 2.24) also quoted in Cengel [84].

4.2 MODEL DESCRIPTION

This chapter presents the two models of the receiver that were developed. The first model (model A), modelled the forced convection heat transfer in the receiver, heat conduction in the absorber tube, radiation heat transfer between the absorber tube's outer wall and the glass cover's inner wall, heat conduction through the glass cover and radiation between the glass cover and the sky, and convection heat transfer between the glass cover and the ambient temperature. The representation of model A is shown in Fig. 4.1.

The second model (model B) considered a simplified receiver. In this model, only the forced convection heat transfer in the absorber's receiver tube and heat conduction through the absorber tube walls was considered. Radiation exchange between the absorber tube's outer wall and the glass cover inner wall was applied as a radiation boundary condition.

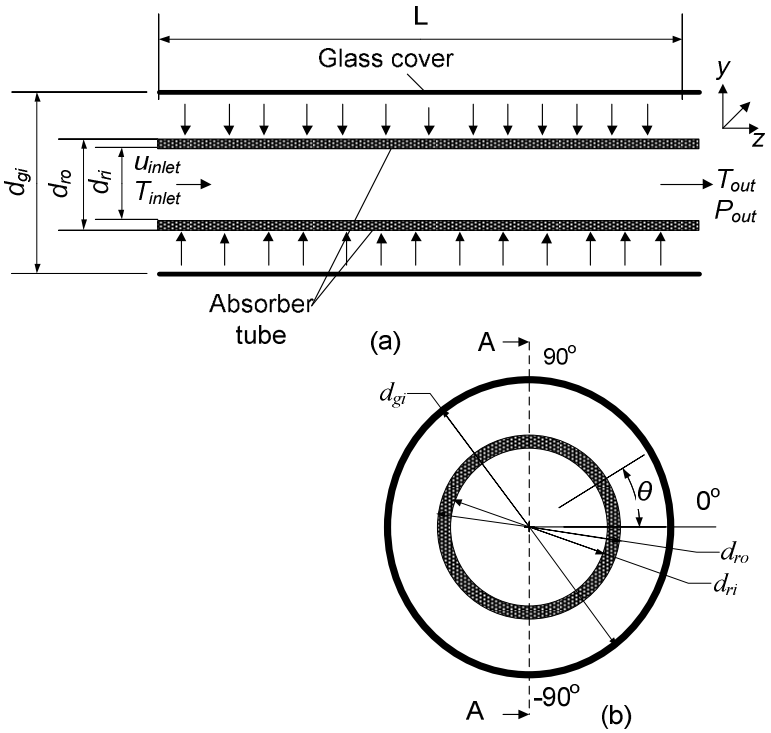

Fig. 4.1: Schematic diagram of receiver model A: (a) longitudinal view and (b) cross-section view.

4.3 RAY TRACING

The actual heat flux profile on the receiver's absorber tube is non-uniform. Several methods can be used to obtain the heat flux or temperature distribution on the receiver's absorber tube. These range from measurements [46], ray tracing methods [34,105] and analytical methods [106,107].

In this study, the Monte Carlo ray-tracing method was used to obtain the heat flux distribution on the receiver's absorber tube. In Monte Carlo ray-tracing, a number of rays are selected and traced as they undergo several optical interactions. For the purposes of this study, SolTrace was used, which is an optical modelling software developed by the National Renewable Energy Laboratory for modelling concentrated solar power systems [108]. The ray-tracing procedure involves specifying the sun's shape, the optical properties of the collector and the receiver, and the geometries of the collector and the receiver. Then a maximum number of rays to be generated by the sun are selected and desired number of ray

intersections specified. The rays are then traced as they are reflected by the reflecting mirror, transmitted through the glass cover and absorbed by the absorber tube. A sample of ray intersection obtained from SolTrace is shown in Fig. 4.2(a) for a rim angle of 80^o and aperture width of 10 m and in Fig. 4.2(b) for a rim angle of 40^o and an aperture width of 10 m. The heat flux received on the absorber tube's circumference can then be obtained from the contours of heat flux available in SolTrace once the ray tracing is complete [108].

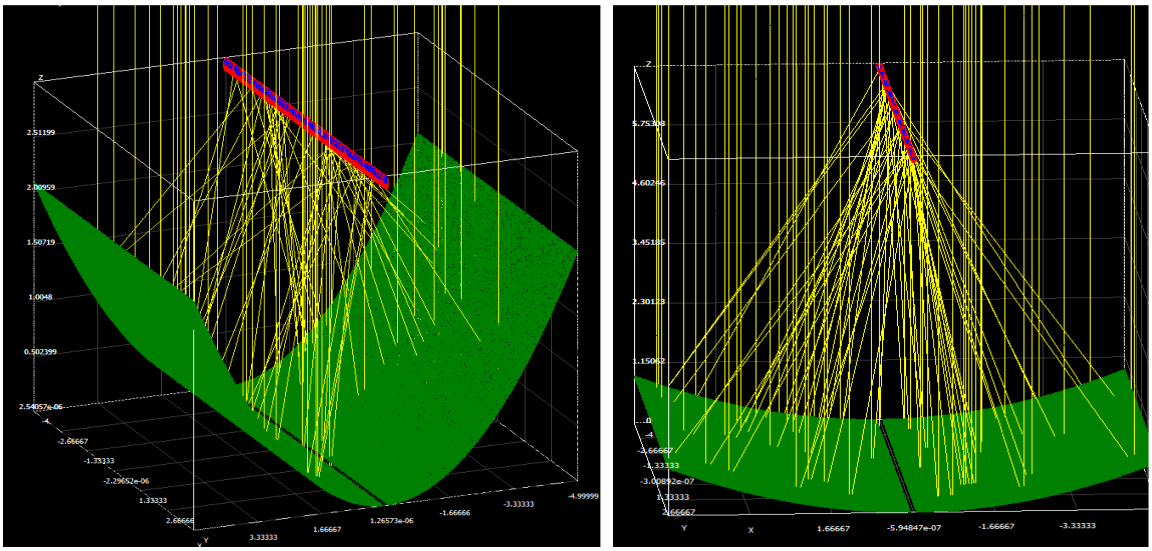

(a) $\varphi_r = 80^o$ (b) $\varphi_r = 40^o$

Fig. 4.2: Ray tracing results for a parabolic trough collector with an aperture width of 10 m for different rim angles: (a) rim angle, φ_r = 80^o and (b) rim angle, φ_r = 40^o.

The results obtained in the present study from the Monte Carlo ray-tracing were validated with available data from the literature [34,105,106]. As shown in Fig. 4.3, for half the circumference of the receiver's absorber tube, our results for the local concentration ratio, LCR (the ratio of actual heat flux on the absorber tube to that incident on the reflector) show good agreement with the available data. In this study, the concentrator was taken to be of perfect shape and perfect alignment. The pillbox sun shape was assumed and 10^6 ray intersections were used. The geometry of the collector and receiver was specified using Eqs. (2.1) – (2.7) given in Section 2.3.1 of Chapter 2. The absorber tube circumferntial angle, θ is measured as shown in Fig. 4.1.

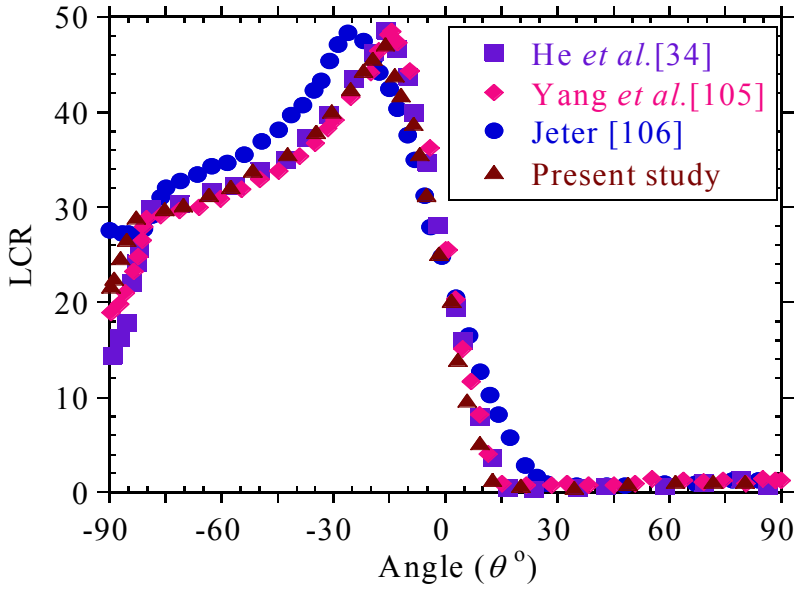

Fig. 4.3: Comparison of the present study prediction of local concentration ratio (LCR) as a function of circumferential angle (θ) with literature.

4.4 BOUNDARY CONDITIONS

The boundary conditions used in the present work depend on the geometry under consideration as well as the computational domain used. This section on receiver thermal model development considers the full receiver length. The following boundary conditions were used for model A. (1) Non-uniform heat flux on the absorber tube's outer wall. The sample heat flux distribution used in this study is shown in Fig. 4.4 as determined using ray tracing in SolTrace [108] for different rim angles and an aperture width of 6 m or a concentration ratio (C_R) of 86. A direct normal irradiance (DNI) of 1 000 W/m^2 was assumed. (2) Velocity inlet and pressure outlet boundary conditions were used for the absorber tube's inlet and outlet respectively. (3) The inner absorber tube walls were considered no-slip and no-penetration. (4) For the inlet and outlet of the receiver's annulus space, a symmetry boundary condition was used such that the normal gradients of all flow variables were zero. (5) For the outer wall of the glass cover, a mixed boundary condition was used to account for both radiation and convection heat transfer. Stefan Boltzmann's law with the sky as the external radiation enclosure gives radiation between the glass cover and the sky. Convection

heat transfer was modelled by specifying a convection heat transfer coefficient and fluid temperature.

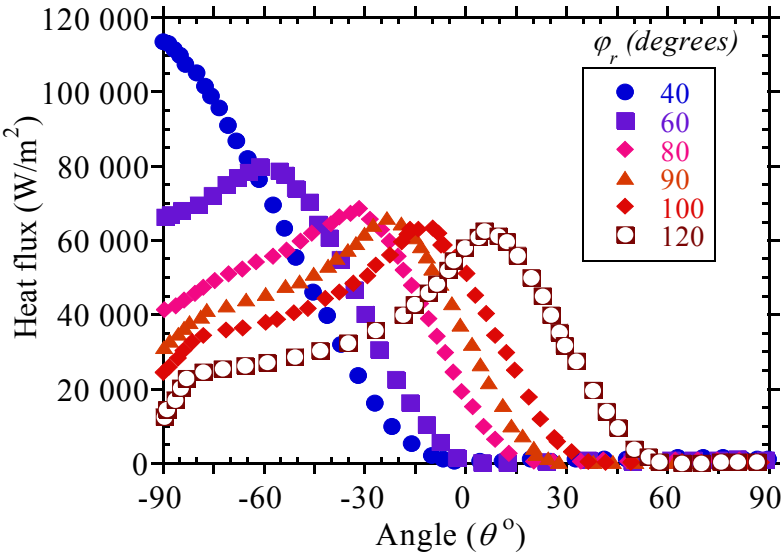

Fig. 4.4: Absorber tube heat flux as a function of circumferential angle (θ) and rim angle (φ_r) for a concentration ratio (C_R) of 86, $Re = 1.02\times10^4$ and inlet temperature of 400 K.

The sky temperature is given by [86] as

$$T_{sky} = 0.0552 T_{amb}^{1.5} \tag{4.1}$$

Several expressions for determining the wind heat transfer coefficient have been proposed as given by Eqs. (2.17) - (2.19). Mullick and Nanda [109] give a more accurate expression for the wind heat transfer coefficient as

$$h_w = V_w^{0.58} d_{go}^{-0.42} \tag{4.2}$$

The boundary conditions used in model A, for flow inside the absorber tube (1-4), also apply to model B. In addition to these boundary conditions, a radiation boundary condition was applied to simulate the radiation exchange between the absorber tube and the glass cover. The external radiation temperature (average glass-cover temperature) for model B was determined from the results of model A at different inlet temperatures and Reynolds numbers.

The geometrical and simulation parameters used are shown in Table 4.1. The values are the same as those of commercially available receivers [40].

Table 4.1: Geometrical parameters and environmental conditions used in this study

Reflector		**Receiver**	
Aperture width, W_a	4 – 10 m	Absorber tube inner diameter, d_{ri}	0.066 m
Collector length, L_c	5 m	Absorber tube outer diameter, d_{ro}	0.07 m
Reflectivity, ρ_c	0.96	Glass cover inner diameter, d_{gi}	0.11 m
Rim angle, φ_r	40-120^o	Glass transmissivity, τ_g	0.97
Concentration ratio, $C_R=A_c/A_r$	57 – 143	Absorber tube absorptivity, α_{abs}	0.96
		Glass cover emissivity, ξ_g	0.86
Environmental conditions			
Direct normal irradiance, DNI	1 000 W/m^2		
Ambient temperature, T_{amb}	300 K		
Wind velocity, V_w	2 m/s		
Inlet temperature, T_{inlet}	350 – 650 K		

The Reynolds number and the mass flow rate depend on the properties of the heat transfer fluid, which vary with fluid temperature. For flow rates in the range 4.9 m^3/h – 154 m^3/h used, the Reynolds number varies in the range 6 730 – 1 676 100 and the mass flow rate is in the range 0.78 kg/s – 37.8 kg/s.

4.5 NUMERICAL ANALYSIS

In actual parabolic trough plants, the flow rates in the turbulent flow regime are used. In this study, the flow inside the absorber tube was also considered turbulent for both models, such that the RANS equations, Eqs. (3.2) - (3.4) are applied. In model A, the radiation heat transfer between the absorber tube's outer wall and the inner wall of the glass cover was accounted for by using the discrete ordinates model [88,89], with air taken as radiatively non-participating. The thermal conductivity of air in the vacuum space was calculated according to Eq. (2.31). In both models, stainless steel was used as the absorber tube material, its thermal conductivity is temperature dependent as given by Eq. (2.25). The coating on the absorber tube was modelled to have a temperature-dependent thermal emissivity given in Eq. (2.33). In model A, the receiver's glass cover was made of Pyrex® with properties similar to those of current receivers as given by Forristall [45].

For model A, the convection and radiation heat exchange between the glass cover and the ambient temperature was modelled using a mixed radiation and convection boundary condition. The convection heat transfer coefficient was approximated from Eq. (4.2). The emissivity of the glass cover was taken as 0.86 [45]. The sky radiation temperature was obtained from Eq. (4.1).

4.6 SOLUTION METHODOLOGY

The solution of the RANS equations, together with/without equations for radiation heat transfer in the receiver's annulus space and equation for conduction heat transfer in the absorber tube's wall for both model A and B were obtained from ANSYS® release 14 and 14.5. The geometry was modelled in the ANSYS design modeller, the descretisation of the computational domain in ANSYS meshing and the solution were obtained using ANSYS FLUENT [88,89]. ANSYS FLUENT is a commercial computational fluid dynamics code that uses the finite volume method to solve the governing equations. Turbulence closure was achieved using the realisable k-ε model and the near-wall phenomenon was modelled using the enhanced-wall treatment option. Values of $y^+ \approx 1$ were used to fully resolve the viscous sublayer. Hexahedral and quadrilateral mesh elements were used for the discretisation of the computational domain. Second-order upwind schemes were employed for integrating the governing equations together with the boundary conditions over the computational domain.

In model A, radiation heat transfer in the annulus was modelled using the discrete ordinates model. Air was taken as a radiatively non-participating medium. In model B, a radiation boundary condition was used to account for the radiation exchange between the absorber tube and the glass cover. The radiation temperature of the glass cover was determined from the results of model A for each Reynolds number and fluid temperature.

Convergence was obtained with scaled residuals of mass, momentum, turbulent kinetic energy (k) and turbulence dissipation rate (ε) less than 10^{-4} while the energy residuals were less than 10^{-6}. In addition, the solution was also considered fully converged when monitors of the convergence history of the absorber tube's outlet temperature and glass cover temperature flattened for more than 200 successive iterations.

Mesh independence studies for several refinements of the mesh were carried out with the receiver heat loss *(q_l)* and heat gain *(q_u)* as monitored quantities for model A. For model B, the only monitored quantity was the heat gain (q_u). According to Eq. (4.3)

$$\left|\frac{q_u^i - q_u^{i+1}}{q_u^{i+1}}\right| \le 0.01 \text{ and } \left|\frac{q_l^i - q_l^{i+1}}{q_l^{i+1}}\right| \le 0.01 \qquad 4.3$$

where *i* is the value before mesh refinement and *i+1* is the value after mesh refinement.

The mesh used in the simulation is shown in Fig. 4.5. Figure 4.5 (a) shows the cross-section mesh of the receiver tube for model A. It includes the heat transfer fluid inside the absorber tube, the absorber tube wall and the annulus space between the glass cover and the absorber tube. Figure 4.5 (b) shows the cross-section mesh of the absorber tube for model B. It includes only the absorber tube wall and the heat transfer fluid inside the absorber tube. Figure 4.5 (c) shows the 3-D mesh for some receiver walls for model A. The mesh was generated in a way that it was refined in the absorber tube wall's normal direction with prism layers to ensure a $y^+ \approx 1$ for both models.

Model A was also refined in the receiver's annulus space; at the interface between the absorber tube and annulus space; and between the annulus space and the glass cover.

The heat transfer fluid used throughout the present work was SYLTHERM 800. Its properties are temperature-dependent as defined in the product's technical details [110]. From the manufacturer's technical data, the thermal physical properties have been represented by temperature-dependent polynomials by curve fitting as given by Eqs. (4.4) – (4.8) and used in the numerical simulations. Unless specified, the properties of the heat transfer fluid used in the numerical simulations were the temperature-dependent polynomials given by Eqs. (4.4) – (4.8).

The specific heat capacity c_p, for the temperature range $233.15 \le T \le 673$ K is given by

$$c_p = 1.01787 + 1.70736 \times 10^{-3} T \quad (kJ/kgK) \qquad 4.4$$

The density ρ, for the temperature range $233.15 \le T \le 673.15$ K is given by

$$\rho = 1.2691\times10^{3} - 1.52115T + 1.79133\times10^{-3}T^{2} - 1.67145\times10^{-6}T^{3} \ (kg/m^{3}) \quad 4.5$$

The thermal conductivity λ, for the temperature range $233.15 \leq T \leq 673.15$ K is given by

$$\lambda = 1.90134\times10^{-1} - 1.88053\times10^{3}T \quad (W/mK) \quad 4.6$$

The variation of the heat transfer fluid's viscosity is given by a piece-wise polynomial. For the temperature range $233 \leq T \leq 343$ K, it is

$$\mu = 5.14887\times10^{4} - 9.61656\times10^{2}T + 7.50207T^{2} - 3.12468\times10^{-2}T^{3} + 7.32194\times10^{-5}T^{4} - 9.14636\times10^{-8}T^{5} + 4.75624\times10^{-11}T^{6} \ (mPa.s) \quad 4.7$$

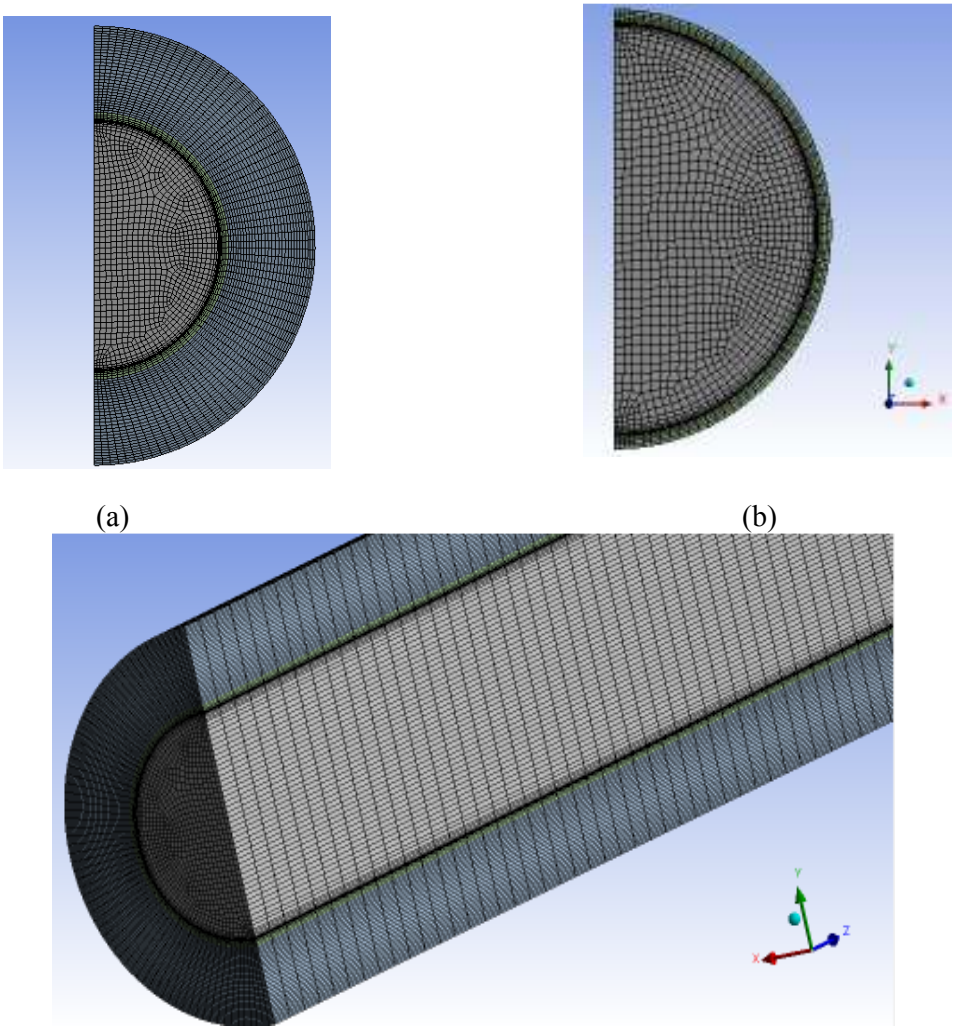

(a) (b)

(c)

Fig. 4.5: Representative mesh of the developed receiver models: (a) cross-section view of model A, (b) cross-section view of model B and (c) lateral view of model A.

For the temperature range $343 \leq T \leq 673$ K, the viscosity of the heat transfer fluid is given by

$$\mu = 9.88562\times10^{1} - 7.30924\times10^{-1}T + 2.21917\times10^{-3}T^{2} - 3.42377\times10^{-6}T^{3} + 2.66836\times10^{-9}T^{4} - 8.37194\times10^{-13}T^{5}\,(mPa.s) \quad 4.8$$

Samples of the thermal physical properties of SYLTHERM 800 at T_{inlet} = 400 K, 550 K and 650 K are shown in Table 4.2.

Table 4.2: Syltherm 800 thermal properties at T_{inlet} = 400 K, 550 K and 650 K

Thermal property	T_{inlet} (K)		
	400 K	550 K	650 K
Specific heat capacity (c_p), J/kg K	1791	2047	2218
Density (ρ), kg/m^3	840	696	578
Thermal conductivity (λ), W/m K	0.115	0.087	0.068
Viscosity (μ), Pa.s	0.002160	0.000555	0.000284

4.7 RESULTS

4.7.1 RECEIVER MODEL VALIDATION

The selected test points from Dudley's experimental results used for the validation of the receiver thermal models are listed in Table 4.3.

Table 4.3: Experimental data used in validation of parabolic trough receiver model [40]

	DNI (W/m^2)	Wind speed (m/s)	Air temperature (°C)	Flow rate (L/min)	T_{inlet} (°C)	T_{out} (°C)	ΔT (°C)
1	933.70	2.60	21.20	47.70	102.20	124.00	21.80
2	968.20	3.70	22.40	47.78	151.00	173.30	22.30
3	982.30	2.50	24.30	49.10	197.50	219.50	22.00
4	909.50	3.30	26.20	54.70	250.70	269.40	18.70
5	937.90	1.00	28.80	55.50	297.80	316.90	19.10
6	880.60	2.90	27.50	55.60	299.00	317.2	18.20
7	920.90	2.60	29.50	56.80	379.50	398.00	18.50
8	903.20	4.20	31.10	56.30	355.90	374.00	18.10

Figure 4.6 (a) shows a comparison of temperature gain for the present models. It can be seen that both models predict the same variation of temperature gain. Model B slightly over-predicts the temperature gain compared to model A, because heat loss is not explicitly modelled in a way that takes into consideration the effect of wind speed and sky radiation. In both models, the percentage variation compared with experimental data from Dudley *et al.* [40] is within ± 7.0% for all data points. The comparison of model A's temperature gain and collector efficiency is shown in Fig. 4.6 (b). The collector efficiency is within 5% of the experimental results, except for the third-last point where it is higher.

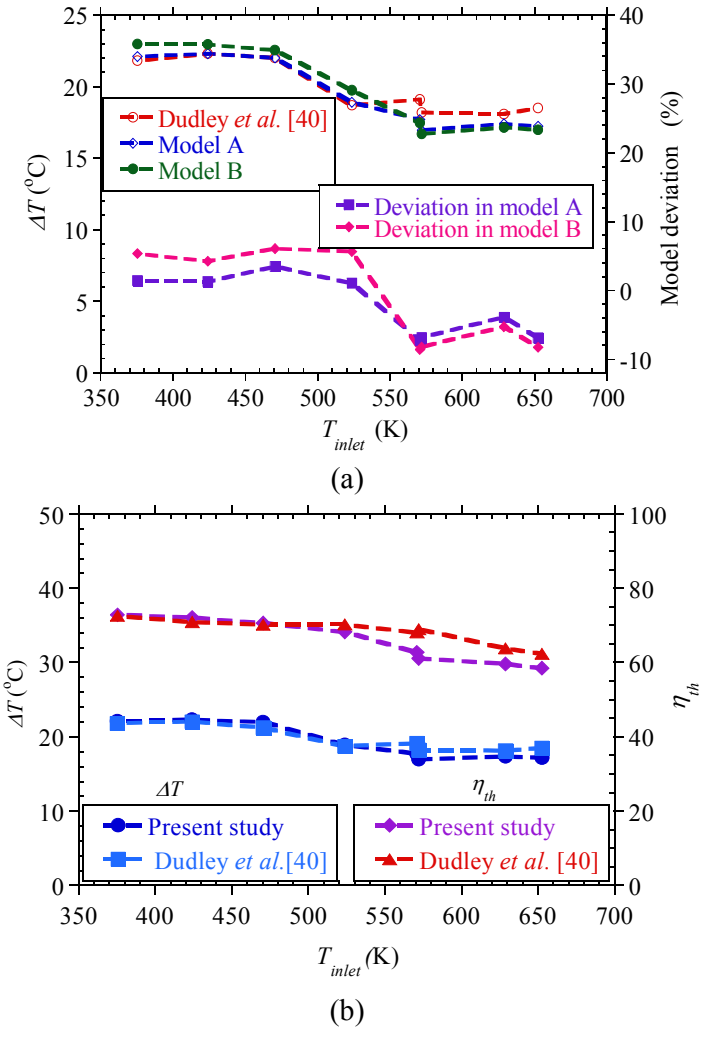

Fig. 4.6: Comparison of present study receiver thermal model with experimental results from SANDIA national laboratory [40]: (a) validation of receiver temperature gain (ΔT) for models A and B and (b) temperature gain and collector thermal efficiency validation for model A.

Figure 4.7 shows the validation of the present models' heat loss with the test results from Burkholder and Kutscher [31]. Only model A explicitly models the heat loss, for model B the heat loss was determined by using Burkholder and Kutscher's correlation [31] which relates heat loss with absorber tube temperature. The figure indicates that both models give nearly the same heat-loss prediction because the predicted absorber tube temperatures for model A and model B are almost the same. The agreement is within less than 6.5% with most points within less than 4%.

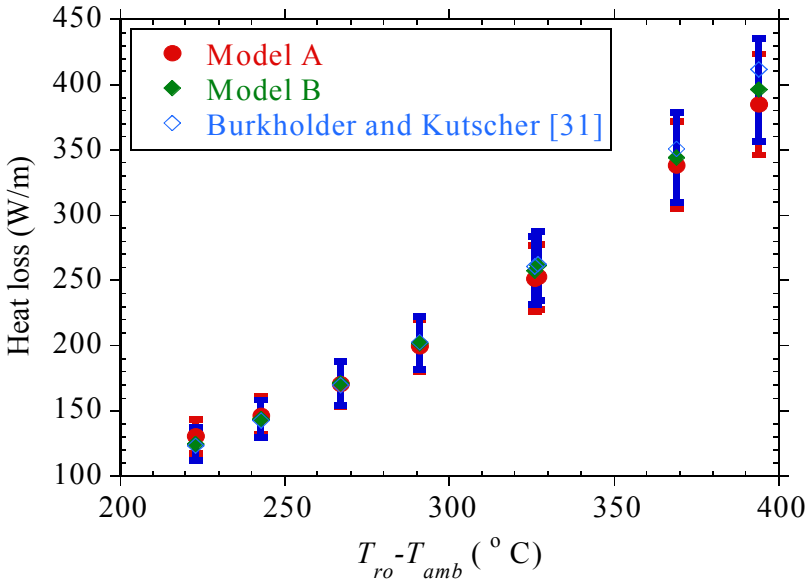

Fig. 4.7: Comparison of predicted receiver heat loss for model A and model B as a function of absorber tube - ambient temperature difference with experimental data.

The two models give similar results for heat loss, since the heat loss for evacuated receiver tubes is shown to depend more strongly on the absorber tube's wall temperature than on wind speed, ambient temperature and sky temperature [30,31]. Figure 4.7 further shows that the receiver heat loss increases as the absorber-ambient temperature difference rises. The absorber tube temperature is dependent on the inlet temperature. The absorber tube temperature increases as the inlet temperature rises.

4.7.2 HEAT TRANSFER AND PRESSURE DROP VALIDATION FOR A PLAIN ABSORBER TUBE

The heat transfer in the absorber tube of the receiver was validated using the Gnieliski equation for the Nusselt number (Eq. 2.23). Figure 4.8 shows that the agreement of the Nusselt number for the eight points used in the validation is within ± 8% of the values given by the correlation.

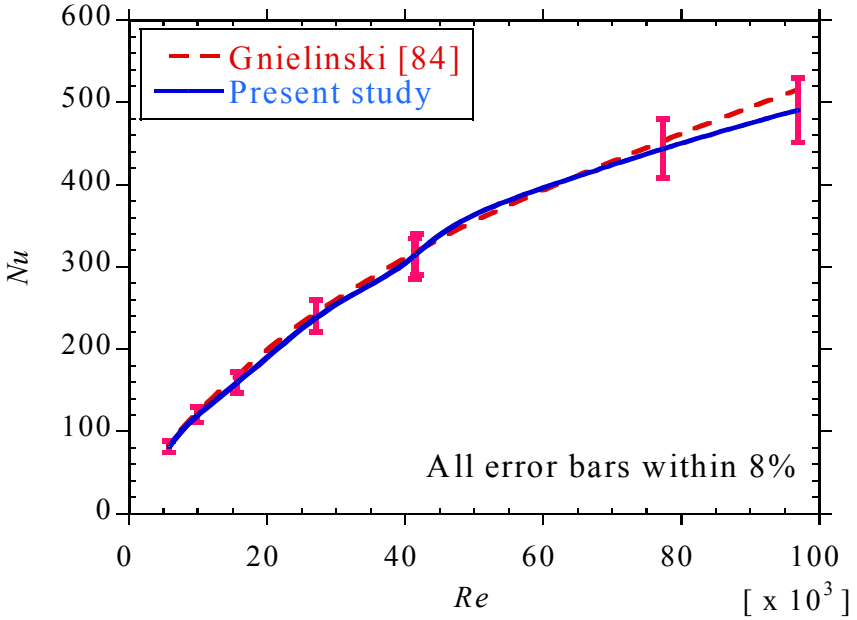

Fig. 4.8: Comparison of present study receiver's heat transfer performance as a function of Reynolds number with Gnielinski's correlation [84].

The friction factor was validated with Petukhov's first equation (Eq. 2.24) for the calculated friction factor. Figure 4.9 shows the variation in the friction factor for the data points used in the validation. The percentage error is within ± 6% except for the first and second points corresponding to low heat transfer fluid inlet temperatures and a Reynolds number of about 5 750 and 8 340 respectively. The percentage error for these two points was about 14.6% and 9.5% respectively.

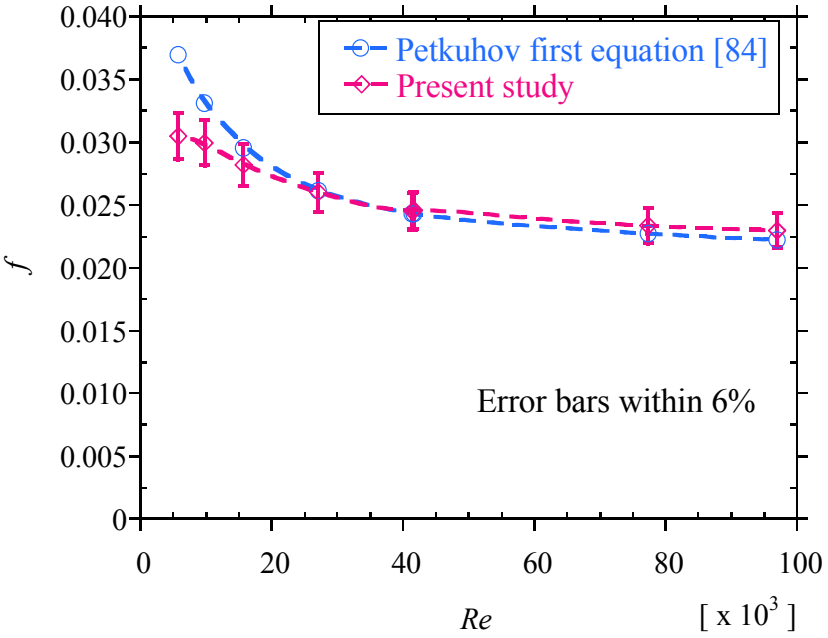

Fig. 4.9: Comparison of present study receiver friction factor as a function of Reynolds number with Petukhov's first equation [84].

In this study, simpler correlations for heat transfer performance and fluid friction were derived using curve fitting and regression analysis. The correlations predict the Nusselt number and friction factor within ± 4% and ± 3.5% respectively.

The Nusselt number for the receiver with a plain absorber tube is given by

$$Nu = 0.0104\,\mathrm{Pr}^{0.374}\,\mathrm{Re}^{0.885} \qquad 4.9$$

R^2 = 1.0 for this correlation and the correlation predicts the Nusselt number within ± 4%.

The friction factor correlation is

$$f = 0.173\,\mathrm{Re}^{-0.1974} \qquad 4.10$$

R^2 = 0.994 for the friction factor correlation and the correlation is valid within ± 3.5%.

Equations (4.9) – (4.10) were obtained with parameters in the range

$$1.02\times 10^4 \leq \mathrm{Re} \leq 1.68\times 10^6$$

$$9.29 \leq \mathrm{Pr} \leq 33.7 \text{ and } 400\ \mathrm{K} \leq T_{inlet} \leq 650\ \mathrm{K}$$

The Nusselt number and friction factor obtained from the correlations in Eqs. (4.9) and (4.10) were compared with known correlations. A scatter plot for Nusselt number and friction factor is shown in Fig. 4.10.

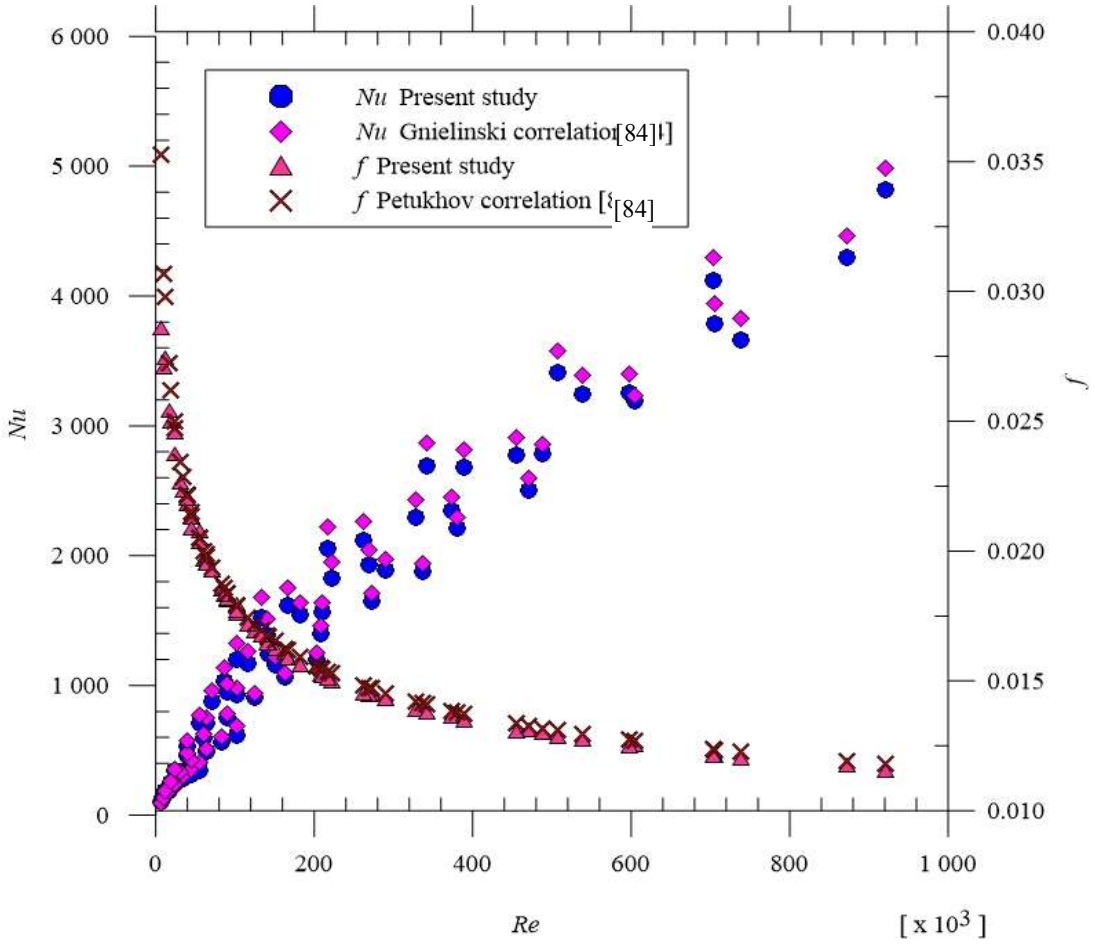

Fig. 4.10: Comparison of present study heat transfer and fluid friction correlations with Gnielinski and Petukhov correlations respectively [84] on a scatter plot.

4.7.3 HEAT FLUX AND TEMPERATURE DISTRIBUTION

The heat flux on the receiver's absorber tube circumference varies with the rim angle and the concentration ratio. Figure 4.11(a) and 4.11(b) show the variation of heat flux on the absorber tube's circumference at various rim angles for concentration ratios of 86 and 143 respectively. As shown in the figures, the heat flux profile varies greatly around the absorber tube's circumference, depending mainly on the rim angle.

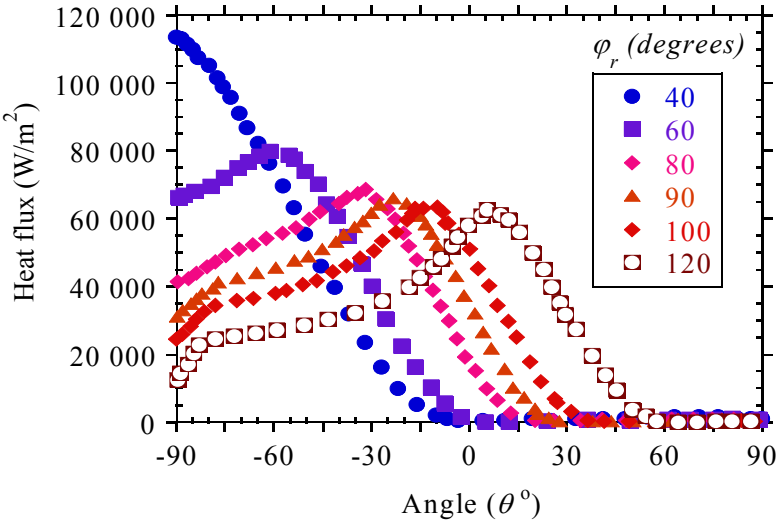

(a)

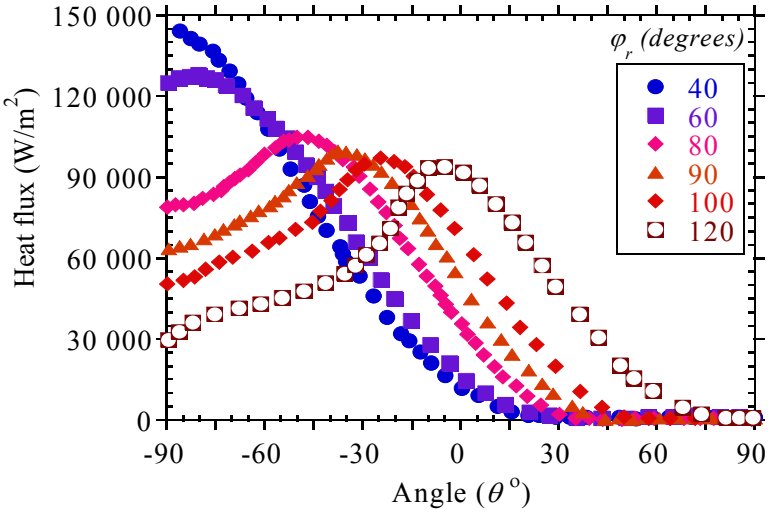

(b)

Fig. 4.11: Absorber tube heat flux as a function of circumferential angle (θ) and rim angle (φ_r) for an inlet temperature of 400 K, Re = 1.02 ×10^4 and a given concentration ratio (C_R): (a) C_R = 86 and (b) C_R = 143.

The heat flux distribution is characterised by an area where the absorber tube shadows the collector depending on the rim angle (at a rim angle of 120^o and concentration ratio of 86, this area is in the range -90^o ≤ θ ≤ -80^o). An area where the heat flux is increasing also depends on the rim angle (is in the range -80^o ≤ θ ≤ 15^o, at a rim angle of 120^o and concentration ratio of 86). An area where the heat flux is reducing, also depends on the rim angle (is in the range

$15^o \leq \theta \leq 55^o$, at a rim angle of 120^o and concentration ratio of 86). And an area where only direct solar radiation is incident on the absorber tube (in the range $55^o \leq \theta \leq 90$ at a rim angle of 120^o and concentration ratio of 86).

These regions are more distinct at rim angles above 60^o. The shadow effect is significant as the rim angles increase, whereas the area receiving direct solar radiation decreases as the rim angles increase. The figure also shows that the peak heat flux increases as the rim angle decreases. At rim angles above 80^o, the change in the peak heat flux is not significant. At a rim angle of 40^o, there is almost no shadowing effect and no heat flux increasing area. The heat flux will be concentrated on the half of the absorber tube facing the collector. As shown, at such low rim angles, high heat flux peaks and large circumferential temperature gradients will result.

Figures 4.12(a) and 4.12(b) show the variation of heat flux around the absorber tube's circumference at various concentration ratios for rim angles of 40^o and 100^o. As expected, as the concentration ratio increases, the heat flux on the absorber tube increases. At larger rim angles, the heat flux profile consists of a shadow effect area, an increasing heat flux area, a decreasing heat flux area and a direct solar heat flux area [34].

It is clear from the figures that at very low rim angles, the shadow effect and heat flux increasing area do not exist and the peak heat flux increases. As the rim angles increase the shadow effect and heat flux increasing areas become more pronounced and the peak heat flux decreases.

Therefore, higher rim angles are necessary to avoid such larger temperature differences, especially when low flow rates and higher concentration ratios are desirable. However, using larger rim angles increases the material requirements for the collector. Therefore, a trade-off has to be made on how large the rim angle should be to avoid larger temperature difference while using as little material as possible to keep costs low. Figures 4.11 (a) and 4.11(b) indicate that above a rim angle of 80^o, the peak heat flux does not decrease significantly, as the rim angle is increased further. Accordingly, no significant reduction in temperature absorber tube circumferential temperature difference will be achieved as the rim angles are increased above 80^o.

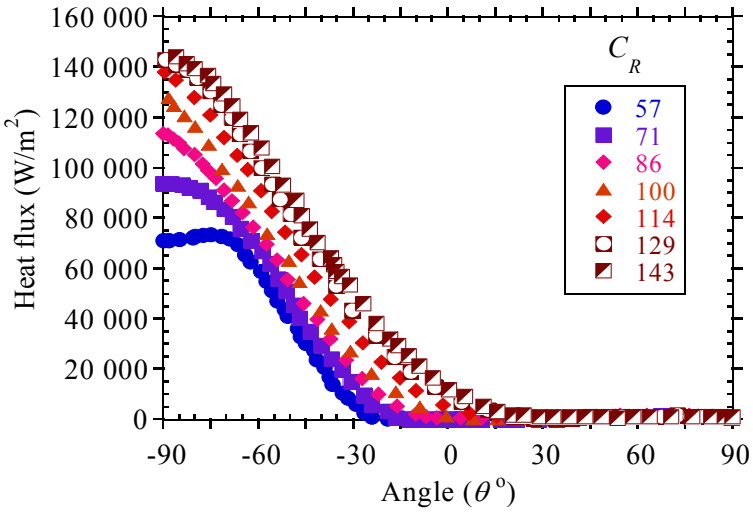

(a)

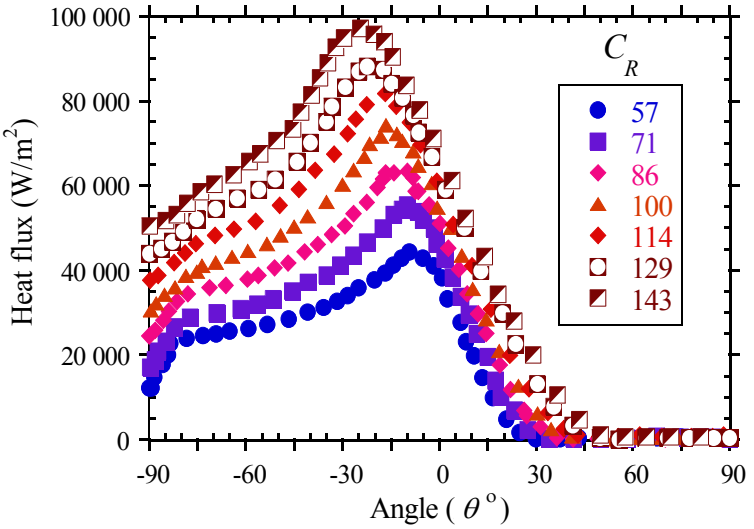

(b)

Fig. 4.12: Absorber tube heat flux as a function of circumferential angle (θ) and concentration ratio (C_R) for an inlet temperature of 400 K, Re = 1.02 ×10^4 and a given rim angle (φ_r): (a) φ_r = 40^o and (b) φ_r = 100^o.

4.7.4 ABSORBER TUBE'S CIRCUMFERENTIAL TEMPERATURE DIFFERENCE

At each concentration ratio, the peak heat flux increases as the rim angle decreases. This increase in peak heat flux increases the peak temperature and therefore the finite temperature difference. Figures 4.13(a) and 4.13(b) show the temperature contours of the receiver's

absorber tube at rim angles of 40° and 120° respectively at a Reynolds number of 1.02×10^4, T_{inlet} = 400 K and a concentration ratio of 86.

As expected, the temperature difference in the absorber tube at a rim angle of 40° is higher than that at 120°. The absorber tube's temperature difference at these rim angles for the conditions considered is about 192 °C and 87 °C respectively. As shown, the uneven heating of the receiver's absorber tube results in a temperature difference across the absorber tube's circumference.

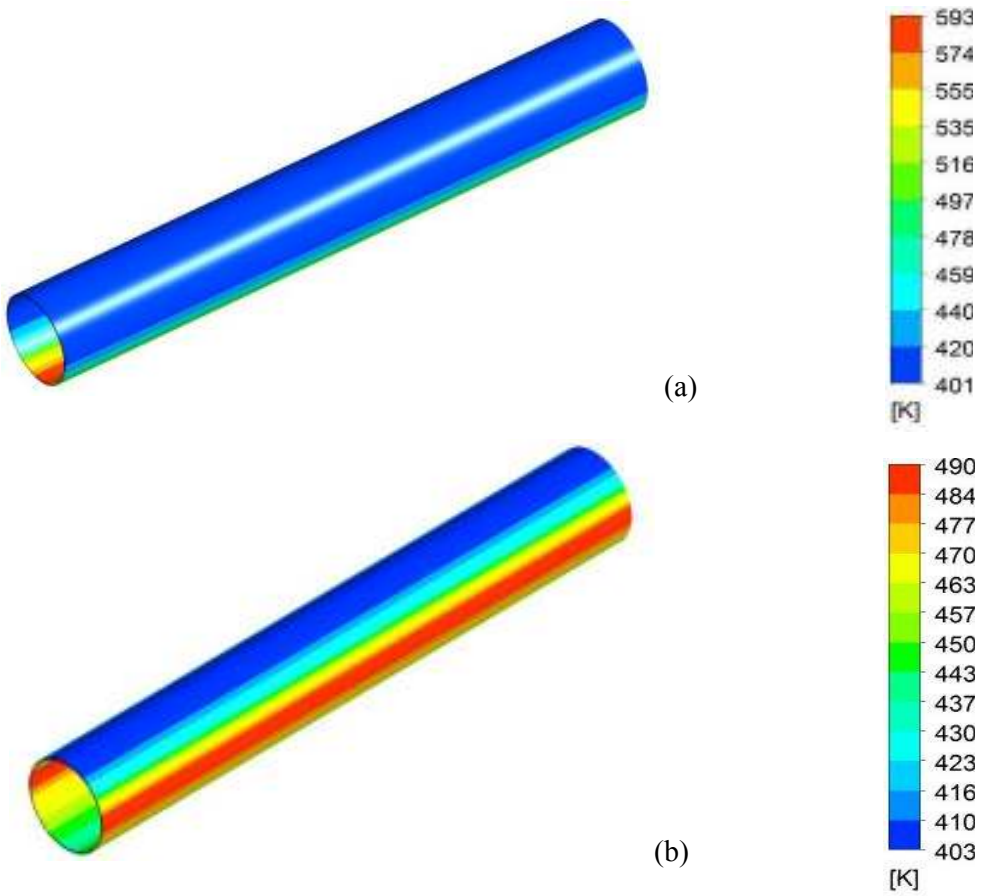

Fig. 4.13: Contours of absorber tube temperature at $Re = 1.02 \times 10^4$, an inlet temperature of 400 K, concentration ratio (C_R) of 86 and a given rim angle (φ_r): (a) φ_r = 40° and (b) φ_r = 120°.

Figure 4.14 (*a* – *f*) shows the contours of temperature for some selected cases on the absorber tube's outlet as well as the receiver's annulus space section. In Fig. 4.14 (*a* – *f*), the inlet

temperature is kept at 350 K, the concentration ratio is fixed at 86 and the direct normal solar irradiance is fixed at 1 000 W/m^2. The figures clearly show the presence of a temperature difference in the absorber tube's circumference. As expected, the absorber tube's circumferential temperature difference decreases with an increasing rim angle, as discussed above. High flow rates give rise to high flow Reynolds numbers and better heat transfer coefficients.

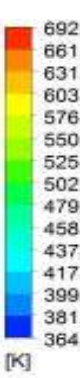

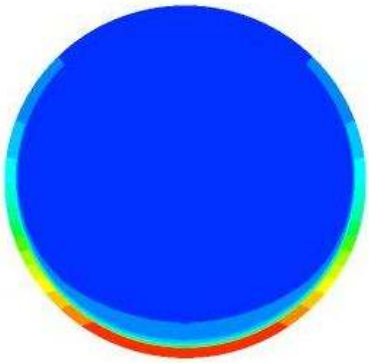

(a) Absorber tube outlet temperature at Re = 6 913 and φ_r = 60°

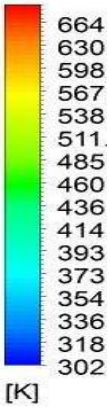

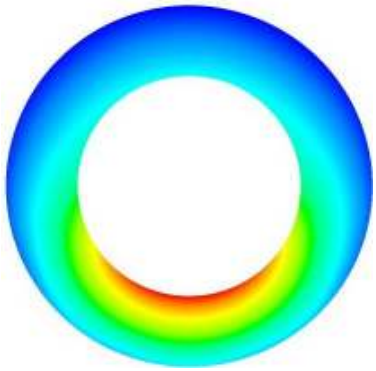

(b) Reveiver annulus temperature at Re = 6 913 and φ_r = 60°

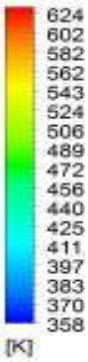

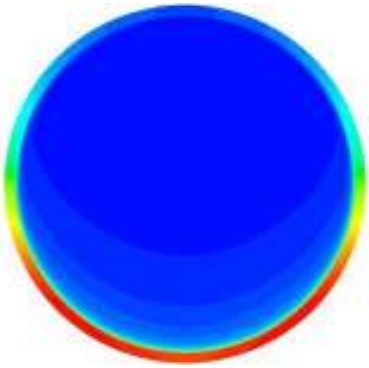

(c) Absorber tube outlet temperature at Re = 6 913 and φ_r = 80°

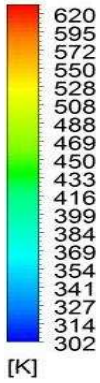

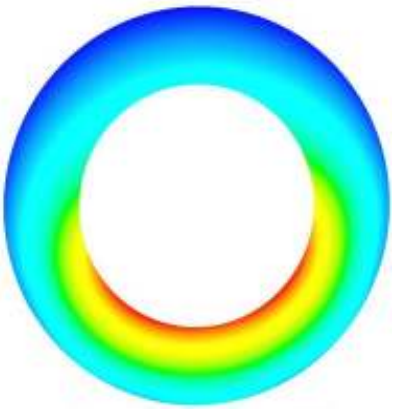

(d) Receiver annulus temperature at Re = 6 913 and φ_r = 80°

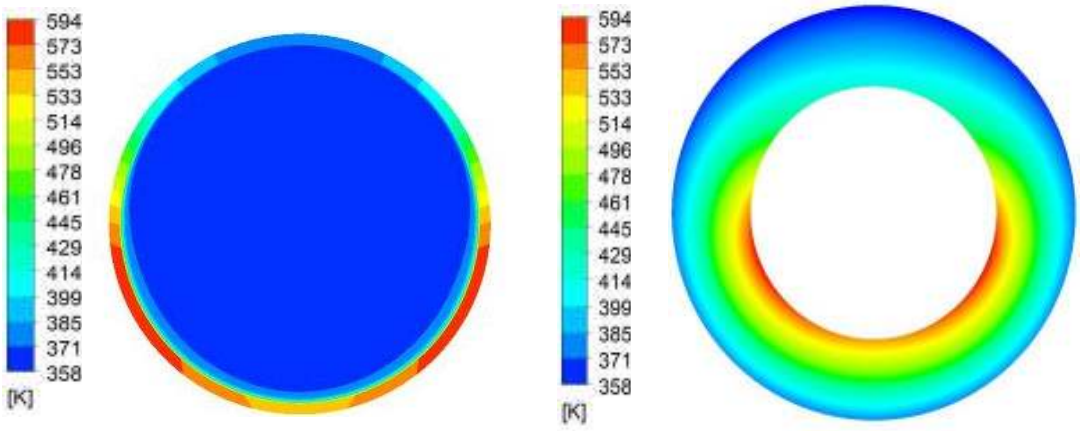

(e) Absorber tube outlet temperature at Re = 6 913 and φ_r = 100º

(f) Receiver annulus temperature at Re = 6 913 and φ_r = 100º

Fig. 4.14: Temperature contours at the absorber tube's outlet and receiver's annulus space at different Reynolds numbers and rim angles (φ_r) for direct normal irradiance (I_b) of 1 000 W/m^2, concentration ratio (C_R) of 86 and inlet temperature of 350 K.

For this reason, when the solar radiation is high and heat flux on the absorber tube increases, the flow rates of the heat transfer fluid also increase. At a given flow rate, increasing fluid temperatures also reduce the differences in the absorber tube circumferential temperature. Figure 4.15 shows the variation of temperature difference with Reynolds number and inlet temperatures.

It can be seen from Fig. 4.15 (a) that the absorber tube's circumferential temperature differences are strong functions of the Reynolds number of flow. An increase in the heat transfer fluid temperature slightly reduces the absorber tube's circumferential temperature difference at a given flow rate, as seen in Fig. 4.15(b). This is because, as the temperatures increase, the heat transfer properties of the heat transfer fluid improve. In Fig. 4.15 (a and b), $\phi = T_{abs,max} - T_{abs,min}$.

The reduction in absorber tube's circumferential temperatures as flow rates increase is the motivation for operating in the turbulent flow regime for high heat fluxes on the absorber tube.

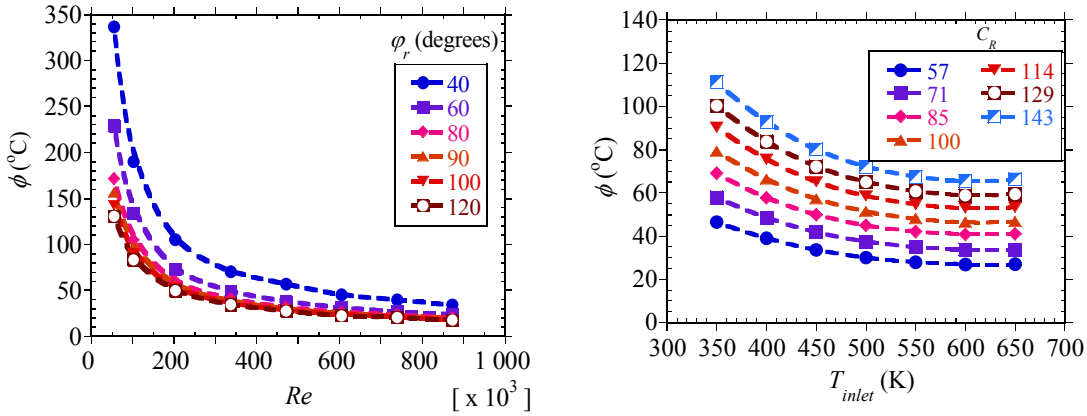

(a) (b)

Fig. 4.15: Variation of absorber tube circumferential temperature difference (ϕ): (a) as a function of Reynolds number and rim angle (φ_r) for an inlet temperature of 650 K and a concentration ratio (C_R) of 86 (b) as a function of inlet temperature and concentration ratio (C_R) for a rim angle (φ_r) of 80° and flow rate of 31 m^3/h.

Figure 4.16 shows the variation of the absorber tube's circumferential temperature difference with the Reynolds number at different concentration ratios. The figure indicates that, as the concentration ratio increases, the absorber tube's circumferential temperature difference increases. The increase in temperature difference is very high at low Reynolds numbers. At the lowest Reynolds number in this figure, the absorber tube circumferential temperature difference increases from 145 °C to about 378 °C as the concentration ratio increases from 57 to 143. At the highest Reynolds number, the absorber tube's circumferential temperature difference increases from about 13 °C to 30 °C as the concentration ratio increases from 57 to 143. Therefore, at high concentration ratios, operation at high flow rates is necessary to achieve low temperature differences in the absorber tube's circumferential temperature. The maximum temperature difference for the safe operation of the receiver is about 50 K. Therefore, the flow rate to achieve temperature differences lower than 50 K will depend on the rim angle and the concentration ratio. Flow rates higher than 43 m^3/h (about 8.61 kg/s at 400K, 7.66 kg/s at 500 K, 6.56 kg/s at 550 K and 5.92 kg/s at 650 K) will give absorber tube circumferential temperature differences lower than 50 K.

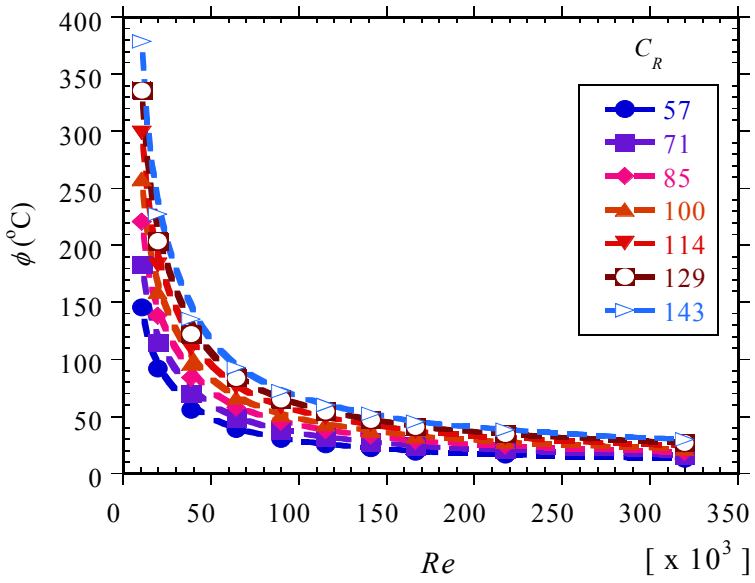

Fig. 4.16: Absorber tube circumferential temperature difference (ϕ) as a function of Reynolds number and concentration ratio (C_R) for an inlet temperature of 400 K and a rim angle (φ_r) of 80°.

Even though using higher flow rates reduces the absorber tube's circumferential temperature differences, the available energy or the exergetic performance of the receiver and the parabolic trough receiver system depends on the mass flow rate and the outlet temperature. An increase in mass flow rate will reduce the exergetic performance of the collector and reduce the absorber tube's outlet temperatures. By contrast, low mass flow rates will give excessively high absorber tube's circumferential temperature differences. Low mass flow rates will also result in high outlet temperatures, high finite temperature differences, and therefore in less exergetic performance.

For this reason, the mass flow rate for the optimal performance of the receiver should be determined, at which the system's exergetic performance is not significantly affected and at which the absorber tube's circumferential temperature difference is low. The other way of minimising the irreversibilities or improving the exergetic performance of the receiver is to use moderate flow rates and consider heat transfer enhancement in the receiver's absorber tube. This method improves heat transfer performance while minimising the irreversibilities due to heat transfer across a finite temperature difference. It will also minimise the absorber tube's circumferential temperature difference at low flow rates. The thermodynamic

performance of the receiver is discussed further in Chapter 5. The potential improvements in receiver performance due to heat transfer enhancement are discussed in Chapters 6 and 7.

4.8 THERMAL PERFORMANCE

The thermal performance of the receiver is characterised by the receiver's thermal loss or the thermal efficiency of the collector. The equations needed for the thermal analysis of the receiver are presented in Section 2.3.3 of Chapter 2.

Figure 4.17 (a) shows the variation of the receiver's thermal loss with inlet temperature at a flow rate of 4.9 m^3/h (1.14 kg/s at 400 K, 1.01 kg/s at 500 K, 0.86 kg/s at 600 K and 0.78 kg/s at 650 K). Generally, the thermal loss increases as the inlet temperature increases. At high inlet temperatures, the absorber tube's temperatures are high and so the radiation heat loss is high. The radiation heat loss increases further because the emissivity of the absorber tube's selective coating increases as the absorber tube temperature rises. Figure 4.17 (a) also shows that the thermal loss increases slightly as the rim angle reduces. As discussed above, low rim angles lead to higher heat flux peaks and therefore to higher temperature peaks, which lead to the increase in receiver heat loss.

The variation of receiver thermal loss with rim angle becomes negligible at higher flow rates because of better heat transfer and a significant reduction in temperature gradients. The thermal efficiency compares the useful heat gain to the incident solar radiation. In Fig. 4.17 (b), the thermal efficiency is shown to be slightly higher at rim angles above 80^o than at lower rim angles of 40^o and 60^o. At the flow rate in Fig. 4.17 (4.9 m^3/h), the difference in efficiency for rim angles 40^o and 80^o is in the range 5.8% - 7.2% depending on the rim angle and inlet temperature.

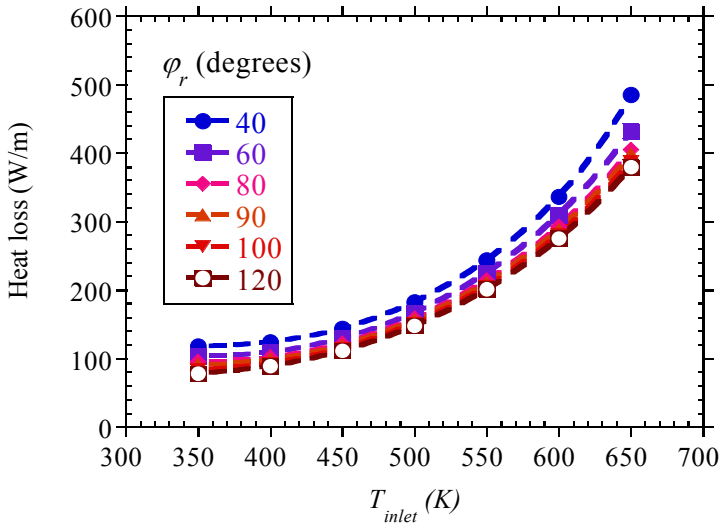

(a)

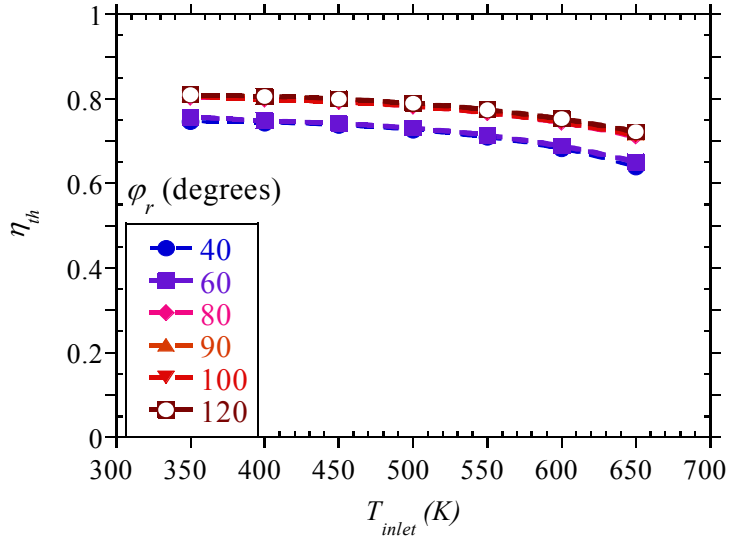

(b)

Fig. 4.17: Change in receiver thermal performance: (a) receiver heat loss as a function of inlet temperature and rim angle (φ_r) for a flow rate of 4.9 m^3/h and (b) receiver thermal efficiency as a function of inlet temperature and rim angle (φ_r) for a flow rate of 4.9 m^3/h.

As the flow rates increase, the temperature peaks decrease and the heat loss do not vary significantly with rim angle. The difference in efficiency as the rim angles increase will also slightly reduce. At 31 m^3/h (about 7.18 kg/s at 400 K, 6.79 kg/s at 500 K, 5.46 kg/s at 600 K and 4.93 kg/s at 650 K), the difference in efficiency as the rim angle increases from 40° to 80°

is about 5% for all inlet temperatures. Therefore, rim angles higher than 80^o give higher receiver thermal performance and should be used instead of lower rim angles. However, the increase in the cost of the collector as rim angles increase should be weighed up against the gain in receiver performance.

Figure 4.18(a) and (b) show the variation of receiver thermal loss with inlet temperature. The variation of receiver thermal loss with inlet temperature at different concentration ratios is presented at two flow rates i.e. 4.9 m^3/h and 31 m^3/h respectively. As shown in the figure, there is a general trend of increasing thermal loss with inlet temperature. At very low flow rates, the increase in thermal loss as the concentration increases is significant. For example, at a flow rate of 4.9 m^3/h, the thermal loss increases from 229 W/m at a concentration ratio of 57 to 520 W/m at a concentration ratio of 143 when the rim angle is 80^o and inlet temperature is 600 K as shown in Fig. 4.18 (a). At a flow rate of 31 m^3/h, close to the maximum flow rates in commercial plants, the thermal loss increases from about 170 W/m at a concentration ratio of 57 to 196 W/m at a concentration ratio of 143 for a rim angle of 80^o and inlet temperature of 600 K as shown in Fig. 4.18(b). At the flow rates close to those in current commercial plants, the thermal loss increases only slightly as the concentration ratio increases. The increase in the thermal loss as the concentration ratio increases can be attributed to higher absorber tube temperatures from high heat fluxes as the concentration ratios increase. At high flow rates, the heat transfer rates are higher and increasing the concentration ratio does not significantly affect the receiver's thermal performance.

The thermal efficiency of the collector, defined as the ratio of useful heat gain and incident solar radiation, was plotted and is shown in Fig. 4.19. Figure 4.19 (a) shows that the thermal efficiency depends more strongly on inlet temperature than on the concentration ratio. As shown in Figs 4.19 (a) and 4.19 (b), the thermal efficiency increases with flow rate up to some flow rate/ Reynolds number and stays constant.

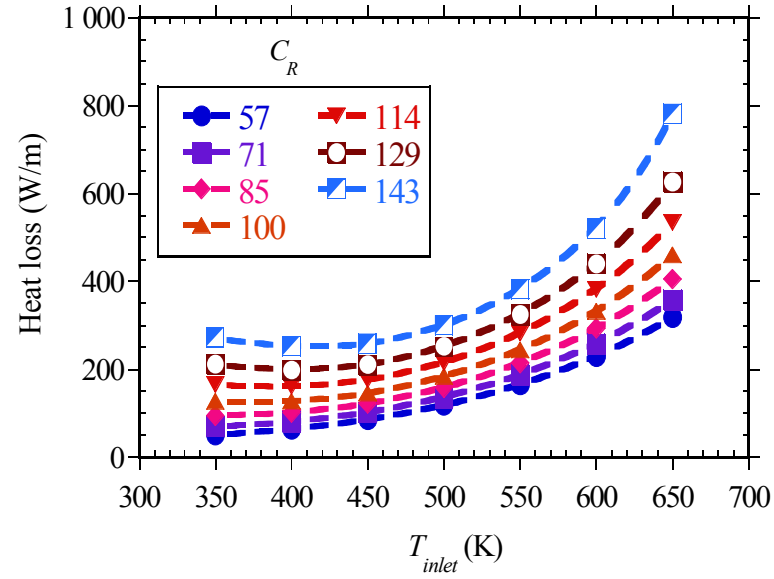

(a)

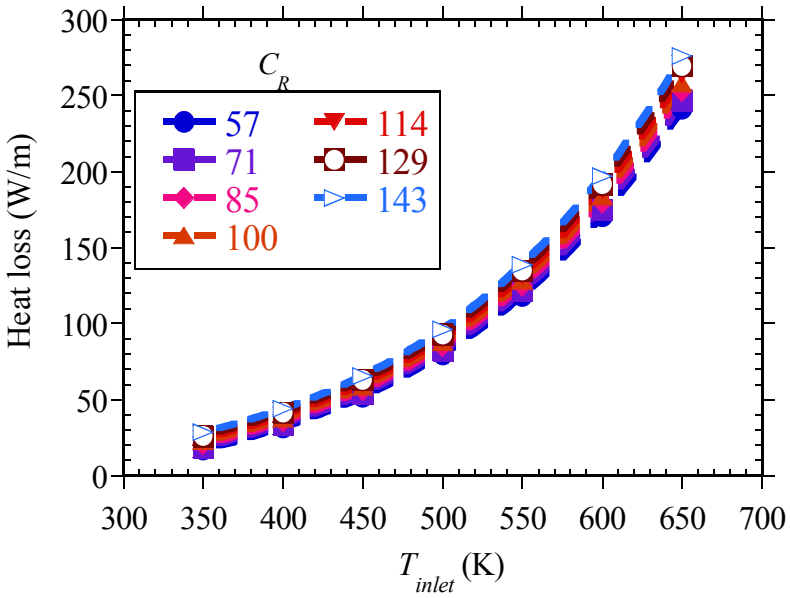

(b)

Fig. 4.18: Receiver heat loss as a function of inlet temperature and concentration ratio (C_R) for a rim angle (φ_r) of 80°: (a) flow rate of 4.9 m^3/h and (b) flow rate of 31 m^3/h.

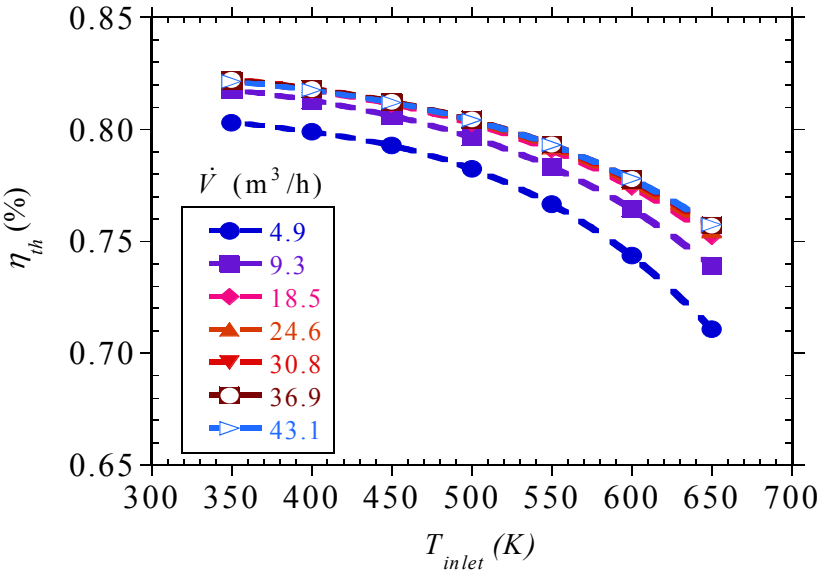

(a)

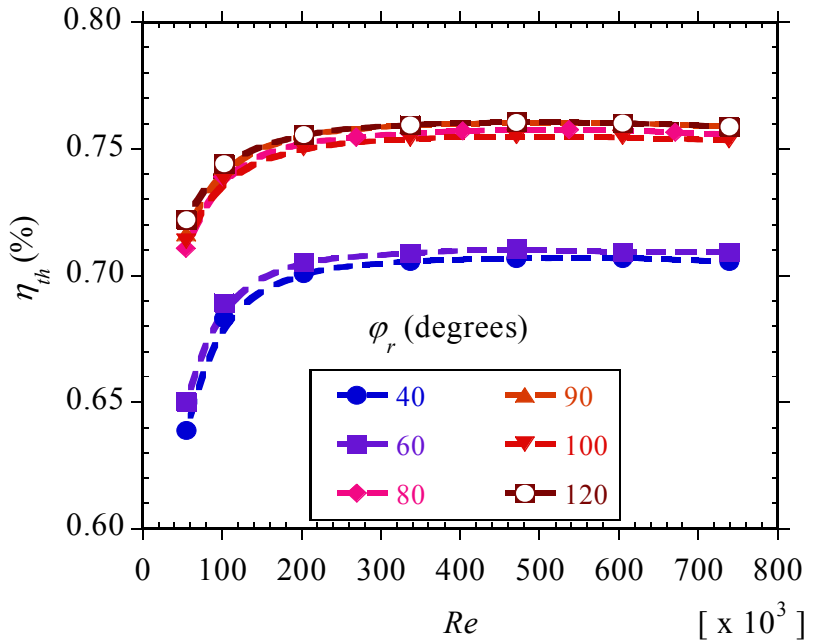

(b)

Fig. 4.19: Variation of receiver thermal efficiency: (a) receiver thermal efficiency as a function of inlet temperature and flow rate for a rim angle (φ_r) of 80^o and (b) receiver thermal efficiency as a function of Reynolds number and rim angle (φ_r) for a concentration ratio (C_R) of 86.

As discussed above, low rim angles will result in higher temperature peaks, thus increasing radiation heat loss from the receiver's absorber tube to the glass cover and subsequently to the surroundings. The high temperature peaks will also lead to high emissivity of the absorber tube coating, which will further increase the radiation loss. At rim angles above 80^{o}, there is no significant change in the collector's thermal efficiency as rim angles increase.

4.9 CONCLUDING REMARKS

This chapter presents the development and validation of the parabolic trough receiver thermal model. The determination of the heat flux profile using Monte Carlo ray-tracing is demonstrated and the results are validated using data from the available literature. The two different models developed for the receiver are shown to give nearly the same results. The percentage deviation for the two models is within ± 7% for temperature gain, within ± 7% for collector thermal efficiency and within ± 6.5% for receiver heat loss when compared with experimental data from SANDIA national laboratories [40].

The dependence of heat flux on the collector's rim angle and concentration ratio is presented and discussed. Low rim angles are shown to give high peak heat fluxes and thus high absorber tube circumferential temperature differences. A thermal analysis at different rim angles shows that the receiver's thermal loss is high at low rim angles. Lower rim angles (lower than 60^{o}) are shown to reduce thermal efficiency by efficiencies of up to 7.2% in the range of the parameters considered. This is due to the higher temperature peaks that are obtained at these rim angles, which result in greater absorber tube emissivity and thus higher radiation heat loss. At higher flow rates, increasing the concentration ratio does not significantly affect the collector's thermal performance.

In general, for rim angles 80^{o} and above, there is no significant increase in receiver thermal loss and absorber tube circumferential temperature gradients. Hence, rim angles higher than 80^{o} are recommended for all ranges of flow rates. At low rim angles or high concentration ratios, careful matching of flow rates with incident solar radiation is essential to keep absorber tube circumferential temperature gradients at desirable levels. At flow rates close to or greater than 31 m^{3}/h, the influence of rim angles and concentration ratios was shown to be insignificant.

CHAPTER FIVE

CHAPTER FIVE: NUMERICAL INVESTIGATION OF ENTROPY GENERATION IN A PARABOLIC TROUGH RECEIVER AT DIFFERENT CONCENTRATION RATIOS AND RIM ANGLES

5.1 INTRODUCTION

Parabolic trough systems represent one of the most technically and commercially developed concentrated solar power technologies. The evacuated receiver tube of the parabolic trough collector system is a component that is central to system performance. It is one of the reasons for the high efficiencies obtained in this type of concentrated solar power technology [21].

Several options for reducing the cost of parabolic trough collector systems have been proposed and the cost of the electricity from these systems is decreasing and becoming competitive with the cost of electricity from medium-sized coal-fired power plants [17-19,21,23]. One of the options for further reducing the cost of parabolic trough systems is to increase the collector size as well as the use of higher concentration ratios, thereby reducing the number of connections, drives and controls needed [18,23,24,27].

With the increase in concentration ratios, the receiver's absorber tubes will be subject to high heat fluxes and high temperatures. These high heat fluxes and temperatures will lead to high heat transfer irreversibilities due to the presence of a high finite temperature difference in the receiver's absorber tube. The increased heat transfer irreversibilities will lead to increased entropy generation rates. These irreversibilities can be minimised by increasing the flow rate of the heat transfer fluid, but increasing flow rates will also result in an increase in the fluid friction irreversibility. For this reason, an optimum flow rate has to be established, at which the entropy generation from the two competing irreversibilities is at a minimum.

The second law of thermodynamics provides a basis for characterising the systems and system components in terms of the irreversibility occurring in them. For energy systems, the determination of the available energy and quality of this energy is of fundamental importance to characterising their performance. The determination of the system's available energy is possible through the simultaneous application of the first and second laws of thermodynamics through the method called exergy analysis [61]. In the exergy analysis method, the theoretical operating conditions of the system in the reversible limit are obtained. The entropy generated is then related to the exergy destroyed, by using the Gouy-Stodola theorem [61]. By contrast, another method for modelling and optimising thermal systems, called the entropy generation method (EGM), bridges the gap between thermodynamics, heat transfer and fluid mechanics to determine the entropy generated or the exergy destroyed in thermal systems and system components [61,111].

In the EGM method, the entropy generated (S_{gen}), is a function of physical parameters of the model, and the main aim of the method is the minimisation of the calculated entropy generation rate [111]. To minimise the entropy generation rate, the degree of thermodynamic non-ideality must be related to the physical characteristics of the system, such as the finite dimensions, shapes, materials, finite speeds and finite time intervals of operation [61].

The entropy generation minimisation method has developed since its introduction by Bejan [62] and has become widely applied to the design and optimisation of thermal systems [61]. The entropy generation minimisation method combines the fundamental principles of fluid mechanics, heat transfer and thermodynamics when establishing the entropy generation rates in thermal systems and system components.

Several researchers have used the entropy generation minimisation method in the design and optimisation of thermal systems and system components, while others have applied the EGM method to the analysis of entropy generation in fluid flow and heat transfer for various system configurations and boundary conditions [16,93,94,112-126]. These studies show the importance of the entropy generation method for thermodynamic optimisation in a wide range of applications ranging from forced convection, natural convection, heat transfer enhancement, power plant optimisation, heat exchanger design and optimisation, etc.

For the purposes of the present study, a review is presented of studies related to entropy generation due to heat transfer and fluid flow. Like most engineering processes, heat transfer and fluid flow processes are also irreversible, and according to the second law of thermodynamics, they generate entropy, which results in the destruction of available work. Therefore, study of entropy generation due to heat transfer and fluid flow processes is essential in the search for optimal configurations that minimise the generated entropy.

Kock and Herwig [93,94] used the Reynolds averaging process to derive model equations for calculating the local entropy production rates in turbulent shear flows from the entropy balance equations. The equations account for the entropy generation due to dissipation in mean and fluctuating velocity fields, and for entropy generation due to heat flux for mean and fluctuating temperature fields.

Ko and Ting [115] numerically analysed entropy generation due to forced convection in a curved rectangular duct with external heating. They investigated the effect of the Dean number, external wall heat flux and cross-sectional aspect ratios on entropy generation due to frictional irreversibility and heat transfer irreversibility. The study also showed the existence of an optimal Dean number, which increased with wall heat flux. Ko and Wu [117] numerically studied entropy generation induced by turbulent forced convection in a curved rectangular duct with external heating for various aspect ratios. They used the method proposed by Kock and Herwig [93,94] to determine the entropy generation rates. For the considered parameters, the resultant entropy generation rates in the flow fields were found to be dominated by fluid friction irreversibilities. The optimum aspect ratio at which entropy generation was minimum, was found to be 1.

Herpe *et al*. [118] used the finite volume method to numerically investigate the entropy generation in a finned oval tube with vortex generators. In their study, they showed that the entropy generation method is a useful tool for studying local conjugate heat transfer and defining the global heat exchange criterion. Satapathy [123] used the second law of thermodynamics to determine the irreversibilities in a coiled tube heat exchanger for both laminar and turbulent flow conditions. They showed the presence of an optimum diameter

ratio at which the entropy generation is minimum for a given value of Prandtl number, Dean number and heat exchanger duty parameter.

Şahin [127] used the second law of thermodynamics to compare analytically the irreversibilities in ducts with various geometries. In terms of minimum entropy generation, the circular duct gave the best performance, whereas triangular and rectangular duct geometries showed inferior performance. In another study, Şahin [128] presented the results of the thermodynamic analysis of turbulent fluid flow through a smooth duct subject to constant heat flux, using the entropy generation minimisation method. Abu-Nada [129] numerically studied entropy generation over a backward-facing step for various values of expansion ratios (ER) and Reynolds numbers in the laminar flow regime. An increase in Reynolds number was found to increase the total entropy generation.

Khan *et al.* [130] used the entropy generation minimisation method to optimise the overall performance of micro channel heat sinks. They formulated the entropy generation in terms of the pressure drop and thermal resistance and studied the effect of several values of flow rates, Knudsen numbers, channel aspect ratios, fin spacing and the thermal conductivity of the heat sink material on the entropy generation rate. Herwig and Kock [131] compared the direct and indirect methods of calculating entropy generation rates in turbulent convection heat transfer problems. They used the equations derived in their earlier work (Kock and Herwig [94]), called the direct method, and compared their results with those of the indirect method, based on the analytical expression for the volume integrated time-average entropy balance equation. The direct method was superior for determining entropy generation in cases where the flow field is complex and when complex boundary conditions are involved.

In other studies, Sahiti *et al.* [132] used the entropy generation minimisation method to study heat transfer enhancement in a double pipe-pin fin heat exchanger. Esfahani and Shahabi [133] studied the entropy generation for developing laminar flow. Ozalp [134] numerically investigated the entropy generation for fully developed, forced convection laminar flow in a micro-pipe. Giangaspero and Sciubba [135] recently applied the entropy generation to a forced convection-cooling problem of an LED-based spotlight. They showed that the best performance, i.e. minimum entropy generation occurs when the fins are periodically spaced

in the radial direction. Amani and Nobari [136] present a numerical and analytical study of entropy generation in the entrance region of curved pipes at a constant heat flux. Amani and Nobari [137] numerically and analytically investigated entropy generation in the entrance region of curved pipes with a constant wall-temperature boundary condition. In the numerical method, they present the local entropy generation rates due to friction and heat transfer and compare their results with approximate analytical solutions. Both methods predict the presence of an optimal Reynolds number at which entropy generation is minimum.

Many other studies on entropy generation for heat transfer and fluid flow problems can be found in literature. Interested readers are directed to these additional studies: Wu *et al.* [138], Ko [139], Mansour *et al.* [140], Ilis *et al.* [141], Dagtekin *et al.* [142], Jankowski [143], Sciubba [144], Balaji *et al.* [145], Hooman *et al.* [146], Mahmud and Fraser [147], Mahmud and Fraser [148] and recently Zhang *et al.* [149].

It is clear from the above literature that the entropy generation minimisation method is an effective tool for the design and optimisation of thermal systems and system components as well as heat transfer devices. It is also clear that the entropy generation rates depend on the geometry of the problem under consideration, the boundary conditions and the nature of the flow field.

For parabolic trough collectors, the presence of high heat fluxes and high temperatures at high concentration ratios will lead to high entropy generation rates due to heat transfer irreversibility. With the feasibility of high optical efficiencies in parabolic trough systems, larger parabolic trough collector sizes and therefore larger concentration ratios are now possible, as discussed above. For this reason, a study on the effect of high concentration ratios on entropy generation in parabolic trough systems is necessary to establish the optimal flow rates at which entropy generation is a minimum. Moreover, as the geometry of the collector changes, the thermodynamic performance of the receiver is expected to change. Therefore, it becomes crucial to investigate the effect of different collector rim angles on entropy generation rates in the receiver.

Studies on entropy generation behaviour in parabolic trough systems are not widespread in the literature. Bejan [61] and Kalogirou [10,16] present a method for determining entropy generation in a solar collector system and the subsequent determination of the optimal collector temperature and flow rate. The method they present relates the entropy generation to the mass flow rate, the collector's inlet and outlet temperatures, heat loss and solar radiation. Though Kalogirou [16] adapted the method presented by Bejan [61] to imaging collectors, entropy generation due to heat transfer and fluid friction in the receiver of the parabolic collector trough system is not explicitly accounted for. Nor is the non-uniformity of the heat flux on the receiver's absorber tube considered. With low rim angles, the peak heat flux will be high, as already shown in Chapter 4, and the heat transfer irreversibility will also be high. This is why the actual heat flux profiles have to be used for an accurate representation of entropy generation in the receiver.

According to Bejan [61] and Kalogirou [10,16], the entropy generation in the parabolic trough collector system is a strong function of the flow conditions in the receiver's absorber tube. Accordingly, minimising the entropy generation in the receiver's absorber tube will reduce the total entropy generated by the collector. In the present study, the entropy generation minimisation method was applied to the receiver tube of the parabolic trough system to account for heat transfer and fluid flow irreversibilities. Minimising the entropy generation due to heat transfer and fluid friction is expected to reduce the total entropy generation of the collector system. This is in line with the suggestion made by Bejan [150]. He suggests that irreversibility minimisation at system component level would result in the minimisation of the total entropy generation rate of the entire system, even if the entropy generation in other components of the system is not changed. Emanating from the reviewed studies, the determination of entropy generation due to heat transfer and fluid flow in parabolic trough receivers can help to establish the optimum flow rates for minimum entropy generation and therefore maximum power delivery by the collector system. Moreover, this chapter provides a basis for the entropy generation analysis of heat transfer enhancement techniques in the receiver's absorber tube. Knowledge of entropy generation rates in the non-enhanced receiver help to determine which configurations of heat transfer enhancement techniques make thermodynamic sense.

5.2 MODEL DESCRIPTION

5.2.1 PHYSICAL MODEL

The heat collection element of the parabolic trough system is fundamental to the performance of the entire system. To ensure high efficiencies, the heat collection element consists of a steel absorber tube enclosed in a glass jacket, which is evacuated to pressures below the Knudsen gas conduction level (0.013 Pa) [21] to suppress convection heat loss. Moreover, the receivers are made with absorber tubes, which are selectively coated to ensure higher absorptivity of incoming solar radiation and low emissivity of infrared radiation. Because current heat transfer fluids decompose when temperatures exceed about 400 ^{o}C [29,55], getter material is provided to absorb the hydrogen formed inside the receiver's annulus since its accumulation drastically increases the receiver's thermal loss [45].

The model of the parabolic trough receiver analysed in the present study is shown in Fig. 5.1. The space between the absorber and the glass cover is considered evacuated so that only radiation heat loss takes place. The concentration ratio is defined as $C_R = A_a/A_r$ where A_a is the area of the collector's aperture and A_r is the projected area of the absorber tube. Because of symmetry, only half of the receiver was considered, as shown by Section AA.

The upper half receives direct solar radiation, whereas the lower half receives concentrated solar radiation. The emissivity of the absorber tube varies with temperature according to Eq. (2.33).

The assumptions used in the study are as follows:

- Flow is steady-state
- Flow is turbulent for effective heat transfer and for the reduction of absorber tube temperature gradients

The geometrical parameters and simulation parameters used in this study are shown in Table 5.1. Other parameters are similar to those used in Chapter 4, as shown in Table 4.1.

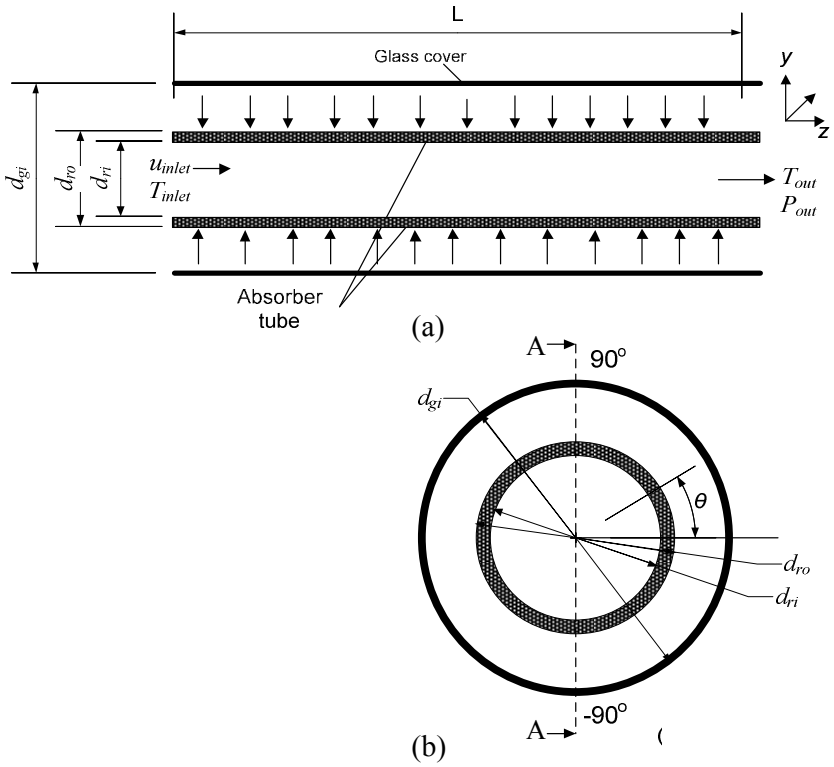

Fig. 5.1: 2-D schematic representation of the parabolic trough receiver computational domain: (a) longitudinal view and (b) cross-section view.

5.2.2 GOVERNING EQUATIONS

High heat transfer fluid mass flow rates are essential for the high heat fluxes and high temperatures achievable at high concentration ratios and the flow in the absorber tube is in the turbulent regime. In addition, the flow inside the absorber tube is considered to be steady state. The Reynolds Averaged Navier-Stokes equations (RANS) (Eqs. 3.2 - 3.4) detailed in Section 3.3.1 are applicable to this kind of problem. The realisable *k-ε* was used for turbulence closure. This model is an improvement of the standard k-ε and has superior performance for separated flows and flows with complex secondary features. The model solves two additional equations for the turbulent kinetic energy (Eq. 3.7) and turbulent dissipation rate (Eq. 3.8) as detailed in Section 3.31 of this work. The entropy generation rates are determined from the equations (Eqs. 3.35-3.41) given in Section 3.4.1 of Chapter 3.

Table 5.1: Geometrical parameters of the receiver used in this study

Parameter	Value
d_{gi} (cm)	11.5
d_{ri} (cm)	6.6
d_{ro} (cm)	7
L (m)	5
W_a (m)	4 -10
I_b (W/m^2)	1 000
φ_r (Degrees)	40, 60, 80, 90, 100, 120
C_R	57, 71, 86, 100, 114, 129, 143

5.2.3 BOUNDARY CONDITIONS

The boundary conditions adopted for this study are discussed in Chapter 4, Section 4.4. Due to symmetry, only half of the receiver was considered and the end effects as well as the effect of the receiver's supports were deemed negligible. This chapter uses the full receiver model described as model A.

5.2.4 SOLUTION PROCEDURE

The numerical solution was implemented in a commercial software package ANSYS® 13 and 14.5. The geometry was built in ANSYS design modeller and the computational grid created in ANSYS meshing. The numerical solution was obtained in ANSYS FLUENT, which uses a finite volume method for solving the governing continuity, momentum, energy and k-ε model equations. The SIMPLE algorithm proposed by Patankar and Spalding [92] was used for coupling the pressure and velocity. Second-order upwind schemes were employed for integrating the governing equations together with the boundary conditions over the computational domain.

Given the need to capture a high resolution of gradients near the wall, the enhanced wall functions [88,89] were used and $y^+ \approx 1$ was used in all simulations. Where $y^+ = y\mu_\tau/\nu$, ν is the fluid's kinematic viscosity, y is the distance from the wall and u_τ is the friction velocity given by $\mu_\tau = \sqrt{(\tau_w/\rho)}$. To predict the near-wall cell size, the distance y was calculated as $y^+\mu/u_\tau\rho$, for internal flow, $\tau_w = c_f \rho U_\infty^2/2$; where $c_f = 0.079 Re_d^{-0.25}$.

Convergence was obtained with scaled residuals of mass, momentum, turbulent kinetic energy and a turbulence dissipation rate of less than 10^{-4} whereas the energy residuals were less than 10^{-7}. Convergence was also monitored by using the convergence history of volume-averaged entropy generation in the absorber tube. The solution was considered converged when the volume-averaged entropy generation remained constant for more than 200 successive iterations.

Mesh independence studies for several refinements of the mesh were carried out with the volume integral entropy generation as a monitored quantity. Accordingly, the solution was considered mesh independent when $|(S_{gen}^{\,i} - S_{gen}^{\,i-1})/S_{gen}^{\,i-1}| \leq 0.01$. The indices i and $i-1$ represent the values before and after refinement respectively. The sample mesh used in this study is the same as that presented in Chapter 4, Fig. 4.5.

Syltherm 800 [110] was used as the absorber tube's heat transfer fluid; its properties were entered as temperature-dependent polynomials for specific heat capacity (c_p), density (ρ) and thermal conductivity (λ) and the piece-wise temperature-dependent polynomial for viscosity (μ) as derived from the manufacturer's specifications [110] given in Chapter 4 by Eqs. (4.4 – 4.8). The sample thermal properties of Syltherm 800 at T_{inlet} = 400 K, 550 K and 650 K were shown in Table 4.2. The absorber tube material is stainless steel with a temperature-dependent thermal conductivity [45] given according to Eq. (2.25).

5.3 RESULTS

5.3.1 VALIDATION OF NUMERICAL RESULTS

The validation of the receiver model is presented in Chapter 4. This section presents the validation of the entropy generation model. The indirect method of determining entropy generation as proposed by Bejan [61] was used to validate the results obtained in this study by the direct method. This same validation was used by Herwig and Kock [131] to validate the proposed expressions for the direct method of determining entropy generation. The example studied by Bejan [61] was reproduced in the present study for validation purposes. A tube with a diameter D and a fully developed turbulent flow of water is heated by a constant

heat flux of 10^5 W/m^2 over its length L, so that the temperature is raised from 300 K to 310 K. The values of D and L are varied for a constant heat transfer surface area $\pi DL = 0.42$ m^2.

Figure 5.2 shows that the direct method and indirect method give almost similar values except for cases of low Reynolds numbers. Although the direct and indirect methods give similar results for simple cases of tube configurations under different operating conditions or complex geometries, the direct method gives more accurate results for entropy generation [131].

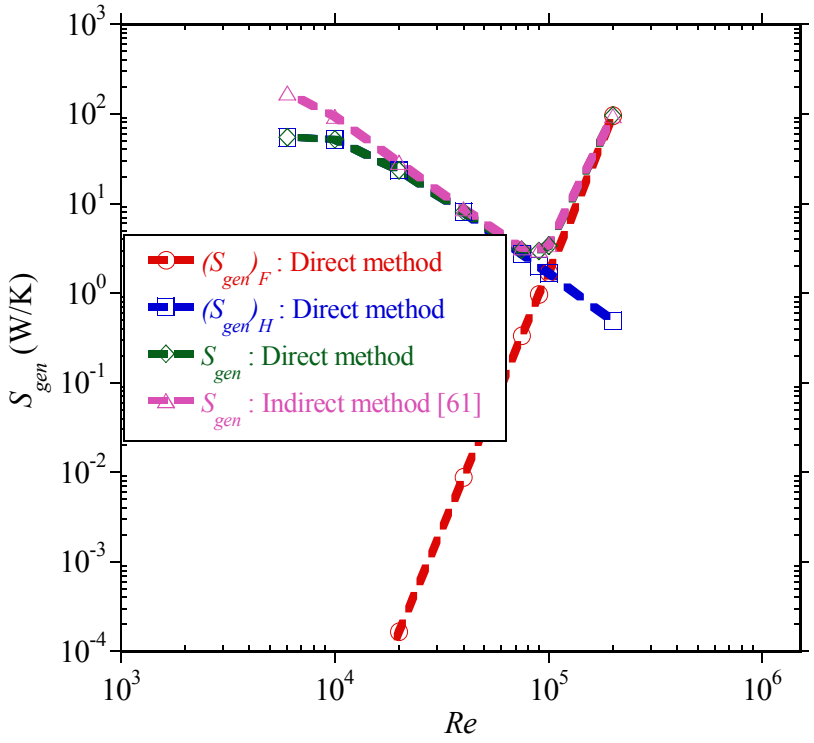

Fig. 5.2: Comparison of predicted entropy generation as a function of Reynolds number with Bejan's analytical expression [61].

Shown in Fig. 5.3 is the entropy generation in the absorber tube at a constant heat flux, with the direct and indirect method for a 4 m length. If the actual heat flux on the receiver is considered (concentrated heat flux on the lower half and direct solar radiation on the upper half), the values of entropy generation differ greatly. The optimum operating conditions also differ slightly.

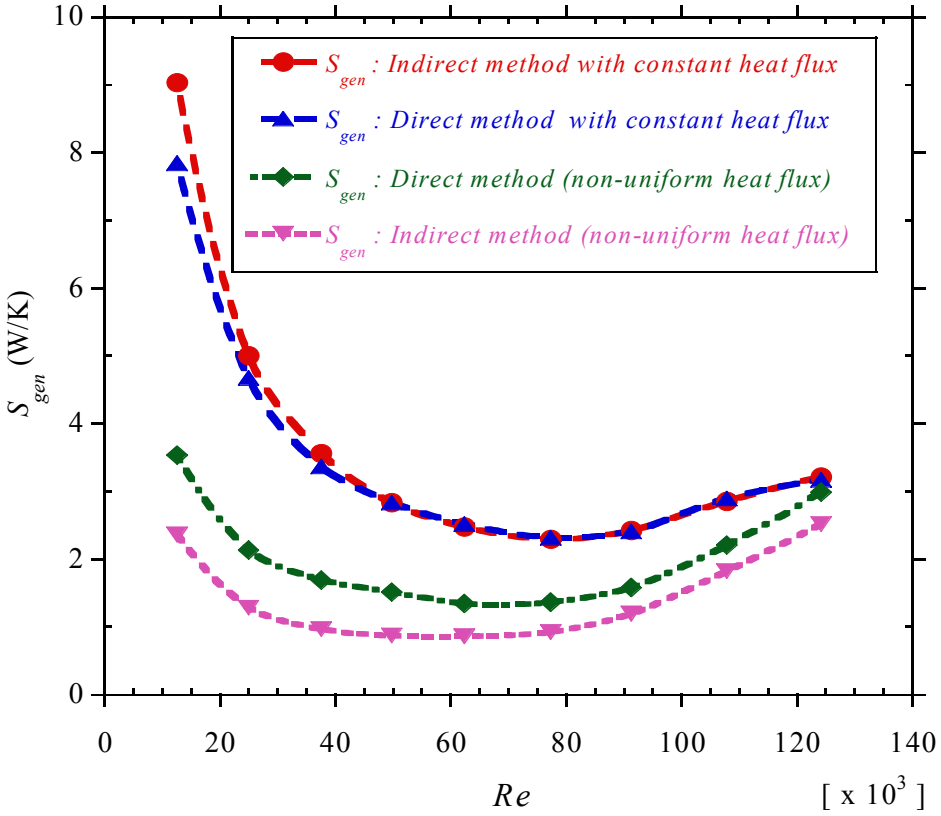

Fig. 5.3: Entropy generation in the receiver's absorber tube as a function of Reynolds number for a receiver with constant heat flux and one with non-uniform heat flux.

5.3.2 DISTRIBUTION OF ENTROPY GENERATION IN THE ABSORBER TUBE

The value of $y^+ \approx 1$ was used in all simulations to ensure the correct prediction of entropy generation close to walls. To study the distribution of entropy in the absorber tube, a concentration ratio of 86, inlet fluid temperature of 500 K and a Reynolds number of 2.69×10^5 were used. Entropy generation at different locations in the absorber tube's streamwise direction, x/L = 0.5, 0.75 and dimensionless radial positions, y/R were determined (y/R = 0 represents the centre of the tube, y/R =1 the absorber tube's upper wall and y/R = -1 the absorber tube's lower wall at any given value of x/L). As shown in Fig. 5.4, the entropy generation is higher close to the walls, given the high temperature and velocity gradients in the near-wall regions.

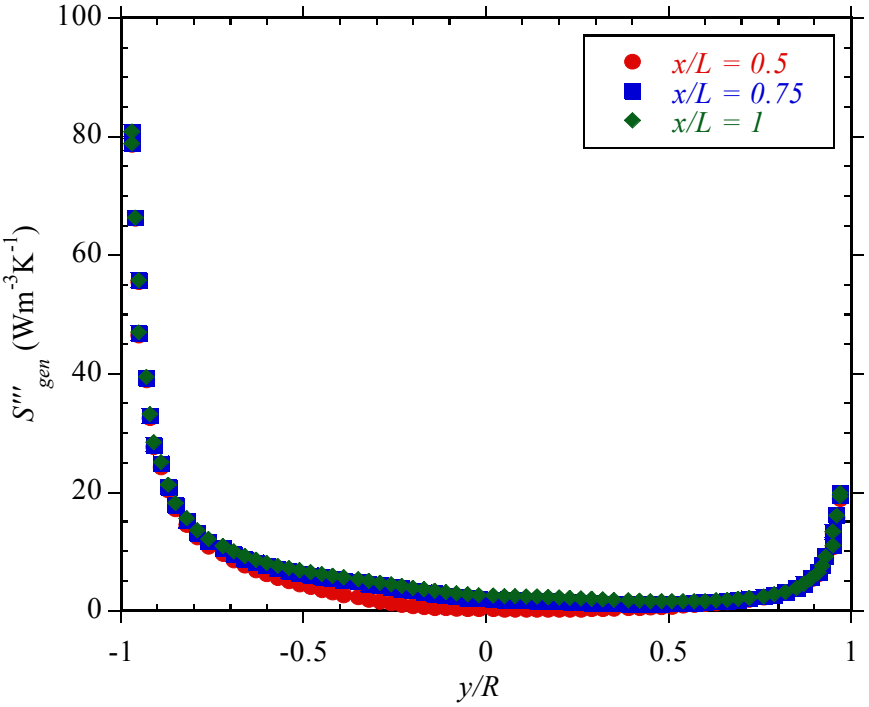

Fig. 5.4: Entropy generation in the receiver's absorber tube as a function of absorber tube's radial position (y/R) and different positions along the tube's streamwise direction (x/L).

The figure also shows that the entropy generation is higher on the lower half of the absorber tube (y/R = -1) than on the upper half (y/R = 1) since the lower half receives the concentrated heat flux. At half the length of the absorber tube (x/L = 0.5), the entropy distribution shows a minimum at y/R = 0. The entropy generation distribution at x/L = 0.75 and 1 shows a more constant profile for the entropy generation rate given that, at these distances, the flow is thermally fully developed.

Figure 5.5 shows entropy generation at different values of y/R along the length of the absorber tube, both S'''_{gen} and $(S'''_{gen})_H$ are shown. $(S'''_{gen})_H$ is the dominant source of irreversibility in the regions very close to the lower wall, as shown at y/R = -0.91. The heat transfer irreversibility is high when close to the absorber tube's lower wall because of the concentrated heat flux incident on the lower half of the absorber tube. Far from the lower-absorber tube wall, the contribution of $(S'''_{gen})_H$ to the total entropy generation rate decreases.

For example, at y/R = 0.91 (close to the upper-absorber tube wall), the contribution of $(S'''_{gen})_H$ to total entropy generation is just above zero and S'''_{gen} is 5 W m^{-3}K^{-1}.

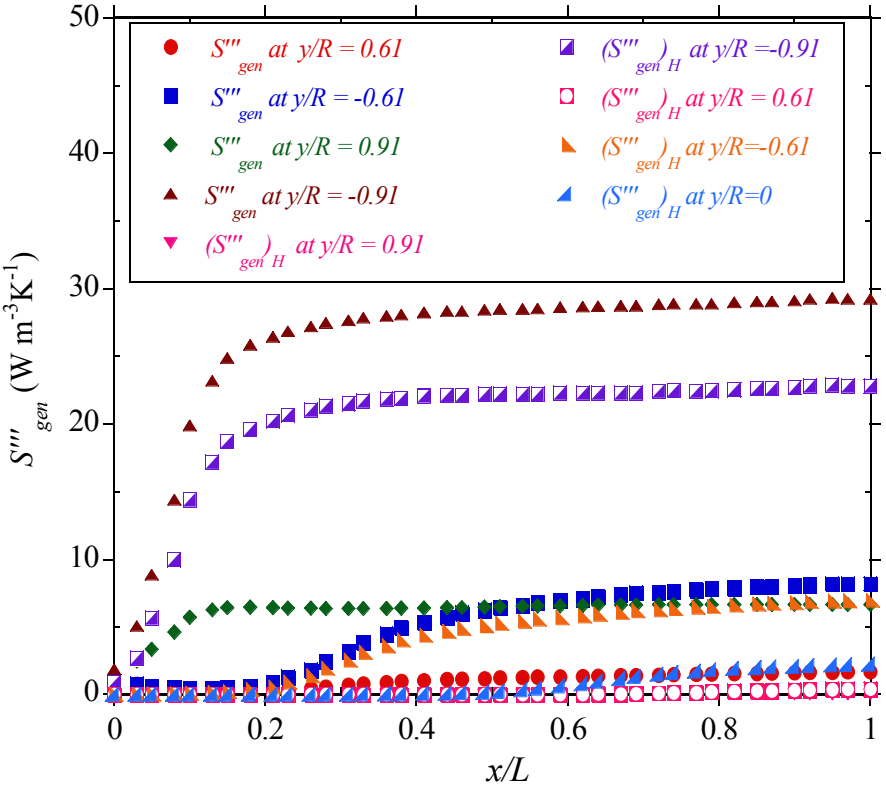

Fig. 5.5: Total entropy generation and entropy generation due to heat transfer irreversibility in the receiver's absorber tube as a function of absorber tube's streamwise position (x/L) and tube's radial position (y/R).

Compared to the lower wall of the absorber tube, the upper wall receives only direct solar radiation, hence the observed lower values of heat transfer irreversibility. Figure 5.6 shows the contribution to the total entropy generation that is due to heat transfer irreversibility in the absorber tube at various locations using the Bejan number. The Bejan number approaches 1 in the lower half of the absorber tube and is about zero close to the upper wall of the absorber tube.

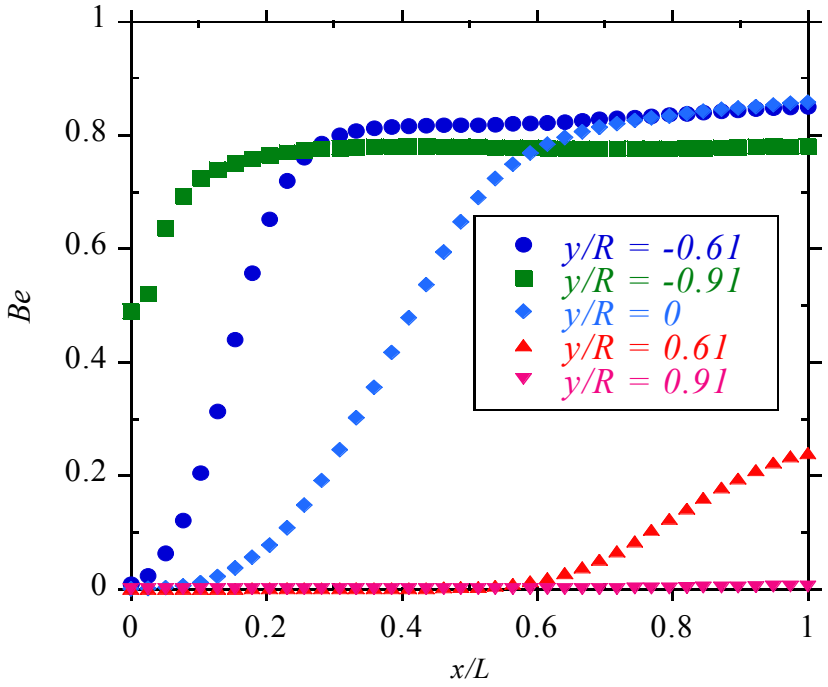

Fig. 5.6: Bejan number as a function of absorber tube streamwise position (*x/L*) and absorber tube radial position (*y/R*).

5.3.3 EFFECT OF CONCENTRATION RATIO ON ENTROPY GENERATION

To investigate the effect of the concentration ratio on total entropy generation (S_{gen}) in the receiver, concentration ratios of 57, 71, 86, 100, 114, 129 and 143 were considered. For a fluid element of volume V, the total entropy generation is given by $S_{gen} = \iiint_V S'''_{gen} dV$. S'''_{gen} is the volumentric entropy generation rate given by Eq. (3.35). Since Reynolds numbers depend on the fluid inlet temperature and flow rates, for comparison purposes, the fluid's flow rate is used (where the flow rate is $(\dot{V} = u_{inlet} \times A_c)$. Two flow rates $\dot{V}$ = 18.5 m^3/h (Fig. 5.7) and $\dot{V}$ = 104.8 m^3/h (Fig. 5.8) were used to show the variation of entropy generation due to the inlet temperature and concentration ratio.

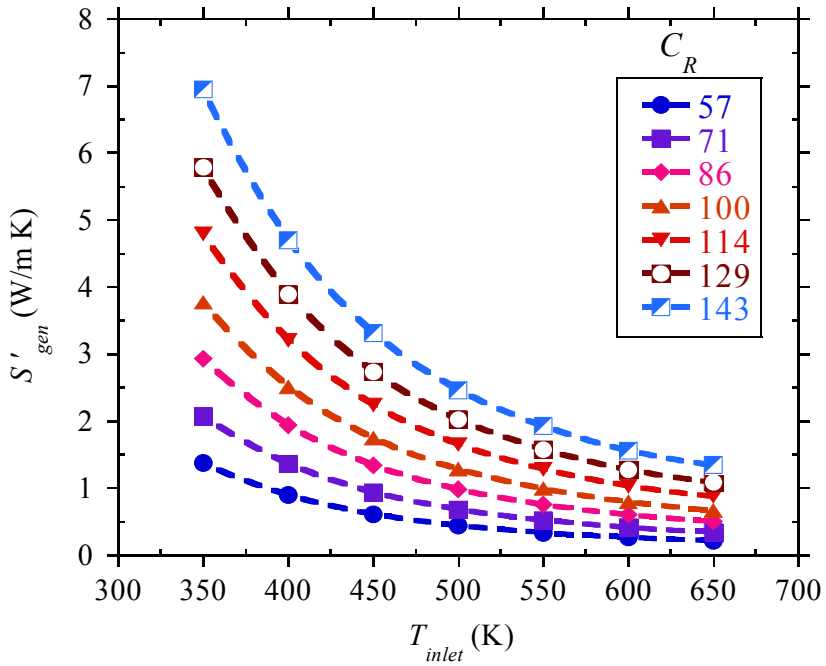

Fig. 5.7: Entropy generation in the receiver's absorber tube as a function of inlet temperature and concentration ratio (C_R) for a flow rate of 18.5 m^3/h and a rim angle (φ_r) of 80°.

Figures 5.7 and 5.8 show that at a given flow rate, the entropy generation rate per unit length ($S'_{gen}= S_{gen}/L$) decreases as the absorber tube inlet temperature increases. Furthermore, at a given flow rate and inlet temperature, the entropy generation increases as the concentration ratio increases. Increasing the concentration ratios means increased heat flux on the absorber tube, therefore such higher temperature gradients and increased heat transfer irreversibility require a higher fluid flow rate or heat transfer augmentation for better heat transfer.

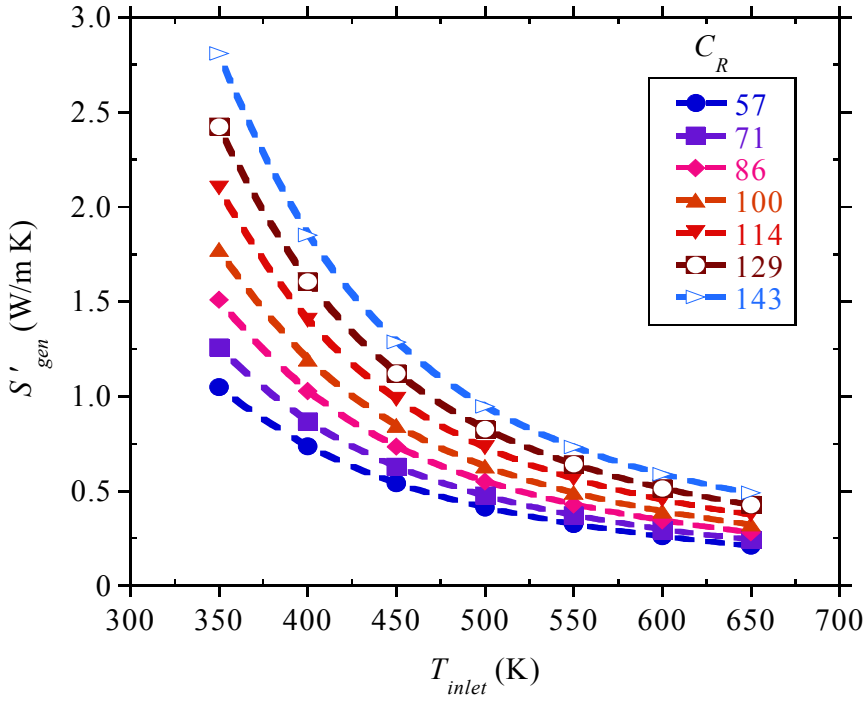

Fig. 5.8: Entropy generation in the receiver's absorber tube as a function of inlet temperature and concentration ratio (C_R) for a flow rate of 104.8 m^3/h and a rim angle (φ_r) of 80^o.

The entropy generation rates are higher at lower flow rates, as shown in Fig. 5.7 compared with entropy generation rates at high flow rates as shown in Fig. 5.8. As the flow rate increases, the heat transfer irreversibility is reduced, but the fluid friction irreversibility increases. Both figures show a reduction in the entropy generation as the heat transfer fluid inlet temperatures increase. The reduction in entropy generation as the inlet temperature increases is due to the variation of the fluid's thermal properties with temperature: as the inlet temperatures increase, the fluid becomes less dense and less viscous, leading to reduced fluid friction irreversibility.

Specific fluid inlet temperatures are considered so as to present the results in terms of the Reynolds numbers. Figures 5.9 and 5.10 show the Nusselt number and friction factor respectively for an inlet temperature of 550 K. The figures show that increasing the concentration ratio has no effect on the Nusselt number and friction factor. They also show that continually increasing the Reynolds numbers increases the Nusselt numbers and reduces

the friction factor. Therefore, based on the first law of thermodynamics, there is no clear optimal operation point. However, an analysis based on the second law of thermodynamics shows that at a given concentration ratio, an increase in the Reynolds number reduces the heat transfer irreversibility while increasing the fluid friction irreversibility. Accordingly, there is a Reynolds number at which the sum of the heat transfer irreversibility and fluid friction irreversibility is a minimum.

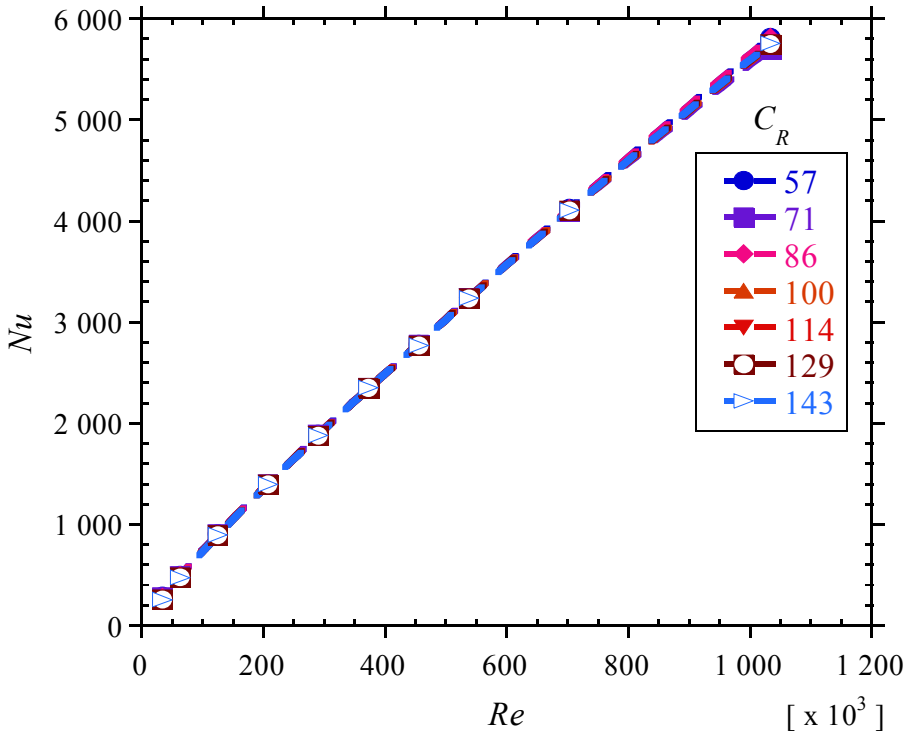

Fig. 5.9: Receiver heat transfer performance as a function of Reynolds number and concentration ratio (C_R) for an inlet temperature of 550 K and rim angle (φ_r) of 80º.

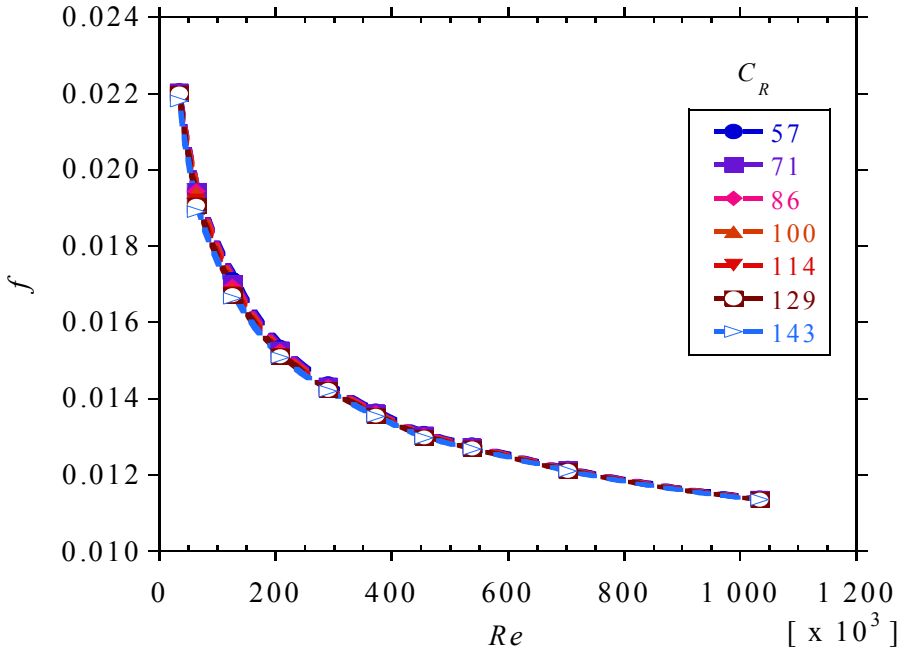

Fig. 5.10: Receiver friction factor as a function of Reynolds number and concentration ratio (C_R) for an inlet temperature of 550 K and rim angle (φ_r) of 80°.

Figures 5.11 and 5.12 show that for every concentration ratio and a given inlet temperature, there is a Reynolds number that minimises the entropy generation in the absorber tube. The figures also show that high concentration ratios result in higher entropy generation rates owing to increased heat transfer irreversibility. The optimum Reynolds number is shown to increase as the concentration ratio increases. Therefore, an increase in concentration ratio would require a corresponding increase in the fluid flow rate to minimise the heat transfer irreversibility for minimum entropy generation.

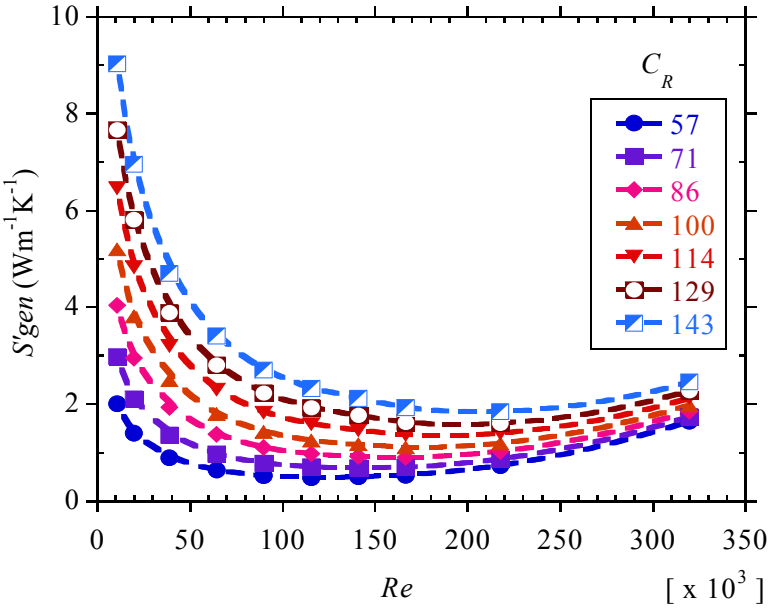

Fig. 5.11: Entropy generation in the receiver's absorber tube as a function of Reynolds number and concentration ratio (C_R) for an inlet temperature of 400 K and a rim angle (φ_r) of 80°.

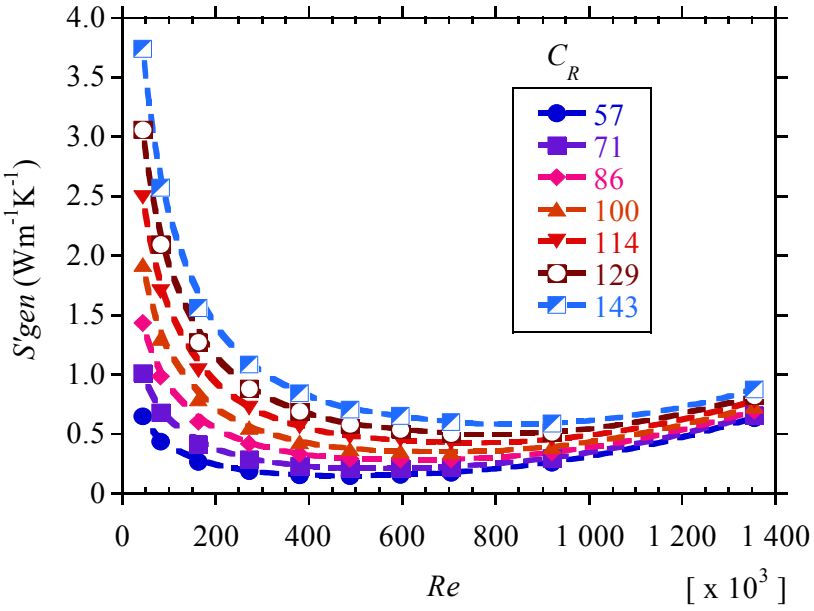

Fig. 5.12: Entropy generation in the receiver's absorber tube as a function of Reynolds number and concentration ratio (C_R) for an inlet temperature of 600 K and a rim angle (φ_r) of 80°.

Figure 5.13 shows the distribution of entropy generation at concentration ratios of 71 and 129 at T_{inlet} = 500 K. The fluid friction irreversibility increases as the Reynolds number increases, but does not change when the concentration ratio changes, whereas the heat transfer irreversibility decreases with increasing Reynolds numbers and increases significantly as the concentration ratios increase. The entropy generation due to heat transfer is dominant at low Reynolds numbers, since the low heat transfer coefficients and entropy generation due to fluid friction become the dominant source at high values of Reynolds number because of the increased drop in pressure.

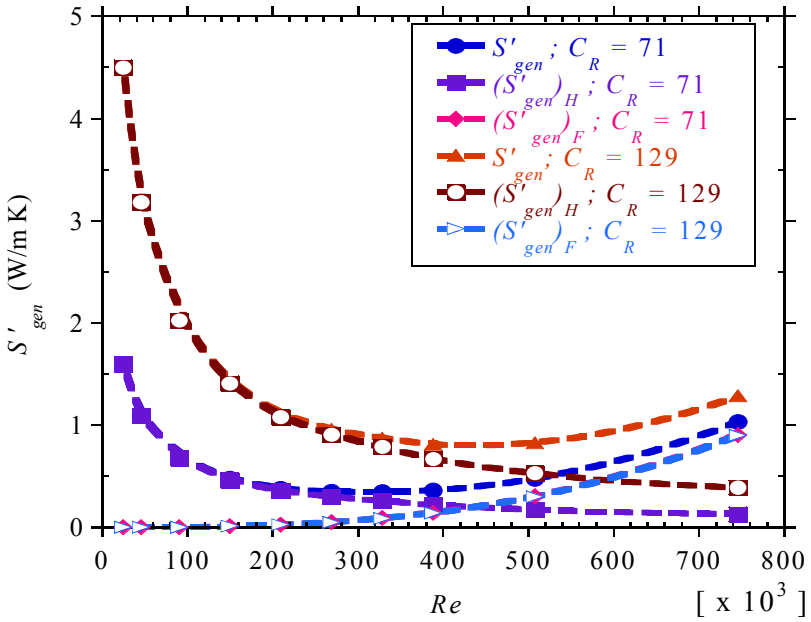

Fig. 5.13: Total entropy generation, entropy generation due to heat transfer irreversibility and entropy generation due to fluid friction irreversibility in the receiver's absorber tube as functions of Reynolds number for concentration ratios (C_R) of 71 and 129 and inlet temperature of 500 K.

For all concentration ratios, Fig. 5.14 shows the variation of the Bejan number with concentration ratio and the Reynolds number at T_{inlet} = 500 K. The Bejan number approaches 1 at very low Reynolds numbers and approaches zero as Reynolds numbers are increased for low concentration ratios. The Bejan number is also shown to increase with an increase in the concentration ratios.

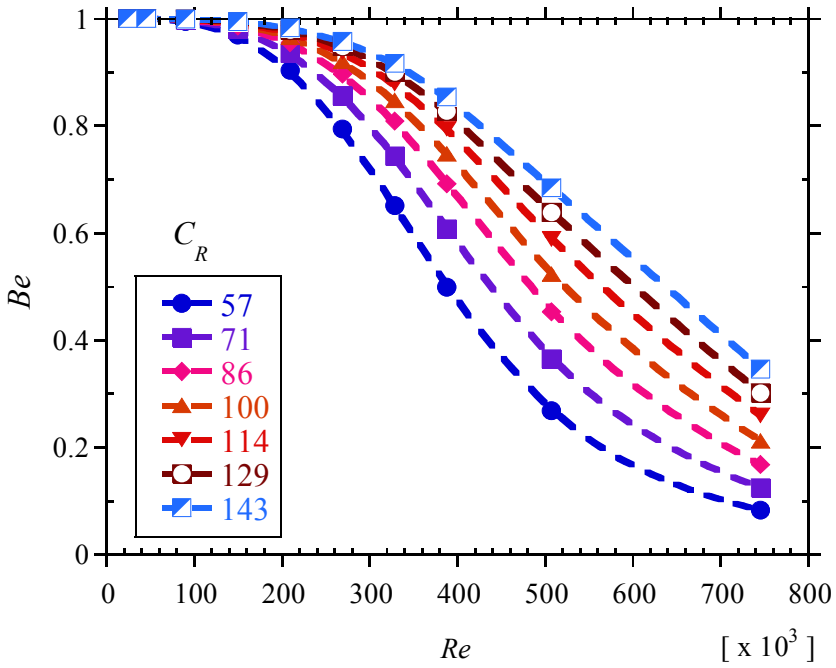

Fig. 5.14: Bejan number as a function of Reynolds number and concentration ratio (C_R) for an inlet temperature of 500 K and a rim angle (φ_r) of 80°.

The optimal Reynolds number (at which entropy generation is a minimum) is shown to increase as the concentration ratio increases, as shown in Figs 5.11 – 5.13 and 5.15 for specific inlet temperatures. Figure 5.15 also shows that as the inlet temperatures increase, the optimal Reynolds number also increases because the density and viscosity of the fluid were taken to vary with temperature. Based on the heat transfer fluid flow rate, the flow rates corresponding to the optimal Reynolds number are nearly the same for the different inlet temperatures at a given concentration ratio. For all inlet temperatures, the average optimal flow rates are shown in Table 5.2 at the different concentration ratios considered in this study.

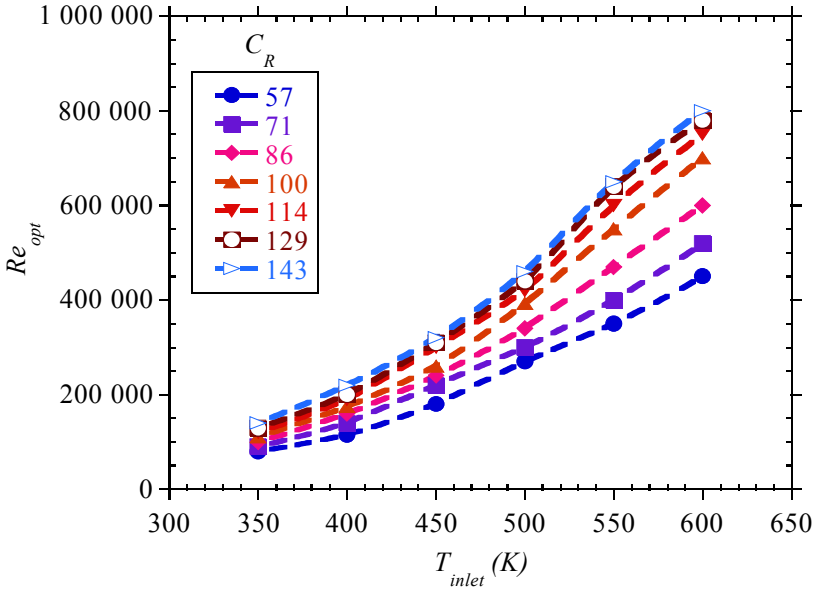

Fig. 5.15: Optimal Reynolds number as a function of inlet temperature and concentration ratio (C_R) and a rim angle (φ_r) of 80°.

Table 5.2: Optimal flow rates at different concentration ratios.

Concentration ratio (C_R)	Optimal flow rate (m^3/h)
57	52.7
71	62.4
86	70.3
100	79.5
114	87.0
129	91.2
143	95.1

For a fair evaluation of entropy generation at different concentration ratios, the non-dimensional entropy generation number N_s, which relates the entropy generated to the inlet temperature and heat transfer rate was defined as:

$$N_s = \frac{S_{gen}}{\dot{q}/T_{inlet}}$$, where $\dot{q}$ - is the heat transfer rate and T_{inlet} - is the inlet temperature.

Figure 5.16 shows the variation of N_s with the Reynolds number at an inlet temperature of 550 K. The location of the optimal Reynolds number is clearly shown and does not differ

from that indicated in Figs 5.11 and 5.12. However, Fig. 5.16 shows that the entropy generation number is higher as the concentration ratios increase for low Reynolds numbers and becomes lower as the concentration ratios increase for higher flow rates. Therefore, higher flow rates are undesirable for lower concentration ratios.

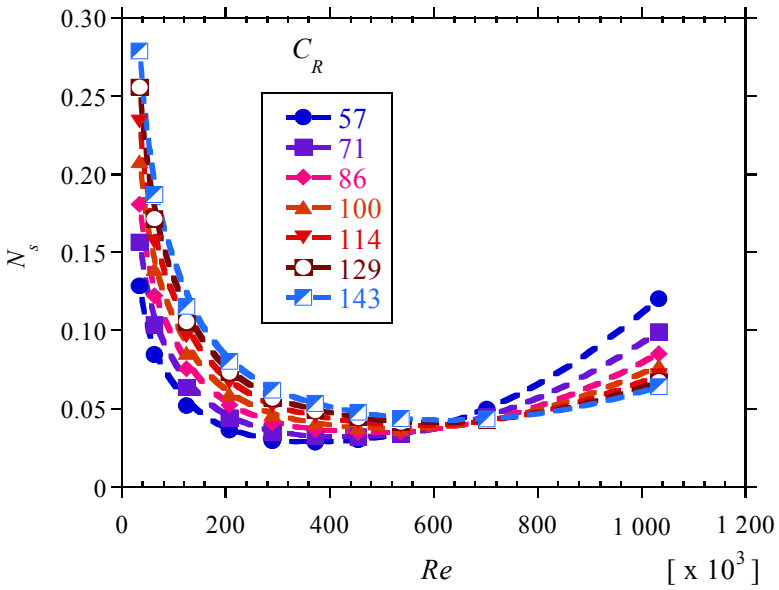

Fig. 5.16: Entropy generation number as a function of Reynolds number and concentration ratio (C_R) for an inlet temperature of 550 K and rim angle (φ_r) of 80°.

5.3.4 EFFECT OF RIM ANGLE ON ENTROPY GENERATION

As discussed, rim angles have a significant influence on the peak heat fluxes as well as the peak temperatures in the receiver. Accordingly, the heat transfer irreversibility is expected to increase as the rim angle reduces. The increase in the heat transfer irreversibility is more pronounced at higher Reynolds numbers. When looking at the Bejan number in Fig. 5.17 it can be seen that the heat transfer irreversibility increases as the rim angle reduces. From the point of view of entropy generation, the higher the finite temperature difference, the greater the heat transfer irreversibility. Therefore, at the same flow rate/Reynolds number and concentration ratio the entropy generation is expected to reduce as the rim angle increases.

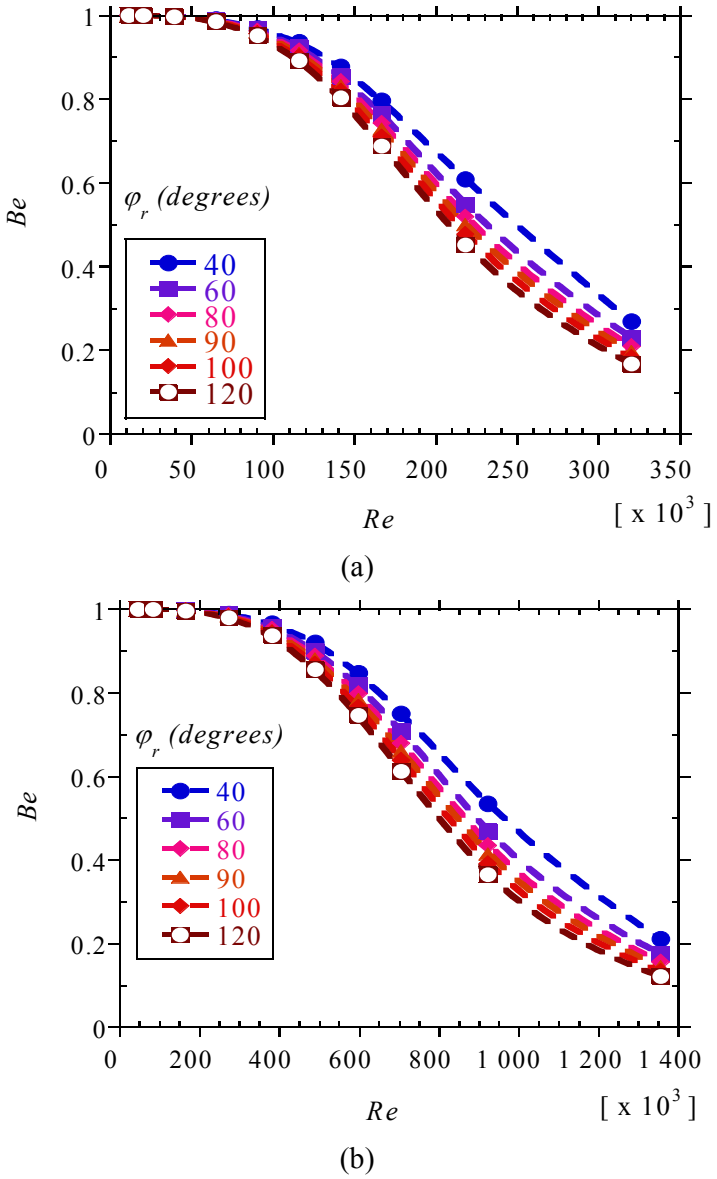

Fig. 5.17: Bejan number as a function of Reynolds number and rim angle (φ_r) for a concentration ratio (C_R) of 86: (a) inlet temperature of 400 K and (b) inlet temperature of 600 K.

Figures 5.18(a) and 5.18(b) show the variation of entropy generation with Reynolds numbers at different rim angles for inlet temperatures of 400 K and 600 K respectively.

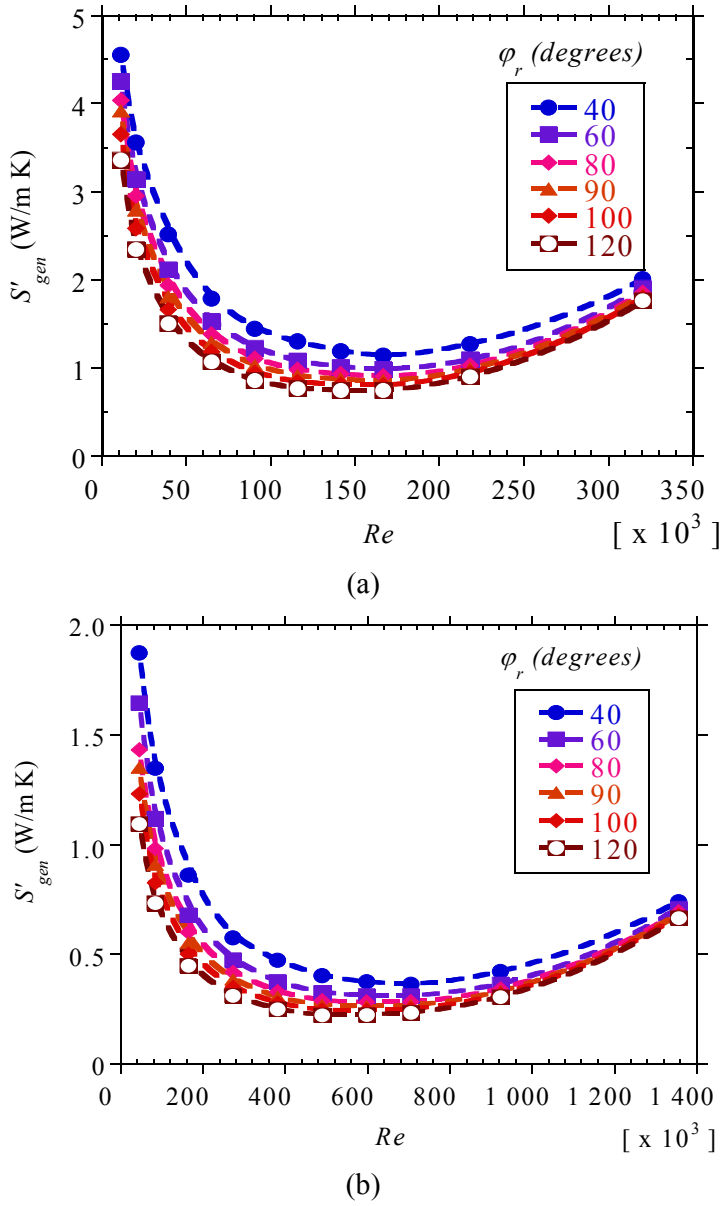

Fig. 5.18: Entropy generation in the receiver's absorber tube as a function Reynolds number and rim angle (φ_r) for a concentration ratio (C_R) of 86: (a) inlet temperature of 400 K and (b) inlet temperature of 600 K.

As anticipated, the entropy generated increases as the rim angle reduces at each temperature considered. At the lowest Reynolds number in the figures, the entropy generation reduces by about 35% and 72% at the respective temperatures as the rim angle increases from 40^o to

120^o. Therefore, in addition to reducing the absorber tube's temperature difference, the use of higher rim angles also ensures the efficient utilisation of the available energy. It can also be noted from the figures that the entropy generation is smaller at higher temperatures than at lower temperatures, as already discussed. In addition, the rim angle does not have any significant effect on the optimal flow rates or Reynolds number at any given concentration ratio and fluid temperature.

5.3.5 COMPARISON WITH ENTROPY GENERATION FOR THE ENTIRE COLLECTOR SYSTEM

So far, we have presented the results of entropy generation due to heat transfer and fluid flow in the parabolic trough receiver alone. To compare this with the entropy generation for the entire collector system, the method proposed by Bejan [61] for solar collectors was used. The method considers entropy generation upstream of the collector, downstream of the collector and inside the collector. The exergy flow diagram is given in Fig. 5.19 [10,16] for a collector of area A_a, receiving solar radiation at a rate Q^* from the sun.

Where Q^* is proportional to the area of the collector and the direct normal irradiance, I_b. The incident solar radiation is partly delivered to the user as heat transfer Q at the receiver temperature T_r, the remaining fraction, Q_o is lost to the ambient air. The entropy generation due to these processes for a non-isothermal collector, without considering the pressure drop between the inlet and outlet, is given as [10,16,61]

$$S_{gen,col} = \dot{m}c_p \ln\frac{T_{outlet}}{T_{inlet}} - \frac{Q^*}{T_*} + \frac{Q_o}{T_o} \qquad 5.1$$

where T_* is the apparent temperature of the sun as an energy source approximately equal to $\frac{3}{4}T_s$ [10], T_s is the apparent blackbody temperature of the sun, T_o is the ambient temperature, $Q_o = Q^* - Q$ and $Q = \dot{m}c_p(T_{outlet} - T_{inlet})$.

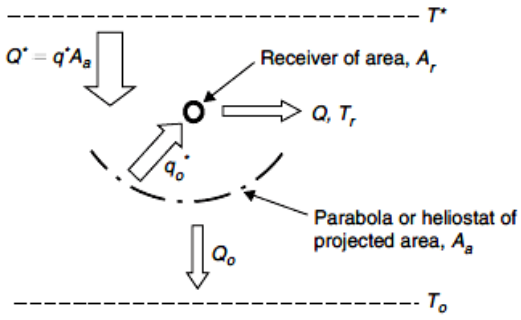

(a)

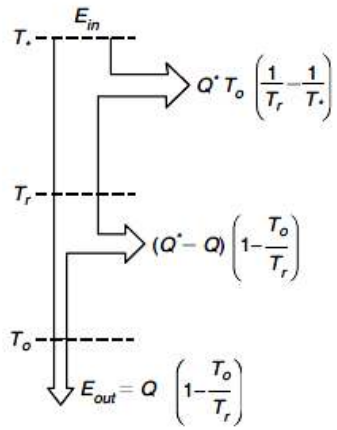

(b)

Fig. 5.19: Representation of energy and exergy analysis for concentrating collectors: (a) energy flow diagram for concentrating solar collectors and (b) exergy flow diagram.

Figure 5.20 shows the entropy generation rate per unit length ($S'_{gen,col} = S_{gen,col} / L$) of the entire collector system at T_{inlet} = 400 K at different concentration ratios and Reynolds numbers. The figure shows that the entropy generation rate of the collector system depends more strongly on the concentration ratio than on Reynolds numbers. This is due to the increase in the entropy generation from heat transfer as concentration ratios increase.

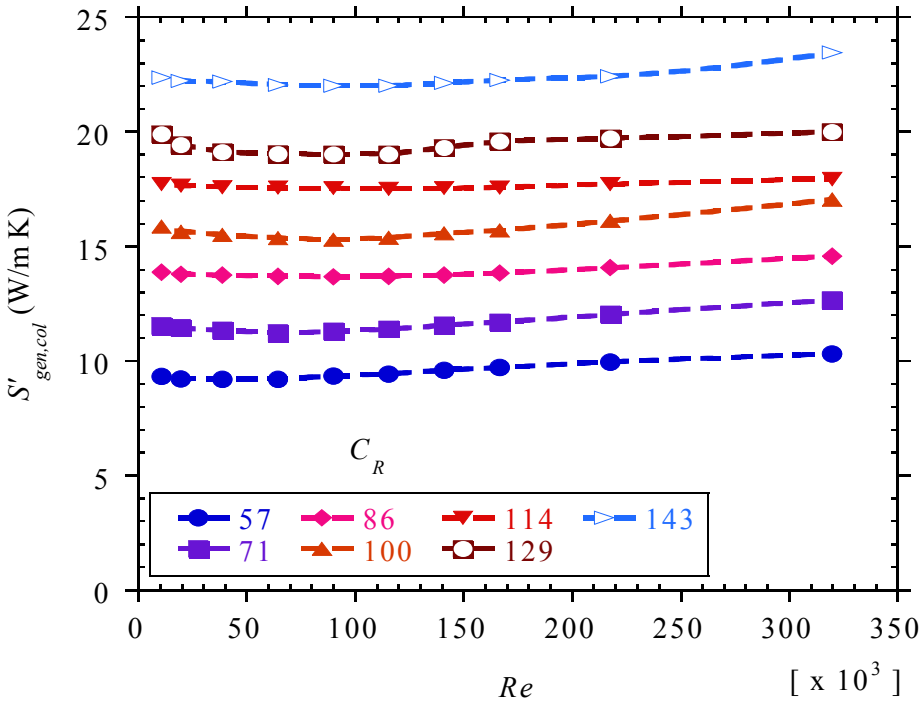

Fig. 5.20: Entropy generation for an entire parabolic trough collector system as a function of Reynolds number and concentration ratio (C_R) for an inlet temperature of 400 K and a rim angle (φ_r) of 80°.

A closer look at each concentration ratio shows that the entropy generation is minimum at some Reynolds number as shown in Fig. 5.21 for C_R = 86. This is in agreement with our analysis when only entropy generation due to heat transfer and fluid friction was considered.

Therefore, the entropy generation due to heat transfer and fluid friction in the receiver is related in some way to the collector's entropy generation through the first term in Eq. (5.1). The point of minimum entropy will exist in this case because the mass flow rate and outlet temperature in the first term of Eq. (5.1) are interdependent. Increasing the mass flow rate increases the contribution due to $\dot{m}c_p$ while at the same time reducing the contribution due to $\ln(T_{out}/T_{inlet})$, so that there is a point at which the product of the two terms is a minimum.

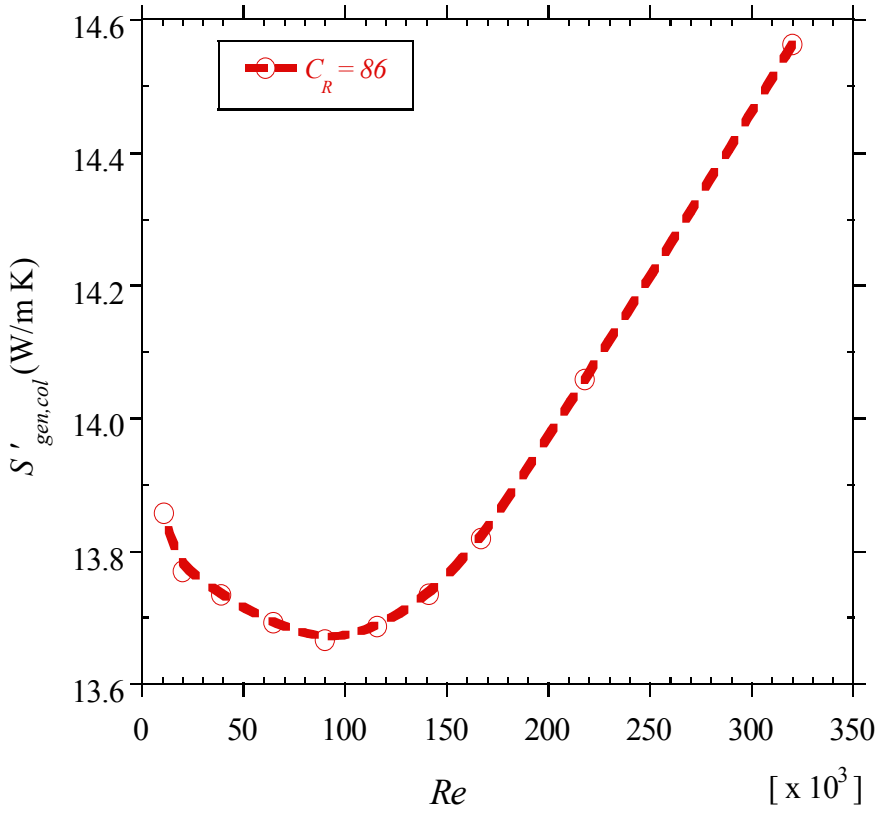

Fig. 5.21: Entropy generation for an entire parabolic trough collector system as a function of Reynolds number at a concentration ratio (C_R) of 86, rim angle (φ_r) of 80° and an inlet temperature of 400 K.

Table 5.3 summarises the entropy generation of the different processes given in Eq. (5.1) and also compares the entropy generation due to heat transfer with the fluid flow determined by the CFD analysis. Given the assumed constant value of the direct normal irradiance (I_b), the entropy generation from solar radiation (Q^*/T_*) remains constant at a given concentration ratio. The entropy generation due to heat transfer ($(\dot{m}c_p \ln(T_{outlet}/T_{inlet}))$) is the largest contributor to the entropy generation budget of the collector system, as shown in Table 5.3. Our analysis (4-m long collector system) noted a slight variation of the entropy generation due to heat transfer at each inlet temperature and concentration ratio. This variation is because at a given inlet temperature and concentration ratio, the heat transfer rate does not vary much over the 4-m long collector system considered.

Table 5.3: Entropy generation due to heat transfer and fluid flow compared with entropy generation in the collector.

(a) T_{inlet} = 400 K, C_R = 86

Flow rate (m^3/h)	$\dot{m}c_p \ln \frac{T_{outlet}}{T_{inlet}}$ (W/K)	Q^*/T_* (W/K)	Q_o/T_o (W/K)	$S'_{gen,col}$ (W/m K)	S'_{gen} (W/m K)	$S'_{gen}/S'_{gen,col}$ (%)
9.2	52.46	5.17	10.50	14.45	2.14	14.83
18.5	51.95	5.17	10.28	14.26	1.35	9.48
30.8	51.62	5.17	10.20	14.16	0.95	6.69
43.1	51.53	5.17	10.18	14.13	0.76	5.39
55.4	51.50	5.17	10.16	14.12	0.68	4.78
80.1	51.80	5.17	10.08	14.18	0.67	4.75
104.7	52.43	5.17	10.06	14.33	0.85	5.94
153.9	56.72	5.17	9.95	15.37	1.70	11.08

(b) T_{inlet} = 550 K, C_R =86

Flow rate (m^3/h)	$\dot{m}c_p \ln \frac{T_{outlet}}{T_{inlet}}$ (W/K)	Q^*/T_* (W/K)	Q_o/T_o (W/K)	$S'_{gen,col}$ (W/K)	S'_{gen} (W/K)	$S'_{gen}/S'_{gen,col}$ (%)
9.2	35.65	5.17	12.74	10.81	0.85	7.82
18.5	35.10	5.17	12.33	10.56	0.51	4.83
30.8	34.50	5.17	12.21	10.38	0.32	3.05
43.1	34.50	5.17	12.15	10.37	0.28	2.68
55.4	35.00	5.17	12.05	10.47	0.25	2.38
80.1	35.80	5.17	11.90	10.63	0.27	2.50
104.7	36.65	5.17	11.80	10.82	0.36	3.32
153.9	38.34	5.17	11.70	11.22	0.79	7.00

The entropy generation due to heat loss (Q_o/T_o) reduces with an increase in flow rates owing to the reduced heat loss (Q_o) resulting from the reduced temperature difference between the receiver and the surroundings.

The entropy generation due to heat transfer and fluid flow is a small percentage of the entropy generation for the entire collector system given by Eq. (5.1). The percentage depends on the inlet temperature and the flow rate; S'_{gen} is about 15% of $S'_{gen,col}$ at T_{inlet} = 400 K, C_R = 86 when the flow rate is 9.2 m^3/h and 7.8% of $S'_{gen,col}$ when the inlet temperature is 550 K at the same flow rate and concentration ratio. Even though the entropy generation

predicted for the entire collector system is larger than the entropy generation due to heat transfer and fluid flow, they all show the same variation with temperature, concentration ratio and Reynolds number. Either of the two methods can be used to optimise the performance of solar collector systems since it has been shown in this study that minimising the entropy generation due to heat transfer and fluid flow minimises the entropy generation for the entire collector system and vice versa.

5.4 CONCLUDING REMARKS

A numerical analysis on entropy generation for a receiver of a parabolic trough collector at different rim angles, concentration ratios, inlet temperatures and Reynolds numbers was carried out. Even though the analysis based on the first law of thermodynamics shows no variation in the Nusselt number and friction factor as concentration ratios change, using the second law of thermodynamics has shown that increasing the concentration ratios increases the entropy generation rates in the receiver.

From the local determination of entropy generation rates in the receiver's absorber tube, it has been shown that high entropy generation rates occur in the lower half of the receiver owing to the highly concentrated heat flux incident on it. This results in high temperature gradients and thus high heat transfer irreversibility.

The entropy generation rates increase as the rim angle reduces because of the higher temperature peaks associated with low rim angles. The increase in entropy generation as the rim angles increase is not very significant for rim angles above 80^{o} and for flow rates higher than 31 m^3/h.

For a given inlet temperature, it has been shown using the Bejan number that entropy generation due to heat transfer dominates for lower values of Reynolds numbers, whereas entropy generation due to fluid friction dominates for higher values of Reynolds numbers. The Bejan number approaches 1 for $Re < 2 \times 10^5$ for all the concentration ratios and is less than 0.4 for $Re > 8 \times 10^5$ for all concentration ratios when $T_{inlet} = 550$ K. The Bejan number also increases as the concentration ratio increases for a given inlet temperature and Reynolds number.

Also shown is that, at a given concentration ratio and inlet temperature, there is a Reynolds number *(Re_{opt})* for which the entropy generation is a minimum. The value of the optimum Reynolds number increases as the concentration ratio increases. Because of the variation in the fluid's heat transfer properties, the optimal Reynolds number is shown to increase as the inlet temperature increases.

However, the obtained optimal Reynolds numbers correspond to volumetric flow rates of 52.7 m^3/h, 62.4 m^3/h, 70.3 m^3/h, 79.5 m^3/h, 87 m^3/h, 91.2 m^3/h, 95.1 m^3/h at concentration ratios 57, 71, 86, 100, 114, 129 and 143 respectively, regardless of the inlet temperature used. It has also been shown that minimising the entropy generation due to heat transfer and fluid flow in the receiver minimises the entropy generation for the entire collector system.

CHAPTER SIX

CHAPTER SIX: HEAT TRANSFER ENHANCEMENT IN PARABOLIC TROUGH RECEIVERS USING WALL-DETACHED TWISTED TAPE INSERTS

6.0 INTRODUCTION

The need to further reduce the costs of parabolic trough collector systems has motivated the use of larger as well as longer concentrator modules [18,21,23]. An increase in concentrator size ensures a reduced number of drives as well as controls, thus a reduction in capital costs and operation costs. Larger concentrator sizes lead, however, to higher concentration ratios and therefore to high heat fluxes on the receiver's absorber tube. These high heat fluxes significantly increase the circumferential temperature difference in the receiver's absorber tube, increase the heat transfer irreversibilities (as shown in Chapters 5) and reduce the reliability of the receivers. Therefore, with higher concentration ratios, it becomes necessary to improve the heat transfer performance of parabolic trough receivers in order to: (i) improve their thermal performance; (ii) reduce the absorber tube's circumferential temperature difference; and (ii) minimise the heat transfer irreversibilities.

Heat transfer enhancement is one way of improving the heat transfer performance of heat exchangers. The field of heat transfer enhancement has been extensively developed and an enormous database of technical literature is available on the subject [53,54]. The need to improve the thermal performance of heat transfer exchangers and heat transfer devices is motivated by the possible reductions in energy utilisation, materials and costs. Several techniques have been developed for heat transfer enhancement and are widely used in many applications. They are classified as active or passive heat transfer enhancement techniques. Passive heat transfer enhancement techniques have been extensively researched and are widely used in many industrial applications since they require no direct power input in comparison to active techniques which require a direct power input. A detailed review of

various heat transfer enhancement techniques is presented by Manglik [54], Bergles [52,151] and Webb [53].

Of the several passive heat transfer enhancement techniques developed and researched, techniques that generate swirl flow in tubes are very attractive and much utilised. Passive swirl flow techniques come in many arrangements, such as inserts, geometrically modified flow arrangements and duct modifications [56]. Tube inserts include twisted tapes, axial cores with screw-type windings, helical vane inserts, static mixers and periodically spaced propellers [56].

Twisted tape inserts are the most widely used swirl-generating devices and are broadly employed in many applications for enhancing single-phase and two-phase as well as laminar and turbulent forced convention heat transfer. The wide application and interest in using twisted tape inserts can be seen in the number of studies dedicated to heat transfer enhancement using twisted tape inserts, provided in reviews by Manglik [56], Bergles [52] Webb [53], Dewan *et al.*[152], Nithiyesh [153] and Liu and Sakr [154]. Twisted tape inserts generally give high heat transfer rates with a moderate increase in pressure drops.

The wide applicability of twisted tape inserts is also partly due to their ease of manufacture and installation in heat exchangers. Several features exhibited by twisted tape inserts result in heat transfer enhancement. These features include: fluid agitation and mixing induced by the cross-section secondary circulation, a thinner boundary layer, a longer path due to the helical twisting of fluid motion, partitioning and blockage of the tube flow cross-section and an induced tangential flow velocity component.

Several studies are available in the literature regarding heat transfer enhancement using twisted tape inserts of varying configurations. The configurations include: (i) conventional or typical twisted tape inserts – a thin metallic strip with the same width as the tube's inside diameter is twisted into a constant pitch helix and inserted in a tube; (ii) modified twisted tape inserts – including short lengths of twisted tape placed at tube inlet, variations of tape geometry and/or surface and interspaced short-length twisted tape inserts [56];

(iii) compound enhancement with twisted tapes – twisted tape inserts are used with one or more other enhancement techniques [56].

Marner and Bergles [155] compared heat transfer enhancement in a tube using twisted tape inserts and internal fins using Polybutene 20 as a heat transfer fluid for laminar flow conditions. They showed that twisted tape inserts perform better than internal fins for cooling applications. Agarwal and Raja Rao [156] also demonstrate the use of twisted tape inserts with high Prandtl number fluids. For twist ratios of 2.41 – 4.84, using Servotherm oil as the heat transfer fluid and Reynolds numbers in the range $70 \leq Re \leq 4\,000$, they report an increase in Nusselt numbers in the range 1.31 – 3.70 and 1.21 – 3.70 times compared to those of plain tubes for constant flow rate and constant pumping power respectively at the minimum twist ratio. The friction factors increased by 3.13 – 9.71 times compared to those of plain tubes.

Kumar and Prasad [157] investigated heat transfer enhancement in solar water-heating systems using twisted tape inserts. For Reynolds numbers in the range $4\,000 \leq Re \leq 21\,000$, they showed an increase in heat transfer performance between 18% to 70% and a pressure drop increase between 87% and 132%. Jaisankar *et al.* [158-160] also present the results of studies on heat transfer enhancement in solar water-heating systems, using twisted tape inserts. They report an increased heat transfer performance due to the use of twisted tape inserts. In all their studies, the temperatures of the absorber plate are shown to decrease with the use of twisted tape inserts. Minimum twist ratios are shown to give the largest reduction in absorber plate temperature.

Noothong *et al.* [161] experimentally investigated heat transfer enhancement in a concentric heat exchanger, using twisted tape inserts of twist ratios 5 and 7. The experiments were carried out using water as the test fluid, for Reynolds numbers in the range $2\,000 \leq Re \leq 12\,000$. Small twist ratios were found to give higher heat transfer, pressure drops and thermal enhancement efficiency.

Several modifications of twisted tapes have been studied and reported in the literature. The modifications are intended to either reduce the pressure drop or increase the heat transfer rate.

The modifications include modifications of the twisted tape arrangement or of the twisted tape geometry.

Saha e*t al.* [162] present an experimental investigation of heat transfer enhancement using regularly spaced twisted tape inserts for laminar flow conditions. The twist ratio was varied in the range $3.18 \leq y \leq \infty$ while the spacing ratio $2.5 \leq y \leq 10$. Pumping power was shown to significantly reduce with no significant reduction in heat transfer, when using regularly spaced twisted tape inserts. In another study, Saha *et al.* [163] used the same twist ratios and spacing ratio for turbulent flow conditions. They report that using regularly spaced twisted tape significantly reduces the pressured drop with less impact on heat transfer. Date and Saha [164] present a study on laminar prediction and heat transfer in a tube with regularly spaced twisted tape inserts. Date and Gaitonde [165] developed correlations for predicting the characteristics of laminar flow in a tube with regularly spaced twisted tape inserts.

Saha and Dutta [166] experimentally investigated heat transfer enhancement using regularly spaced twisted tapes with smoothly varying pitch and uniform pitch. They used Servotherm oil as the test fluid and Reynolds numbers in the range $10\,000 \leq Re \leq 20\,200$. Their study shows that smoothly varying pitch twisted tapes have a worse performance than those of a uniform pitch. Eiamsa-ard *et al.* [167] experimentally investigated the use of regularly spaced twisted tape inserts for heat transfer in a double-pipe heat exchanger. Two twist ratios, 6 and 8, were used and three spacing ratios 1.0, 2.0 and 3.0 considered. They show that the heat transfer and fluid friction increase with a reduction in the twist ratio and free-spacing ratio.

Wang *et al.* [168] present a numerical and experimental investigation of regularly spaced twisted tape inserts with twist ratios in the range 2.5 – 8.0. Air was used as the test fluid, and a constant wall temperature boundary condition was used for Reynolds numbers in the range $10\,000 \leq Re \leq 20\,200$. Better heat transfer performance was achieved with smaller twist ratios. Enhancement efficiency was achieved, based on a constant pumping-power comparison in the range $0.84 \leq \eta \leq 1.4$. Eiamsa-ard *et al.* [169] report the results of an experimental investigation on dual and regularly spaced twisted tape inserts, in which smaller spacing ratios show higher heat transfer performance and pressure drop.

Jaisankar *et al.* [170] experimentally investigated the use of twisted tape inserts with a rod or spacer at the trailing edge in a thermosyphon solar water-heating system. For the twist ratios of 3 and 5 and a rod or space length of 100 mm, 200 mm, 300 mm and laminar flow regime, they showed that using rods and spacers at the trailing edge reduced the heat transfer performance by 17% – 29% respectively, and reduced the pressure drop by 39% – 47% respectively. They conclude that using rods and spacers at the trailing edge is advantageous for reducing the friction factor with less impact on heat transfer enhancement. Seemawute [171] report the results for decaying swirl in round tubes, using short-length twisted tapes inserts. They demonstrate that the short-length twisted tape inserts have a poorer heat transfer performance than full-length twisted tape inserts. Eiamsa-ard [172] report the results of an experimental investigation for heat transfer enhancement with short-length twisted tape inserts. They also show that short length tapes have lower Nusselt numbers and friction factors than full-length twisted tapes.

Several authors have also investigated other modifications of the twisted tape geometries. Eiamsa-ard *et al.* [173] experimentally investigated and compared the performance of typical twisted tape, alternate clockwise and counter-clockwise tapes. In another study, Eiamsa-ard *et al.* [174] experimentally and numerically investigated the use of twin counter/co-swirl twisted tape inserts. They reported more heat transfer enhancement in counter-swirl tapes than co-swirl tapes. Chiu and Jang [175] numerically and experimentally investigated heat transfer enhancement with twisted tape inserts of different angles with holes. Eiamsa-ard *et al.* [176] investigated heat transfer enhancement with twisted tape inserts that had centre wings, alternate axes and centre wings with alternate axes. Eiamsa-ard *et al.* [177] experimentally investigated delta-winglet twisted tape inserts for twist ratios 3, 4 and 5 with wing cut ratios of 0.11, 0.21 and 0.32. They report higher heat transfer enhancement in delta-winglet twisted tapes inserts than in typical twisted tapes.

Other geometry modifications reported in the literature include: twisted tapes with serrated edges [178], broken twisted tapes [179], twisted tapes with alternate axes and triangular, rectangular and trapezoidal wings [180], twisted tapes with square cuts [181], twisted tapes with wire nails [182], converging and diverging tubes with twin counter-swirling twisted tapes [183].

Several authors have also investigated compound heat transfer enhancement using twisted tape inserts. Zimparov [184] experimentally studied the heat transfer performance in corrugated tubes with twisted tape inserts. In Zimparov's other studies correlations were mathematically derived for friction factor: Zimparov [185], and for heat transfer coefficients: Zimparov [186], for corrugated tubes with twisted tape inserts. Thianpong *et al.* [187] experimentally studied the heat transfer performance of a dimpled tube with twisted tape inserts. Eiamsa-ard *et al.* [188] experimentally investigated heat transfer performance for a non-uniform wire coil and twisted tape insert. Bharadwaj *et al.* [189] studied the combined use of twisted tapes and spiral grooves for heat transfer enhancement in a circular tube, for both laminar flow and turbulent flow. Promvonge and Eiamsa-ard [190] studied the combined use of twisted tape inserts and conical rings for heat transfer enhancement in a tube. Promvonge *et al.* [191] experimentally investigated heat transfer enhancement in a helically ribbed tube together with twin twisted tape inserts. Liao and Xin [192] experimentally investigated heat transfer enhancement in a tube using a combination of twisted tape inserts or segmented tape inserts with internal fins. In these studies, heat transfer performance was significantly increased by combining twisted tape inserts with other enhancement methods. However, the fluid friction also increased significantly.

Several authors have proposed several modifications of twisted tapes as a way of reducing fluid friction. Apart from regularly spaced twisted tape inserts, the use of twisted tapes inserts placed separately from the wall is another way of reducing fluid friction and has been investigated by several researchers. Twisted tape inserts placed separately from the wall are also useful to prevent deposition and the build-up of foreign material on the tube's inner surface, thereby maintaining high heat transfer rates. Several studies have shown that the fluid friction depends largely on the gap between the wall and the twisted tape, for example the studies by Ayub and Al-Fahed [193], Al-Fahed and Chakroun [194], Bas and Ozceyhan [195] and Eiamsa-ard *et al*. [196].

Ayub and Al-Fahed [193] first reported an experimental investigation on fluid friction for twisted tape inserts placed separately from the wall. They found that the gap between the tube and the tape is responsible for the enormous pressure drop. Al-Fahed and Chakroun [194] later investigated the use of wall-separated twisted tape inserts on heat transfer for fully

developed turbulent flow. They report that the heat transfer enhancement decreases with tube-tape clearance and that tighter fitting tapes result in higher heat transfer enhancement than loose fitting twisted tapes. Guo *et al.* [197] numerically studied heat transfer enhancement using centre-cleared twisted tape inserts in comparison with short-width twisted tape inserts. They report that both methods are effective for reducing the flow resistance. The centre-cleared twisted tape enhanced heat transfer by 7% – 20% compared with a tube with a conventional twisted tape insert, whereas for short-width tapes, heat transfer and thermo-hydraulic performance were weakened by cutting off the tape edge.

Eiamsa-ard *et al.* [196] also considered the use of loose-fit twisted tape inserts on heat transfer enhancement in a tube. They report high heat transfer enhancement at the lowest twist ratio and the smallest clearance ratio. Friction factors are shown to reduce as clearance ratios increase. The best thermal performance factor was obtained at clearance ratio of 0. Bas and Ozceyhan [195] recently presented an experimental investigation on the use of twisted tape inserts placed separately from the wall. They report that the twist ratio has a major effect on heat transfer enhancement compared to the clearance ratio. A reduction in pumping power as the clearance ratio increases is reported.

Recently Zhang *et al.* [198] used the principles of heat transfer enhancement in the core flow, to study heat transfer and flow characteristics numerically for laminar flow, using multiple regularly spaced twisted tape inserts. They considered several arrangements of twisted tapes with a relative twist ratio of 2.5 placed separately from the wall and laminar flow conditions. They report that the heat transfer enhancement factor increases with the distance between the tapes, that heat transfer enhancement as well as the friction factor increase as the number of tapes increase. The heat transfer enhancement is shown to increase in the range of 162% – 189% while the friction factor increases in the range 5.33 – 7.02 times compared to a plain tube.

According to the literature review above, several studies have been done on the use of typical twisted tapes, modified twisted tapes and twisted tapes combined with other enhancement techniques for heat transfer enhancement and these studies have reported useful information on heat transfer enhancement, fluid friction and enhancement efficiencies. Low twist ratios

are desirable for better heat transfer enhancement, but the pressure drop also increases as the twist ratio decreases. Several modifications aimed at reducing the pressure drop have been studied, but most of these modifications also reduce the heat transfer enhancement. Similarly, the use of compound enhancement provides better heat transfer, but with greater fluid friction.

Heat transfer enhancement in core flow has shown potential for heat transfer enhancement with less fluid friction. Therefore, there appears to be potential for better heat transfer enhancement and less friction factors with smaller twist ratios and twisted tape inserts placed separately from the wall. This arrangement provides a means of increasing fluid agitation and mixing with a lower twist ratio, while ensuring reduced pressure drop by placing the tapes separately from the tube walls. This arrangement has not been widely investigated. Moreover, twisted tape inserts appear to be a better heat transfer enhancement technique for a parabolic trough receiver where the absorber tube walls are differentially heated in such a way that fluid mixing and agitation will help improve the heat transfer performance and reduce the absorber tube's circumferential temperature difference. The fluid mixing and longer helical path provided by twisted tape inserts with a low twist ratio are expected to significantly improve their heat transfer performance. Moreover, reduced absorber tube temperatures will further improve the performance of the receiver by reducing the radiation heat loss between the absorber tube and the glass cover. The reason is that the emissivity of the coating increases with the temperature of the absorber tube, and the radiation heat loss increases with the temperature of the absorber tube.

Moreover, it is known that for high heat fluxes and high temperatures in solar collectors, heat transfer irreversibilities increase causing an increase in the entropy generation rates [16,199]. This is why entropy generation analysis is necessary for concentrating solar collector systems used for high temperature applications. Most of the studies reported in the literature on heat transfer enhancement rely on the first law of thermodynamics. Studies on entropy generation analysis are limited. As discussed in Chapter 5, the efficient use of energy is crucial to the performance of thermal systems. Therefore, an assessment of the quantity as well as the quality of the available energy becomes crucial. The determination of the quality of energy is only possible with the use of the second law of thermodynamics. Using the second law of

thermodynamics, the entropy generation rates as well the irreversibilities present in the systems and system components can be determined.

The present work investigates a low twist ratio and wall-detached twisted tape inserts for heat transfer enhancement in parabolic trough receivers. Using the second law of thermodynamics, the entropy generation rates due to the use of twisted tape inserts were investigated. With the further use of multi-objective optimisation, solutions were obtained for which the heat transfer is maximum and fluid friction minimum. To the best of the present authors' knowledge, this type of twisted tape arrangement has not been investigated for heat transfer enhancement in parabolic trough receivers. Moreover, no studies are reported in the literature on the use of the entropy generation minimisation method for the analysis of parabolic trough receivers with twisted tape inserts.

6.1 MODEL DESCRIPTION

This section briefly describes the model of a parabolic trough receiver whose absorber tube is fitted with twisted tape inserts.

6.1.1 PHYSICAL MODEL AND COMPUTATIONAL DOMAIN

Figure 6.1 shows the physical model of a parabolic trough receiver with a twisted tape insert placed separately from the wall. For conventional receivers, the annulus space between the absorber tube and glass cover is evacuated to very low pressures so that only radiation heat transfer takes place. In the annulus space, only the absorber tube temperature and the emissivity of the selective coating influence the radiation heat transfer. Therefore, the physical model discussed here is for the absorber tube only. The physical model for the entire receiver is discussed in earlier chapters. In addition, the flow is periodically fully developed far from the entrance region. Therefore, periodic boundary conditions are used at the absorber tube's inlet and outlet. For the periodic module considered, Fig. 6.2 shows the computational domain for the absorber tube used in this study.

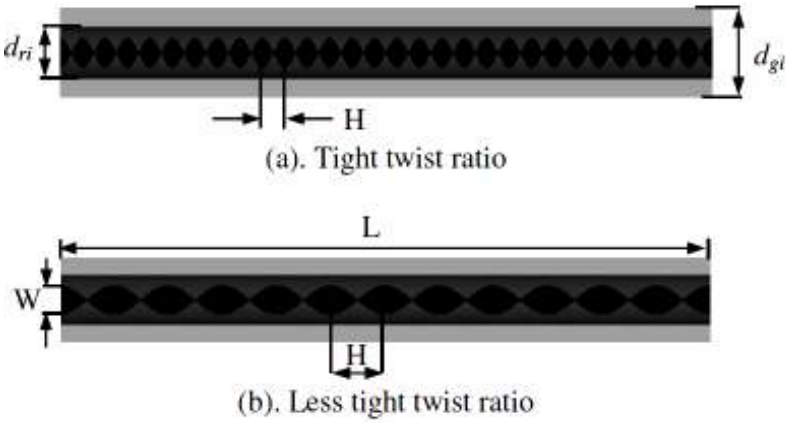

Fig. 6.1: Schematic diagram of the parabolic trough receiver physical model: (a) with very tight twist ratio and (b) with less tight twist ratio.

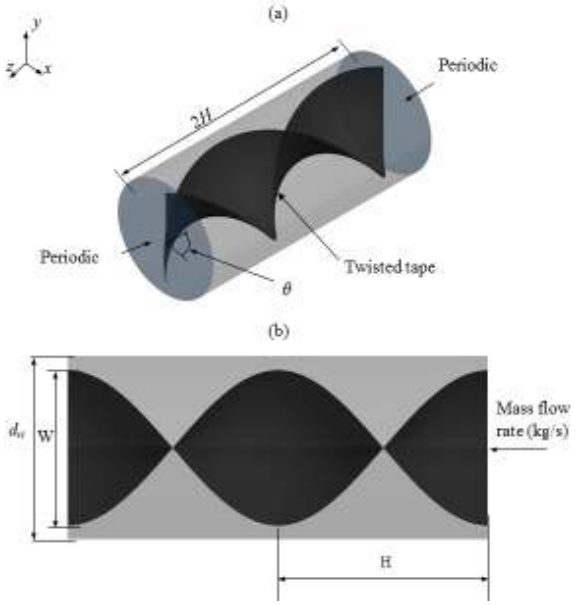

Fig. 6.2: Schematic diagram of the periodic computational domain of the receiver's absorber tube with a twisted tape insert: (a) lateral view and (b) longitudinal view.

The twist ratio is defined as the ratio of the pitch through the 180^{o} turn, H and the diameter of the receiver's absorber tube as

$$\tilde{y} = \frac{H}{d_{ri}} \qquad 6.1$$

The dimensionless twisted tape width ratio $\tilde{w}$, defines the clearance between the twisted tape and the absorber tube's wall. For zero clearance between the tube and the twisted tape, $\tilde{w} = 1$.

$$\tilde{w} = \frac{W}{d_{ri}} \tag{6.2}$$

The size of the receiver and absorber tube is determined through an optical analysis of the entire parabolic trough collector system. In this study, a commercially available receiver was used where the diameter of the absorber tube was fixed at 6.6 cm. The geometrical parameter, optical parameters and other simulation parameters used in this study are shown in Table 6.1. The other receiver and environmental parameters given in Table 4.1 apply.

Table 6.1: Simulation parameters for a receiver with twisted tape inserts

Parameter	**Value**	
Absorber tube diameter (m)	0.066	[40,45]
Absorber tube thickness (m)	0.002	[40,45]
Inlet temperature (K)	400, 500, 600	
Reynolds number	$1.02 \times 10^4 - 1.36 \times 10^6$	
Pitch, $\tilde{y}$	0.50 - 2.00	
Width ratio, $\tilde{w}$	0.53 - 0.91	
Tape width (m)	0.0005	
Direct normal solar irradiance (W/m^2)	1 000	
Glass cover transmissivity,τ_g	0.97	
Geometrical concentration ratio, C_R	86	
Absorber tube absorptivity, α_{abs}	0.96	

6.1.2 GOVERNING EQUATIONS

For the high heat fluxes and high temperatures achievable at high concentration ratios in parabolic trough receivers, high heat transfer fluid mass flow rates are essential and the flow in the absorber tube is in the turbulent regime. In this study, the assumption of steady-state flow conditions was made. Accordingly, the Reynolds Averaged Navier-Stokes equations (RANS) given by Eqs. (3.2) – (3.4) and detailed in Section 3.3.1 of Chapter 3 are applicable.

For turbulence closure, the realisable k-ε is used. As discussed in Chapter 3, this model is an improvement of the standard k-ε with superior performance for separated flows and flows with complex secondary features. The model solves two additional equations for turbulent kinetic energy (Eq. 3.7) and turbulent dissipation rate (Eq. 3.8) as detailed in Chapter 3, Section 3.31 of this thesis.

6.1.3 BOUNDARY CONDITIONS

As described in Chapter 4, model A of the receiver was used in this study with the inlet and outlet replaced by periodic boundary conditions. Therefore, the boundary conditions used include periodic boundary conditions at the inlet and outlet, non-uniform heat flux at a rim angle of 80 and a concentration ratio of 86 as given in Fig. 4.11 (a). In Fig. 4.11 (a), the heat flux is presented for half the circumference of the absorber tube. Since the heat flux distribution is symmetrical, the heat flux profile of the other half of the absorber tube has the same distribution.

6.1.4 SOLUTION PROCEDURE

The numerical solution was implemented in a commercial software package ANSYS® 14 and 14.5. The geometry was built in the ANSYS design modeller and the computational grid created in ANSYS meshing. The numerical solution was obtained in ANSYS FLUENT, which uses a finite volume method for solving the governing continuity, momentum, energy and k-ε model equations. The SIMPLE algorithm was used for coupling the pressure and velocity. Second-order upwind schemes were employed for integrating the governing equations together with the boundary conditions over the computational domain.

A structured mesh was used in this study. Even though generating the mesh was tedious, it significantly reduced the number of required mesh elements compared to a tetrahedron mesh. Figure 6.3 shows the sample mesh used in this study.

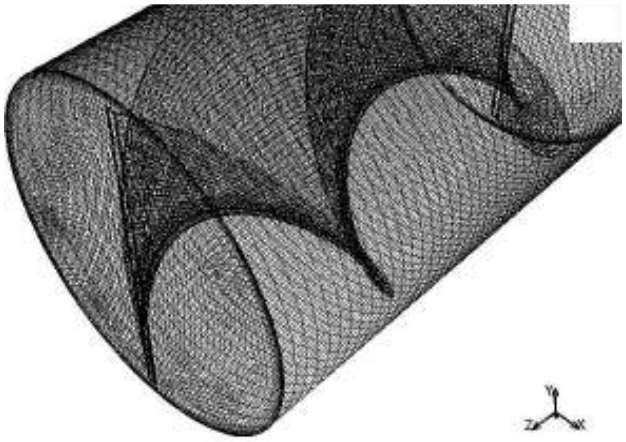

(a) Lateral view

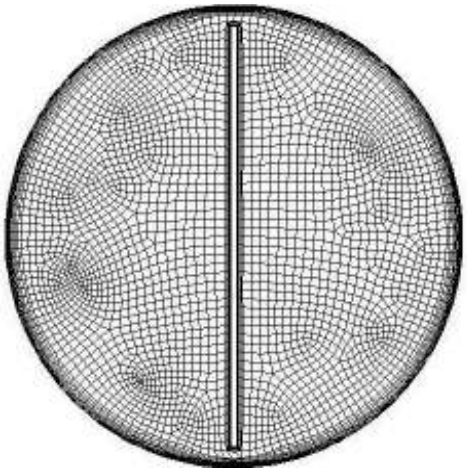

(b) Front view – periodic boundaries

Fig. 6.3: Discretised domain of the absorber tube for a receiver with a twisted tape insert.

Grid dependence studies for several refinements of the mesh were carried out with the volume integral entropy generation, Nusselt number and fluid friction as the monitored quantities for representative cases. The number of mesh elements depends on the twist ratio and the width ratio of the twisted tape used. Table 6.2 shows the grid dependence tests in some cases. Given the need to capture a high resolution of gradients near the wall, the enhanced wall treatment was used, with $y^+ \approx 1$ in the absorber tube's wall normal direction ensured in all simulations.

Table 6.2: Mesh dependence tests for a parabolic trough receiver with twisted tape inserts

Mesh elements	f	Nu	S'_{gen}	$\left\|\frac{f^{i+1}-f^{i}}{f^{i+1}}\right\|$	$\left\|\frac{Nu^{i+1}-Nu^{i}}{Nu^{i+1}}\right\|$	$\left\|\frac{S_{gen}{}^{i+1}-S_{gen}{}^{i}}{S_{gen}{}^{i+1}}\right\|$
	$\tilde{y}=0.5$ and $\tilde{w}=0.91$, $Re_p = 1.02 \times 10^4$, $T_{inlet} = 400$ K					
75 761	0.3214	307	2.322	-	-	
122 302	0.3213	315	2.243	0.000	0.028	0.040
204 723	0.3213	318	2.245	0.000	0.009	0.002
	$\tilde{y}=0.5$ and $\tilde{w}=0.91$, $Re_p = 1.42 \times 10^5$, $T_{inlet} = 500$ K					
82 500	0.1660	6853	2.350	-	-	
156 024	0.1644	6882	2.397	0.001	0.004	0.02
268 916	0.1639	6900	2.406	0.003	0.003	0.004

Convergence was obtained when the scaled residuals of mass, momentum, turbulent kinetic energy and turbulence dissipation rate were less than 10^{-4} while the energy residuals were less than 10^{-7}. Convergence was also monitored using the convergence history of volume - averaged entropy generation in the absorber tube. The solution was considered converged when the volume-averaged entropy generation remained constant for more than 200 successive iterations.

Syltherm 800 [110] was used as the absorber tube's heat transfer fluid. Given the limitations of the periodic model, the properties of the heat transfer fluid were evaluated at the bulk temperatures of 400, 500 and 600 K at all Reynolds number simulations. Therefore, the properties used were specific heat capacity (c_p) of 1791 J/kg K, density (ρ) of 840 kg/m^3, thermal conductivity (λ) of 0.115 W/m K and viscosity (μ) of 0.00216 Pa.s as determined from the manufacturer's specifications for a temperature of 400 K. At other temperatures, the properties used are presented in Tables 4.2 and 5.2 [110]. Stainless steel was used as the absorber tube material; the emissivity of the absorber tube coating is temperature depended as given by Eq. (2.33), and the thermal conductivity depends on temperature as given by Eq. (2.25).

6.1.5 DATA REDUCTION

The heat transfer performance is given in terms of the heat transfer coefficient and Nusselt numbers. The average heat transfer coefficient is given by

$$h = \frac{q''}{T_{ri} - T_b} \tag{6.3}$$

where T_{ri} is the inner wall temperature of the absorber tube and T_b represents the bulk temperature of the fluid at the periodic boundaries. From the average heat transfer coefficient, the average Nusselt number is given by

$$Nu = h\frac{d_{ri}}{\lambda} \tag{6.4}$$

where λ is the thermal conductivity of the heat transfer fluid and d_{ri} is the inner diameter of the absorber tube.

The friction factor is related to the pressure drop according to

$$f = \frac{\Delta P}{\frac{1}{2}\rho \cdot u_m^2 \frac{L}{d_{ri}}} \tag{6.5}$$

where ΔP is the pressure drop, ρ is the density of the heat transfer fluid, u_m is the mean velocity of flow inside the absorber tube, L is the length of the periodic module and d_{ri} is the inner diameter of the absorber tube.

For the preliminary evaluation of heat transfer enhancement techniques at constant pumping power, the thermal enhancement factor [200] was used, according to this:

$$\left(\dot{V}\Delta P\right)_p = \left(\dot{V}\Delta P\right)_{en} \tag{6.6}$$

Expressing $\dot{V}$ and ΔP in terms of friction factors and Reynolds numbers Eq. (6.6) becomes

$$\left(f\,\mathrm{Re}^3\right)_p = \left(f\,\mathrm{Re}^3\right)_{en} \tag{6.7}$$

The thermal performance factor χ for the absorber tube fitted with twisted tape inserts for constant pumping power comparison is given as

$$\chi = \left.\frac{Nu_{en}}{Nu_p}\right|_{pp} = \left(\frac{Nu_{en}}{Nu_p}\right)\left(\frac{f_p}{f_{en}}\right)^{1/3} \qquad 6.8$$

Where Nu_{en} is the Nusselt number for an enhanced absorber tube, Nu_p is the Nusselt number for the plain absorber tube, f_{en} is the friction factor for an enhanced absorber tube and f_p is the friction factor for a plain absorber tube.

Another evaluation criterion for heat transfer enhancement is based on the second law of thermodynamics [61,201,202]. The rates of entropy generation in an enhanced tube are compared with those of plain tubes. The enhancement entropy generation number $N_{s,en}$ was used in this work. It is defined as [202]

$$N_{s,en} = \frac{(S_{gen})_{en}}{(s_{gen})_p} \qquad 6.9$$

Enhancement techniques with $N_{s,en} < 1$ are taken to be thermodynamically advantageous [202]. In addition to enhancing heat transfer, such techniques also reduce the irreversibilities in the heat transfer component. In this study, the entropy generation rates were determined using the direct method [131] according to Eqs. (3.35 -3.41) discussed in Chapter 3, Section 3.4.1.

Overall system performance is another important factor to consider when evaluating the performance of parabolic trough systems used for electricity generation. With heat transfer enhancement, it is expected that the heat transfer performance will increase but with increasing fluid friction. Using the overall collector performance as an evaluation tool helps determine the performance characteristics at which the gain in performance is higher than the increase in pumping power.

To investigate the actual collector thermal performance, the actual gain in collector performance due to heat transfer enhancement should be compared with the corresponding increase in pumping power. Collector performance can be characterised in terms of the collector's thermal efficiency, which is a function of the heat transfer rate, pumping power and incident solar radiation as

$$\eta_{th} = \frac{\dot{Q}_u - \dot{W}_p}{A_a I_b} \tag{6.10}$$

In Eq. (6.10), $\dot{Q}_u = \dot{m} c_p (T_{outlet} - T_{inlet})$ is the heat transfer rate; $\dot{W}_p = \dot{V} \Delta P$ is the pumping power; A_a is the collector's aperture area and I_b is the incident solar radiation.

6.2 RESULTS AND DISCUSSION – HEAT TRANSFER AND FLUID FLOW

6.2.1 MODEL VALIDATION

For the analysis using computational fluid dynamics, the validation of the obtained numerical results is fundamental to their acceptance. Therefore, comparing the numerical results with the experimental results is essential for determining the accuracy of the numerical model developed. Chapter 4 explains the validation of the heat transfer and friction factors for the plain absorber tube and Chapter 5 explains the validation of the entropy generation model. For the absorber tube fitted with twisted tape inserts, the present model was validated by using the experimental data of Manglik and Bergles [203]. The comparison shows good agreement of the present work with the experimental data for heat transfer performance as shown in Fig. 6.4 for Nusselt numbers. The Nusselt numbers from this study are within ± 6.5% of those in the experimental data. The friction factor has also been shown to be in good agreement with the experimental data as seen in Fig.6.5. The friction factors obtained are within ± 8% of those in the experimental data.

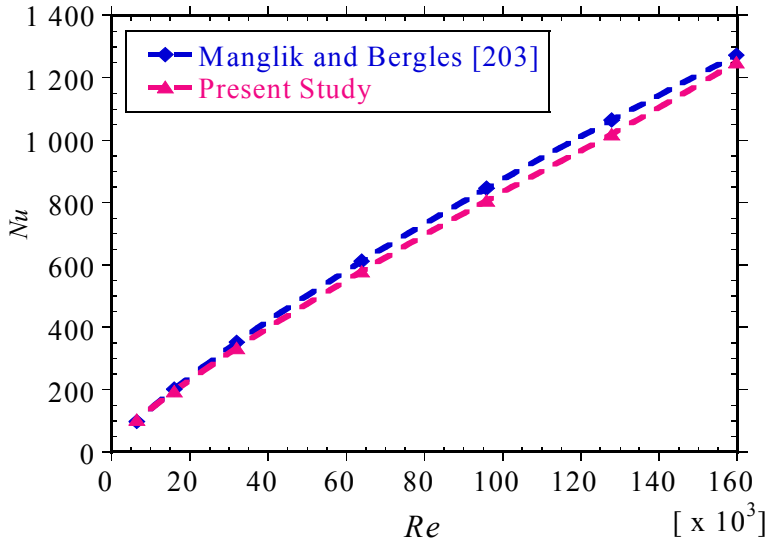

Fig. 6.4: Comparison of present study heat transfer performance for a tube with a twisted tape insert as a function of Reynolds number with Manglik and Bergles correlation [203]

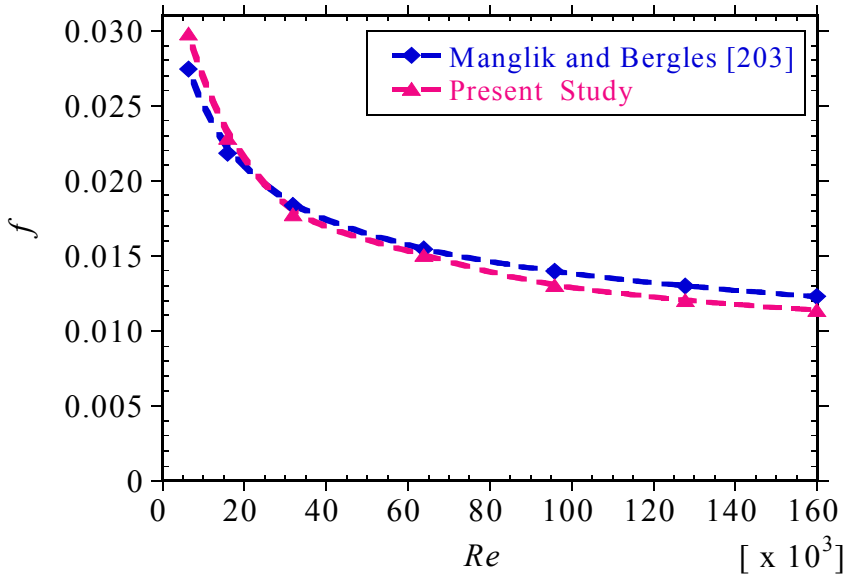

Fig. 6.5: Comparison of present study friction factor for a tube with a twisted tape insert as a function of Reynolds number with Manglik and Bergles correlation [203]

6.2.2 HEAT TRANSFER PERFORMANCE

The heat transfer performance of a tube with twisted tape inserts is dependent on the twist ratio, the twisted tape width to tube diameter ratio and the Reynolds number.

Figure 6.6 (a – c) shows the variation of Nusselt numbers with Reynolds numbers at different twist ratios.

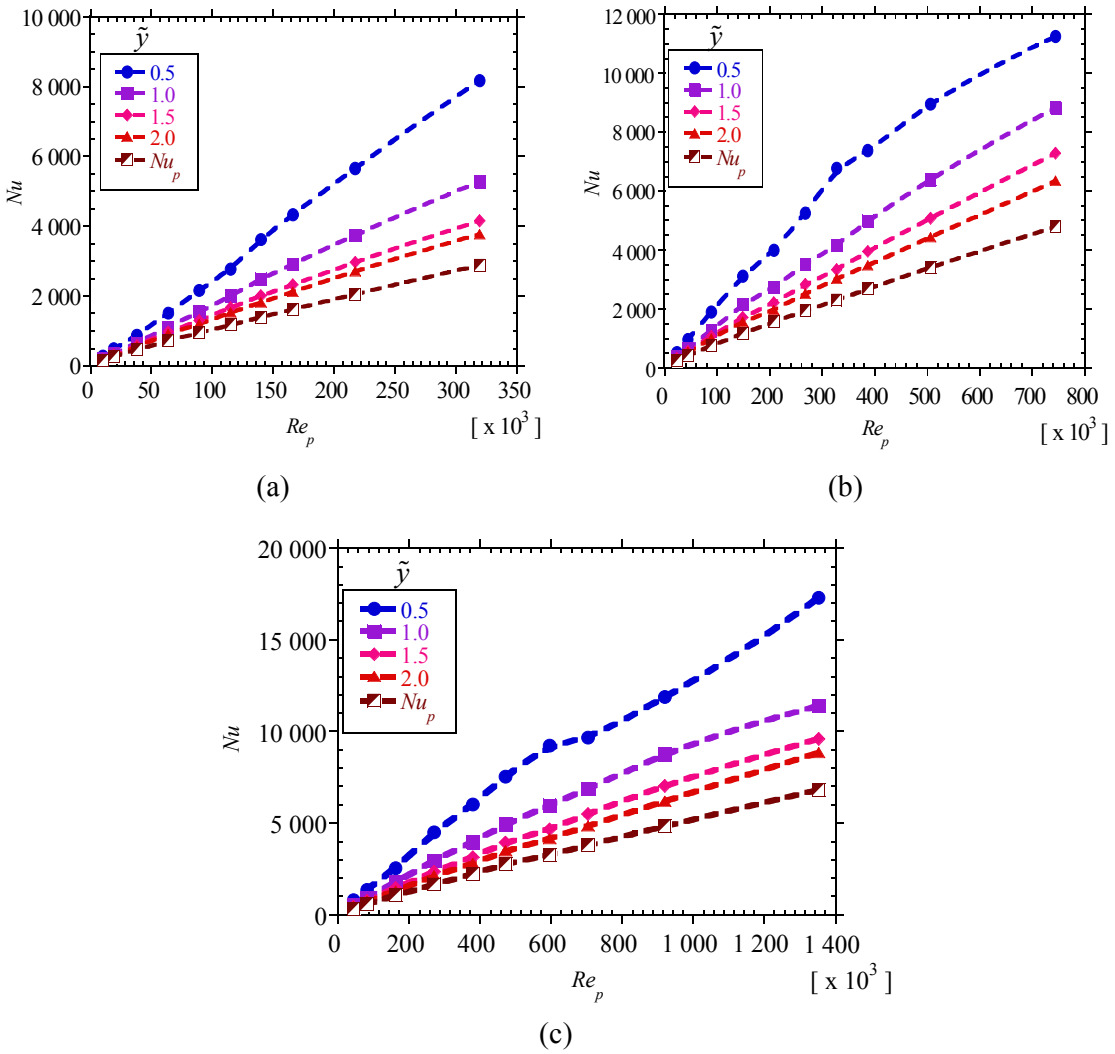

Fig. 6.6: Heat transfer performance in a receiver with twisted tape inserts as a function of Reynolds number and twist ratio ($\tilde{y}$): (a) width ratio ($\tilde{w}$) of 0.76 and inlet temperature of 400 K, (b) $\tilde{w}$ = 0.91 and inlet temperature of 500 K and (c) $\tilde{w}$ = 0.91 and inlet temperature of 600 K.

All the figures show an increase in the Nusselt number with increasing Reynolds numbers and decreasing twist ratios. As the clearance ratio reduces (higher values of $\tilde{w}$) there is an increase in the Nusselt number. For a given value of Reynolds number and twist ratio, the

Nusselt number increases as $\tilde{w}$ increases. Smaller twist ratios mean an increased helical length that the fluid must cover within a unit length of the absorber tube, therefore, increased fluid mixing and turbulent intensity, which result in improved heat transfer. Appendix A shows the flow field and temperature contours for the twisted tape model. The helical path is shown by the streamlines in A.1 and A.2.

Figure 6.7 (a and b) shows clearly the variation of the Nusselt number with width ratio at given Reynolds numbers at the same flow rate (19 m^3/h) for fluid temperatures of 400 K and 600 K respectively. As shown, the Nusselt number increases as the width ratio increases. An increase in the width ratio reduces the tube-tape clearance and tends to partition the absorber tube into two halves, allowing for higher fluid acceleration in the absorber tube and therefore better heat transfer.

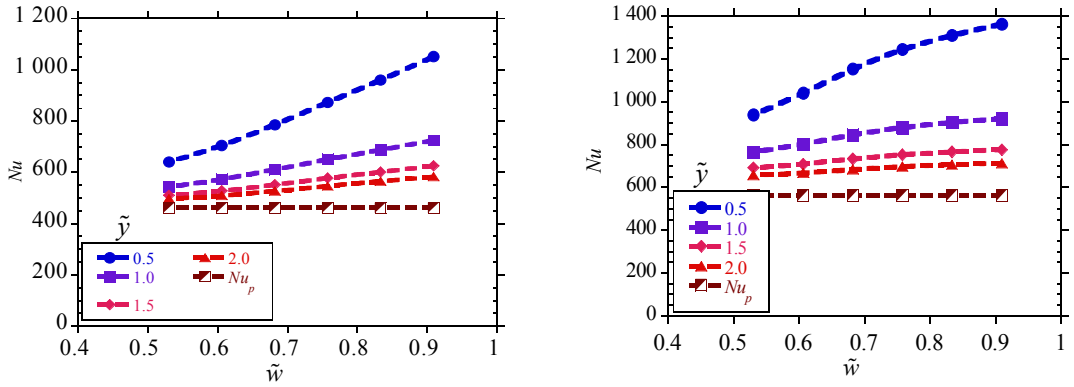

Fig. 6.7: Heat transfer performance in a receiver with twisted tape inserts as a function of width ratio ($\tilde{w}$) and twist ratio ($\tilde{y}$): (a) inlet temperature of 400 K and $Re_p = 3.84 \times 10^4$ and (b) inlet temperature of 600 K and $Re_p = 8.13 \times 10^4$.

A comparison between the heat transfer performances of an absorber tube with twisted tape inserts against a plain absorber tube is given by heat transfer enhancement factor, $Nu^+ = Nu/Nu_p$. Figure 6.8 (a and b) show the variation of Nu^+ with Reynolds numbers for different values of $\tilde{y}$ when $\tilde{w}$= 0.91 at 400 K and $\tilde{w}$=0.91 at 600 K respectively. The variation in the heat transfer performance factor depends mainly on the twist ratio and width ratio. It increases at low Reynolds numbers, and attains a more or less constant value at high

Reynolds numbers. At the different temperatures the heat transfer enhancement factors were shown to have the same trend with the Reynolds numbers. At a given Reynolds number, twist ratio and width ratio, the heat transfer enhancement factor is nearly the same for the different temperatures considered. Only a slight increase occurs as the temperatures increase. For a given width ratio and Reynolds number, higher values of heat transfer enhancement are shown to exist at the lowest twist ratio. Tight twist ratios ensure effective mixing and a longer path of the heat transfer fluid in the absorber tube, therefore improved heat transfer. Depending on the Reynolds number, twist ratio, width ratio and fluid temperature, the Nusselt numbers increased between 1.05 – 2.69 times compared with a plain tube.

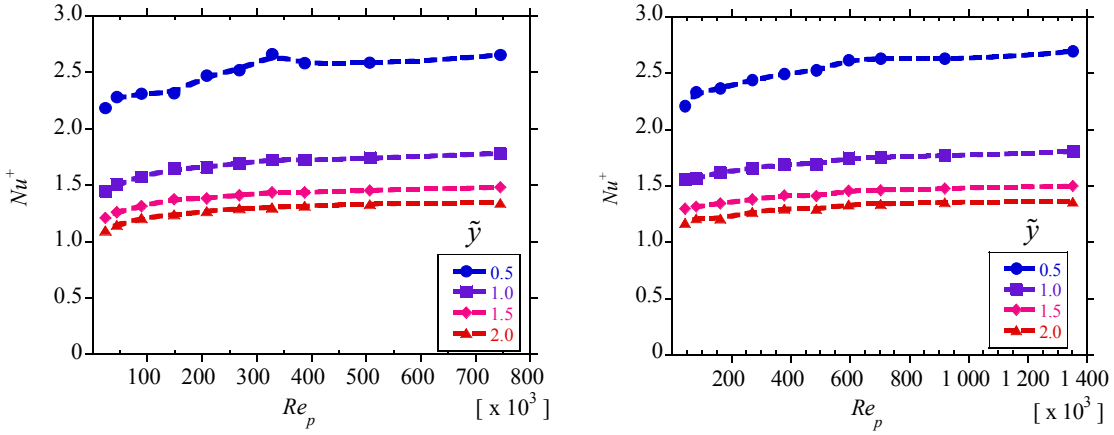

Fig. 6.8: Heat transfer enhancement factors for a receiver with twisted tape inserts as a function of Reynolds number and twist ratio ($\tilde{y}$): (a) inlet temperature of 400 K and width ratio ($\tilde{w}$) of 0.91 and (b) inlet temperature of 600 K and $\tilde{w}$ = 0.91.

6.2.3 FRICTION FACTORS

The use of twisted tape inserts causes an increase in the pumping power requirements compared to plain absorber tubes. Figure 6.9 (a – c) shows the variation of friction factors with Reynolds numbers and twist ratios at width ratios $\tilde{w}$ = 0.76 and 0.83 for a temperature of 400 K and $\tilde{w}$ = 0.91 for a temperature of 600 K. As expected, the friction factor is shown to reduce as the Reynolds numbers increase. The figures also show that the friction factor increases as the width ratio increases and as the twist ratio reduces. This is due to an increase

in flow resistance because of swirl flow, impingement on the absorber tube as well as the obstruction to flow from the twisted tape. The friction factor is shown to be significantly higher at the lowest twist ratio. This is probably due to the high chaotic mixing likely at low twist ratios and the possible fluid impingement on the twisted tape as well as the tube walls. The friction factor used here depends on the actual velocity inside the enhanced tube. This is lower than the friction factor, based on the velocity of a comparable plain absorber tube.

The pressure drop penalty factor, (f/f_p) gives a comparison of the increment in pressure drop due to the use of enhancement devices. Figure 6.10 (a and b) shows the variation of the pressure drop penalty factor with Reynolds number. As shown in the figure, the pressure drop penalty factor has a nearly constant variation with Reynolds number. The pressure drop penalty factor depends mainly on the twist ratio and width ratio of the twisted tape. For the range of parameters considered, the pressure drop increases 1.6 – 14.5 times compared with a plain receiver.

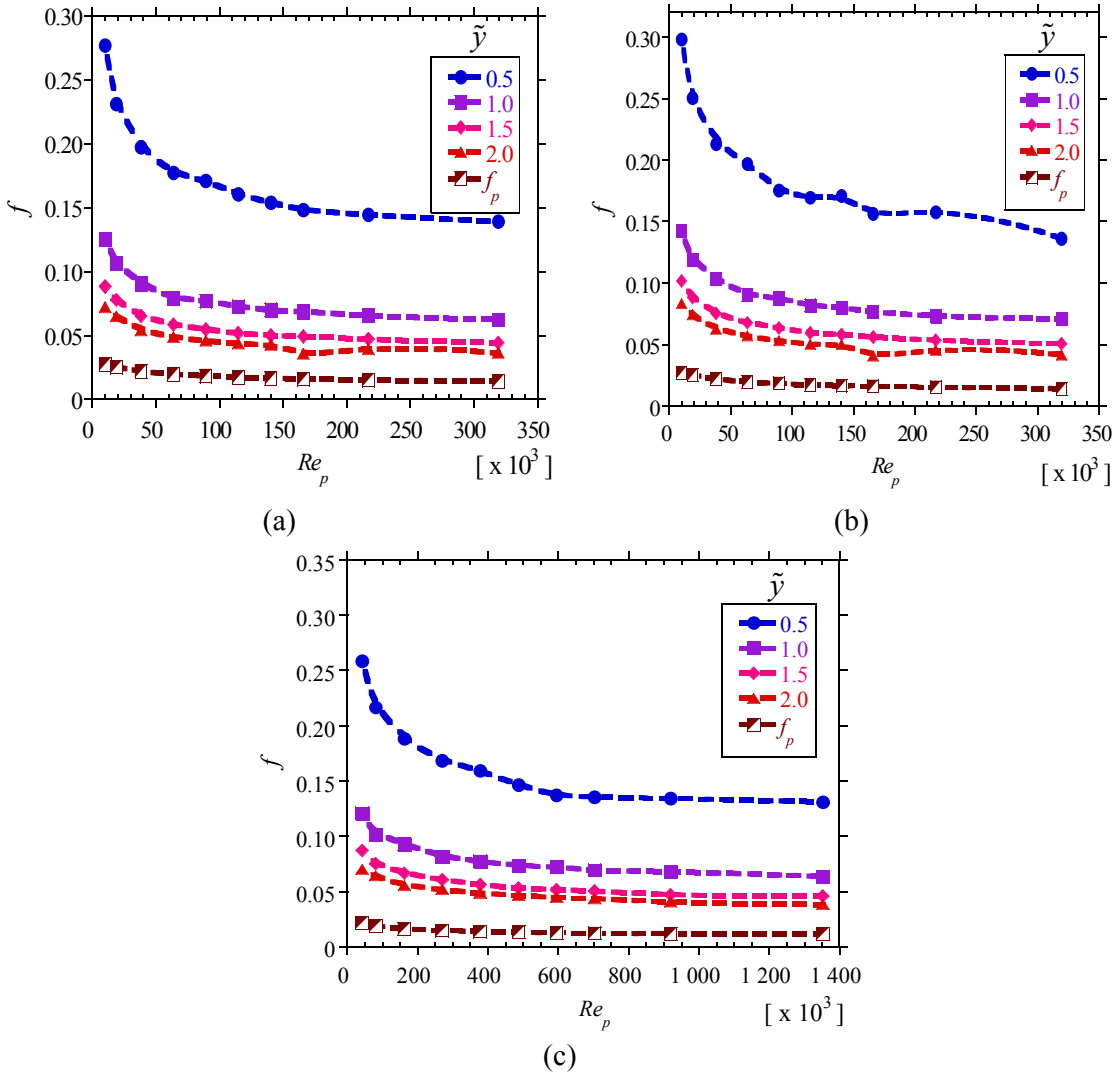

Fig. 6.9: Friction factor in a receiver with twisted tape inserts as a function of Reynolds number and twist ratio ($\tilde{y}$): (a) inlet temperature of 400 K and width ratio ($\tilde{w}$) of 0.76, (b) inlet temperature of 400 K and $\tilde{w}$ = 0.83 and (c) inlet temperature of 600 K and $\tilde{w}$ = 0.91.

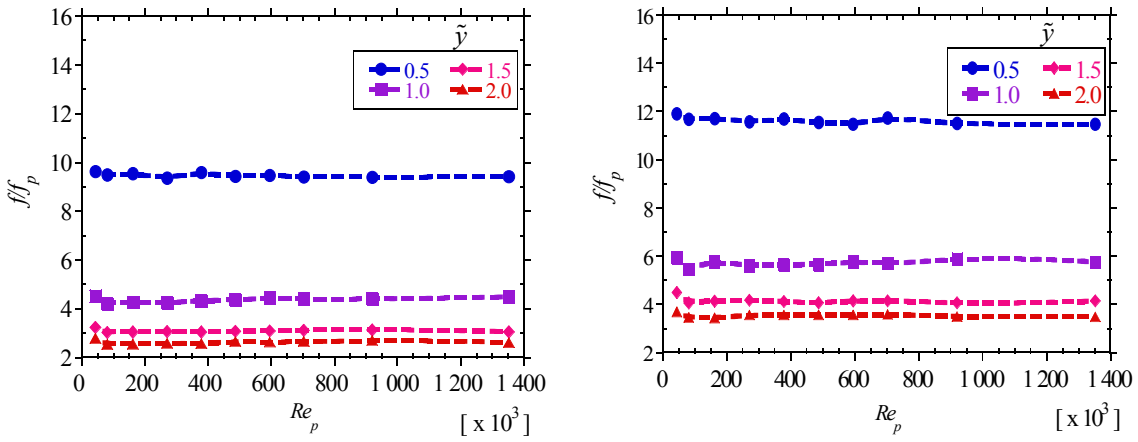

Fig. 6.10: Pressure drop penalty factor as a function of Reynolds number and twist ratio ($\tilde{y}$) for an inlet temperature of 600 K: (a) width ratio ($\tilde{w}$) of 0.76 and (b) $\tilde{w}$ = 0.91.

6.2.4 PERFORMANCE EVALUATION

As a preliminary measure of the thermal performance of heat transfer enhancement techniques, Webb [200] developed a performance evaluation criterion based on a constant pumping comparison. For constant power comparison, the thermal enhancement factor given by Eq. (6.8) should be greater than 1.0, if the heat transfer enhancement technique is to be considered better.

The variation of the thermal enhancement factor with Reynolds number for different values of twist ratios is given in Fig. 6.11 (a – c) for $\tilde{w}$= 0.91 at temperatures 500 K and 600 K and $\tilde{w}$ = 0.76 at 500 K respectively. Generally, the variation is the same as that shown by the heat transfer enhancement factor. The thermal enhancement factor increases with the Reynolds number and attains a nearly constant value at high values of Reynolds numbers at each temperature considered. At low width ratios, the variation of the thermal enhancement factor with twist ratio is not as much when considered with that at high twist ratios. The thermal enhancement factor is shown to increase as the width ratio increases because of the better heat transfer rates at higher width ratios.

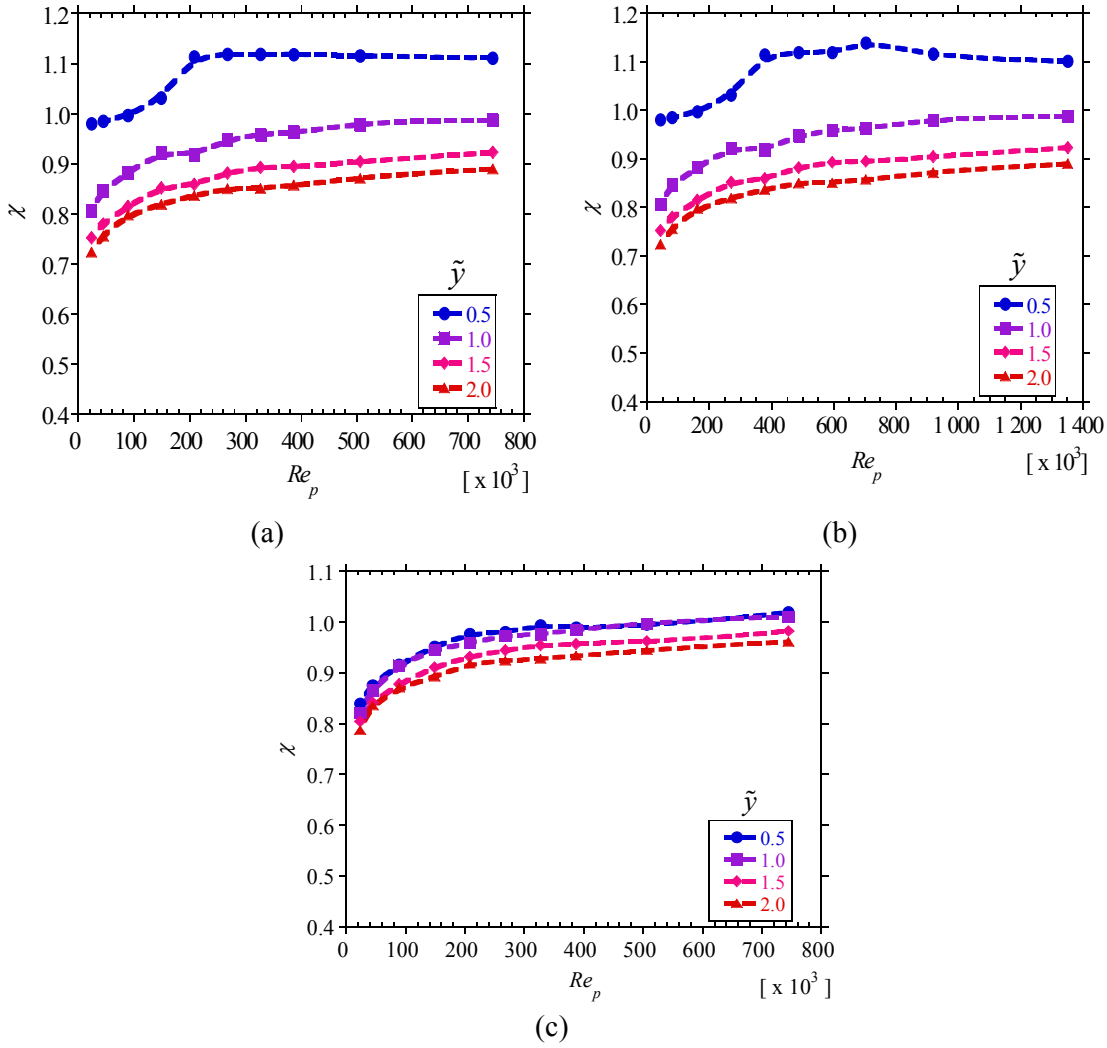

Fig. 6.11: Thermal enhancement factor as a function of Reynolds number and twist ratio ($\tilde{y}$): (a) inlet temperature of 500 K and width ratio ($\tilde{w}$) of 0.91, (b) inlet temperature of 600 K and $\tilde{w}$ = 0.91 and (c) inlet temperature of 500 K and $\tilde{w}$ = 0.76.

The thermal enhancement factor was shown to depend largely on the twist ratio and width ratio of the twisted tape. For the range of parameters considered in this work, the thermal enhancement factor varied between 0.74 and 1.27.

As mentioned earlier, the thermal efficiency of the collector system should be evaluated to obtain the actual performance of the collector. Figure 6.12 (a) – (c) show the variation of the

thermal efficiency with Reynolds number at different values of twist ratios. In the figures, $(\eta_{th})_p$ is the thermal efficiency with an absorber tube having no twisted tape inserts.

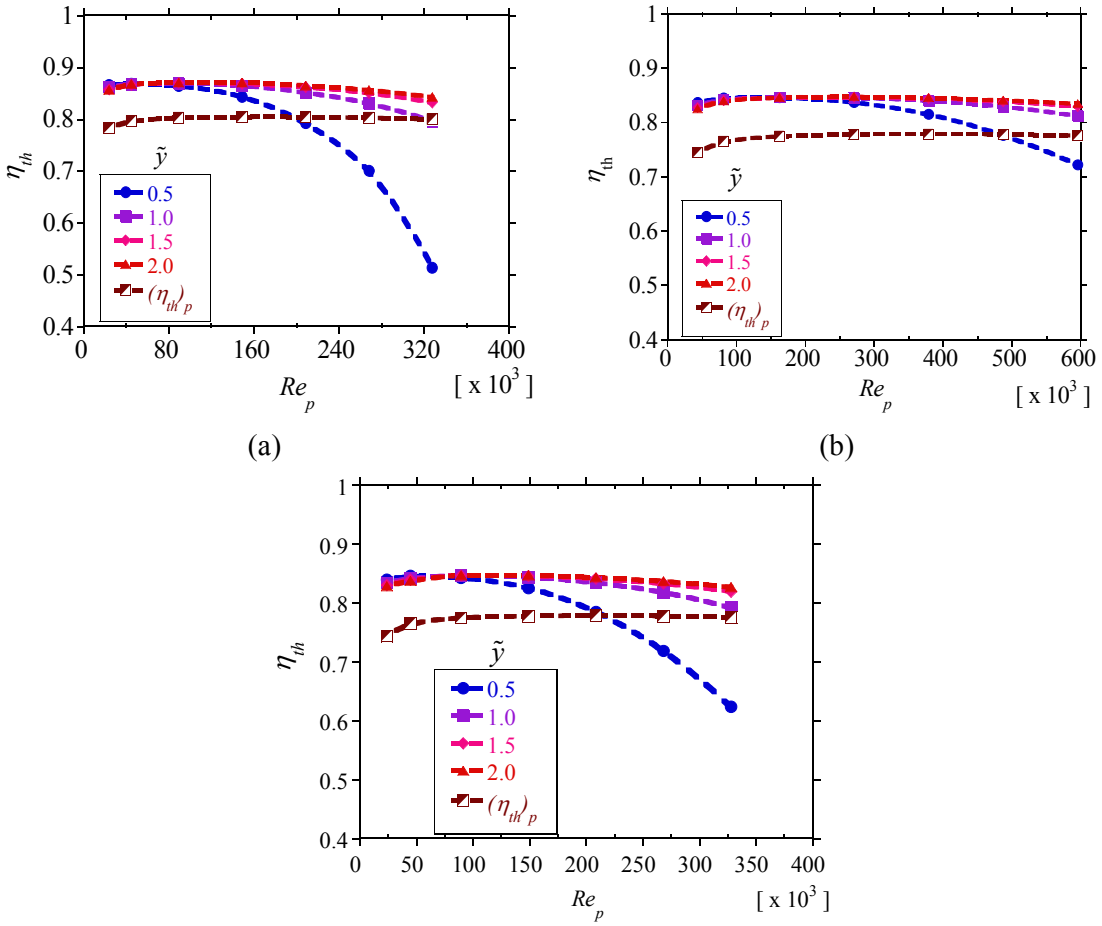

Fig. 6.12: Thermal efficiency as a function of Reynolds number and twist ratio ($\tilde{y}$): (a) inlet temperature of 400 K and width ratio ($\tilde{w}$) of 0.91, (b) inlet temperature of 600 K and $\tilde{w}$ = 0.76 and (c) inlet temperature of 500 K and $\tilde{w}$ = 0.91.

It can be observed from Fig. 6.12 (a – c) that the thermal efficiency of the collector increases with heat transfer enhancement for some range of Reynolds numbers at every value of twist ratio. Increases in efficiency in the range 5% – 10% are achievable for twist ratios $\tilde{y}$ greater than 1.0 for almost all width ratios provided that the flow rate is lower than 43 m^3/h. This flow rate corresponds to 10.05 kg/s at 400 K, 8.94 kg/s at 500 K, 7.65 kg/s at 600 K and

6.91 kg/s at 650 K. At twist ratios lower than 1, the efficiency will increase at low Reynolds numbers, but as the Reynolds numbers increase, the pumping power required will be higher than the gain in heat transfer rate, so the efficiency will become lower than one in a collector with a non-enhanced receiver. The highest increase in efficiency will be at the lowest Reynolds numbers, since it is at these low Reynolds numbers that the heat transfer performance is low and the absorber tube's temperatures are higher.

The increase in the efficiency of the collector is due to improved heat transfer performance and the associated reduction in absorber tube temperatures. Heat transfer enhancement will reduce the absorber tube's temperatures. As a result, the emissivity will also reduce since it varies with temperature. This will lead to reduced radiation heat loss. The thermal efficiency of a collector with a non-enhanced receiver tube is shown to increase with Reynolds numbers up to some values, after which it becomes constant. This is because at higher flow rates, the reduction in absorber tube temperatures is not significant as has been shown in the present study.

Performance evaluation using collector thermal efficiency showed that the efficiency of the collector could be significantly improved with the use of twisted tape inserts. This is probably because the evaluation based on a comparison of constant pumping power does not consider the reduction in the radiation heat loss due to heat transfer enhancement.

6.2.5 ABSORBER TUBE TEMPERATURE DIFFERENCE

The improved heat transfer performance in the receiver's absorber tube due to the use of twisted tape inserts reduces the absorber tube's circumferential temperature difference. Figures 6.13 (a –c) show the variation of absorber tube temperature gradients with Reynolds numbers at different values of twist ratios, width ratios and temperatures. In the figures, ϕ_p is the absorber tube's circumferential temperature difference for a receiver with no twisted tape inserts. Generally, the absorber tube's circumferential temperature difference decreases with a reducing twist ratio and Reynolds number at any given value of the width ratio.

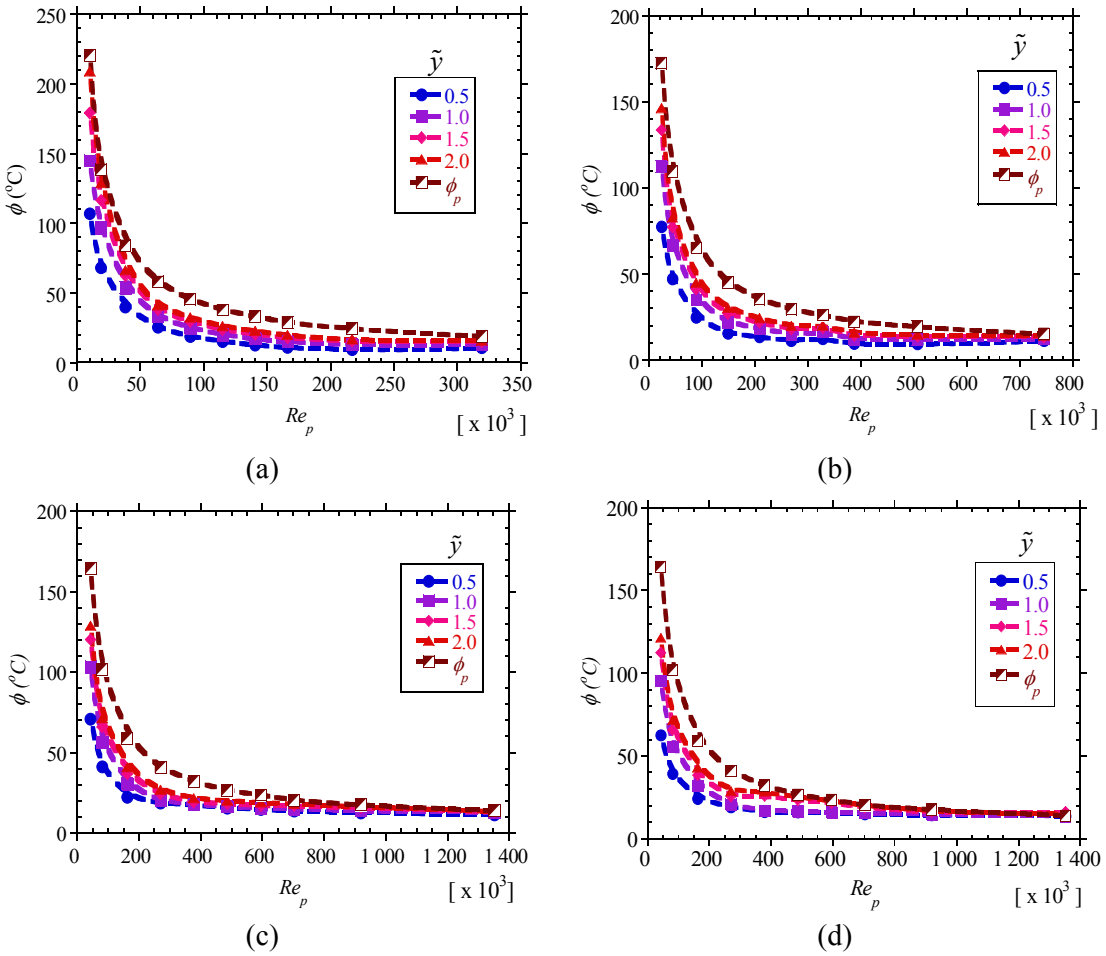

Fig. 6.13: Absorber tube circumferential temperature difference (ϕ) as a function of Reynolds number and twist ratio ($\tilde{y}$): (a) inlet temperature of 400 K and width ratio ($\tilde{w}$) of 0.76, (b) inlet temperature of 500 K and $\tilde{w}$ = 0.83, (c) inlet temperature of 600 K and $\tilde{w}$ = 0.76 and (d) inlet temperature of 600 K and $\tilde{w}$ = 0.91.

At a given Reynolds number, the absorber tube's circumferential temperature difference decreases as the twisted tape's width ratio increases. This is in line with the variation of the Nusselt number, as higher heat transfer performance leads to lower absorber tube's circumferential temperature differences. As the Reynolds numbers increase, the absorber tube's circumferential temperature difference reduces to small values. The absorber tube's circumferential temperature difference is shown to reduce between 4% – 68% for the range of

parameters considered. The greatest reduction in temperature difference occurs at lower flow rates.

6.2.6 EMPIRICAL CORRELATIONS FOR HEAT TRANSFER AND FRICTION FACTORS

Based on the results of the numerical simulations, empirical correlations for the Nusselt numbers were derived for the range of parameters studied. The correlations were derived by means of the curve-fitting method using regression analysis.

The Nusselt numbers are correlated by:

$$Nu = 0.01709 Re_p^{0.8933} \, \mathrm{Pr}^{0.3890} \, \tilde{y}^{-0.4802} \tilde{w}^{0.3881} \qquad 6.11$$

Valid for $1.02\times10^4 \le Re_p \le 1.35\times10^6$ and $10.7 \le Pr \le 33.7$

$400\ \mathrm{K} \le T \le 600\ \mathrm{K}$

$0.53 \le \tilde{w} \le 0.91$

$0.50 \le \tilde{y} \le 2.0$

The correlation in Eq. (6.11) is valid within ± 15% as shown in the parity plot for the observed Nusselt numbers and those predicted from the correlations in Fig. 6.14.

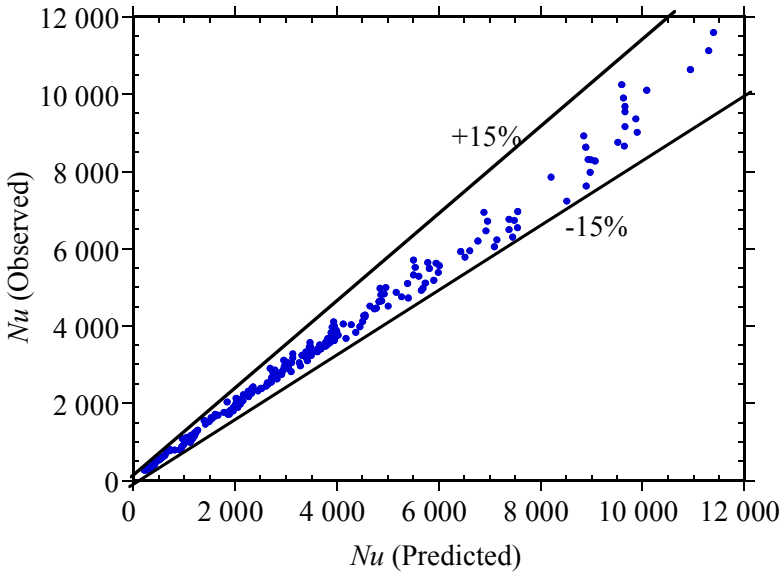

Fig. 6.14: Comparison of the predicted heat transfer performance with the observed heat transfer performance for a receiver with twisted tape inserts.

The friction factors are correlated by

$$f = 1.1289\tilde{y}^{-1.0917}\tilde{w}^{1.1802}Re_{en}^{-0.1923} \qquad 6.12$$

Valid for $1.02 \times 10^4 \leq \text{Re} \leq 1.35 \times 10^6$ and $10.7 \leq \text{Pr} \leq 33.7$

$400\ \text{K} \leq T \leq 600\ \text{K}$

$0.53 \leq \tilde{w} \leq 0.91$

$0.50 \leq \tilde{y} \leq 2.0$

Equation (6.12) predicts the friction factors within ± 16% for the entire range of Reynolds numbers. Figure 6.15 shows the parity plot for the friction factors.

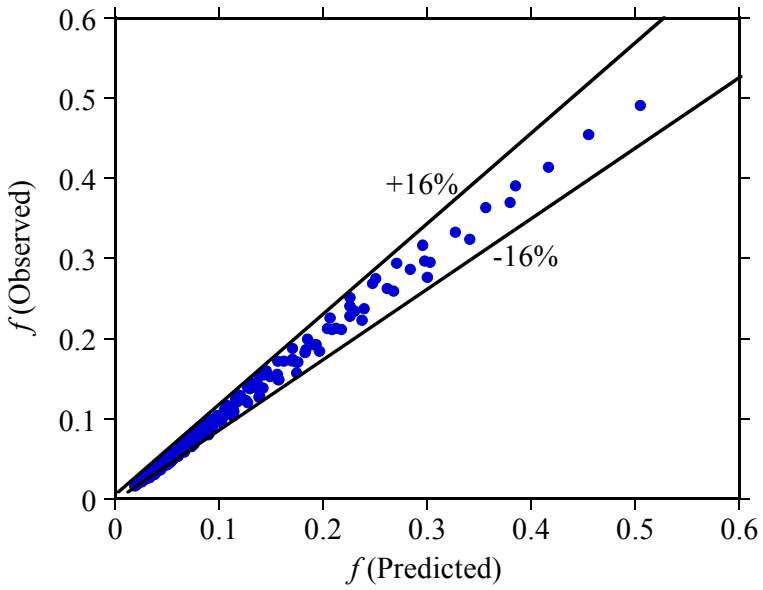

Fig. 6.15: Comparison of the predicted friction factor with the observed friction factor for a receiver with twisted tape inserts.

In Eq. (6.11) and Eq. (6.12), Re_p is the Reynolds number based on the mean velocity and inner diameter of a plain absorber tube. For the same mass flow rates, the use of twisted tape inserts increases the mean velocity in the tube, therefore Re_{en} is the Reynolds number based on the mean velocity in the absorber tube with twisted tape inserts and the inner diameter of the plain absorber tube.

The use of Eq. (6.12) requires knowledge of the actual mean velocity in the enhanced absorber tube to obtain Re_{en}. Then Re_{en} can be related to Re_p according to

$$Re_{en} = 1.9681\tilde{y}^{-0.4048}\tilde{w}^{0.6364}Re_p^{0.9818} \qquad 6.13$$

The friction factor, f and the correlation for f are based on the actual mean flow velocity. This gave the best curve fit compared to friction factors based on the mean velocity in a plain tube's mean velocity.

6.3 RESULTS AND DISCUSSION – ENTROPY GENERATION

Another way of assessing the performance of enhancement techniques is to consider the entropy generation rates as a result of applying the enhancement technique [61,202]. With this, the aim is to minimise the irreversibilities so that the most desirable technique or configuration has the lowest entropy generation rates. In heat transfer problems, two irreversibilities i.e. heat transfer irreversibility and fluid flow irreversibility, always compete with one another.

Regarding entropy analysis in heat transfer problems, the objective of heat transfer enhancement is to reduce these irreversibilities. As the heat transfer irreversibility reduces, the fluid flow irreversibility will increase. For this reason, the determination of entropy generation distribution is fundamental to establishing the conditions and configurations for which entropy generation is a minimum. This section presents the entropy generation rates due to the use of twisted tape inserts in parabolic trough receivers. Chapter 5 shows that the entropy generation rates reduce as the fluid inlet temperature increases, and increase as the concentration ratio increases. Equations (3.35) – (3.41) in Chapter 3 of this thesis were used to obtain the local entropy generation rates in the receiver's absorber tube.

6.3.1 ENTROPY GENERATION DISTRIBUTION

Figure 6.16 (a – c) shows the variation of entropy generation rates with Reynolds numbers at the lowest and greatest twist ratio for width ratios of 0.61, 0.76 and 0.91 respectively when the inlet temperature is 600 K. At every width ratio, the figures show that for a given twist

ratio, there is a Reynolds number for which the total entropy generation rate (S'_{gen}) is a minimum.

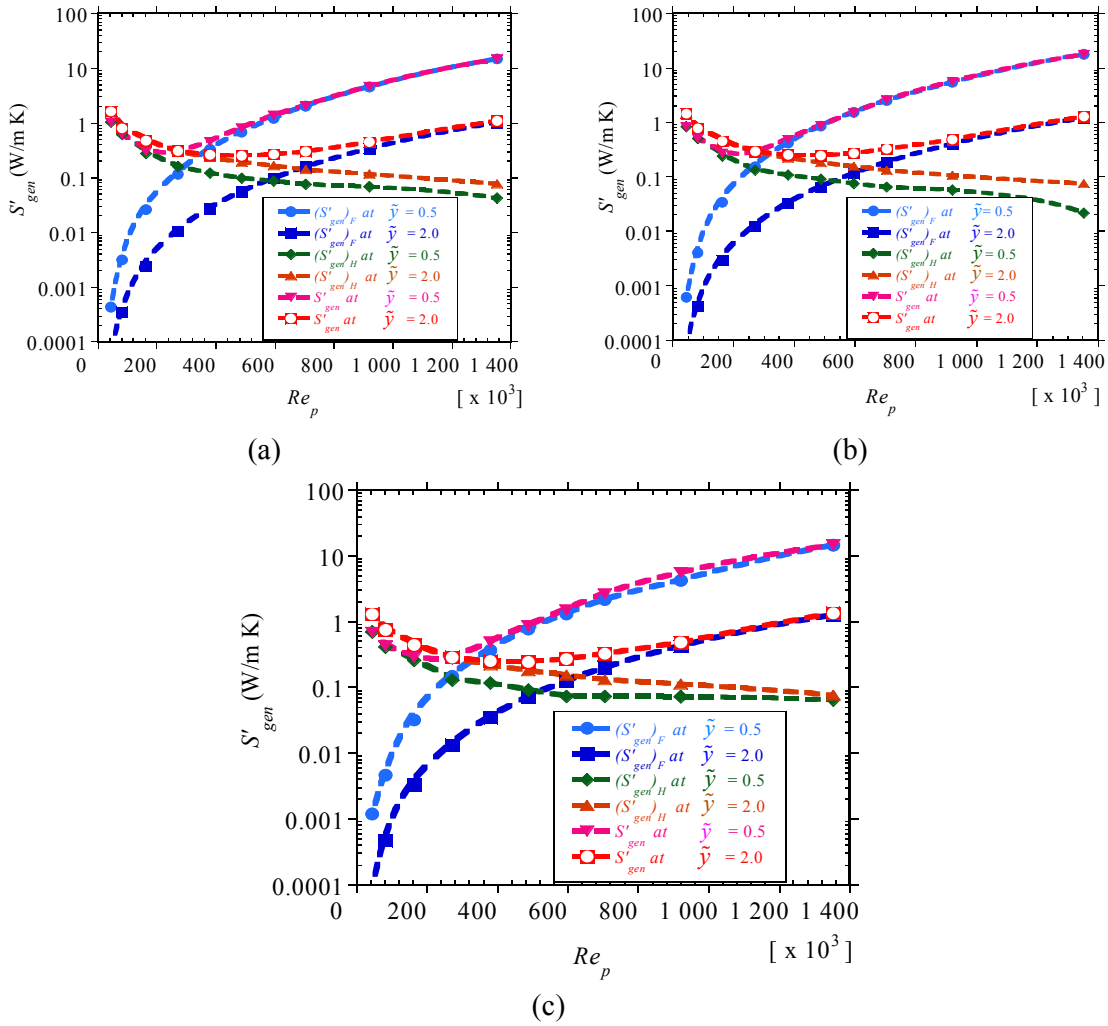

Fig. 6.16: Total entropy generation, entropy generation due to heat transfer irreversibility and entropy generation due to fluid friction irreversibility in the receiver's absorber tube as functions of Reynolds number and twist ratio ($\tilde{y}$) for an inlet temperature of 600 K: (a) width ratio ($\tilde{w}$) of 0.61, (b) $\tilde{w}$ = 0.76 and (c) $\tilde{w}$ = 0.91.

There is the same variation at the other inlet temperatures. The figures also show that the entropy generation due to heat transfer irreversibility decreases as the Reynolds numbers increase, while the entropy generation due to fluid flow irreversibility increases as the

Reynolds numbers increase. As the width ratio increases, the increasing fluid flow irreversibility leads to higher entropy generation rates while the heat transfer irreversibility decreases due to increased heat transfer performance. This causes a shift to the left in the optimal Reynolds number at each twist ratio as the width ratio increases. The variation of the two irreversibilities with the width ratio can be clearly seen in Fig. 6.17 (a – d).

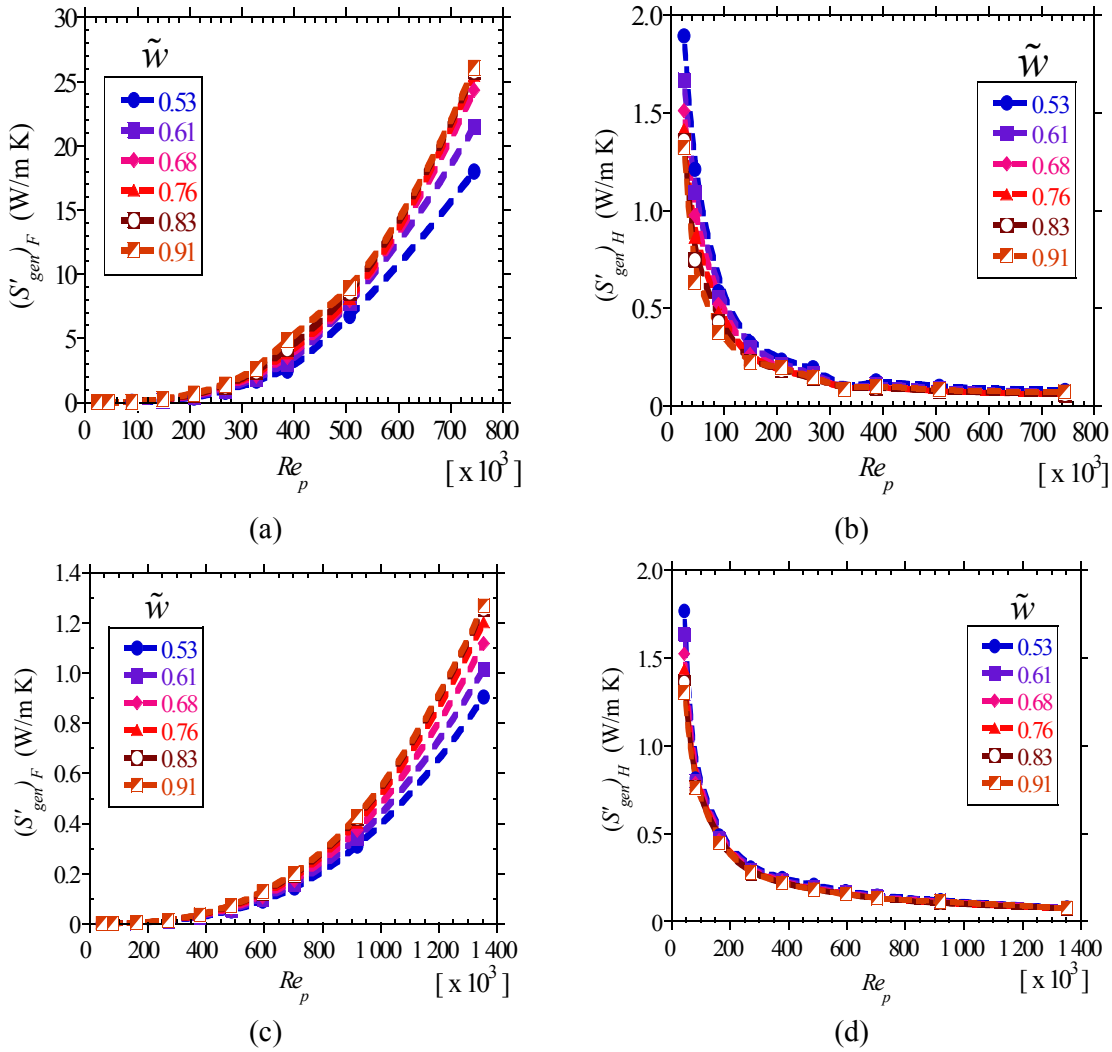

Fig. 6.17: Entropy generation due to heat transfer irreversibility $(S'_{gen})_H$ and entropy generation due to fluid friction irreversibility $(S'_{gen})_F$ in the receiver's absorber tube as functions of Reynolds number and width ratio ($\tilde{w}$): (a) $(S'_{gen})_F$ for an inlet temperature of 500 K and twist ratio ($\tilde{y}$) of 0.5, (b) $(S'_{gen})_H$ for an inlet temperature of 500 K and $\tilde{y}$ = 0.5, (c) $(S'_{gen})_F$ for an inlet temperature of 600 K and $\tilde{y}$ = 2.0 and (d) $(S'_{gen})_H$ for an inlet temperature of 600 K and $\tilde{y}$ = 2.0.

At a given twist ratio and fluid temperature, the fluid flow irreversibility increases as the width ratio and Reynolds number increase, while the heat transfer irreversibility reduces as the width ratio and Reynolds numbers increase.

Figure 6.18 (a – d) shows the variation of heat transfer and fluid flow irreversibilities with Reynolds numbers at different values of twist ratios.

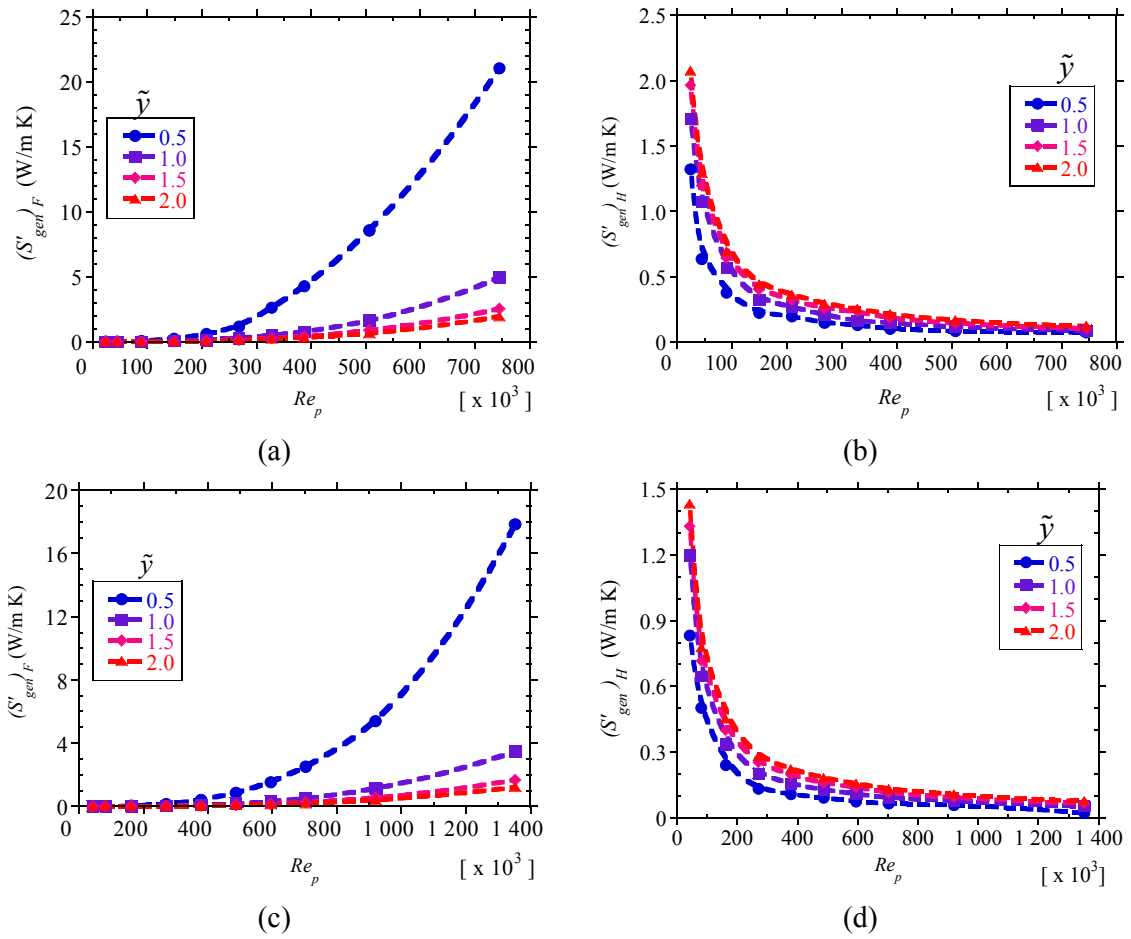

Fig. 6.18: Entropy generation due to heat transfer irreversibility $(S'_{gen})_H$ and entropy generation due to fluid friction irreversibility $(S'_{gen})_F$ in the receiver's absorber tube as functions of Reynolds number and twist ratio ($\tilde{y}$): (a) $(S'_{gen})_F$ for an inlet temperature of 500 K and width ratio ($\tilde{w}$) of 0.91, (b) $(S'_{gen})_H$ for an inlet temperature of 500 K and $\tilde{w}$ = 0.91, (c) $(S'_{gen})_F$ for an inlet temperature of 600 K and $\tilde{w}$ = 0.76 and (d) $(S'_{gen})_H$ for an inlet temperature of 600 K and $\tilde{w}$ = 0.76.

As shown in the figures, the fluid flow irreversibility increases significantly as the twist ratio reduces below 1.0 at high Reynolds numbers. The heat transfer irreversibility reduces as the twist ratio reduces. Significant reductions in the heat transfer irreversibility are shown to exist at low Reynolds numbers. At high Reynolds numbers, there is a low temperature difference between the absorber tube and heat transfer fluid. At low Reynolds numbers, heat transfer irreversibility is the dominant source of entropy generation due to the presence of a high finite temperature difference.

A more reasonable and clear representation of the distribution of irreversibilities is by using the Bejan number, as it relates the entropy generation due to heat transfer to the total entropy generation according to [61]

$$Be = \frac{\left(S_{gen}\right)_H}{S_{gen}} \tag{6.14}$$

The Bejan number ranges from $0 \leq Be \leq 1$, the heat transfer irreversibility dominates if Be is close to one, whereas the fluid friction irreversibility dominates if Be is close to zero. Accordingly, the heat transfer enhancement at a given Reynolds number should be considered if Be is close to 1. Figure 6.19 (a – c) shows the variation of Bejan number with Reynolds number at different twist ratios for $\tilde{w}$ = 0.61, 0.76 and 0.91 respectively.

The figures show that the Bejan number reduces when compared with the Bejan number of a plain absorber tube. The Bejan number also reduces with an increase in the Reynolds number due to increasing fluid flow irreversibility. Accordingly, a reduction in Be implies a reduction in the heat transfer irreversibility and/or an increase in the fluid friction irreversibility. Figure 6.19 (d) shows the variation of the Bejan number with the Reynolds number at different values of width ratios for $\tilde{y}$ = 0.5. The figure shows a significant reduction in heat transfer irreversibilities at this twist ratio. Larger width ratios give lower values of the Bejan number, due to a reduction in the heat transfer irreversibility and an increase in the fluid flow irreversibility. Figure 6.19 (a – d) also shows that lower twist ratios and large width ratios are more desirable for reduced heat transfer irreversibility than larger twist ratios and smaller width ratios.

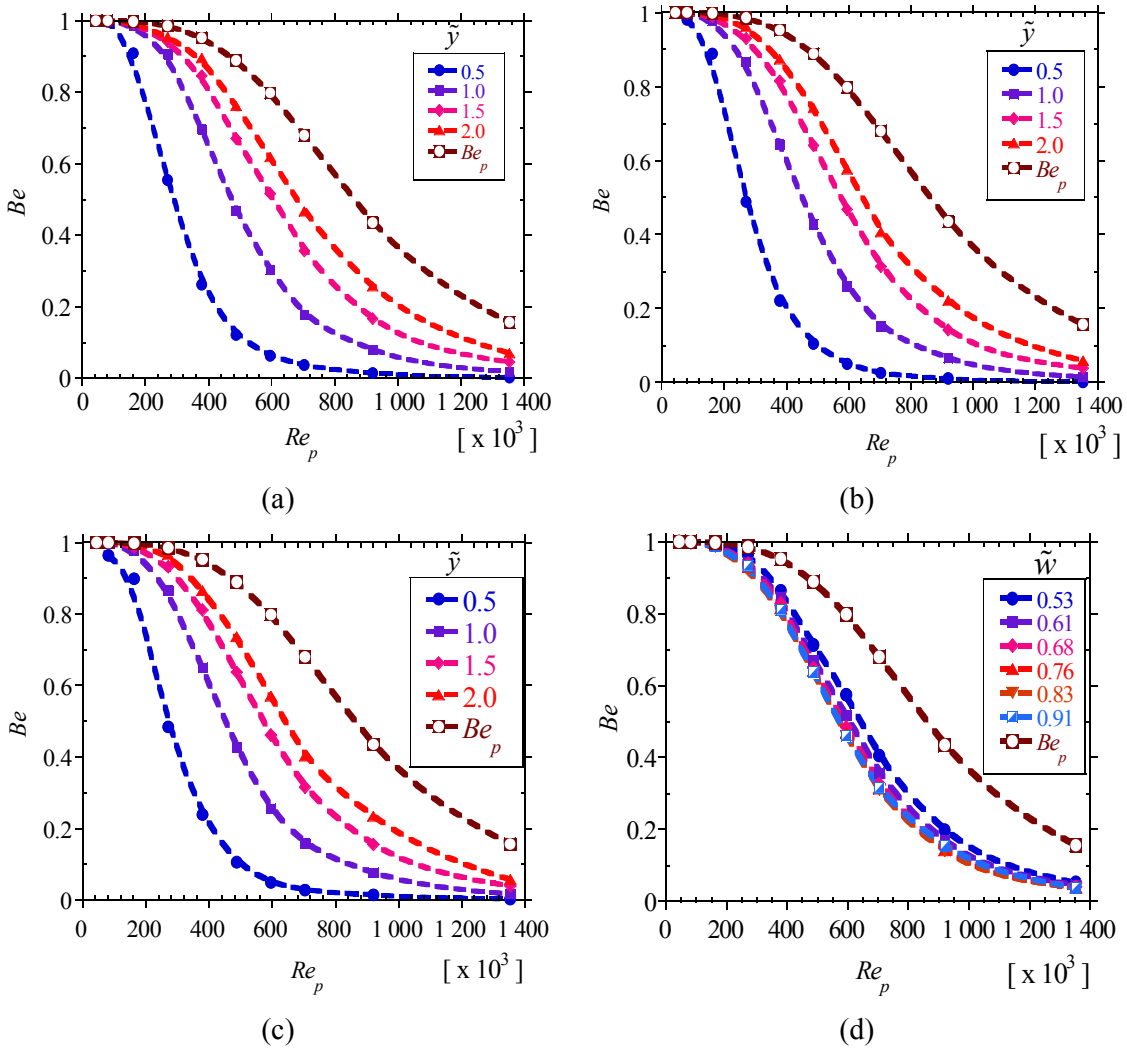

Fig. 6.19: Bejan number in a receiver with twisted tape inserts for an inlet temperature of 600 K as a function of Reynolds number and: (a) twist ratio ($\tilde{y}$) for $\tilde{w}$ = 0.61, (b) twist ratio ($\tilde{y}$) for $\tilde{w}$ = 0.76, (c) twist ratio ($\tilde{y}$) for $\tilde{w}$ = 0.91 and (d) width ratio ($\tilde{w}$) for $\tilde{y}$ = 0.5.

However, it should be noted that at high Reynolds numbers, low twist ratios and large width ratios also significantly increase the fluid flow irreversibility, as discussed above. A closer look at the effect of the width ratio on the Bejan number shows that at a given Reynolds number, the Bejan number reduces slightly with an increase in width ratio, as shown in Fig. 6.20 (a – d) for Reynolds numbers 1.94 $\times 10^4$, 6.4 x 10^4, 8.9 $\times 10^4$ and 1.45 $\times 10^5$

respectively and an inlet temperature of 400 K. The reduction is more visible for lower twist ratios due to the improved heat transfer performance.

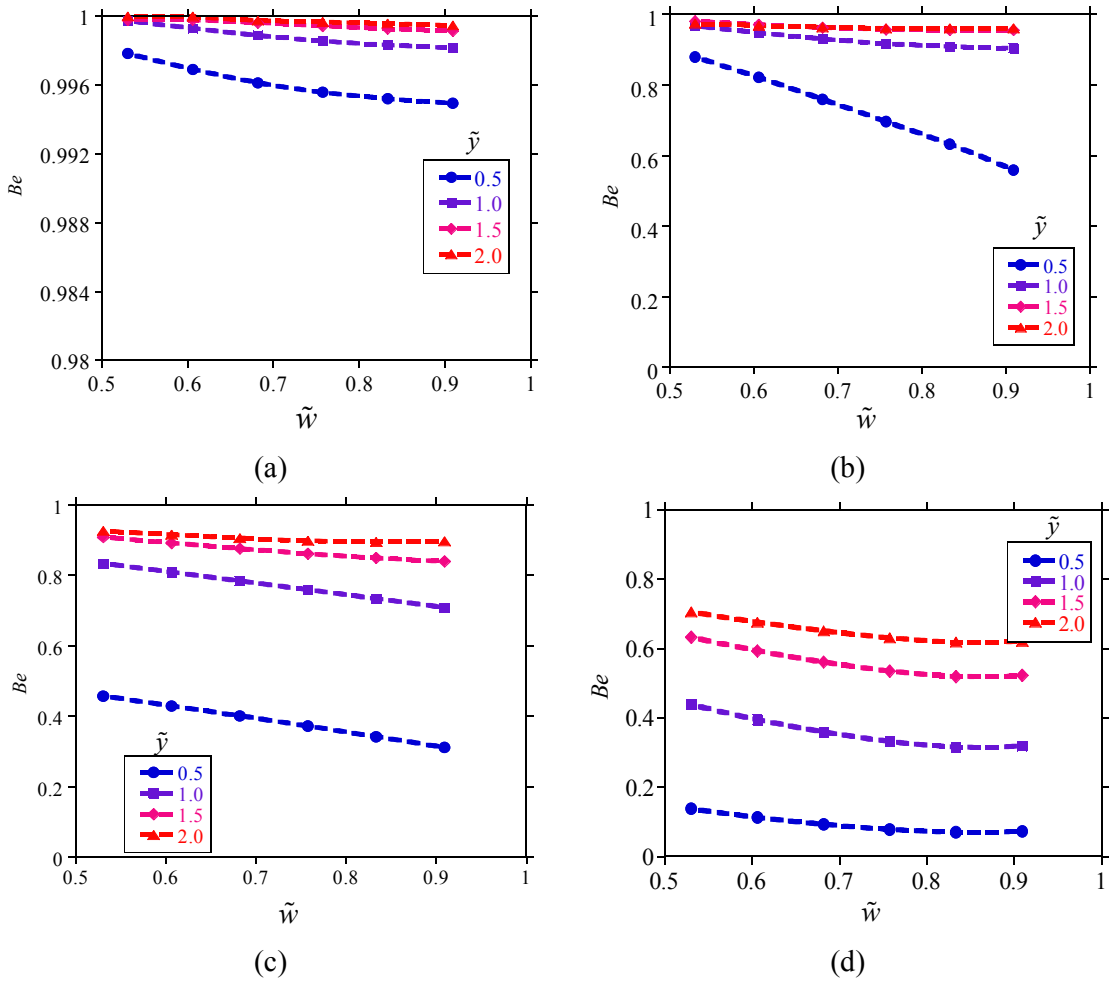

Fig. 6.20: Bejan number in a receiver with twisted tape inserts as a function of width ratio ($\tilde{w}$) and twist ratio ($\tilde{y}$) for an inlet temperature of 400 K: (a) Re_p = 1.94 × 10^4, (b) Re_p = 6.40 × 10^4, (c) Re_p = 8.94 × 10^4 and (d) Re_p = 1.45 × 10^5.

Generally, the Bejan number reduces as the width ratio increases, at any given Reynolds number. Figure 6.20 (a – d) also shows that as the Reynolds number increases, the Bejan number reduces; for lower values of the twist ratios the Bejan number is low and shows a significant reduction as the width ratio increases. This is mainly due to the high fluid flow irreversibilities at low twist ratios. Therefore, at a given lower Reynolds number, lower twist

ratios are desirable for reduced heat transfer irreversibilities. For higher Reynolds numbers, the heat transfer irreversibility is small compared to the fluid friction irreversibility, so heat transfer enhancement may not make thermodynamic sense.

When added, the fluid flow irreversibility and heat transfer irreversibility yield the total entropy generation rate. Given the variation of the fluid flow and heat transfer irreversibilities discussed above, the total entropy generation rate is expected to reduce with increased in Reynolds numbers up to some minimum value due to the reduction in heat transfer irreversibility, and then increase with the Reynolds numbers due to the significant increase in fluid flow irreversibility.

Figure 6.21 (a and b) shows the variation of the total entropy generation rate with Reynolds numbers at different width ratios for twist ratios of $\tilde{y}$ = 1.0 and 2.0 respectively when the inlet temperature is 600 K. As shown in the figure, there is a Reynolds number (optimal Reynolds number) at which the entropy generation rate is a minimum at each width ratio for any given twist ratio. The figures also show that the optimal Reynolds number becomes lower as the width ratio increases. Figure 6.21 (c and d) show the variation of the total entropy generation rate with Reynolds numbers at different twist ratios for width ratios of $\tilde{w}$ = 0.91 at 500 K and 600 K respectively. The figures also show the presence of an optimal Reynolds number at every twist ratio for the two temperatures considered. In all the figures, when compared with the entropy generation rate for a plain absorber tube, there is a point at which the entropy generation becomes higher than that in a plain absorber tube. Beyond such a point, heat transfer enhancement using twisted tape inserts does not make thermodynamic sense.

In Fig. 6.21 (a – d), it is shown that below the optimal Reynolds number, high heat transfer rates are essential to significantly reduce the heat transfer irreversibility. Therefore, lower twist ratios and large width ratios are essential.

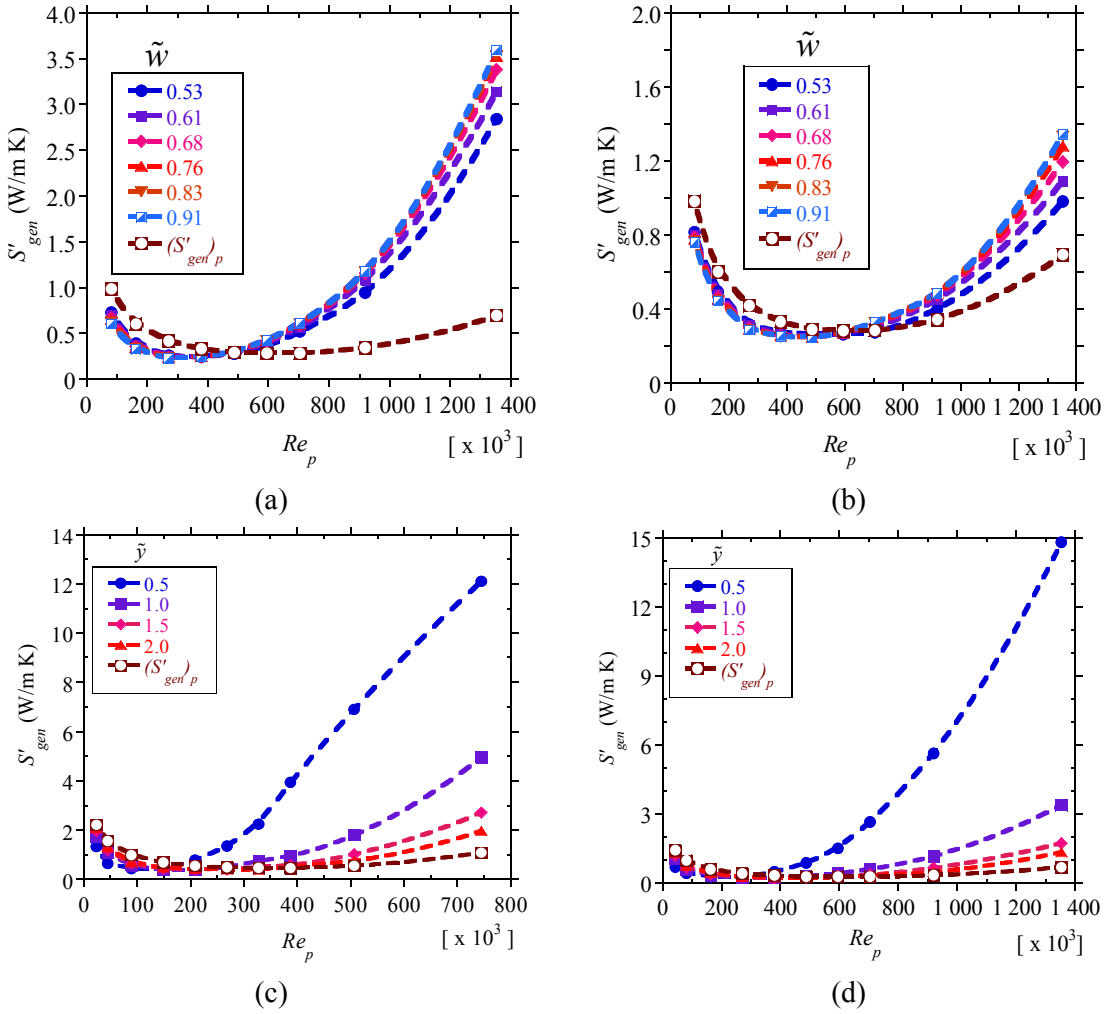

Fig. 6.21: Total entropy generation rate in a receiver with twisted tape inserts as a function of Reynolds number and: (a) width ratio ($\tilde{w}$) for an inlet temperature of 600 K and twist ratio ($\tilde{y}$) of 1.0, (b) width ratio for an inlet temperature of 600 K and $\tilde{y}$ = 2.0, (c) twist ratio for an inlet temperature of 500 K and $\tilde{w}$ = 0.91 and (d) twist ratio for an inlet temperature of 600 K and $\tilde{w}$ = 0.91.

After the optimal Reynolds number, an increase in the Reynolds numbers increases the entropy generation rate significantly due to the significant increase in fluid flow irreversibility at high Reynolds numbers, so that low twist ratios and large width ratios result in very high entropy generation rates.

The sample variation of the optimal Reynolds number with the twist ratio is shown in Fig. 6.22 at an inlet temperature of 400 K. The optimal Reynolds number is correlated logarithmically within 5% by the following correlation when $\tilde{w} = 0.91$.

$$Re_{opt} = 74,687 + 1.0692 \times 10^5 \log(\tilde{y}) \qquad 6.15$$

For $\tilde{w} = 0.61$, the optimal Reynolds number is also correlated logarithmically within 5% by

$$Re_{opt} = 94,462 + 8.2130 \times 10^4 \log(\tilde{y}) \qquad 6.16$$

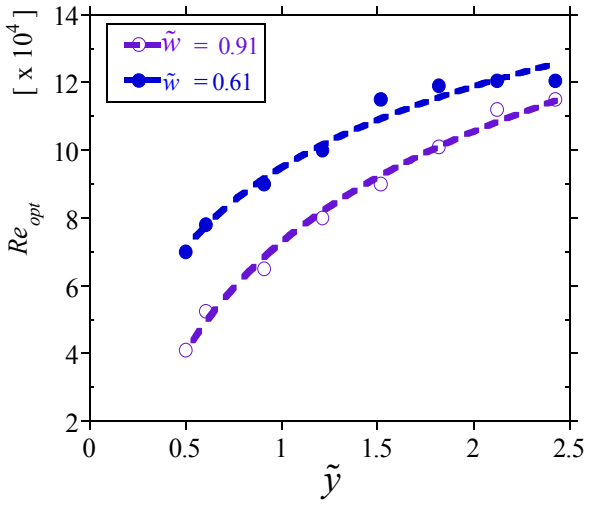

Fig. 6.22: Optimal Reynolds number for a receiver with twisted tape inserts as a function of twist ratio ($\tilde{y}$) at width ratios ($\tilde{w}$) of 0.61 and 0.91 and an inlet temperature of 400 K.

Generally, the optimal Reynolds number increases as the twist ratio increases and as the width ratio reduces. The optimal Reynolds number also depends on the concentration ratio and the incident solar radiation.

6.3.2 THERMODYNAMIC EVALUATION OF TWISTED TAPE INSERTS

For evaluating the thermodynamic effectiveness of a given heat transfer technique, the enhancement entropy generation number, $N_{s,en}$ given in Eq. (6.9) is used. In general, the value of this ratio should be less than 1 if the enhancement technique is to be thermodynamically feasible. For ratios less than 1.0, the irreversibilities are reduced when compared to a plain

tube and for ratios greater than 1, the enhancement techniques lead to more irreversibilities compared to a plain tube.

In Fig. 6.23 (a – d), $N_{s,en}$ decreases as the twisted tape's width ratio increases at low Reynolds numbers. As the Reynolds numbers increase, $N_{s,en}$ begins to increase. At high Reynolds numbers, $N_{s,en}$ increases with the Reynolds numbers and is significantly greater than 1.0.

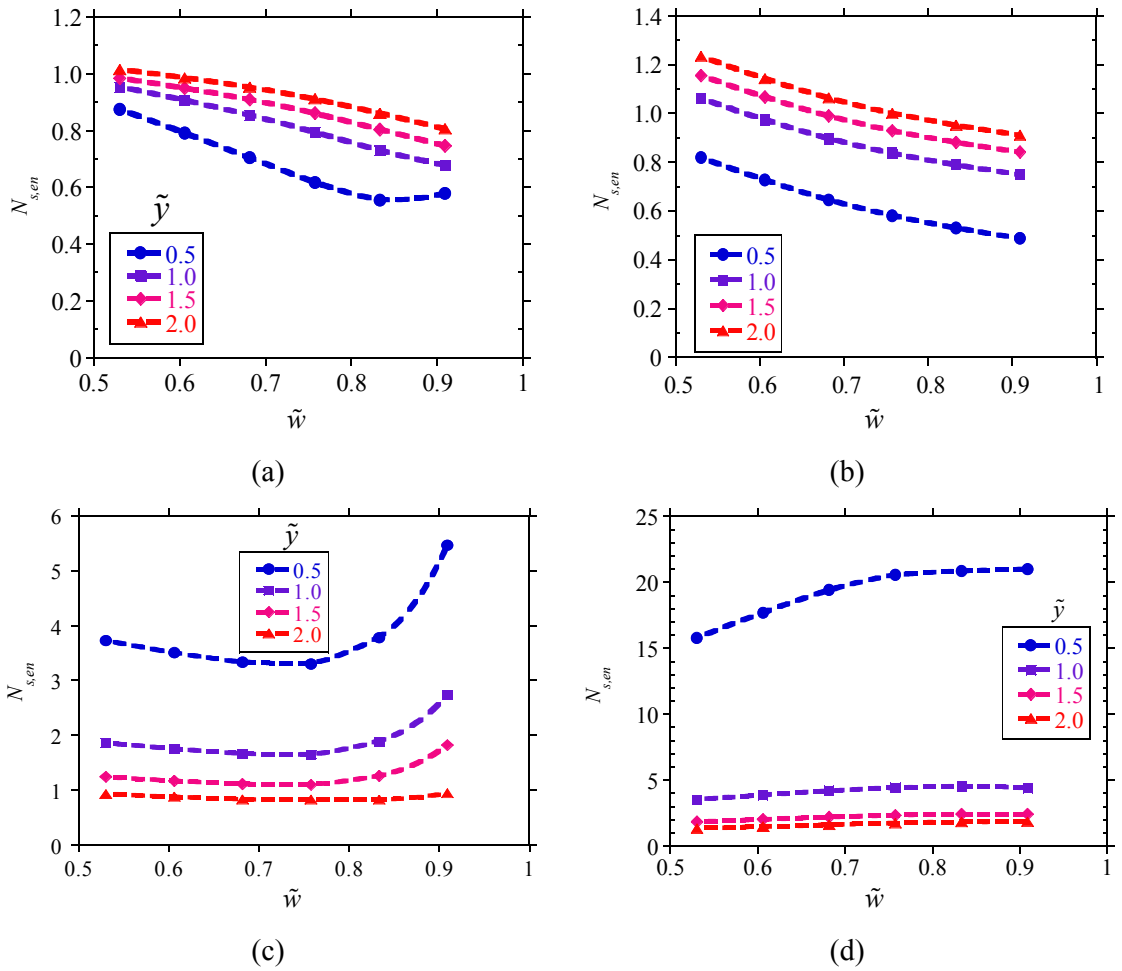

Fig. 6.23: Enhancement entropy generation number ($N_{s,en}$) for a receiver with twisted tape inserts as a function of width ratio ($\tilde{w}$) and twist ratio ($\tilde{y}$) for an inlet temperature of 400 K: (a) $Re_p = 3.84 \times 10^4$, (b) $Re_p = 8.33 \times 10^4$, (c) $Re_p = 1.66 \times 10^5$ and (d) $Re_p = 3.20 \times 10^5$.

For the inlet temperature of 400 K, above a Reynolds number of about 1.0×10^5, the high fluid flow irreversibilities make the value of $N_{s,en}$ greater than 1 for most twist ratios and width

ratios. For large values of Reynolds numbers ($Re_p \geq 1.0 \times 10^5$), the value of $N_{s,en}$ increases with the increase in the width ratio and reducing twist ratio owing to the increased contribution of the fluid flow irreversibility to entropy generation. Therefore, at high Reynolds numbers, less tight twisted tapes will be desirable since they will result in low entropy generation rates.

Figure 6.24 (a – d) shows the variation of $N_{s,en}$ with Reynolds number at different twist ratios, width ratios and inlet temperatures. Generally, the figures show that as the Reynolds number increases above a given Reynolds number, the entropy generation ratio becomes greater than 1 for most twist ratios. This Reynolds number depends on the twist ratio and width ratio of the insert used. For all inlet temperatures, the flow rate at which an entropy generation ratio lower than 1 is obtained is about 43 m^3/h (10.05 kg/s at 400 K, 8.94 kg/s at 500 K, 7.65 kg/s at 600 K and 6.91 kg/s at 650 K) for twist ratios greater than 1.0 and widths greater than 0.61. At flow rates higher than this, the reduction in entropy generation is not significant or the entropy generation ratio is much greater than 1.0. For twist ratios lower than 1.0 and all width ratios, significant reductions in entropy generation are possible, provided that the flow rates are lower than 31 m^3/h (about 7.18 kg/s at 400 K, 6.38 kg/s at 500 K, 5.46 kg/s at 600 K and 4.93 kg/s at 650 K).

As shown in Fig. 6.24 (a – d), the use of tight twist ratios at high Reynolds numbers is not desirable since the ratio $N_{s,en}$ is increased to more than 1.0. Entropy generation ratios up to 22 were obtained, depending on the twisted tape width ratio, twist ratio, Reynolds number and inlet temperature used. In general, at a given temperature, higher values of the entropy generation ratio were obtained at the lowest twist ratio, largest width ratio, largest Reynolds numbers and lowest inlet temperature. At low Reynolds numbers, entropy generation ratios lower than 1.0 were obtained due to the improved heat transfer and significant reduction in the finite temperature difference and lower fluid friction irreversibility. This study showed that the entropy generation rates were reduced up to 59% at flow rates lower than 43 m^3/h, twist ratios greater than 1.0 and width ratios greater than 0.61.

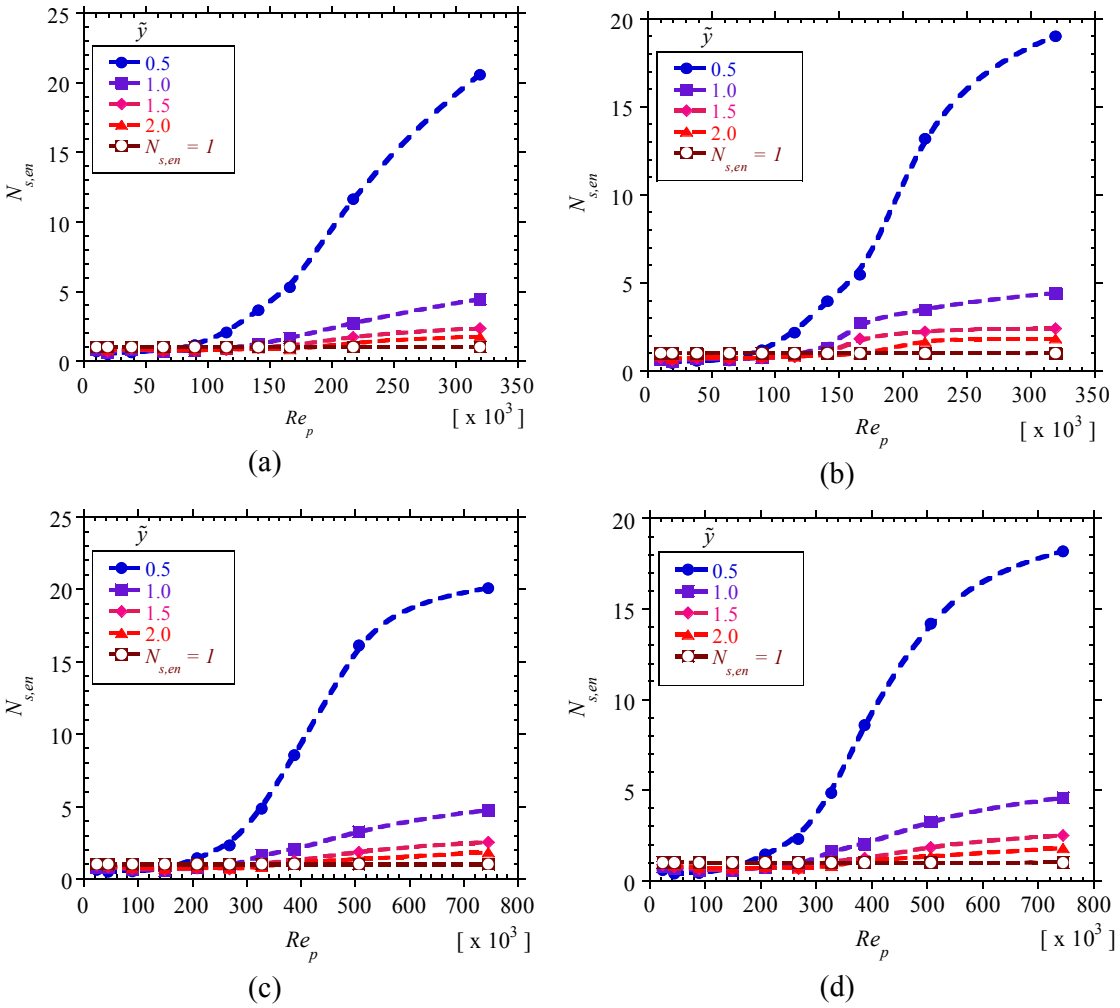

Fig. 6.24: Enhancement entropy generation number ($N_{s,en}$) for a receiver with twisted tape inserts as a function of Reynolds number and twist ratio ($\tilde{y}$): (a) inlet temperature of 400 K and width ratio ($\tilde{w}$) of 0.76, (b) inlet temperature of 400 K and $\tilde{w}$ = 0.91, (c) inlet temperature of 500 K and $\tilde{w}$ = 0.83 and (d) inlet temperature of 500 K and $\tilde{w}$ = 0.91.

6.4 MULTI-OBJECTIVE OPTIMISATION

As discussed above, heat transfer enhancement leads to an increase in the heat transfer performance of a given heat exchanger but with a greater pressure drop. As the twist ratio was reduced and width ratio increased, both the heat transfer and pressure drop increased. Therefore, in the optimisation of heat transfer enhancement techniques, both objectives should be considered. The objectives in this case were to maximise heat transfer performance

and minimise fluid friction. As such, a multi-objective optimisation problem arises. As presented in Section 3.4.2, genetic algorithms are suited to such types of problems. Multi-objective genetic algorithms use the concept of dominations to search the decision variable space for a set of solutions that are non-dominated with respect to one another and that dominate all other solutions. In the absence of further information, all these solutions are equally important. This set of solutions is known as the Pareto optimal solutions. In this section, the hybrid variant of the non-dominated sorting genetic algorithm II (NSGA II) available in ANSY design explorer [99] was used to obtain such solutions.

6.4.1 FORMULATION OF THE OPTIMISATION PROBLEM

The multi-objective optimisation problem under consideration can be written according to Eq. (3.42) as

$$\text{Maximise } f_1(\mathbf{x}) / \text{ Minimise } f_2(\mathbf{x}) \tag{6.17}$$

The objective functions $f_1(\mathbf{x})$ and $f_2(\mathbf{x})$ are heat transfer performance expressed as the Nusselt number, Nu and pressure drop expressed as the fluid friction, f according to Eqs. (6.4) and (6.5) respectively.

The optimisation was considered for fixed-flow Reynolds numbers. The Reynolds numbers considered ranged from $1.04 \times 10^4 \leq Re \leq 1.36 \times 10^6$. The Reynolds numbers depended on the flow rate and inlet temperature considered. The inlet temperatures used were 400 K, 500 K and 600 K and the heat flux on the receivers' absorber tube was kept constant according to the boundary conditions used.

The design variable ranges considered are given as

$$\begin{aligned} 0.42 \leq \tilde{y} &\leq 2.42 \\ 0.53 \leq \tilde{w} &\leq 0.91 \end{aligned} \tag{6.18}$$

6.4.2 OPTIMISATION PROCEDURE

The multi-objective optimisation in this chapter and subsequent sections was carried out using the design exploration toolbox available in ANSYS® release14 [99] as described in Chapter 3 Section 3.7 of this thesis.

The configurations given by the 30 design points were evaluated using ANSYS FLUENT® a commercial computational fluid dynamics code, following the same procedure described in Section 3.7 to obtain the defined performance parameters.

Once all the design points are updated, the next step is building response surfaces or a meta-model to relate the performance parameters to the design parameters. The accuracy of the response surface is essential for the remaining steps. The detailed method for building standard response surfaces and metrics used for determining the response surface accuracy is detailed in Myers and Montgomery [101] as discussed in Section 3.6 of Chapter 3. In the present work, second-order polynomials were sufficient with the values of R^2 given by Eq. (3.52) and R^2_{adj} given in Eq. (3.53) greater than 0.98. The relative mean square errors given by Eq. (3.49) for the parameters of interest were less than 3% at all Reynolds numbers. Appendix A.5 contains the sample metrics for response surface verification. The goodness-of-fit chart shows good accuracy for most parameters. Appendices A.6 and A.7 contain the sensitivity charts that show the variation of output parameters with input parameters. The charts show how the input parameters influence the output parameters.

6.4.3 OPTIMISATION RESULTS

Figure 6.25 (a and b) shows the sample 3-D response surfaces for the variation Nusselt number and friction factor, respectively for a Reynolds number of 8.24×10^4 when the inlet temperature is 600 K. The same trend was obtained at other Reynolds numbers and inlet temperatures. In Fig. 6.25 (a), the Nusselt number is shown to increase with the reducing twist ratios and increasing width ratios of the twisted tape as discussed above. High Nusselt numbers exist at the point of the lowest twist ratio and greatest width.

The variation of the friction factor is similar to that of Nusselt number: the highest friction factors are achieved at low twist ratios and higher twisted tape width, as shown in

Fig. 6.25 (b). The trend shown by the absorber tube's circumferential temperature difference is the inverse of the Nusselt number variation. As the Nusselt numbers increase, the absorber tube's circumferential temperature difference is expected to reduce. The multi-objective optimisation in a case where two objectives are conflicting, yields a set of solutions in which an improvement in one objective sacrifices the quality of the other. As shown in this figure, there is no single optimum point that gives the maximum heat transfer and minimum fluid friction.

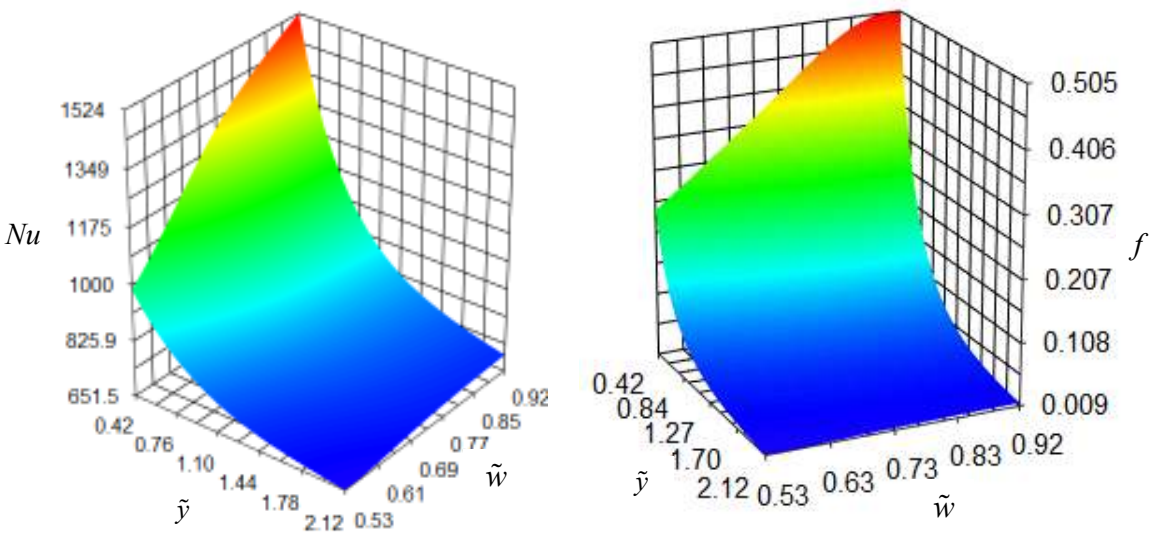

Fig. 6.25: 3-D response surfaces for Nusselt number and friction factor, respectively for a receiver with twisted tape inserts as functions of twist ratio ($\tilde{y}$) and width ratio ($\tilde{w}$) at $Re_p = 8.28 \times 10^4$ and an inlet temperature of 600 K.

In such a case, the Pareto optimal solutions are sought. Figure 6.26 shows such solutions of the multi-objective optimisation. Figure 6.26 (a – c) show the sample 3-D Pareto optimal fronts obtained for variations of the multi-objective optimisation functions with the design variables. From these solutions, a 2-D Pareto optimisation front was obtained for a variation of the multi-objective functions with one another as shown in Fig. 6.26 (d). All the solutions on the Pareto optimal front are equally important and the designer can select any solution depending on the design criteria being used or the availability of higher-level information.

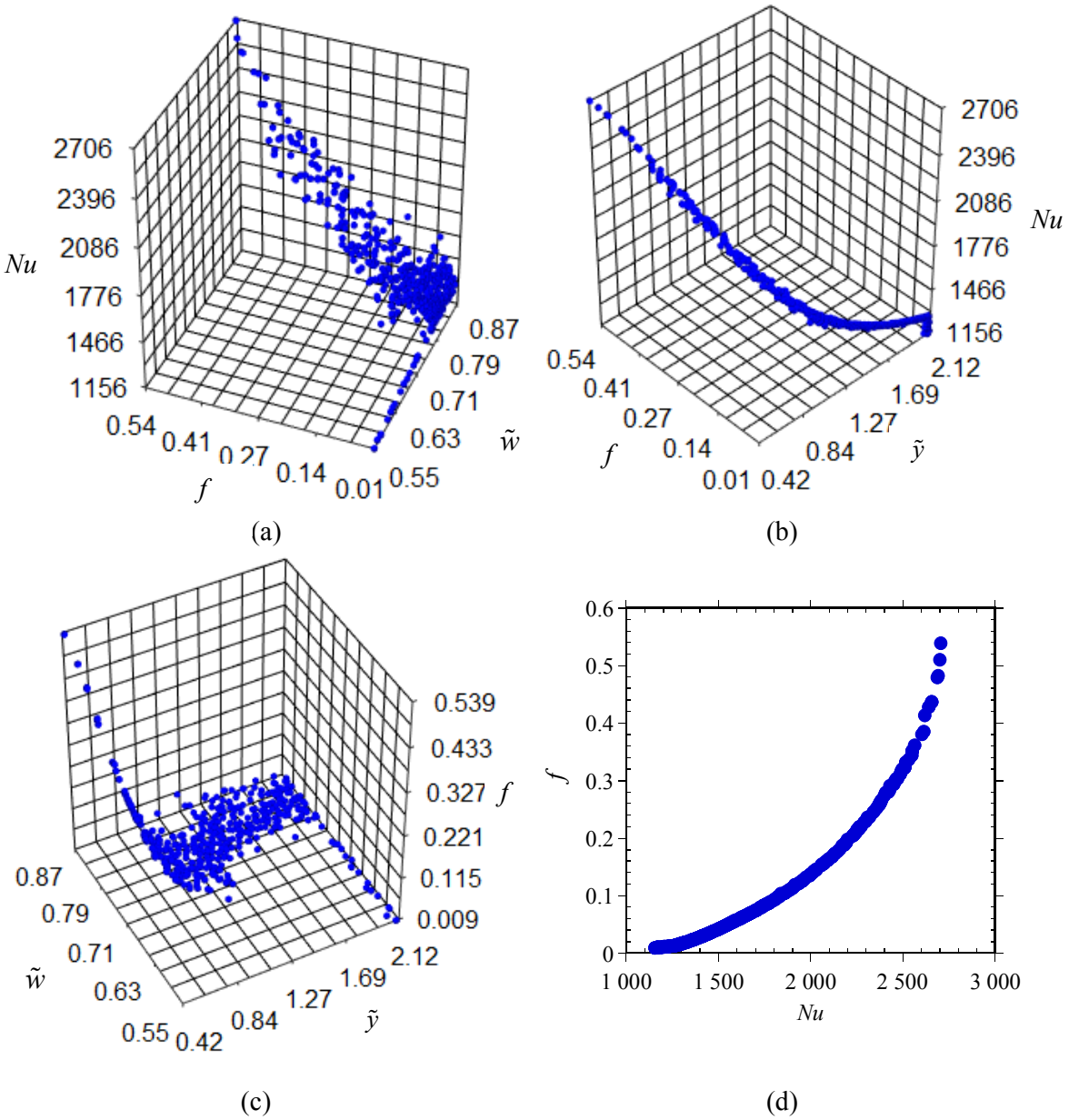

Fig. 6.26: Pareto optimal solutions for a receiver with twisted tape inserts for an inlet temperature of 600 K and $Re_p = 1.64 \times 10^5$: (a) Nusselt number as a function of width ratio ($\tilde{w}$) and friction factor, (b) Nusselt number as a function of friction factor and twist ratio ($\tilde{y}$), (c) friction factor as function of width ratio and twist ratio solutions and (d) Pareto optimal front for Nusselt number and friction factor.

As expected, the Pareto optimal solutions are shown to lie on a continuous curve, along which an increase in Nusselt numbers is accompanied by an increase in fluid friction. The two objectives are conflicting, increasing the quality of one objective decreases the quality of the other objective. In the sense of multi-objective optimisation, all the solutions on the Pareto front in Fig. 6.26 (d) are equally important and no solution can be said to be better than another. The same trend obtained in Fig. 6.26 (a – d) occurs at other values of Reynolds numbers and inlet temperatures.

In most multi-objective optimisation problems, a decision support tool is necessary to help the designer obtain a single design which satisfies specific criteria. If higher-level information concerning the objectives is available (such as whether heat transfer enhancement is more important than fluid friction or if the minimisation of fluid friction is more important than heat transfer enhancement or if all have the same level of importance), a design can be arrived at using a decision support procedure. A decision support process provided in ANSYS® design exploration toolbox is discussed in Section 3.8 of Chapter 3: it is a goal-based, weighted, aggregation-based technique that ranks the design candidates according to the order of importance of the objectives [99].

The detailed description of the decision support process is given in Section 3.8 of Chapter 3.

According to Eqs. (3.55) – (3.60), five cases are possible and can be explored, namely:

- Case A: when the heat transfer enhancement and fluid friction have the same importance and take default values.
- Case B: when maximising the heat transfer enhancement is of greater importance than minimising the fluid friction. Fluid friction has a default level of importance.
- Case C: when minimising the fluid friction is more important than maximising the heat transfer enhancement. Heat transfer enhancement has a default level of importance.
- Case D: when maximising the heat transfer enhancement is of greater importance and minimising the fluid friction is of lesser importance.

- Case E: when minimising the fluid friction is more important and maximising the heat transfer performance is less important.

The weight of the objective defined as more important is 1.00, for a default objective the weight is 0.666 and an objective that is of lower importance takes a weight of 0.333 as given in Eq. (3.56). Considering the case when all objectives are of equal importance (Case A), and using default weights for each objective, we can arrive at single design points at each inlet temperature and flow rate.

Figure 6.27(a and b) shows the variation of the optimal twist ratio and optimal width ratio with Reynolds numbers respectively at the different inlet temperatures used in this study for case A. The figure shows that the optimal twist ratio and width ratio do not vary appreciably with the Reynolds numbers. At a given inlet temperature, the optimal twist ratio stays the same as the Reynolds number changes. It is also noted that, in all cases, a combination of low twist ratios and average width ratios is desirable. At these low twist ratios, a high turbulence intensity and better fluid mixing give better heat transfer rates.

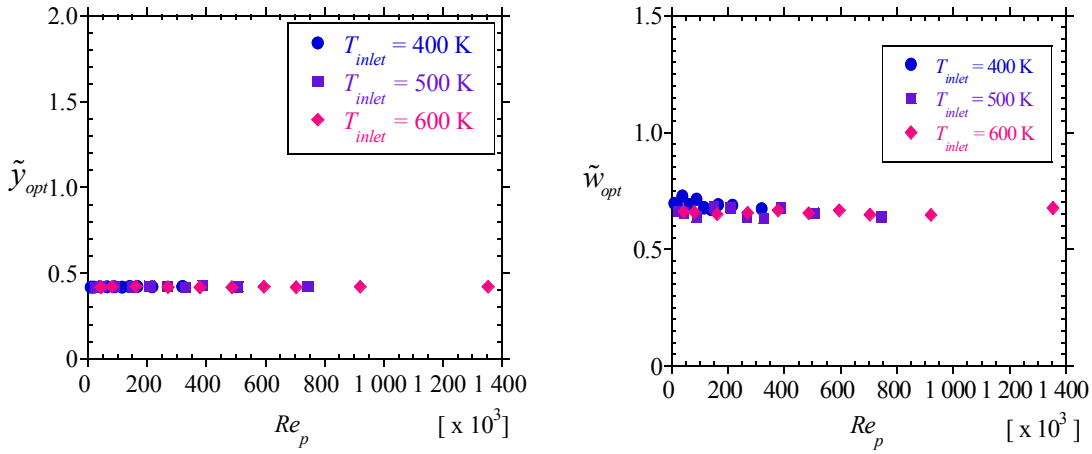

Fig. 6.27: Optimal twisted tape geometry for a receiver with twisted tape inserts as a function of Reynolds number and inlet temperature: (a) optimal twist ratio ($\tilde{y}_{opt}$) and (b) optimal width ratio ($\tilde{w}_{opt}$).

The optimal twist ratio was about 0.42 at all Reynolds numbers and fluid temperatures. The optimal width ratio did not vary with the Reynolds number and fluid temperature. For the range of parameters considered, the average optimal width ratio was about 0.65 with very small fluctuations of about ± 0.2.

Figure 6.28 (a – d) shows the results for optimal heat transfer performance and optimal fluid friction. At all inlet temperatures, the optimal heat transfer enhancement factors are nearly the same. For the range of parameters considered, the optimal designs gave enhancement factors in the range of 1.81 – 2.36 with an increase in thermal efficiency between 3.8 – 8.2% if the flow rate was lower than 43 m^3/h. There was the same trend of Nu and f as discussed in Section 6.2.

The friction factor variation for the optimal parameters is shown in Fig. 6.28 (c). The friction factor ratio shown in Fig. 6.28 (d) does not change significantly with the Reynolds number and fluid temperature, as already discussed. The average optimal friction factor ratio $(f/f_p)_{opt}$ for the range of parameters considered in this study is about 14.0 times compared with that of a receiver with a plain absorber tube.

As shown in Fig. 6.29 (a), the entropy generation for all optimised cases has the same variation with the Reynolds number. This trend is almost similar to the one obtained in Section 6.3. There is a Reynolds number at which the entropy generation rate is a minimum, therefore the combined use of multi-objective optimisation and thermodynamic optimisation can be helpful in determining designs with low friction factors, high heat transfer rates and minimum entropy generation. It should be noted that the optimal flow rates corresponding to the optimal Reynolds number do not vary significantly with the inlet temperature used. Figure 6.29 (b) shows the variation of the enhancement entropy generation ratio, $N_{s,en}$ at each temperature, $N_{s,en} \leq 1$ at some Reynolds numbers.

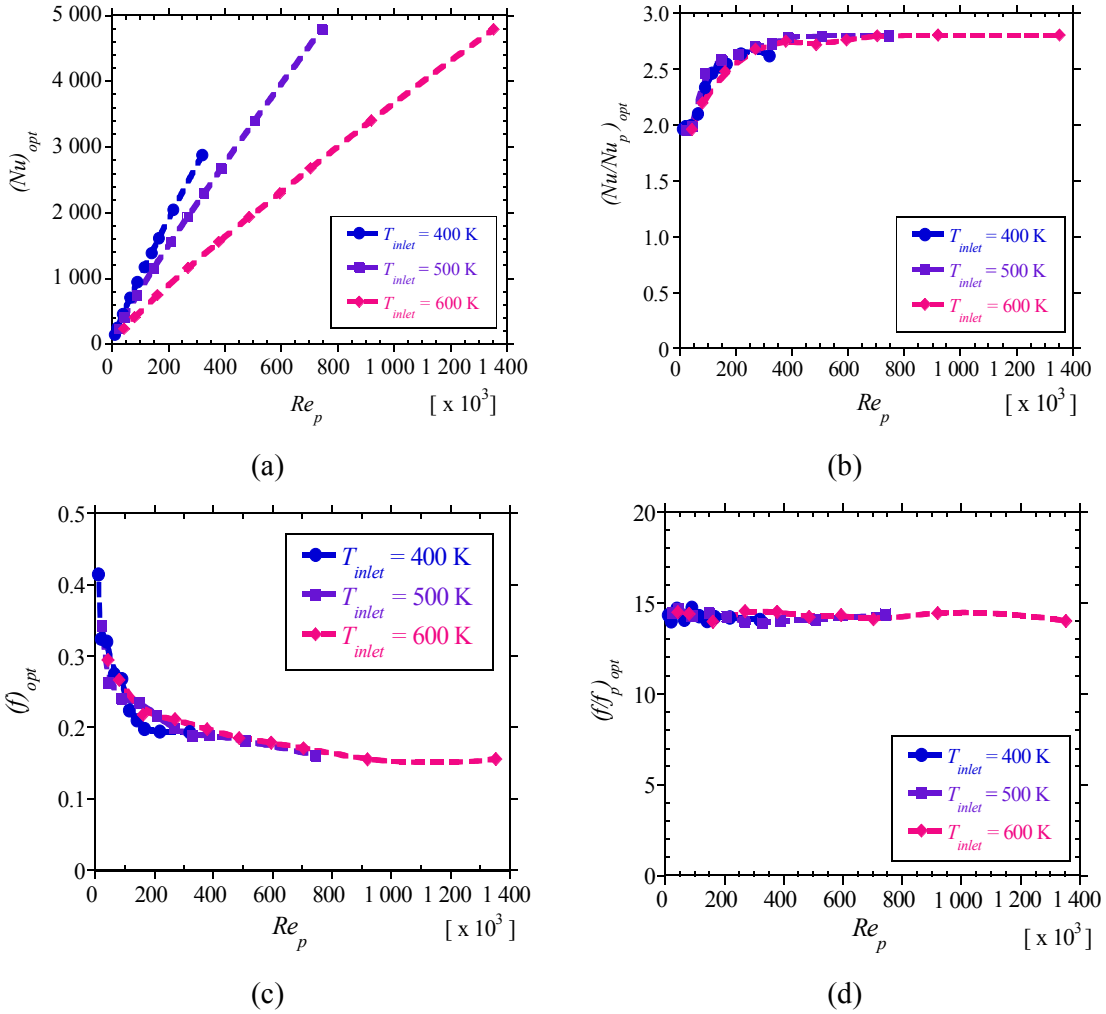

Fig. 6.28: Optimal performance parameters for a receiver with twisted tape inserts as a function of Reynolds number and inlet temperature: (a) optimal Nusselt number, (b) optimal heat transfer enhancement factor, (c) optimal friction factor and (d) optimal pressure drop penalty factors.

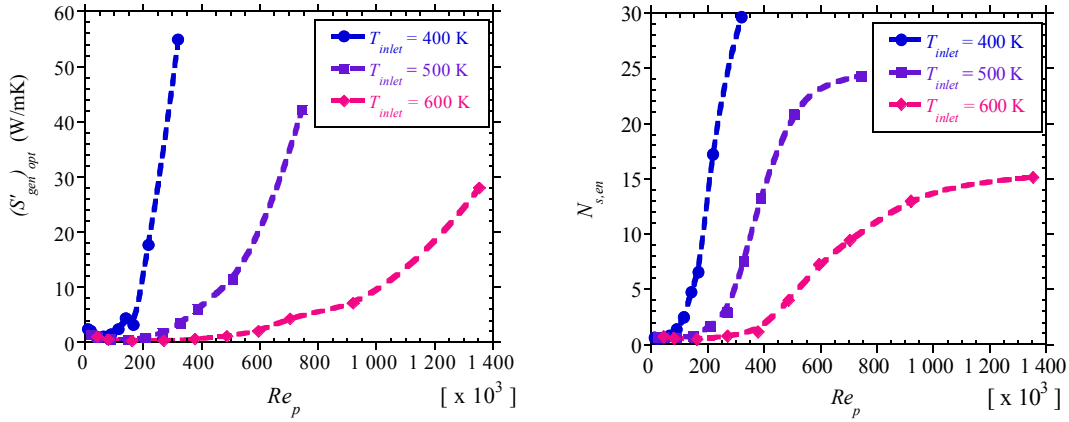

(a) (b)

Fig. 6.29: Optimal entropy generation and enhancement entropy generation number, respectively for a receiver with twisted tape inserts as functions of Reynolds number and inlet temperatures.

From the optimal results, a Reynolds number at which heat transfer enhancement makes thermodynamic sense ($N_{s,en} \leq 1$) can be obtained. The flow rate at which $N_{s,en} \leq 1$ is about 37 m^3/h at all inlet temperatures (about 8.62 kg/s at 400 K, 7.66 kg/s at 500 K, 6.56 kg/s at 600 K and 5.92 kg/s at 650 K). This is lower than the result obtained in Section 5.3 for a receiver with a plain absorber tube which is 62 m^3/h (about 14.36 kg/s at 400 K, 12.78 kg/s at 500 K, 10.94 kg/s at 600 K and 9.88 kg/s at 650 K).

In another approach, three points are selected from the Pareto optimal front corresponding to the maximum heat transfer rate (point A), the minimum fluid friction (point B) and another point obtained as an intersection of the Pareto front and the diagonal of the rectangle, as shown in Fig. 6.30 (Point C). Figure 6.30 shows the location of the three points on a Pareto optimal front for T_{inlet} = 600 K and Re = 1.64×10^4. The graph has a similar trend to the one obtained in Fig. 6.26 (d). The same trend can be obtained for several combinations of Reynolds numbers and inlet temperatures and points A, B and C obtained.

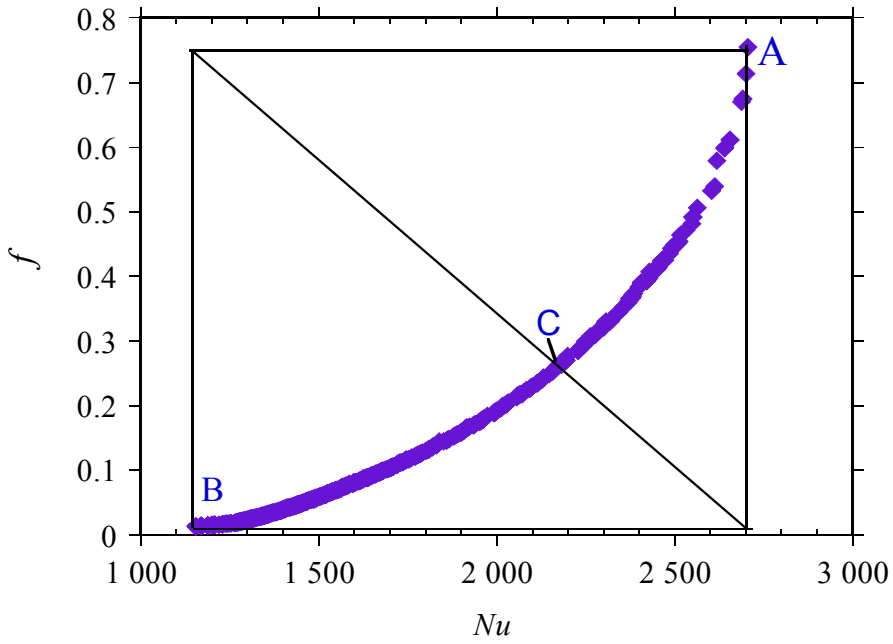

Fig. 6.30: Pareto optimal front for a receiver with twisted tape inserts for an inlet temperature of 600 K and $Re_p = 1.64 \times 10^4$.

For these three points, the optimal twist ratios and width ratios are plotted against the flow Reynolds number for each inlet temperature. As shown in Fig. 6.31 (a), the optimal twist ratio does not vary with temperature at any given point considered. Point A shows a slightly lower twist ratio than C, while point B has the highest twist ratio. The optimal width ratio is shown in Fig. 6.31 (b) for points A, B and C.

At location A, the optimal width ratio is higher. The width ratio is lower at point B. This is because A represents the highest heat transfer and so the width ratio should be higher and twist ratio lower to facilitate high heat removal from the absorber tube wall. At point B, the fluid friction is lower and heat transfer is lower, hence the lower width ratio and higher twist ratio. For point A, the optimal twist ratio is about 0.42, for point B it is about 2.10, for point C it is about 0.64 at all Reynolds numbers and inlet temperatures. The corresponding width ratios are 0.92 at point A, 0.55 at point B and at point C the optimal width ratio is 0.92 at 400 K, 0.72 at 500 K and 0.62 at 600 K.

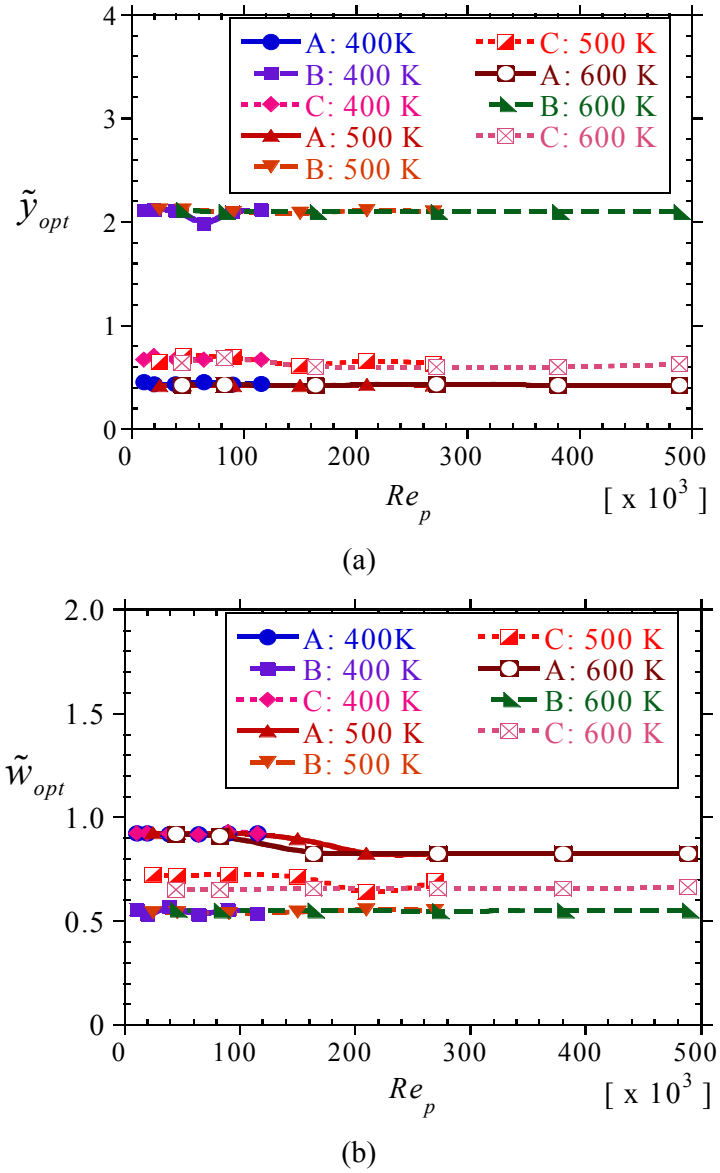

Fig. 6.31: Variation of optimal twisted tape geometry for a receiver with twisted tape inserts as function of Reynolds number and inlet temperature for points A, B and C on the Pareto front in Fig. 6.30: (a) optimal twist ratio ($\tilde{y}_{opt}$) and (b) optimal width ratio ($\tilde{w}_{opt}$).

For the optimal points A, B and C, determining the true performance of the collector with an enhanced tube can further assist with making a decision about which design is better. As discussed above, the collector's thermal efficiency shows a true picture of the performance due to heat transfer enhancement. As shown in Fig. 6.32, at any given Reynolds number and

inlet temperature, operating at point B gives a higher increase in efficiency. Points B and C also give a positive increase in collector efficiency at almost all Reynolds numbers, especially when the fluid temperatures are higher than 500 K.

Heat transfer enhancement in parabolic trough receivers improves efficiency due to a combination of better heat transfer rates, lower absorber tube temperatures and lower absorber tube coating emissivity owing to reduced absorber tube temperatures. For point A, high heat transfer rates are achieved, but the pumping power also increases significantly and becomes higher than the gain in heat transfer rate as the Reynolds numbers increase, in this way lowering the efficiency instead. At point B, the heat transfer enhancement improves heat transfer performance and significantly reduces the absorber tube temperatures, as discussed in Section 6.25. There is a lower increase in the pumping power requirement at point B, the increase in thermal efficiency is higher in some cases at this point. As the temperatures increase, the change in thermal efficiency at points B and C approach one another. Any other points can be chosen from the Pareto front and compared, depending on the designer's needs.

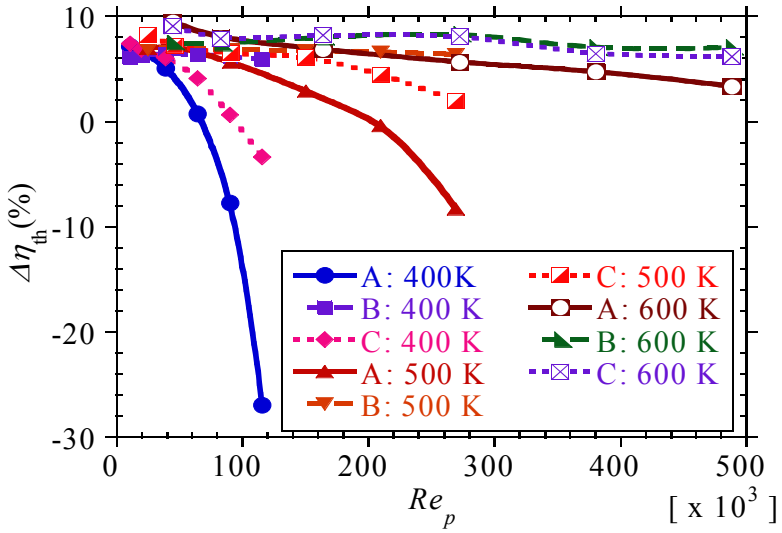

Fig. 6.32: Change in collector's thermal efficiency for a receiver with twisted tape inserts for the optimal twisted tape geometry of Fig. 6.31 as a function of Reynolds numbers and inlet temperature for the different points on the Pareto front.

6.5 CONCLUDING REMARKS

This chapter presents the numerical investigation of the heat transfer, fluid friction and thermodynamic performance of a parabolic trough receiver with low twist ratio wall-detached twisted tape inserts. Further multi-objective optimisation was used to obtain Pareto optimal solution sets for which heat transfer performance is maximum and fluid friction is minimum. The numerical model of the twisted tape insert was validated against the experimental data available in the literature and good agreement obtained. It was shown that an analysis based only on Nusselt numbers and friction factors does not give a true indication of the performance of the parabolic trough receiver. The entropy generation ratio is essential for characterising thermodynamic performance, whereas collector efficiency is useful for characterising the actual thermal performance of the collector system. The following main conclusions can be drawn from the study:

- The use of twisted tape inserts for heat transfer enhancement in parabolic trough receivers results in high heat transfer rates. This is due to the increased turbulence intensity and the mixing of the heat transfer fluid from that part of the absorber tube receiving concentrated heat flux with the heat transfer fluid from the part receiving only direct solar heat flux.
- In the study, the heat transfer increases in the range 1.05 – 2.69 times, fluid friction increases in the range 1.60 – 14.5 times and the thermal enhancement factor at a constant pumping comparison with a plain receiver tube was in the range 0.74 -1.27. The use of low twist ratios is shown to significantly enhance the heat transfer performance of the receiver tube, even at low width ratios.
- The efficiency increases in the range 5% – 10% for twist ratios greater than 1.0 and for almost all width ratios. This increase in thermal efficiency is achievable, provided the flow rates are lower than 43 m^3/h.
- The absorber tube's circumferential temperature difference reduces by 4% – 68% in the range of the parameters considered. Higher reductions are achievable at flow rates lower than 31 m^3/h.
- There is also an optimal Reynolds number at which the entropy generation rate is minimum at every given twist ratio and width ratio. Below the optimal Reynolds

number, low twist ratios and larger width ratios are preferred for low entropy generation rates. Whereas above the optimal Reynolds numbers, large twist ratios and low width ratios are preferred. For flow rates higher than 43 m^3/h, the use of twisted tape inserts is thermodynamically undesirable for most twist ratios and width ratios.

- A multi-objective optimisation approach was used to obtain Pareto optimal solutions. Moreover, results for different cases defined according to the level of importance of the objectives in the objective function were presented. In a case where the objectives are equally important, the Nusselt number increases in the range 1.81 – 2.36 with an increase in efficiency between 3.8 – 8.2% if the flow rate is lower than 43 m^3/h.

CHAPTER SEVEN

CHAPTER SEVEN: HEAT TRANSFER ENHANCEMENT IN PARABOLIC TROUGH RECEIVERS USING PERFORATED INSERTS

7.0 INTRODUCTION

As discussed above, heat transfer enhancement in parabolic trough receivers has several advantages, including: improvement in heat transfer performance, reduced absorber tube's circumferential temperature difference, increased thermal performance due to low radiation loss and reduced entropy generation rates due to reduced heat transfer irreversibilities.

As discussed above, the need to avoid the forming of hot spots in the receiver's absorber tube makes the use of tube inserts attractive for heat transfer enhancement. Tube inserts or displacement enhancement devices provide heat transfer enhancement by displacing the fluid from the heated or cooled surface with the fluid from the core flow [54]. Displacement enhancement devices as passive heat transfer enhancement techniques result in high fluid friction and are occasionally used for heat transfer enhancement [51,52,54,204]. Therefore, studies of the use of tube inserts are not widespread in the literature. However, several investigators have shown that careful selection of the geometry of these inserts may result in effective heat transfer enhancement with less fluid friction. For solar thermal applications, the gain in the collector's thermal performance achieved from the use of tube inserts may be much higher than the increase in the pumping power required. Moreover, it has also been reported that the use of tube inserts provides a means of reducing fouling in heat exchangers [205,206] and of keeping the heat exchanger's performance high.

Furthermore, for high temperature applications, thermal stresses become a concern for some heat transfer enhancement techniques such as grooved tubes [207]. Moreover, other enhancement techniques exhibit temperature hot spots [208], which can cause degradation of

the heat transfer fluid in parabolic trough receivers [55]. For this reason, for parabolic trough receivers, the use of tube inserts is an attractive alternative for heat transfer enhancement given the need to avoid thermal stresses in the absorber tube's wall and temperature hot spots. The temperature hotspots are of significant concern, given that most heat transfer fluids degrade at elevated temperatures (above 400 ^{o}C). Studies on heat transfer enhancement in parabolic trough receivers are not widespread, but several researchers have studied the use of inserts in other applications.

In their study on comparing the performance of some tube inserts, Wang and Sundén [209] report that the shape of the insert is an important factor for the performance of a given insert. This makes the selection of an insert complicated. They also state that, for the different inserts considered, the thickness of the insert does not affect the performance trend but influences the individual insert's performance. Zimparov and Penchev [210] used extended performance evaluation criteria to evaluate the performance of some tube inserts. They also report that the selection of the best tube insert depends on the shape, geometrical parameters, and geometrical and operational constraints of an insert.

Several other variations of tube inserts have been studied by several researchers. Kurtbaş *et al*. [211] proposed and investigated a novel conical injector-type swirl generator for heat transfer enhancement in a tube with a constant heat flux. They considered cone angles of 30^{o}, 45^{o} and 60^{o}; Reynolds numbers in the range of 10 000 – 35 000 with different numbers of circular holes in the different cross-sections. Using flow directors of different angles, decaying flow was obtained. They report that the heat transfer enhancement ratio decreases with a decrease in Reynolds numbers, and increases as the flow director angle increases. Both heat transfer and pressure drop are shown to be considerably affected by the cone angle. The heat transfer performance ratio measured at constant pumping power was obtained in the range 1.3 – 2.2.

Fan *et al.* [212] demonstrate that the use of conical strip inserts gives good thermo-hydraulic performance in the turbulent flow regime. From their study, the Nusselt number was augmented up to 5 times and the friction factor increased up to 10 times compared to a smooth tube. The performance evaluation criteria based on a constant pumping power

comparison in the range 1.67 – 2.06 was obtained for Reynolds numbers in the range 12 000 – 42 000. Air was used as the working fluid. In their recent study, You *et al.* [213] have shown that conical strip inserts have excellent performance in the laminar flow regime. The Nusselt number was increased in the range 3.70 – 5.51 times, the friction factor was increased 5.31 – 14.77 compared to those of plain tubes and the performance evaluation criteria based on constant pumping power were shown to be in the range 1.17 – 2.97.

Kongkaitpaiboon *et al.* [214] experimentally investigated the convective heat transfer and pressure loss in a round tube fitted with circular-ring turbulators. Using air as a test fluid, a uniform heat flux boundary condition and Reynolds numbers in the range 4 000 – 20 000, they obtained heat transfer augmentation of about 57% – 195% compared to a plain tube. The maximum thermal performance factor based on a constant pumping power comparison was 1.07 and the minimum was about 0.5.

Kongkaitpaiboon *et al.* [215] considered the use of perforated conical rings in turbulent convective heat transfer. Their study used uniform heat flux boundary conditions and Reynolds numbers in the range 4 000 – 20 000. For the range of parameters considered in their experiments, the heat transfer was increased up to 137%. The maximum thermal performance factor was about 0.92 at a pitch ratio of 4, with a conical ring of 8 holes for the lowest Reynolds number. The lowest thermal performance factor was about 0.5.

Promvonge [216] presents an experimental investigation on heat transfer enhancement in round tubes with conical ring inserts. Different diameter ratios were considered (d/D = 0.5, 0.6 and 0.7) with different arrangements for the rings. Air was used as the test fluid with a uniform heat flux boundary condition and the Reynolds numbers were varied in the range 6 000 – 26 000. He obtained heat transfer augmentation of between 91% – 333% with a substantial increase in the friction factor. The enhancement efficiencies based on a constant pumping power comparison were between 0.86 – 1.80.

Promvonge and Eiamsa-ard [217] experimentally investigated the influence of conical-nozzle turbulators on heat transfer and friction characteristics in a circular tube. For diverging nozzle arrangements and converging nozzle arrangements, the pitch ratios were 2.0, 4.0 and 7.0 and

the Reynolds numbers in the range of 8 000 – 18 000. They showed an increase in heat transfer in the range 236% – 344% compared to a plain tube depending on the Reynolds number and the arrangement of the turbulators.

To improve the effectiveness of heat transfer enhancement in the core flow, Liu *et al.* [57,58] suggest mechanisms for heat transfer enhancement in the core flow that might result in high heat transfer enhancement while keeping fluid friction low. They suggest that inserting a heat transfer component in the core flow of a tube may provide sufficient heat transfer enhancement while providing less resistance than the use of the extended surface heat transfer enhancement technique. Liu *et al.* [58] suggest (i) strengthening the temperature uniformity, (ii) increasing the fluid disturbance in the core flow, (iii) reducing the surface area of the heat transfer component in the core flow, and (iv) decreasing the fluid disturbance in the boundary flow, as some of the principles of heat transfer enhancement in the core flow.

These principles for heat transfer enhancement in the core flow and the other benefits of using porous inserts when compared with solid inserts such as: light-weight, low fluid friction and potential for forcing uniform flow distribution, have motivated several investigators to consider the use of porous media for heat transfer enhancement in the core flow [57-59]. Huang *et al*. [59], using porous medium inserts in a tube, investigated the flow resistance and heat transfer characteristics for laminar to turbulent ranges of Reynolds numbers. For porosities of 0.951, 0.966 and 0.975 they report that the heat transfer rate is about 1.6 – 5.5 times larger than that of smooth tubes with an accompanying increase in flow resistance. Using the performance evaluation criteria, they show that the integrated performance of heat transfer enhancement is better for the laminar case than in the turbulent case.

From the above literature review, tube inserts can result in better heat transfer enhancement if certain criteria are met. Their advantage of avoiding hot spots, preventing fouling and avoiding thermal stress in the absorber tube, makes them ideal for use in the parabolic trough receiver's absorber tube. Heat transfer enhancement in parabolic trough receivers has the potential to improve receiver thermal and thermodynamic performance through improved heat transfer performance and a reduction in receiver radiation loss. The reduction in receiver radiation loss is due to the reduced absorber tube temperatures and reduced absorber tube

emissivity. No studies are reported in the literature on the use of perforated inserts for heat transfer enhancement in parabolic trough receivers. Moreover, the available literature on the use of tube inserts uses the first law of thermodynamics to characterise their heat transfer and fluid friction performance. Studies on the use of the second law of thermodynamics to determine the resulting irreversibilities, the resulting entropy generation rates and optimal Reynolds numbers are not widespread.

Therefore, this chapter discusses the investigation of the performance of a parabolic trough receiver whose absorber tube is fitted with two types of perforated inserts for heat transfer enhancement in the core flow. The two inserts considered are: perforate plate inserts (PPI) and perforated conical inserts (PCI). In addition to the analysis of the heat transfer and fluid friction performance, the second law of thermodynamics is used to determine the entropy generation rates resulting from the use of these inserts. Furthermore, a multi-objective optimisation approach was used to determine the optimal solutions for maximum heat transfer and minimum fluid friction.

7.1 MODEL DESCRIPTION

This section briefly describes models of parabolic trough receivers whose absorber tubes are fitted with the above-mentioned two types of inserts.

7.1.1 PHYSICAL MODELS AND COMPUTATIONAL DOMAINS

Figures 7.1 (a and b) show the physical model of a parabolic trough receiver whose absorber tube is fitted with perforated plate inserts (longitudinal and cross-sectional views respectively). Similar to the previous discussion on conventional receivers, the annulus space between the absorber tube and glass cover is evacuated to very low pressures so that only radiation heat transfer takes place. Far from the entrance, the flow is periodically fully developed, therefore, for reduced computational complexity, a periodic module of the receiver was considered. Due to the symmetrical nature of the receiver, only half of the receiver was considered.

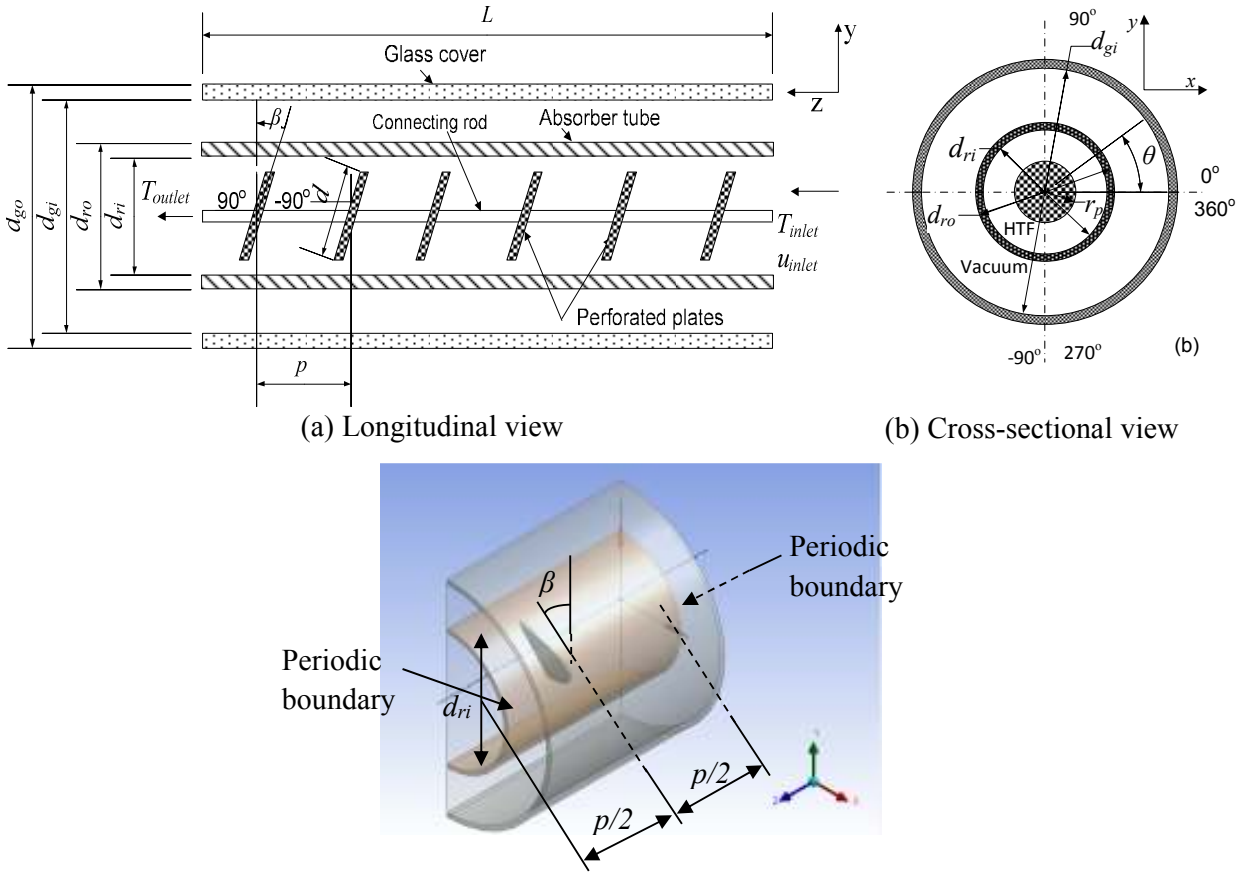

Fig. 7.1: Schematic representation of the physical model and computational domain of a receiver with perforated plate inserts.

Figure 7.1 (c) shows the computational domain adopted for a parabolic trough receiver with perforated plate inserts. From the physical model in Fig 7.1, the following non-dimensional parameters have been defined:

The dimensionless pitch (insert spacing per unit metre) is given by

$$\tilde{p} = \frac{p}{L} \qquad 7.1$$

where L is the length of the receiver, in this case L = 1 m.

The dimensionless plate orientation angle β is given by

$$\tilde{\beta} = \frac{\beta}{\beta_{\max}} \tag{7.2}$$

where β_{max} is 30° for this case. β is taken to be negative in the clockwise direction (plate opposing flow in absorber tube's upper half) and positive in the counter-clockwise direction.

The dimensionless plate diameter is given as

$$\tilde{d} = \frac{d}{d_{ri}} \tag{7.3}$$

Figure 7.2 (a and b) shows the physical model of a parabolic trough receiver model with a perforated conical insert (PCI) (longitudinal and cross-sectional views respectively). For the same reasons as those in the previous discussion, to reduce further the computational cost and time, the flow inside the absorber tube was considered as periodically fully developed and periodic boundary conditions were used at the absorber tube's inlet and outlet. The flow is also symmetric; the computational domain considered for the PCI model is shown in Fig. 7.2 (c).

For the receiver with perforated conical inserts, the dimensionless pitch (insert spacing per unit metre) is defined as

$$\tilde{p}_c = \frac{p}{L} \tag{7.4}$$

where L =1 m

The dimensionless insert cone angle is given by

$$\tilde{\beta}_c = \frac{\beta}{\beta_{\max}} \tag{7.5}$$

where β_{max}= 90º for perforated conical inserts. For β = 0, the insert is similar to a plate placed perpendicular to the flow direction.

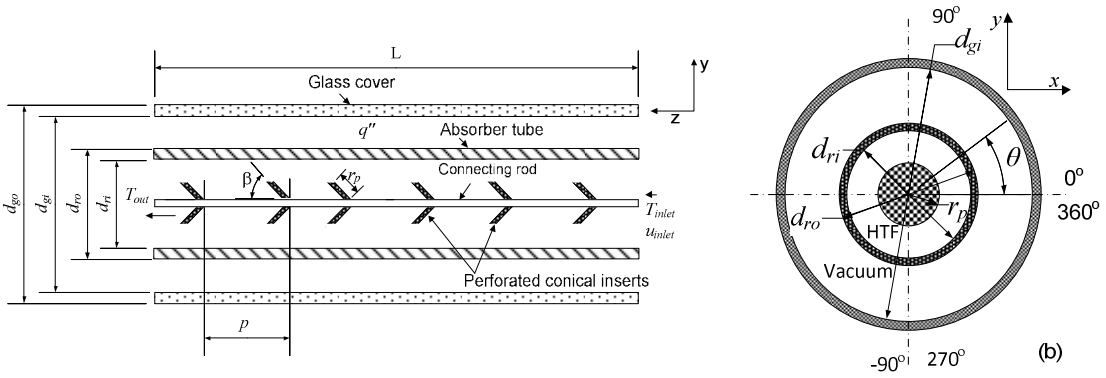

(a) Longitudinal view (b) Cross-sectional view

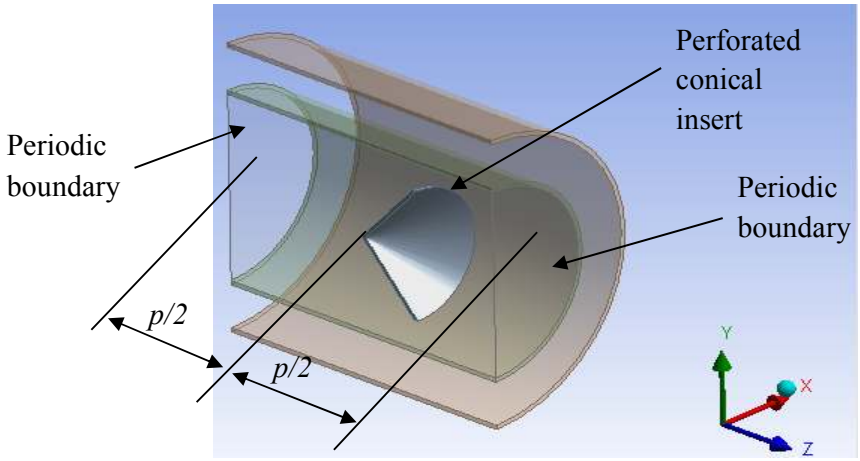

(c)

Fig. 7.2: Schematic representation of the physical model and computation domain of a receiver with perforated conical inserts.

The dimensionless insert radius is defined as

$$\tilde{r}_c = \frac{2r_p}{d_{ri}} \tag{7.6}$$

In Eqs. (7.1) – (7.6), d_{ri} is the absorber tube's inner diameter and p is the spacing between two consecutive inserts.

Similar to the previous chapters, a commercially available receiver was used. The inner diameter of the absorber tube was fixed at 6.6 cm and the outer diameter at 7.0 cm. The other general geometrical parameter, optical parameters and other simulation parameters used in this study are shown in Table 7.1.

7.1.2 GOVERNING EQUATIONS

The flow in the absorber tube is in the fully developed turbulent regime. The flow is also taken to be steady-state. The Reynolds Averaged Navier-Stokes equations (RANS) (Eqs. 3.2-3.4), detailed in Section 3.3.1 are applicable to for this kind of problem. For perforated inserts, the momentum equation is written with an additional source term, so that Eq. (3.3) becomes:

Conservation of momentum

$$\frac{\partial}{\partial x_j}\left(\rho\overline{u}_i\overline{u}_j\right) = -\frac{\partial \overline{P}}{\partial x_i} + \frac{\partial}{\partial x_j}\left[\mu\left(\frac{\partial \overline{u}_i}{\partial x_j} + \frac{\partial \overline{u}_j}{\partial x_i}\right) - \frac{2}{3}\mu\frac{\partial \overline{u}_i}{\partial x_i}\delta_{ij} - \rho\overline{u_i'u_j'}\right] + S_m \qquad 7.7$$

The source term (S_m) added to the momentum equation in Eq. (7.7) represents the pressure drop across the perforated insert. The perforated inserts are modelled as porous media of finite thickness with directional permeability over which there is a pressure drop. The pressure drop is defined as a sum of the viscous term according to Darcy's law [88] and an inertial loss term [88].

$$\nabla p = -\left(\frac{\mu}{\alpha_p}u_i + C_{2p}\frac{1}{2}\rho|u|u_i\right)\Delta m \qquad 7.8$$

where α_p is the permeability of the porous medium, C_{2p} is the inertial resistance factor and Δm is the thickness of the porous media. For perforated plates, it has been shown that the first term representing the viscous loss is so negligible that only the inertial loss term should be considered [88,218,219]. The coefficient C_{2p} has been determined from the data presented by Weber *et al.* [220] for perforated plates and flat bar screens. In the streamwise direction, C_{2p} = 853 m^{-1} for the considered porosity of 0.65, and plate thickness of 0.0015 m. In other

directions, inertial resistance factors of much higher magnitude are specified to restrict the flow in those directions.

For turbulence closure, the realisable k-ε is used. As discussed above, this model is an improvement of the standard k-ε with superior performance for separated flows and flows with complex secondary features. The model solves two additional equations for turbulent kinetic energy (Eq.3.7) and turbulent dissipation rate (Eq.3.8) as detailed in Section 3.31 of this thesis.

7.1.3 BOUNDARY CONDITIONS

7.1.3.1 Perforated plate inserts

The boundary conditions used for the perforated plate insert model were the same as those described in Chapter 4 for model A of the receiver. They include: the periodic boundary conditions at the inlet and outlet, a prescribed temperature at the inlet, a non-uniform heat flux at a rim angle of 80^o and a concentration ratio of 86 as given in Fig. 4.11 (a). This heat flux was coupled with a computational fluid dynamics code using a user-defined function. The radiation heat exchange between the absorber tube and glass cover was modelled as discussed in Chapter 4.0 for model A of the receiver.

7.1.3.2 Perforated conical inserts

For the conical inserts, model A of the receiver was used with periodic boundary conditions. The boundary conditions used include: the periodic boundary conditions at the inlet and outlet (specified mass flow rate and specified temperature at the periodic boundaries), a non-uniform heat flux at a rim angle of 80^o and a concentration ratio of 86 as given in Fig. 4.11 (a). This heat flux was coupled with a computational fluid dynamics code using a user-defined function. The radiation heat exchange between the absorber tube and glass cover was modelled as discussed in Chapter 4 for model A of the receiver.

Detailed simulation parameters for both models are given in Table 7.1.

Table 7.1: Simulation parameters for the parabolic trough receiver with perforated inserts

	Value
Absorber tube diameter (m)	0.066
Absorber tube thickness (m)	0.002
Glass envelope inner diameter (m)	0.115
Inlet temperature (K)	400 – 650
Reynolds number	$1.03 \times 10^4 - 1.35 \times 10^6$
Direct normal solar irradiance (W/m^2)	1 000
Geometrical concentration ratio, C_R	86
$\tilde{p}$	0.04 – 0.20
$\tilde{d}$	0.45 – 0.91
$\tilde{\beta}$	$-1 \leq \tilde{\beta} \leq 1$
$\tilde{p}_c$	0.06 – 0.18
$\tilde{r}_c$	0.45 – 0.91
$\tilde{\beta}_c$	$0.40 \leq \tilde{\beta}_c \leq 0.90$

7.1.4 SOLUTION PROCEDURE

The numerical solution was implemented in the commercial software package ANSYS® 14.5. The geometry was built in ANSYS design modeller and the computational grid created in ANSYS meshing. The numerical solution was obtained in ANSYS FLUENT, which uses a finite volume method for solving the governing continuity, momentum, energy and k-ε model equations. The SIMPLE algorithm [92] was used for coupling the pressure and velocity. Second-order upwind schemes were employed for integrating the governing equations together with the boundary conditions over the computational domain. Radiation heat transfer in the receiver's annulus spaced was modelled using the Discrete Ordinates model in ANSYS FLUENT [88] with air in the evacuated annulus space as non-participating media.

Due to the complexity of the geometry, the domain was discretised with tetrahedral volume elements with a structured mesh in the absorber tube wall's normal direction. The mesh for the 3-D model of the absorber tube with perforated plates used in this study is shown in Fig. 7.3. The mesh for the periodic model of the absorber tube with perforated conical inserts is shown in Fig. 7.4. Grid dependence studies for several refinements of the mesh were

carried out with the volume integral entropy generation, Nusselt number and fluid friction as monitored quantities for representative cases of both types of inserts. The number of mesh elements depends on the pitch, size of the plate and angle of orientation.

Given the need to capture a high resolution of gradients near the wall, the enhanced-wall treatment [88] was used, with $y^+ \approx 1$ in the absorber tube wall's normal direction used for all simulations. Accordingly, the mesh dependence studies were carried out at each different Reynolds number independently. Tables 7.2 and 7.3 show the sample grid dependence tests for sample cases of the perforated plate inserts and perforated conical inserts respectively.

The solution was considered grid-independent when the maximum change in the entropy generation rate, Nusselt number and friction factor was less than 2% as the mesh element size was changed. The changes in friction factor, Nusselt number and entropy generation as the mesh size was changed, are given by

$$\Delta f = \left|(f^i - f^{i+1})/f^{i+1}\right|;\ \Delta Nu = \left|(Nu^i - Nu^{i+1})/Nu^{i+1}\right|;\ \Delta S_{gen} = \left|(\phi^i - \phi^{i+1})/\phi^{i+1}\right|.$$
$$\text{where } \phi = S_{gen}/(S_{gen})_o \qquad 7.9$$

In Eq. (7.9), the indices *i* and *i+1* indicate the mesh before and after refinement respectively.

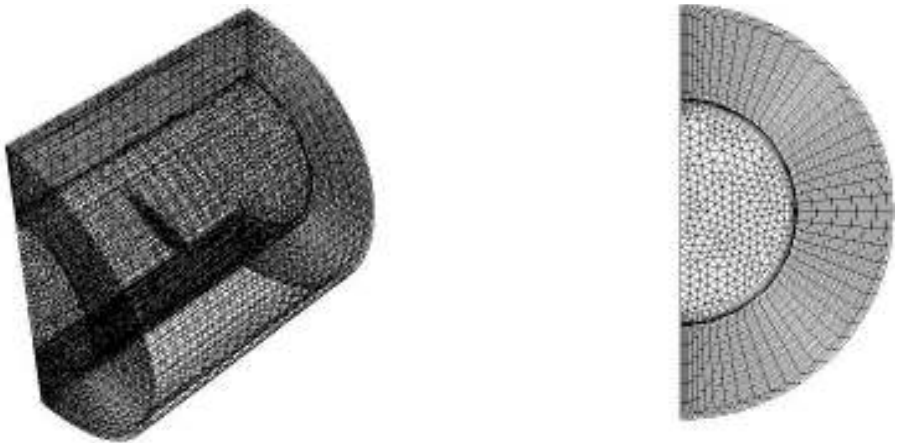

(a) Lateral view (b) Cross-sectional view

Fig. 7.3: Discretised computational domain of a receiver with perforated plate inserts.

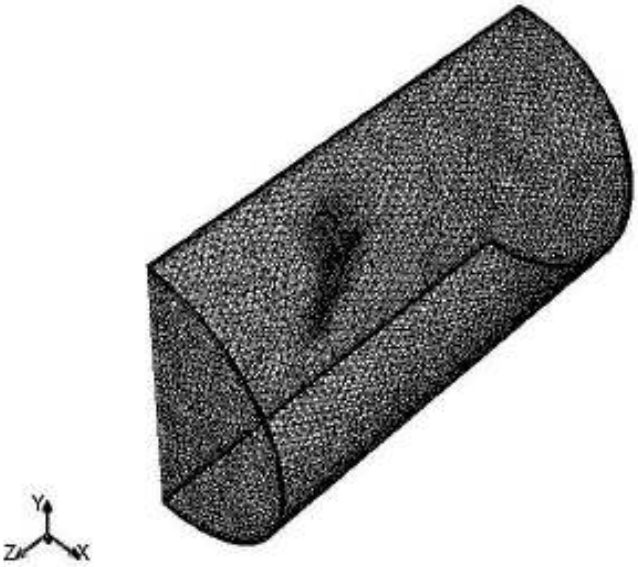

(a) Lateral view

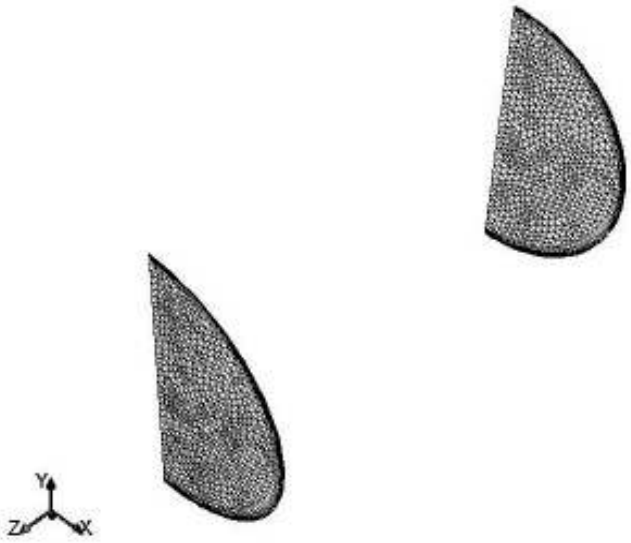

(b) Periodic boundaries

Fig. 7.4: Discretised computational domain of the receiver's absorber tube with perforated conical inserts.

Solution convergence was obtained with scaled residuals of mass, momentum, turbulent kinetic energy and turbulence dissipation rate of less than 10^{-4} whereas the energy residuals were less than 10^{-7}. Convergence was also monitored using the convergence history of

volume-averaged entropy generation in the absorber tube. The solution was considered converged when the volume-averaged entropy generation remained constant for more than 200 successive iterations.

Table 7.2: Mesh dependence studies for a parabolic trough receiver with perforated plate inserts

Mesh elements	f	Nu	$S_{gen}/(S_{gen})_o$	Δf	ΔNu	ΔS_{gen}
(a) $Re = 1.02 \times 10^4$, $\tilde{p} = 0.09$, $\tilde{d} = 0.76$ and $\tilde{\beta} = -1$						
55 635	0.3825	225.8	0.686			
90 863	0.3820	217.7	0.752	0.001	-0.037	0.088
154 925	0.3819	217.8	0.749	0.000	0.000	0.003
(b) $Re = 1.94 \times 10^4$, $\tilde{p} = 0.18$, $\tilde{d} = 0.91$ and $\tilde{\beta} = 0$						
83 557	0.4079	305.6	0.924			
141 617	0.4080	313.0	0.862	0.000	0.023	-0.07
200 900	0.4085	314.0	0.858	0.001	0.003	-0.005
350 855	0.4092	315.2	0.858	0.002	0.004	-0.000

Table 7.3: Mesh dependence studies for a parabolic trough receiver with perforated conical inserts

Mesh elements	f	Nu	$S_{gen}/(S_{gen})_o$	Δf	ΔNu	ΔS_{gen}
(a) Re = 1.94 x 10^4, $\tilde{p}_c$ = 0.06, $\tilde{r}_c$ =0.91 and $\tilde{\beta}_c$ = 0.67						
46 381	0.752	391.8	0.771			
84 668	0.784	388.6	0.757	0.040	0.008	0.018
156 720	0.794	388.2	0.749	0.013	0.001	0.011
(b) Re = 1.94 x 10^4, $\tilde{p}_c$ = 0.15, $\tilde{r}_c$ = 0.91 and $\tilde{\beta}_c$ = 0.67						
77 623	0.380	336.0	0.864			
147 875	0.306	326.1	0.909	0.079	0.030	0.049
250 860	0.305	326.5	0.903	0.002	0.001	0.007
(c) Re = 6.40 x 10^4, $\tilde{p}_c$ = 0.07, $\tilde{r}_c$ = 0.91 and $\tilde{\beta}_c$ = 0.33						
53 424	0.1117	972.7	0.866			
104 004	0.1112	895.1	0.950	0.005	0.087	0.089
205 186	0.1122	873.7	0.965	0.009	0.024	0.015
308 841	0.1109	878.4	0.866	0.012	0.005	0.006
(d) Re = 6.40 x 10^4, $\tilde{p}_c$ = 0.15, $\tilde{r}_c$ = 0.45 and $\tilde{\beta}_c$ = 0.83						
89 553	0.095	858.9	0.983			
157 113	0.094	834.4	0.964	0.007	0.029	0.020
284 443	0.094	826.1	0.958	0.004	0.010	0.006
(e) Re = 1.150 x 10^5, $\tilde{p}_c$ = 0.10, $\tilde{r}_c$ = 0.91and $\tilde{\beta}_c$ = 0.89						
114 510	0.689	2074.4	1.053			
226 331	0.691	1908.6	1.183	0.110	0.087	0.003
319 413	0.690	1885.8	1.185	0.021	0.012	0.002
434 744	0.690	1880.6	1.209	0.002	0.003	0.000

Syltherm 800 [110] was used as the heat transfer fluid in the receiver's absorber tube. Given the limitations of the periodic model, the properties of the heat transfer fluid were evaluated at the fluid temperatures of 400 K, 500 K, 600 K and 650 K used in this study. Sample fluid properties at different temperatures are given in Table 4.2 as determined from the manufacturer's specifications [110].

The receiver parameters and environmental conditions used were the same as those presented in Table 4.1. Stainless steel was used as the absorber tube material in both cases. The coating of the absorber tube has an emissivity that varies with temperature according to Eq. (2.33).

7.1.5 DATA REDUCTION

The heat transfer performance is given in terms of the heat transfer coefficient and Nusselt numbers. The average heat transfer coefficient is given by

$$h = \frac{q''}{T_{ri} - T_b} \tag{7.10}$$

where T_{ri} is the inner wall temperature of the absorber tube and T_b represents the bulk temperature of the fluid. From the average heat transfer coefficient, the average Nusselt number is given by

$$Nu = h\frac{d_{ri}}{\lambda} \tag{7.11}$$

where λ is the thermal conductivity of the heat transfer fluid and d_{ri} is the inner diameter of the absorber tube.

The friction factor is related to the pressure drop according to

$$f = \frac{\Delta P}{\frac{1}{2}\rho \cdot u_{inlet}^2 \frac{L}{d_{ri}}} \tag{7.12}$$

u_{inlet} is the mean velocity at the periodic boundaries. Equation (7.12) for the friction factor can be rewritten as

$$f = \frac{\Delta P}{\frac{1}{2}\rho \cdot u_m^2 \frac{L}{d_{ri}}} \tag{7.13}$$

In Eq. (7.12 and 7.13), ΔP is the pressure drop, ρ is the density of the heat transfer fluid, u_{inlet} is the inlet velocity, u_m is the mean velocity of flow inside the absorber tube, L is the length under consideration and d_{ri} is the inner diameter of the absorber tube.

For the preliminary evaluation of heat transfer enhancement techniques at constant pumping power, the thermal enhancement factor (χ) [200] was used. According to this, the pumping power of the enhanced tube is equal to the pumping power of the plain tube. Such that:

$$\left(\dot{V}\Delta P\right)_p = \left(\dot{V}\Delta P\right)_{en} \tag{7.14}$$

Expressing the volume flow rate ($\dot{V}$) and the pressure drop (ΔP) in terms of friction factors and Reynolds numbers Eq. (7.14) becomes

$$\left(f\,\mathrm{Re}^3\right)_p = \left(f\,\mathrm{Re}^3\right)_{en} \tag{7.15}$$

The thermal performance factor χ of the absorber tube fitted with perforated inserts for the same pumping power criteria is given as [200]

$$\chi = \left.\frac{Nu_{en}}{Nu_p}\right|_{pp} = \left(\frac{Nu_{en}}{Nu_p}\right)\left(\frac{f_p}{f_{en}}\right)^{1/3} \tag{7.16}$$

The heat transfer enhancement factor is defined from Eq. (7.16) as the ratio of the Nusselt number obtained with inserts to that in a plain absorber tube, given by

$$Nu^+ = \frac{Nu_{en}}{Nu_p} \tag{7.17}$$

The pressure drop penalty factor is defined as the ratio of the pressure drop in the absorber tube with inserts to that in a plain absorber tube, as given by

$$f^+ = \frac{f_{en}}{f_p} \tag{7.18}$$

Another performance evaluation criterion for heat transfer enhancement techniques is based on the second law of thermodynamics [61,201,202]. The rates of entropy generation in an enhanced tube are compared to those of plain tubes. The enhancement entropy generation number $N_{s,en}$ is defined as [202]

$$N_{s,en} = \frac{S_{gen,en}}{s_{gen,p}} \tag{7.19}$$

Enhancement techniques with $N_{s,en} < 1$ are taken to be thermodynamically advantageous [202]. As the heat transfer performance is improved, there is a reduction in irreversibilities when compared to the plain tube. The entropy generation rates are determined according to Eqs. (3.35) – (3.41) as detailed in Chapter 3.

Heat transfer enhancement should provide a considerable reduction in the heat transfer irreversibility with a minimum increase in fluid flow irreversibilities. The Bejan number defines the ratio of entropy generation due to heat transfer irreversibility to the total entropy generation rate as

$$Be = \frac{\left(S_{gen}\right)_H}{S_{gen}} \tag{7.20}$$

The Bejan number is in the range $0 \leq Be \leq 1$. For $Be \approx 0$ fluid flow irreversibility are dominant and for $Be \approx 1$, the heat transfer irreversibilities dominate.

7.1.6 MODEL VALIDATION

The validation of the receiver model is presented in Chapter 4, and so too is the validation of heat transfer and friction factors for the plain absorber tube. The validation of the entropy generation model is presented in Chapter 5.

The perforated insert model was validated using data from Guohui and Saffa [221]. The variation of the pressure coefficient $k = p_s/p_v$ with distance from the perforated plate is shown in Fig. 7.5. The same trend as that obtained by Guohui and Saffa [221] was obtained in the current work, with a maximum deviation of less than 3% (p_s is the static pressure and p_v is the velocity pressure given by $p_v = 1/2\rho v^2$).

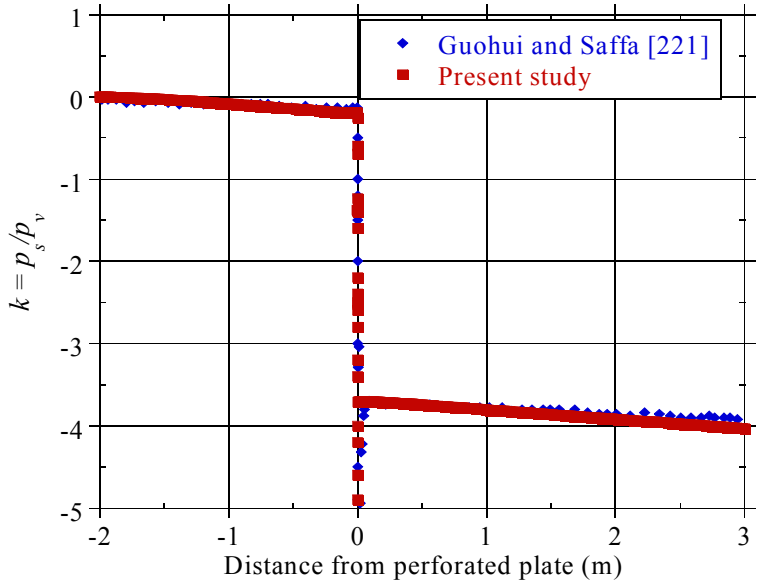

Fig. 7.5: Comparison of present study pressure coefficient as a function of distance from the perforated plate with literature.

Because the perforated plate is modelled in CFD as porous media with negligible viscous loss, numerical data from Kumar and Reddy [49], for a receiver with a wall-mounted porous disc at different angles was also used for further validation and comparison. Table 7.4 shows the comparison of our numerical model with Kumar and Ravi [49] for the orientation of the porous disc of 30°. Good agreement was achieved for both the Nusselt number and the drag coefficient. The porous disc model was then converted to a perforated insert model by assuming negligible viscous loss in Eq. (7.8) for our subsequent investigations.

Table 7.4: Comparison of present study predicted heat transfer and fluid friction performance of the receiver perforated plate model with data from Kumar and Reddy [49]

Reynolds number	Nusselt Number			Drag coefficient $= \frac{2\Delta p}{\rho u^2}$		
	Kumar and Reddy [49]	Present study	Percentage deviation	Kumar and Reddy [49]	Present study	Percentage deviation
6.37×10^4	550	600	9.1	1 380	1 250	-9.4
1.27×10^5	925	986	6.6	1 057	1 150	8.1
1.91×10^5	1 321	1 375	4.1	1 008	1 040	3.1
2.55×10^5	1 704	1 750	2.7	982	1 000	1.8

7.2 RESULTS AND DISCUSSION – PERFORATED PLATE INSERTS

7.2.1 FLOW STRUCTURE

The flow behaviour for the perforate plate model is shown in Fig. 7.6 using contours of velocity.

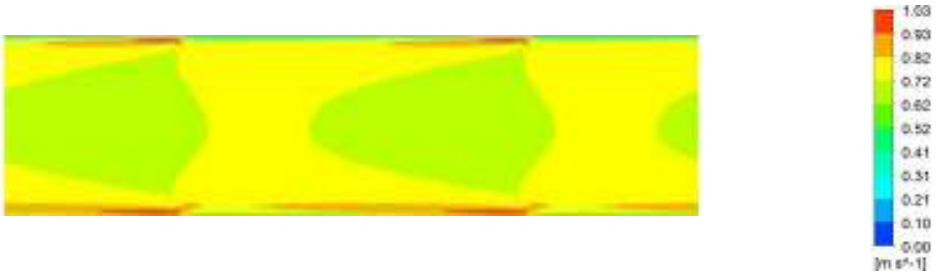

(a) $Re = 1.94 \times 10^4$, $\tilde{\beta} = 0$, $\tilde{d} = 0.91$, $\tilde{p} = 0.18$ and $T_{inlet} = 400$ K

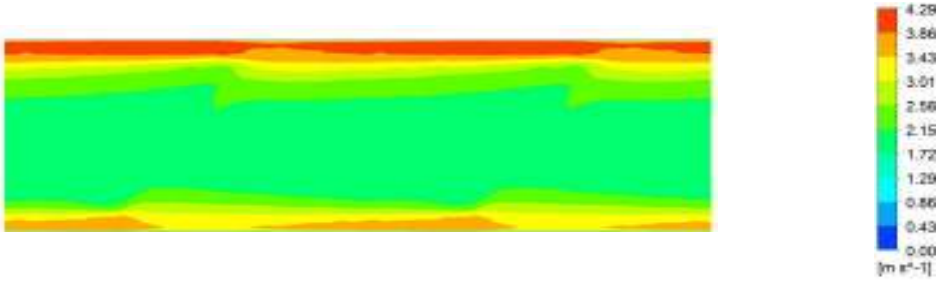

(b) $Re = 1.48 \times 10^5$, $\tilde{\beta} = -1$, $\tilde{d} = 0.91$, $\tilde{p} = 0.09$ and $T_{inlet} = 500$ K

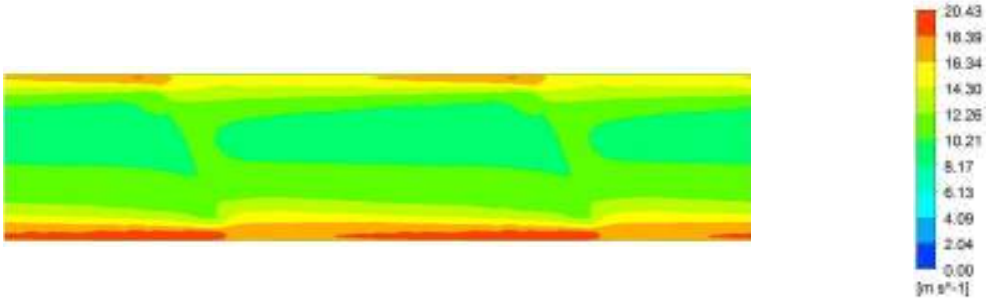

(c) $Re = 1.35$ x10^6, $\tilde{\beta} = 0.83$, $\tilde{d} = 0.91$, $\tilde{p} = 0.15$ and $T_{inlet} = 600$ K

Fig. 7.6: Velocity contours for a receiver with perforated plate inserts on the symmetry plane of the receiver's absorber tube at different values of Reynolds numbers, insert orientation ($\tilde{\beta}$), insert spacing ($\tilde{p}$), insert size ($\tilde{d}$) and inlet temperatures.

The flow behaviour presented by the use of centrally placed perforated plates involves fluid displacement from the core flow, fluid mixing and flow impingement. Figure 7.6 shows the velocity contours for three sample cases. The figure shows the resulting fluid displacement, fluid mixing and flow impingement mechanism at three different angles of orientation ($\tilde{\beta}$= 0, -1 and 0.83 respectively) for different Reynolds numbers, for spacing when the size of the plate is $\tilde{d}$ = 0.91 and inlet temperatures are 400 K, 500 K and 600 K respectively.

At $\tilde{\beta}$ = 0, the flow remains perpendicular to the perforated plate and no considerable mixing is observed as shown in Fig. 7.6 (a). Figure 7.6 (b) shows that, for negative values of $\tilde{\beta}$, flow impingement occurs in the upper half of the absorber tube. The perforated plate causes the displacement of the fluid from the upper to the lower half, and mixes the upper fluid with the lower heated fluid. At positive values of $\tilde{\beta}$, flow impingement is observed on the lower half of the absorber tube and fluid is displaced from the lower half to the upper half of the absorber tube as shown in Fig. 7.6 (c). After impinging on the absorber tube's wall, some of the fluid tends to slide on the plate depending on the angle of orientation. Therefore, the plate angle can be selected well to have high heat transfer rates by achieving high impingement rates on the absorber tube's lower wall while keeping the fluid friction lower.

7.2.2 HEAT TRANSFER PERFORMANCE

7.2.2.1 Nusselt numbers

The heat transfer performance of a parabolic trough receiver whose absorber tube is fitted with a perforated plate inserts is dependent on the plate spacing, plate size and plate angle of orientation. Figure 7.7 (a – d) show the variation of heat transfer performance with the size of the perforated plate at different plate orientation angles for given values of Reynolds numbers. The figures indicate that the Nusselt number will increase with the size of the plate at any Reynolds number and angle of orientation. As the size of the plate increases, higher fluid impingement occurs on the absorber tube's wall. Also, the turbulent intensity in the free space between the insert and tube increases with an increase in plate size. Generally, the heat transfer performance is shown to increase slightly as the angle of orientation increases. For

most cases, the highest heat transfer performance was shown for $\tilde{\beta} = 1$. This is probably due to high impingement on the lower half of the absorber tube at positive angles of orientation.

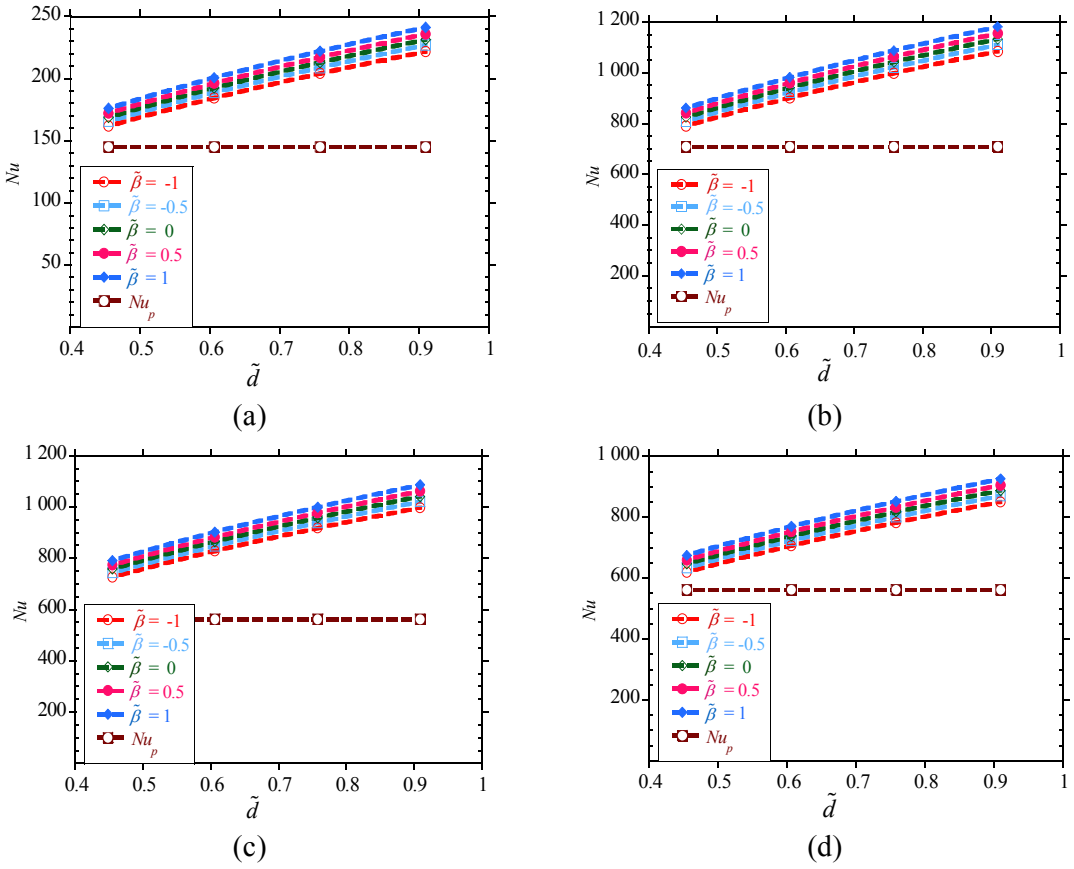

Fig. 7.7: Heat transfer performance of a receiver with perforated plate inserts as a function of insert size ($\tilde{d}$) and insert angle orientation ($\tilde{\beta}$): (a) inlet temperature of 400 K, Re = 1.02×10^4 and insert spacing, $\tilde{p}$ = 0.04, (b) inlet temperature of 400 K, Re = 6.40×10^4 and $\tilde{p}$ = 0.12, (c) inlet temperature of 600 K, Re = 8.05×10^4 and $\tilde{p}$ = 0.04 and (d) inlet temperature of 600 K, Re = 8.05×10^4 and $\tilde{p}$ = 0.12.

Figure 7.8 (a – b) shows the variation of the Nusselt number with Reynolds numbers for different values of insert spacing for $\tilde{d}$ = 0.61 and 0.91 respectively at $\tilde{\beta}$= 1 for 400 K.

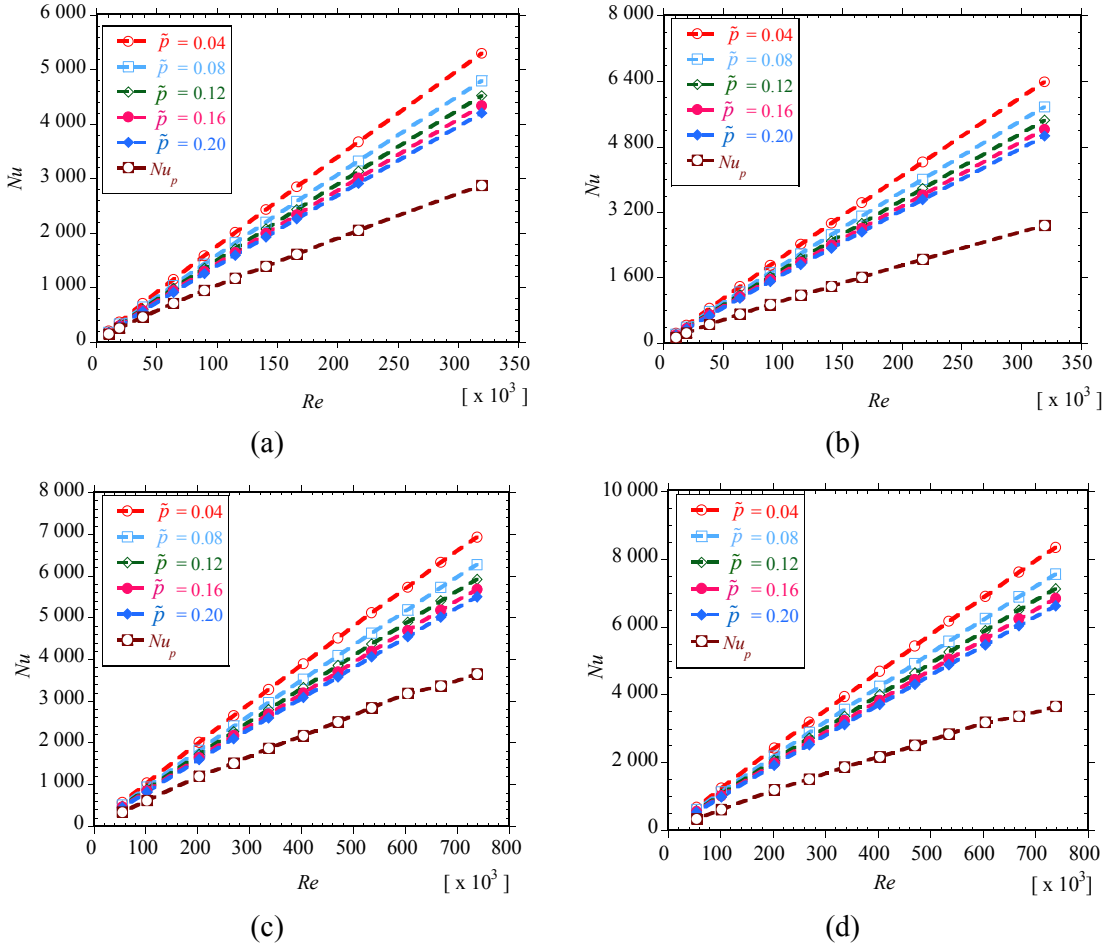

Fig. 7.8: Heat transfer performance of a receiver with perforated plate inserts as a function of Reynolds number and insert spacing ($\tilde{p}$): (a) inlet temperature of 400 K, insert size, $\tilde{d}$ = 0.61 and insert orientation, $\tilde{\beta}$ = 1, (b) inlet temperature of 400 K, $\tilde{d}$ = 0.91 and $\tilde{\beta}$ = 1, (c) inlet temperature of 650 K, $\tilde{d}$ = 0.61 and $\tilde{\beta}$ = 1 and (d) inlet temperature of 650 K, $\tilde{d}$ = 0.91 and $\tilde{\beta}$ = 1.

Figure 7.8 (c-d) shows the same variation and for $\tilde{d}$ = 0.61 and 0.91 respectively at $\tilde{\beta}$ = 1 for 650 K. It can be seen that the Nusselt number increases with the reduction in plate spacing at all values of plate size. The reduction in plate spacing implies an increased number of plates per metre, hence improved fluid mixing and fluid impingement on the absorber tube wall. As seen in Fig. (7.7) and Fig. (7.8), the heat transfer performance depends more strongly on the

size of the plate and the spacing between the consecutive plates than on the angle of orientation.

7.2.2.2 Heat transfer enhancement factor

The heat transfer enhancement factor in Eq. (7.17) gives the ratio of Nusselt number due to heat transfer enhancement to that in a plain absorber tube. It basically shows how much the heat transfer rate has increased. Figure 7.9 shows the variation of the heat transfer enhancement factor with Reynolds numbers for different values of plate spacing.

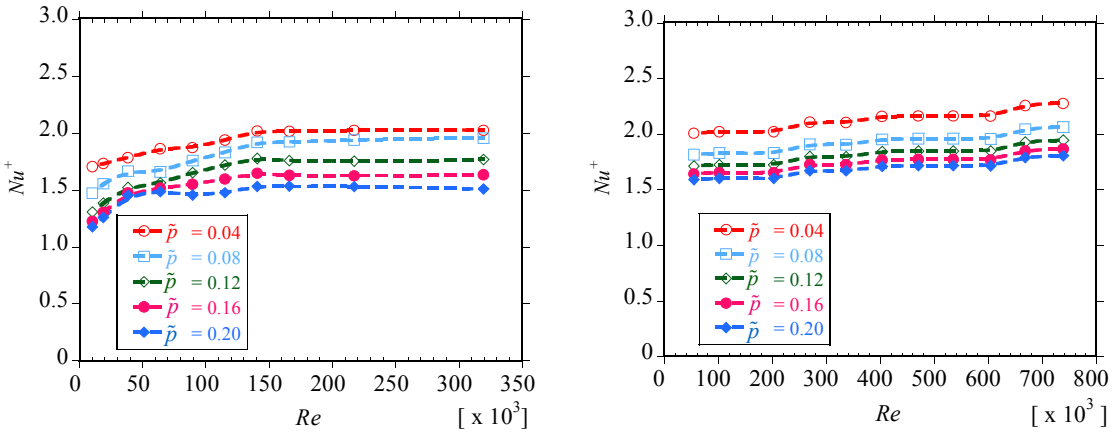

Fig. 7.9: Heat transfer enhancement factors for a receiver with perforated plate inserts as a function of Reynolds number and insert spacing ($\tilde{p}$): (a) inlet temperature of 400 K, insert size, $\tilde{d}$ = 0.91 and insert orientation, $\tilde{\beta}$ = 1 and (b) inlet temperature of 650 K, $\tilde{d}$ = 0.91 and $\tilde{\beta}$ = 1.

Generally, the heat transfer enhancement factor is shown to increase as the Reynolds number increases, after which it becomes nearly constant. In this study, for the range of parameters considered, the value of Nu^+ was in the range $1.08 \leq Nu^+ \leq 2.33$ depending on the angle of orientation, plate spacing and size of the plate.

7.2.2.3 Nusselt number correlation

Based on the results of the numerical simulation, a correlation for the Nusselt number was obtained for the range of parameters considered by using regression analysis.

The Nusselt number is correlated by

$$Nu = \frac{5.817\,\mathrm{Re}^{0.9485}\,\mathrm{Pr}^{0.4050}\,\tilde{p}^{-0.1442}\tilde{d}^{0.4568}(1+0.0742\tan\beta)}{1000} \qquad 7.21$$

Valid for $1 \times 10^4 \leq Re \leq 1.35 \times 10^6$ and $10.7 \leq \mathrm{Pr} \leq 33.7$

$-30 \leq \beta \leq 30^{o}$

$0.04 \leq \tilde{p} \leq 0.20$

$0.61 \leq \tilde{d} \leq 0.91$

$400\ \mathrm{K} \leq \mathrm{T} \leq 600\ \mathrm{K}$

The goodness of fit is given by the correlation coefficient (R^2). $R^2 = 0.998$ for this correlation. The correlation is within less than ± 15% for the range of parameters considered, as shown in the parity plot (Fig. 7.10) for over 450 data points.

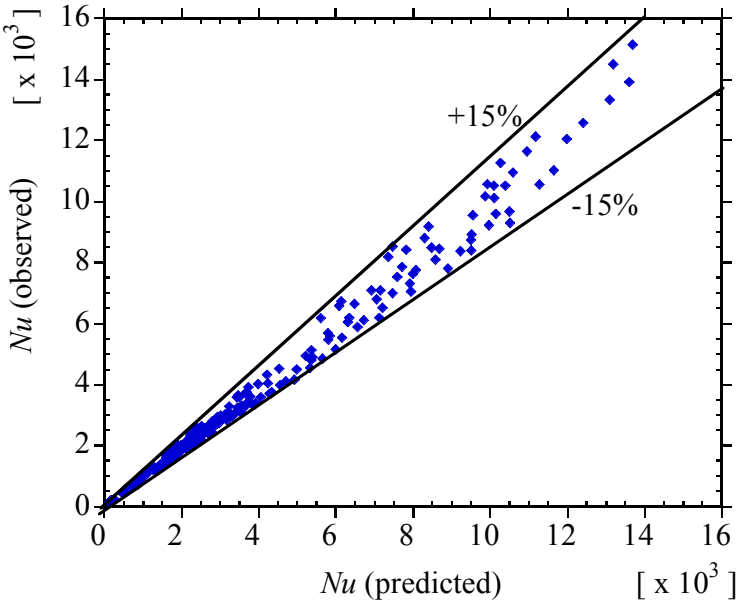

Fig. 7.10: Comparison of present study predicted heat transfer performance with the observed heat transfer performance for a receiver with perforated plate inserts.

7.2.3 PRESSURE DROP

7.2.3.1 Friction factors

The pressure drop is related to the friction factors through Eq. (7.12). An increase in friction factor at a given Reynolds number implies an increase in pressure drop. The variation of friction factors with perforated plate orientation, spacing and size is presented in this section.

Figure 7.11 (a – d) shows the variation of friction factor with the size of the plate at Re = 1.02 ×10^4, $\tilde{p}$ = 0.04 and T_{inlet} = 400 K; Re = 1.02 ×10^4, $\tilde{p}$ = 0.20 and T_{inlet} = 400 K; Re = 4.26 ×10^4, $\tilde{p}$ = 0.04 and T_{inlet} = 600 K, Re = 4.26 ×10^4, $\tilde{p}$ = 0.20 and T_{inlet} = 600 K respectively. As expected, the friction factors in the absorber tube with inserts are significantly higher than those in the absorber tube with no inserts. It can also be observed that the friction factor increases significantly as the size of the perforated plate increases for all the four cases; this is due to the increased obstruction to flow as the plate size increases.

It can also be seen from the figures that the angle of orientation of the perforated plate slightly affects the friction factor at low values of plate size and significantly as the plate size increases. The friction factors at $\tilde{\beta}$ = 1 and -1 are shown to be equal for a given value of plate size and Reynolds number. Similarly the friction factors at $\tilde{\beta}$ = 0.5 and - 0.5 are also equal for a given value of plate size and Reynolds number. This is because there is the same resistance to fluid motion by the perforated plate at these equal but opposite angles. Fluid friction is shown to be higher at angles close to $\tilde{\beta}$ = 0. For a given plate size, the obstruction to fluid flow increases as $\tilde{\beta}$ approaches 0. At the same Reynolds number and inlet temperature, the friction factor is shown to increase significantly as the spacing reduces.

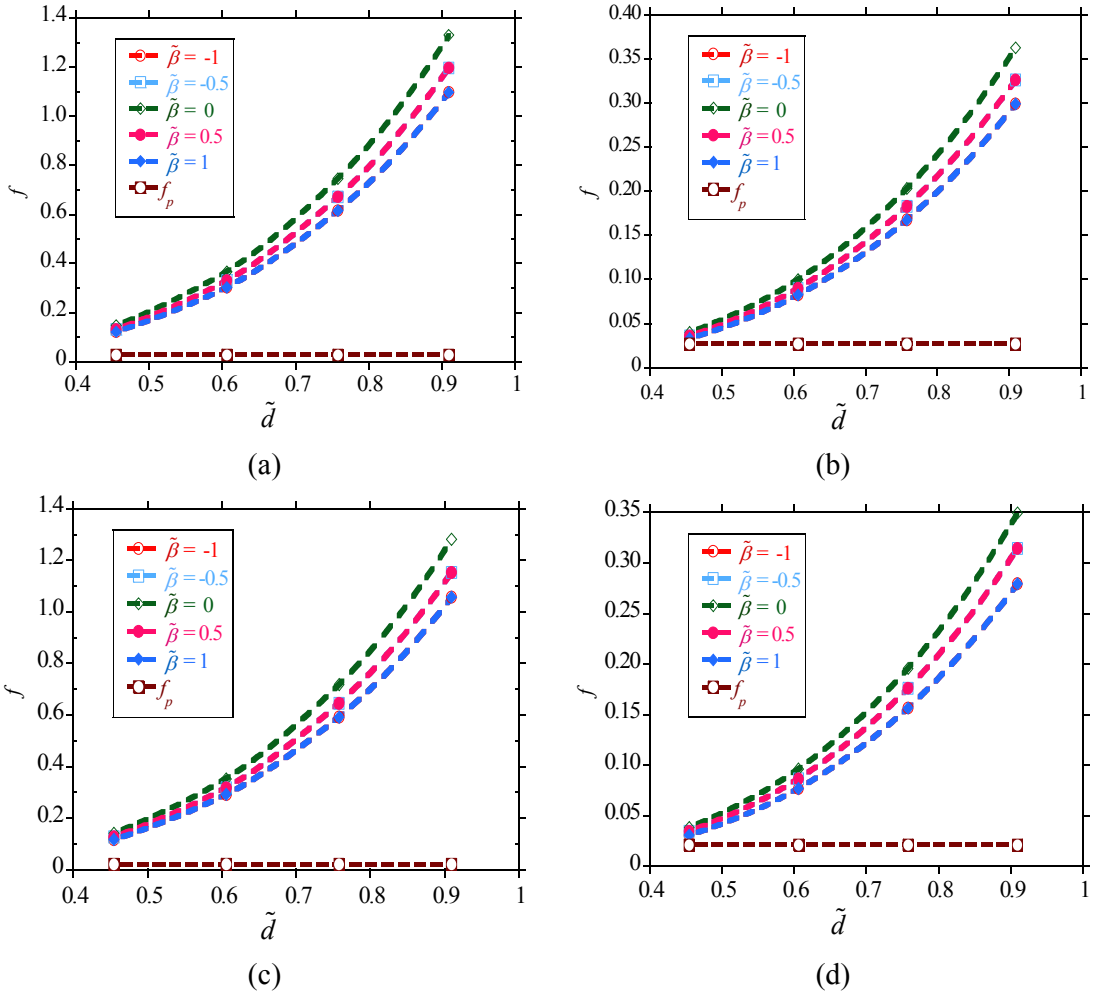

Fig. 7.11: Friction factor for a receiver with perforated plate inserts as a function of insert size ($\tilde{d}$) and insert orientation ($\tilde{\beta}$): (a) inlet temperature of 400 K, Re = 1.02 × 10^4 and insert spacing, $\tilde{p}$ = 0.04, (b) inlet temperature of 400 K, Re = 1.02 × 10^4 and $\tilde{p}$ = 0.20, (c) inlet temperature of 600 K, Re = 4.26 × 10^4 and $\tilde{p}$ = 0.04 and (d) inlet temperature of 600 K, Re = 1.02 × 10^4 and $\tilde{p}$ = 0.20.

Figure 7.12 (a – d) shows the variation of friction factor with Reynolds numbers at different values of plate spacing for $\tilde{d}$ = 0.61, $\tilde{\beta}$ = 1 and T_{inlet} = 400 K; $\tilde{d}$ = 0.91, $\tilde{\beta}$ = 1 and T_{inlet} = 400 K; $\tilde{d}$ = 0.91, $\tilde{\beta}$ = 1 and T_{inlet} = 500 K and $\tilde{d}$ = 0.91, $\tilde{\beta}$ = 1 and T_{inlet} = 600 K respectively. Generally, the friction factor slightly reduces as the Reynolds number increases and is shown to increase as plate spacing is reduced. The increase in fluid friction as the insert spacing

reduces is mainly due to the increased number of plates per metre of the absorber tube that increase the resistance to fluid motion.

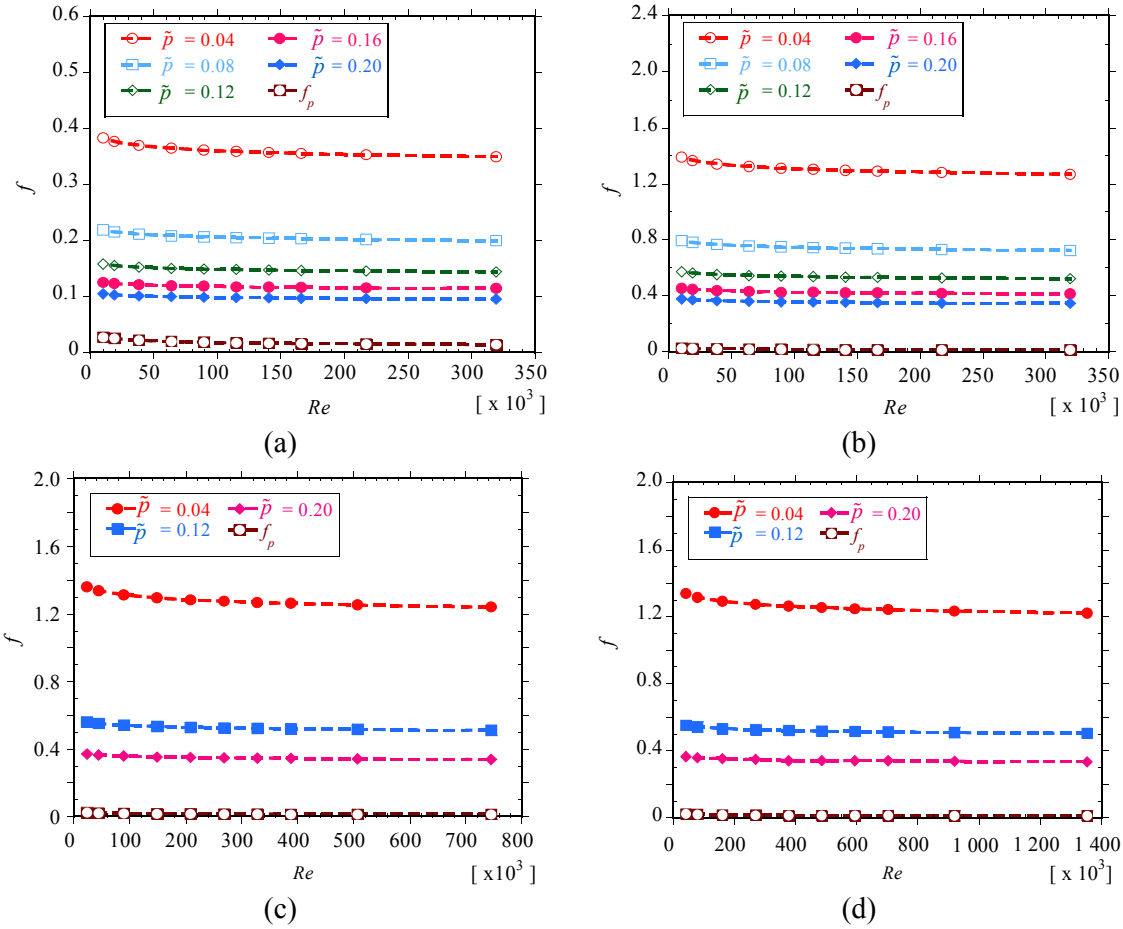

Fig. 7.12: Friction factor for a receiver with perforated plate inserts as a function of Reynolds number and insert spacing ($\tilde{p}$): (a) inlet temperature of 400 K, insert size, $\tilde{d}$ = 0.61 and insert orientation, $\tilde{\beta}$ = 1, (b) inlet temperature of 400 K, $\tilde{d}$ = 0.91 and $\tilde{\beta}$ = 1, (c) inlet temperature of 500 K, $\tilde{d}$ = 0.91 and $\tilde{\beta}$ = 1 and (d) inlet temperature of 600 K, $\tilde{d}$ = 0.91 and $\tilde{\beta}$ =1.

At the same plate size and angle of orientation, the friction factor is almost the same, regardless of the fluid temperature.

7.2.3.2 Pressure drop penalty factors

The pressure drop of a receiver whose absorber tube is fitted with perforated plate inserts is related to that of a receiver with a plain absorber tube using the pressure drop penalty factor according to Eq. (7.18). Figure 7.13 (a and b) shows the variation of the pressure drop penalty factor with Reynolds numbers at different values of plate spacing for $\tilde{\beta}$= 1 and $\tilde{d}$ = 0.91 at two fluid temperatures of 400 K and 600 K respectively. The pressure drop penalty factor increases with a decrease in plate spacing and an increase in the Reynolds number.

For the range of parameters considered, the pressure drop penalty factors were in the range $1.40 \leq f/f_p \leq 95$ depending on the Reynolds number, plate size, plate spacing and plate orientation. The higher the heat transfer enhancement achieved, the higher the fluid friction. The lower the heat transfer enhancement achieved, the lower the fluid friction.

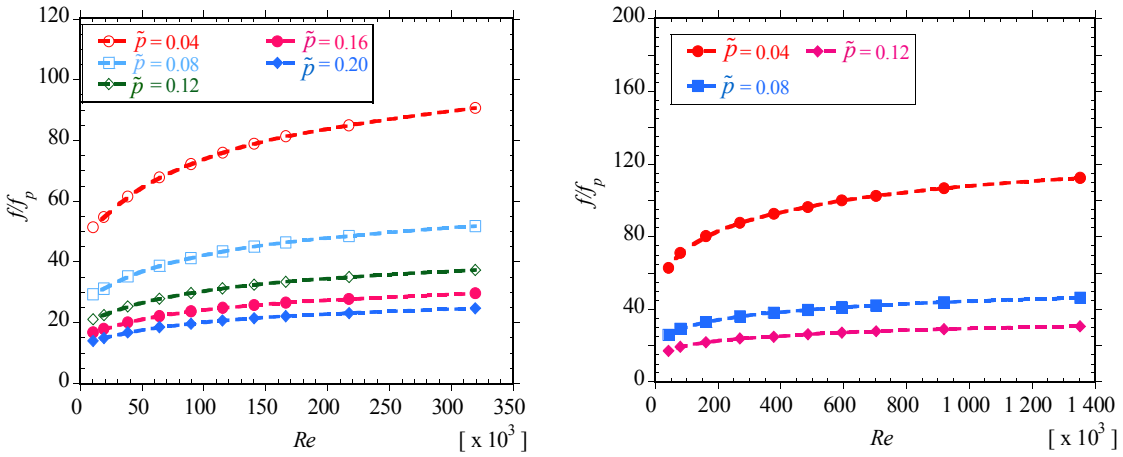

Fig. 7.13: Pressure drop penalty factors for a receiver with perforated plate inserts as a function of Reynolds number and insert spacing ($\tilde{p}$): (a) inlet temperature of 400 K, insert size, $\tilde{d}$ = 0.91 and insert orientation, $\tilde{\beta}$ = 1 and (b) inlet temperature of 600 K, $\tilde{d}$ = 0.91 and $\tilde{\beta}$ = 1.

7.2.3.3 Friction factors

Fluid friction is correlated by

$$f = 0.1713\,\mathrm{Re}^{-0.0267}\,\tilde{p}^{-0.8072}\tilde{d}^{3.1783}(1+0.08996\sin\beta) \qquad (7.22)$$

For this equation $R^2 = 0.96$ and is valid within ± 18%. The parity plot for f is shown in Fig. 7.14.

Valid for $1.0 \times 10^4 \leq \mathrm{Re} \leq 1.35 \times 10^6$ and $10.7 \leq \mathrm{Pr} \leq 33.7$

$-30\text{-} \leq \beta \leq 30^{o}$

$0.04 \leq \tilde{p} \leq 0.20$

$0.61 \leq \tilde{d} \leq 0.91$ and $400\ \mathrm{K} \leq \mathrm{T} \leq 600\ \mathrm{K}$

The Reynolds number depends on the temperature considered. Therefore, the flow rates should be used to determine the velocities to be used in obtaining the Reynolds numbers for the correlations in Eq. (7.21) and Eq. (7.24). The flow rates based on the inner diameter of the plain absorber tube used, vary in the range 4.9 m^3/h to 154 m^3/h at each inlet temperature.

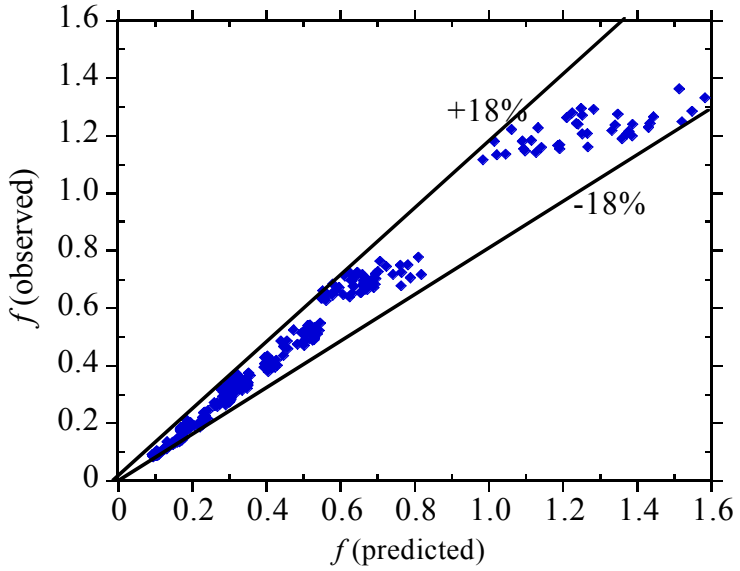

Fig. 7.14: Comparison of present study predicted friction factor with the observed friction factor for a receiver with perforated plate inserts.

7.2.4 THERMAL ENHANCEMENT FACTOR

As a preliminary measure of the thermal performance of heat transfer enhancement techniques, Webb [200] developed a performance evaluation criteria based on a constant pumping comparison. For a constant power comparison, the thermal enhancement factor given by Eq. (7.16) should be greater than 1.0 when pumping power is of concern. Figure 7.15 shows the variation of the thermal enhancement factor with plate size and Reynolds number. As shown in Fig. 7.15 (a and b), at a given Reynolds number, the thermal performance factor continually reduces as the size of the plate increases. This occurs because, despite the increased heat transfer as the plate size increases, the increase in fluid friction is much greater than the increase in heat transfer performance. Also shown by the figures is that the thermal performance reduces as the plate spacing reduces.

Figure 7.15 (c and d) show that the thermal enhancement factor increases with the Reynolds number and attains a maximum value and remains constant depending on the angle and size of the plate. For the range of parameters considered, the thermal enhancement factor was in the range $0.44 \leq \chi \leq 1.05$. For a given Reynolds number, values close to 1 were obtained for the smallest value of plate size and large plate spacing given the small pressure drops at these values.

Chapters 4 and 6 showed that the overall performance evaluation of the collector system gives an intuitive way of evaluating heat transfer enhancement techniques for parabolic trough receivers. Using Eq. (6.10), the thermal efficiency of the collector can be evaluated. Figure 7.16 (a and b) shows the variation of the collector's thermal efficiency with Reynolds numbers at different values of insert spacing.

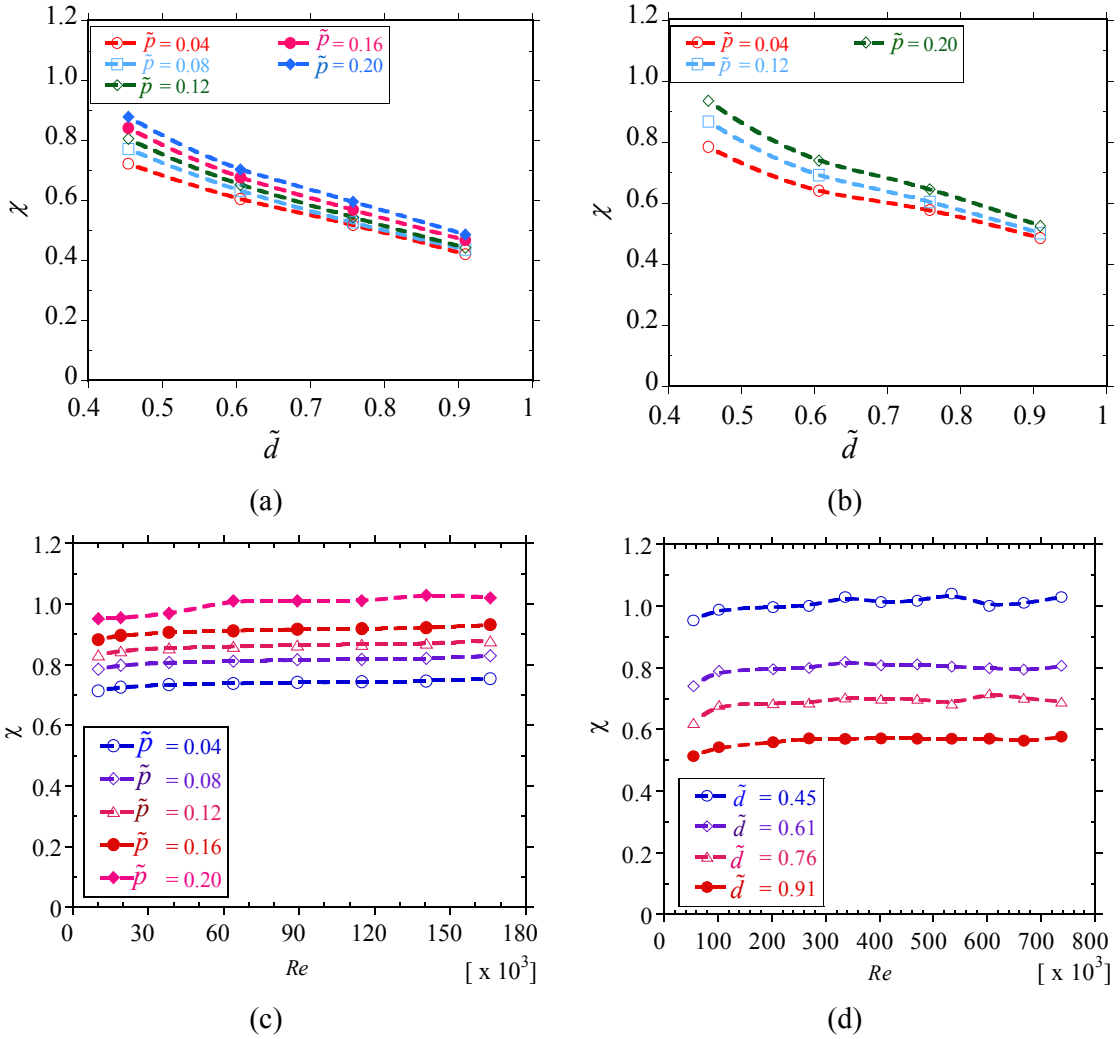

Fig. 7.15: Thermal enhancement factor for a receiver with perforated plate inserts as a function of: (a) insert size ($\tilde{d}$) and insert spacing ($\tilde{p}$) for an inlet temperature of 400 K, Re = 1.02 × 10^4 and insert orientation, $\tilde{\beta}$ = 1, (b) insert size and insert spacing for an inlet temperature of 600 K, Re = 4.26 × 10^4 and $\tilde{\beta}$ = 1, (c) Reynolds number and insert spacing for an inlet temperature of 400 K, $\tilde{d}$ = 0.45 and $\tilde{\beta}$ = 1 and (d) Reynolds number and insert size for an inlet temperature of 600 K, $\tilde{p}$ = 0.20 and $\tilde{\beta}$ = 1.

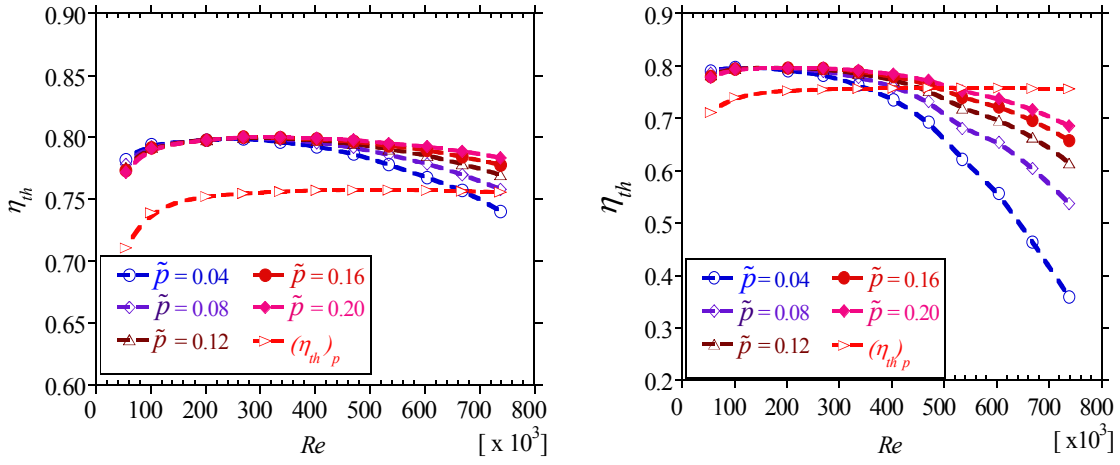

Fig. 7.16: Thermal efficiency of a receiver with perforated plate inserts as a function of Reynolds number and insert spacing ($\tilde{p}$): (a) inlet temperature of 650 K, insert size, $\tilde{d} = 0.45$ and insert orientation, $\tilde{\beta} = 1$ and (b) inlet temperature of 650 K, $\tilde{d} = 0.91$ and $\tilde{\beta} = 1$.

Figure 7.16 (a and b) show the variation of thermal efficiency with Reynolds numbers at different values of insert spacing for $\tilde{d} = 0.45$ and $\tilde{d} = 0.91$ respectively. As shown in Fig. 7.16(a) and 7.16 (b), the thermal efficiency increases with the use of perforated plate inserts at each value of insert spacing and insert size up to some Reynolds numbers and then becomes lower than that of a non-enhanced tube. The efficiency of an enhanced tube will be lower than that of a non-enhanced tube when the gain in heat transfer rate becomes less than the required increase in pumping power. As shown in Fig. 7.16 (a), the thermal efficiency is increased over a wider range of Reynolds numbers when the size of the insert is smallest. As the insert size increases, the thermal efficiency increases over a smaller range of Reynolds numbers as shown in Fig. 7.16 (b). At higher Reynolds numbers, the pumping power increases significantly and reduces the thermal efficiency below that of a plain receiver tube. There is the same variation at the other temperatures considered in this study. At a given insert orientation angle, the increase in thermal efficiency depends on the size of the insert, the spacing between the inserts and the Reynolds number (or flow rate).

The thermal efficiency increases in the range 1.2% - 8% for the range of parameters considered, depending on the insert size, spacing and Reynolds number. However, at all inlet temperatures, a flow rate lower than 37 m^3/h (8.61 kg/s at 400 K, 7.66 kg/s at 500 K, 6.56 kg/s at 600 K and 5.92 kg/s at 650 K) gives an increase in efficiency in the range of 3% – 8% for insert spacing in the range $0.08 \leq \tilde{p} \leq 0.20$, when the insert size is in the range $0.45 \leq \tilde{d} \leq 0.61$. At higher flow rates, an increase in efficiency is still feasible, but the value of the spacing should be higher and the size of the insert should be smaller, as shown in Fig. 7.16 (a). At lower flow rates (lower than 31 m^3/h), an increase in efficiency is possible at most values of insert spacing and insert size, since the increase in pumping power is not significant compared to the gain in performance.

The increase in efficiency is mainly due to the increased heat transfer performance as well as reduced receiver losses. Heat transfer enhancement reduces the absorber tube's temperatures, the reduction in absorber tube's circumferential temperature results in lower coating emissivity, hence lower radiation losses. For this reason, the increase in thermal efficiency is higher at low flow rates where there are significant reductions in absorber tube temperatures. Moreover, there is a far greater increase in performance than the increase in pumping power at low flow rates.

It is worth noting that the use of the performance evaluation criteria at constant pumping power comparison given in Eqs. (6.8) and (7.16) does not give an accurate account of the actual performance of the parabolic trough receiver with heat transfer enhancement. This is probably because it does not account for the additional gain in performance from reduced absorber tube temperatures and the subsequent reduction in radiation heat losses. Moreover, with parabolic trough receivers, the gain in performance with heat transfer enhancement might be much higher than the increase in pumping power.

7.2.5 ABSORBER TUBE TEMPERATURE DIFFERENCE

The improved heat transfer performance in the receiver's absorber tube is expected to reduce the absorber tube's circumferential temperature difference. Figure 7.17 shows the variation of absorber tube's circumferential temperature differences with Reynolds number at different

values of plate spacing. The highest reduction corresponds to the configuration with the highest heat transfer enhancement. The absorber tube's circumferential temperature difference reduces with increasing Reynolds numbers, reducing plate spacing and increasing plate size.

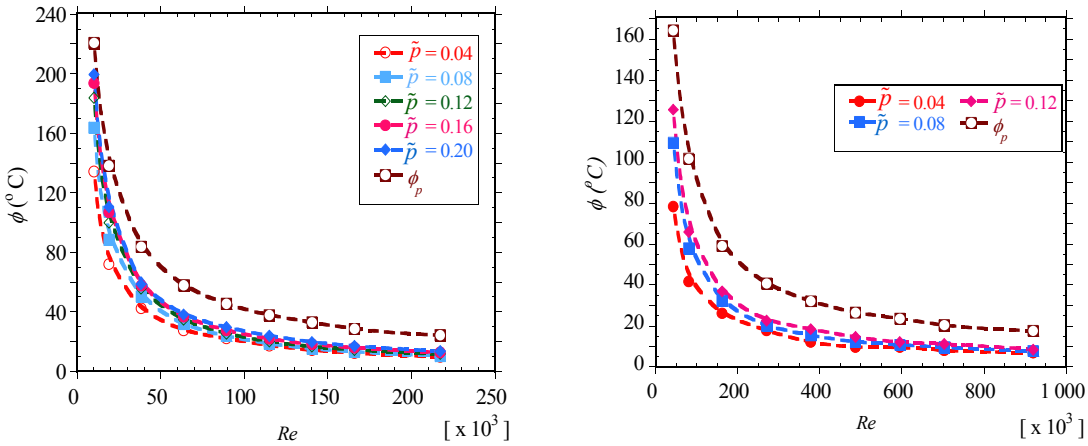

(a) (b)

Fig. 7.17: Absorber tube circumferential temperature difference in a receiver with perforated plate inserts as a function of Reynolds number and insert spacing ($\tilde{p}$): (a) inlet temperature of 400 K, insert size, $\tilde{d}$ = 0.91 and insert orientation, $\tilde{\beta}$ = 1 and (b) inlet temperature of 600 K, $\tilde{d}$ = 0.91 and $\tilde{\beta}$ = 1.

For the range of parameters considered, the absorber tube's circumferential temperature difference reduces by 5% – 67%. As far as the reduction in the absorber tube's circumferential difference is concerned, heat transfer enhancement plays a crucial role only at low Reynolds numbers and low fluid temperatures, since it is at these low Reynolds numbers that the temperature difference is very high. For example, at 4.9 m^3/h, the absorber tube's circumferential temperature difference in a non-enhanced absorber tube is about 220 °C at 400 K, 172 °C at 500 K and 164 °C at 600 K. At the same flow rate, with heat transfer enhancement, for $\tilde{\beta}$ = 1, $\tilde{p}$ = 0.04 and $\tilde{d}$ = 0.91, the absorber tube's circumferential temperature difference reduces to about 124 °C at 400 K, 88 °C at 500 K and 75 °C at 600 K. The reduction in absorber tube temperatures also leads to a significant reduction in the receiver's radiation loss between the absorber tube and the glass cover.

7.2.6 ENTROPY GENERATION

As discussed above, knowledge of the entropy generation rates is essential for determining whether a given heat transfer enhancement technique makes thermodynamic sense. The knowledge of entropy generation rates also provides a way of determining the irreversibilities present in the heat transfer and fluid flow processes. The analysis of entropy generation in solar collector systems is essential for high temperature applications, given the likely high heat transfer irreversibilities. Configurations with minimum entropy generation rates are considered thermodynamically optimal. In general, the entropy generation number given by Eq. (7.19) should be less than 1 for a heat transfer enhancement technique to make thermodynamic sense.

7.2.6.1 Entropy generation distribution

Figure 7.18 (a and b) shows the variation of entropy generation rates due to fluid flow and heat transfer irreversibilities with plate size at different angles of orientation for selected Reynolds numbers. The general trend shown is that the fluid flow irreversibilities continue to increase with an increase in plate size, whereas the heat transfer irreversibilities reduce with an increase in plate size. The increasing trend of the fluid flow irreversibilities is due to the increase in fluid friction as the plate size increases, whereas the reduction in heat transfer irreversibilities as the plate size increases is a result of improved heat transfer, hence reduced temperature differences.

The variation of fluid friction irreversibility with the angle of orientation follows the same trend as the variation of fluid friction. Fluid flow irreversibilities are higher at $\tilde{\beta}$ = 0 and lower at $\tilde{\beta}$ = -1 and $\tilde{\beta}$ = 1. Equal and opposite angles show almost the same fluid flow irreversibilities. The variation of the heat transfer irreversibility with the angle of orientation is the inverse of the Nusselt number variation. The heat transfer irreversibilities reduce as the Nusselt number increases.

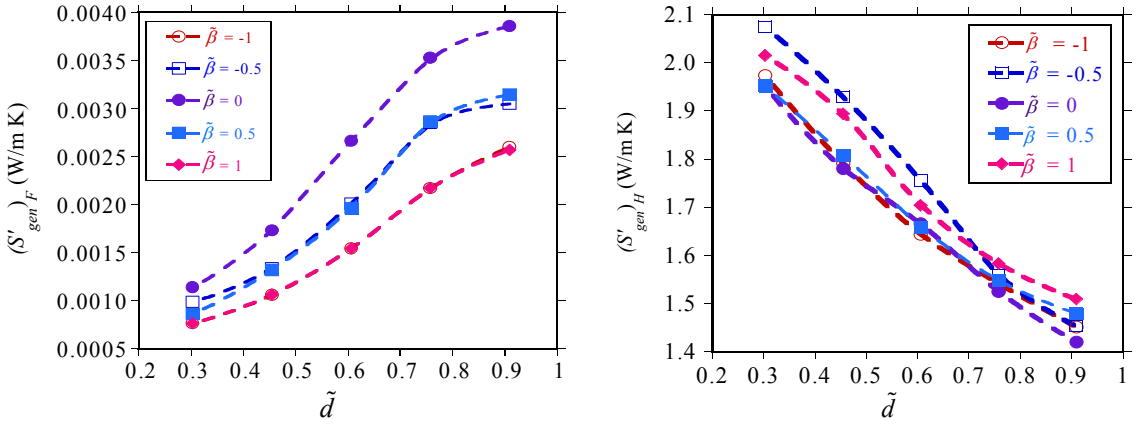

(a) (b)

Fig. 7.18: Entropy generation due to fluid friction irreversibility and entropy generation due to heat transfer irreversibility respectively as functions of insert size ($\tilde{d}$) and insert orientation ($\tilde{\beta}$) for an inlet temperature of 400 K, $Re = 1.94 \times 10^4$ and insert spacing, $\tilde{p} = 0.06$.

Figure 7.19 (a – d) shows the variation of entropy generation rates with Reynolds numbers for different values of plate spacing. Generally, the fluid friction irreversibility increases as the Reynolds numbers increase (Fig. 7.19 (a) for 400 K) whereas the heat transfer irreversibility reduces as the Reynolds numbers increase (Fig. 7.19 (b) for 400 K). The fluid flow irreversibilities are also shown to increase as the plate spacing reduces at a given Reynolds number whereas the heat transfer irreversibilities reduce as the plate spacing reduces at a given Reynolds number. The increase in fluid friction irreversibilities is due to increased resistance to fluid flow as well increasing turbulence intensities. The reduction in heat transfer irreversibilities is due to increasing heat transfer performance and hence a lower finite temperature difference. This variation of the heat transfer irreversibility and fluid flow irreversibility results in an optimal Reynolds number at which the total entropy generation rate is minimum, as was obtained for the plain receiver tube discussed in Chapter 5. The existence of the optimal Reynolds number is shown in Fig. 7.19 (c and d) for $\tilde{p} = 0.09$ and $\tilde{p} = 0.045$ respectively at $\tilde{d} = 0.91$ and $\tilde{\beta} = -1$.

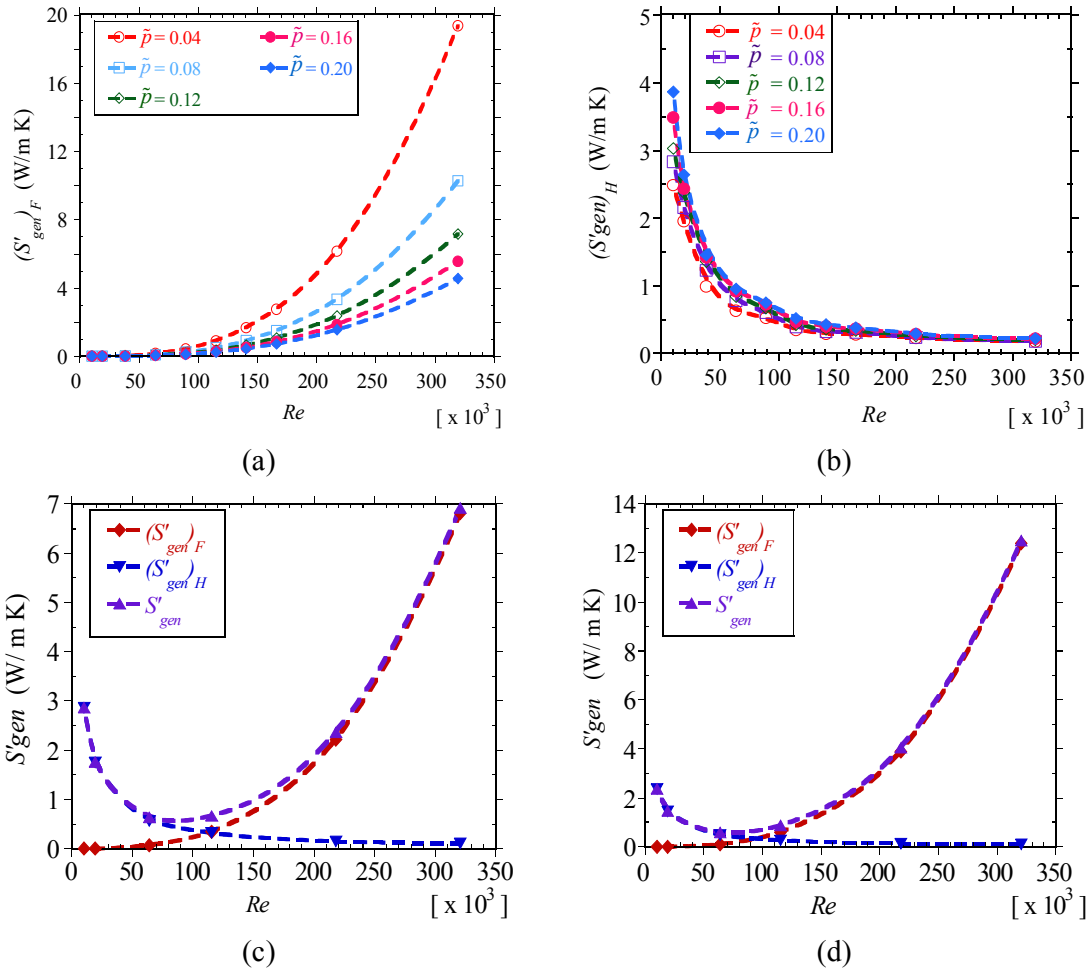

Fig. 7.19: Entropy generation due to fluid friction irreversibility, $(S'_{gen})_F$, entropy generation due to heat transfer irreversibility, $(S'_{gen})_H$ and total entropy generation rate, S'_{gen} as functions of Reynolds number for an inlet temperature of 400 K: (a) $(S'_{gen})_F$ for an insert size, $\tilde{d} = 0.91$ and insert orientation, $\tilde{\beta} = 1$, (b) $(S'_{gen})_H$ for $\tilde{d} = 0.91$ and $\tilde{\beta} = 1$, (c) $(S'_{gen})_F$, $(S'_{gen})_H$ and S'_{gen} for an insert spacing, $\tilde{p} = 0.09$ and $\tilde{d} = 0.91$ and (d) $(S'_{gen})_F$, $(S'_{gen})_H$ and S'_{gen} for $\tilde{p} = 0.045$ and $\tilde{d} = 0.91$.

Figure 7.20 (a – b) shows the variation of the total entropy generation rate per metre of the absorber tube with perforated plate inserts for $\tilde{d} = 0.91$ at $\tilde{\beta} = 1$ and $\tilde{\beta} = 0$ at an inlet temperature of 400 K. Figure 7.20 (c – d) show the total entropy generation rate at $\tilde{d} = 0.91$ at $\tilde{\beta} = 1$ and $\tilde{\beta} = 0$ at an inlet temperature of 600 K. The figures show that at low Reynolds

numbers, the entropy generation rates are lower than those in a plain absorber tube. As the Reynolds numbers increase beyond the optimal Reynolds number, the entropy generation rates increase substantially, making heat transfer enhancement not desirable in the thermodynamic sense. As shown in Fig. 7.20 (a – d), the entropy generation at a higher value of fluid temperature is significantly lower than at a lower temperature for the same perforated plate parameters.

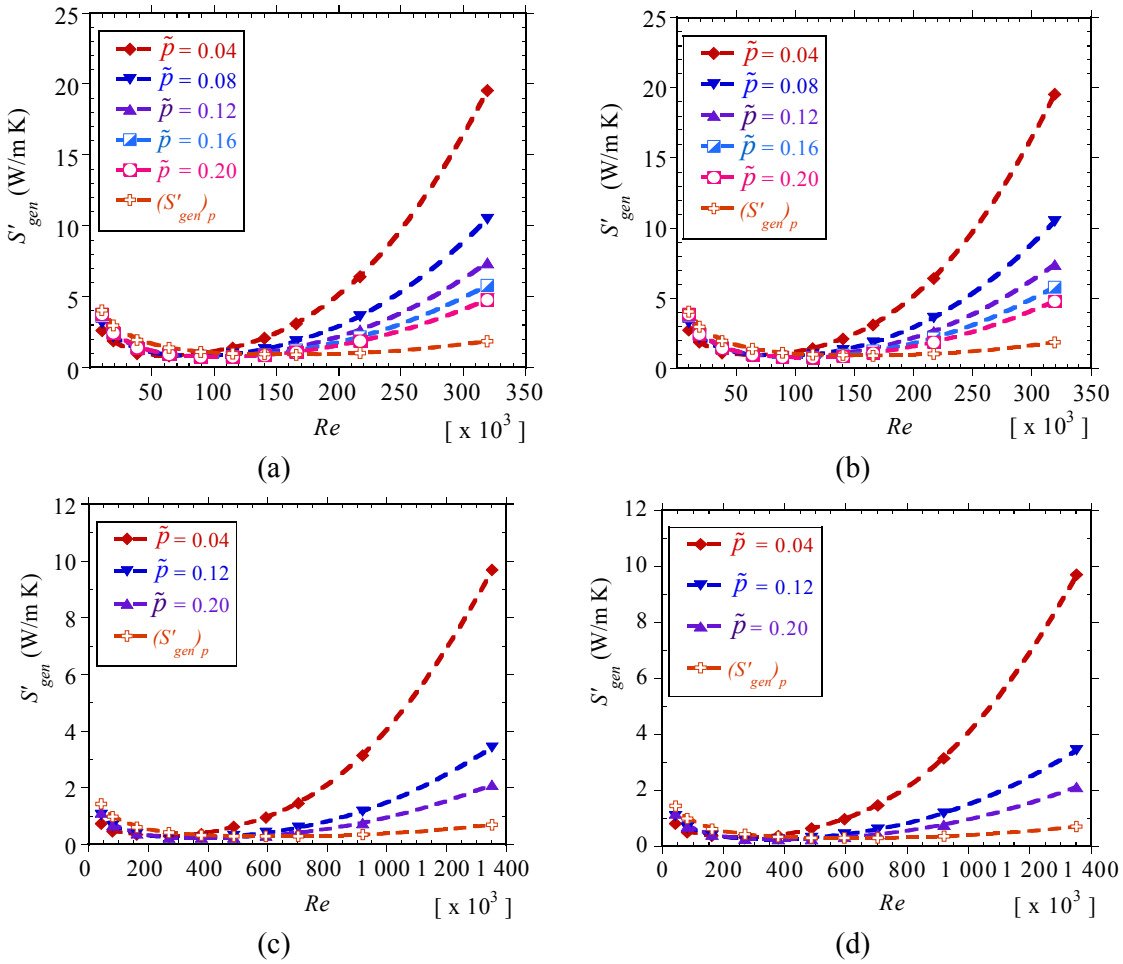

Fig. 7.20: Total entropy generation rate in a receiver with perforated plate inserts as a function of Reynolds number and insert spacing ($\tilde{p}$): (a) inlet temperature of 400 K, insert size, $\tilde{d}$ = 0.91 and insert orientation, $\tilde{\beta}$ = 1, (b) inlet temperature of 400 K, $\tilde{d}$ = 0.91 and $\tilde{\beta}$ = 0, (c) inlet temperature of 600 K, $\tilde{d}$ = 0.91 and $\tilde{\beta}$ = 1 and (d) inlet temperature of 600 K, insert size, $\tilde{d}$ = 0.91 and $\tilde{\beta}$ = 0.

This is because increasing the fluid temperature reduces its density and viscosity and results in increased heat transfer performance. All these reduce the fluid flow and heat transfer irreversibility and therefore reduce the total entropy generation rates.

A closer look at Fig. 7.20 (a – d), shows that using the perforated plates shifts the optimal Reynolds number to a lower value than the optimal Reynolds number in a plain absorber tube. For the plain absorber tube, the optimal Reynolds number was obtained as 1.41×10^5 for T_{inlet} = 400 K and 7.05×10^5 at 600 K. The variation of the optimal Reynolds number with plate size and spacing is shown in Fig. 7.21.

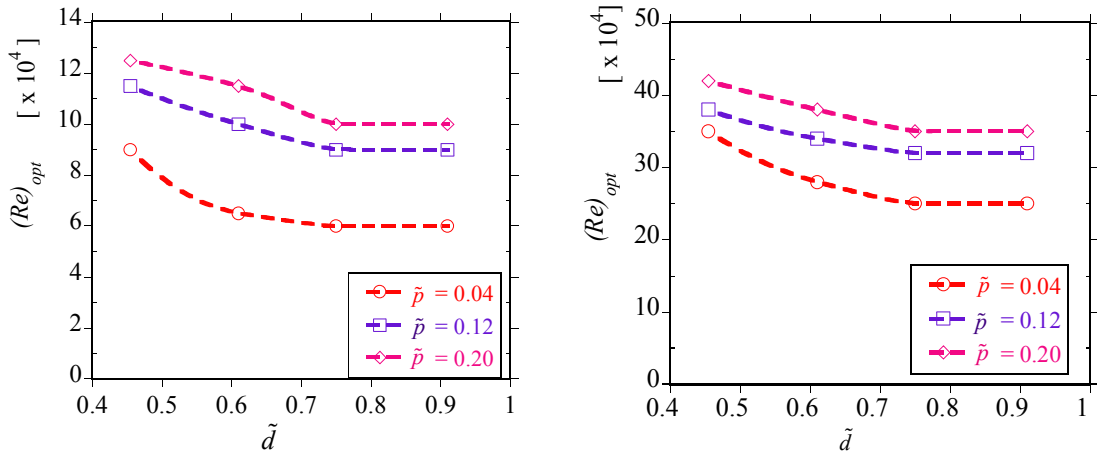

Fig. 7.21: Optimal Reynolds number for a receiver with perforated plate inserts as a function of insert size ($\tilde{d}$) and insert spacing ($\tilde{p}$): (a) inlet temperature of 400 K and insert orientation, $\tilde{\beta}$ = 1 and (b) inlet temperature of 600 K and $\tilde{\beta}$ = 1.

Generally, the optimal Reynolds number reduces with a reduction in plate spacing and with an increase in plate size. The optimal Reynolds number does not significantly depend on plate orientation.

A more reasonable determination of the distribution of irreversibilities is the Bejan number, as it relates the entropy generation due to heat transfer to the total entropy generation according to Eq. (7.20). The Bejan number ranges from $0 \leq Be \leq 1$, the heat transfer irreversibility dominates if *Be* is close to one, whereas the fluid friction irreversibility

dominates if *Be* is close to zero. Accordingly, the heat transfer enhancement at a given Reynolds number should be considered if *Be* is closer to 1 than to zero. A reduction in *Be* implies a reduction in the heat transfer irreversibility or an increase in the fluid friction irreversibility. Figure 7.22 (a – d) shows the variation of Bejan number with Reynolds numbers for different orientation angles, plate sizes and plate spacings at 400 K.

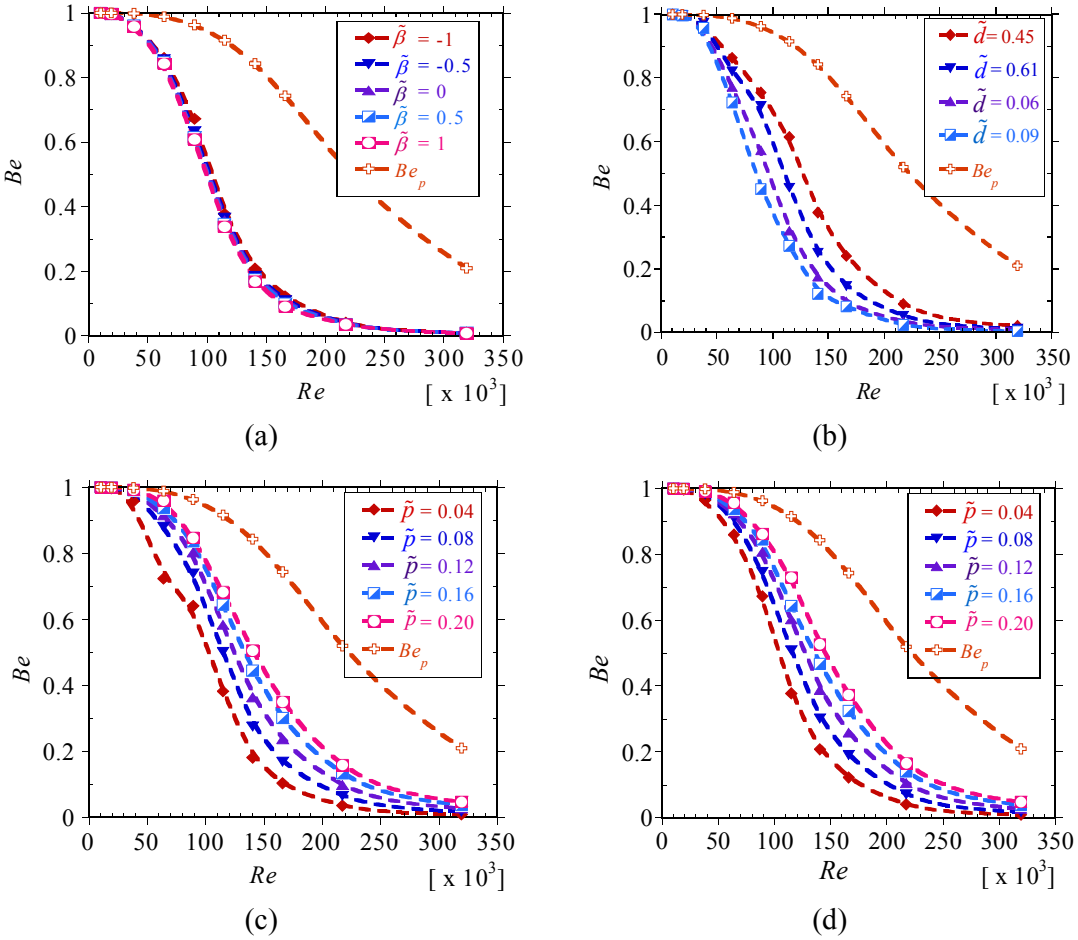

Fig. 7.22: Bejan number for a receiver with perforated plate inserts for an inlet temperature of 400 K as a function of Reynolds number and: (a) insert orientation ($\tilde{\beta}$) for insert spacing, $\tilde{p} = 0.04$ and insert size, $\tilde{d} = 0.91$, (b) insert size ($\tilde{d}$) for $\tilde{p} = 0.04$ and $\tilde{\beta} = 1$, (c) insert spacing ($\tilde{p}$) for $\tilde{d} = 0.91$ and $\tilde{\beta} = 1$ and (d) insert spacing ($\tilde{p}$) for $\tilde{d} = 0.91$ and $\tilde{\beta} = -1$.

Figure 7.22 (a) shows that the angle of orientation does not significantly affect the Bejan number, but the Bejan number at all angles of orientation is lower than the Bejan number for a plain absorber tube. Figure 7.22 (b) shows that at a given Reynolds number, as the plate size increases the Bejan number reduces, due to the improved heat transfer that reduces the heat transfer irreversibility. Figure 7.22 (c and d) shows that at a given Reynolds number, the Bejan number reduces as the plate spacing reduces.

The figure also clearly shows that the heat transfer irreversibility becomes less than the fluid flow irreversibility at higher Reynolds numbers for any value of plate size, angle of orientation and plate spacing. The Bejan number is more strongly dependent on the Reynolds number, plate spacing and plate size than on the angle of orientation. The same general trends occur at other values of fluid temperature.

7.2.6.2 Thermodynamic evaluation of a receiver with perforated plate inserts

For the evaluation of the thermodynamic effectiveness of a given heat transfer technique, the entropy generation ratio given in Eq. (7.19) is used. In general, the value of this ratio should be less than 1 for the enhancement technique to be thermodynamically feasible. For ratios less than 1.0, the irreversibilities are reduced when compared to a plain tube and for ratios greater than 1.0, the enhancement techniques results in more irreversibility than for a plain tube.

Figure 7.23 (a – d) shows the variation of the enhancement entropy generation ratio with Reynolds numbers at different angles of orientation, different plate sizes and different plate spacing at a fluid temperature of 400 K. The use of inserts makes thermodynamic sense below some Reynolds numbers. Generally, at 400 K, for Reynolds numbers greater than 1.0×10^5, $N_{s,en}$ increases significantly and becomes greater than 1 as the Reynolds numbers increase. For almost all the values of plate spacing considered, the value of $N_{s,en}$ is greater than 1 for $Re \geq 1.0 \times 10^5$ regardless of the angle of orientation and plate size. Figure 7.23 (d) shows the same variation of $N_{s,en}$ with Reynolds numbers for different insert spacing, but for a temperature of 600 K. The same trend is obtained as that shown at 400 K.

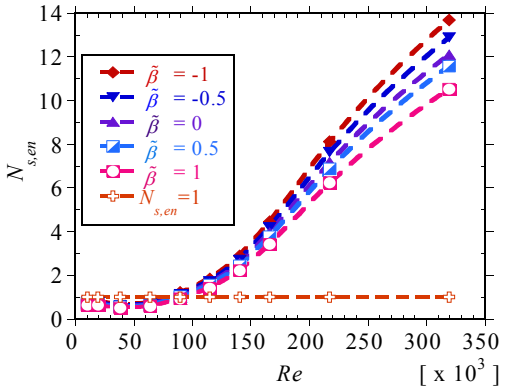

(a) Inlet temperature of 400 K

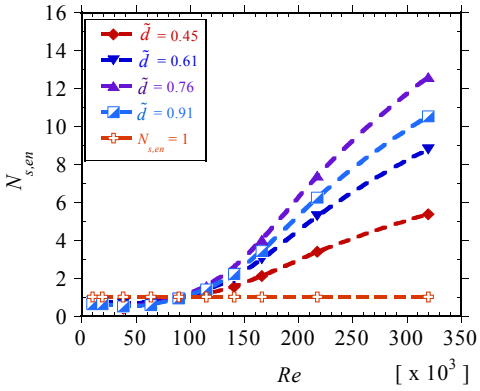

(b) Inlet temperature of 400 K

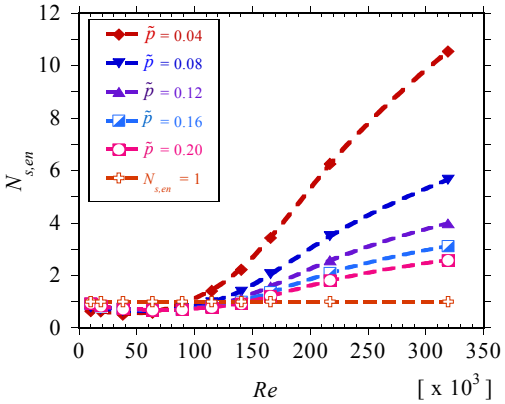

(c) Inlet temperature of 400 K

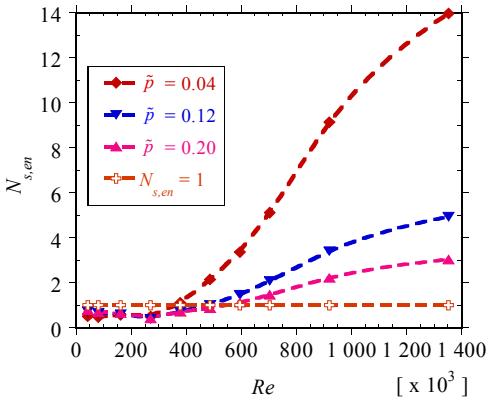

(d) Inlet temperature of 600 K.

Fig. 7.23: Enhancement entropy generation number ($N_{s,en}$) for a receiver with perforated plate inserts as a function of Reynolds number and: (a) insert orientation ($\tilde{\beta}$) for insert spacing, $\tilde{p}$ = 0.04 and insert size, $\tilde{d}$ = 0.91, (b) insert size ($\tilde{d}$) for $\tilde{p}$ = 0.04 and $\tilde{\beta}$ = 1, (c) insert spacing ($\tilde{p}$) for $\tilde{d}$ = 0.91 and $\tilde{\beta}$ = 1 and (d) insert spacing ($\tilde{p}$) for $\tilde{d}$ = 0.91 and $\tilde{\beta}$ = 1.

The same flow rates are also shown to give a Reynolds number for which the use of inserts makes thermodynamic sense. Flow rates of less than 43 m^3/h ($\dot{m}$ = 10.12 kg/s at 400 K, $\dot{m}$ = 8.99 kg/s at 500 K, $\dot{m}$ = 7.69 kg/s at 600 K and $\dot{m}$ = 6.96 kg/s at 650 K) ensure entropy generation ratios less than 1.0 for all values of insert spacing, insert size, plate orientation and heat transfer fluid temperature.

The entropy generation is shown to reduce up to 53% for the range of parameters considered. At higher Reynolds numbers, enhancement entropy generation ratios are as high as 17. Therefore, using inserts at these Reynolds numbers is not beneficial thermodynamically since higher available energy will be destroyed than when no inserts are used.

7.2.7 MULTI-OBJECTIVE OPTIMISATION

In most cases, heat transfer enhancement leads to an increase in the heat transfer performance of a given heat exchanger as well as an increase in the pressure drop. Usually, the objective is to improve heat transfer performance with minimum fluid friction. Therefore, a multi-objective optimisation problem arises. As presented in Section 3.4.2, genetic algorithms are suited to such types of problems. Multi-objective genetic algorithms use the concept of domination to search the decision variable space for a set of solutions that are non-dominated with respect to one another. These solutions also dominate all other solutions. In the absence of further information, all these solutions are equally important. This set of solutions is known as the Pareto optimal solutions. In this section, the hybrid variant of the non-dominated sorting genetic algorithm II (NSGA II) available in ANSYS® release 14 and 14.5 was used to obtain such solutions.

7.2.7.1 Formulation of the optimisation problem

The multi-objective optimisation problem under consideration can be written according to Eq. (3.42) as

$$\text{Maximise } f_1(\mathbf{x}) / \text{ Minimise } f_2(\mathbf{x}) \tag{7.23}$$

The objective functions $f_1(\boldsymbol{x})$ and $f_2(\boldsymbol{x})$ are heat transfer performance expressed as the Nusselt number, Nu and pressure drop in terms of the fluid friction, f.

The numerical simulations and optimisation were carried out for fixed values of Reynolds numbers. The Reynolds numbers were in the range $1.04 \times 10^4 \leq Re \leq 1.36 \times 10^6$ depending on the fluid temperature used. The fluid temperatures were fixed at 400 K, 500 K and 600 K. The concentration ratio (C_R) was fixed at 86, direct normal irradiance was fixed at 1 000 W/m^2. The design space for the optimisation process was defined in terms of lower and upper bounds of design variables as

$$0.04 \le \tilde{p} \le 0.20$$
$$0.30 \le \tilde{d} \le 0.91 \qquad 7.24$$
$$-1 \le \tilde{\beta} \le 1$$

7.2.7.2 Optimisation results

Using the optimisation procedure presented in Chapter 3 (Section 3.7), the following results were obtained from the multi-objective optimisation procedure. Accurate response surfaces or meta-models are essential in any meta-modelling-based optimisation study. In this study, second-order polynomials were not sufficient as the values of R^2 given in Eq. (3.52) and R^2_{adj} given in Eq. (3.53) were not close enough to 1. The relative mean square errors for the parameters of interest were also larger than 10% for some values of plate spacing. Therefore, the Kriging meta-modelling approach was used to improve the accuracy of the response surface.

The Kriging meta-model in ANSYS® 14.5 [99] has an automated refinement procedure. It determines where more design points are needed in a response surface to improve its accuracy. The refinement terminates when the number of specified refinement points is reached or when the predicted relative error has been achieved [99]. The predicted relative error in all cases was set to 5% and 10 refinement points specified. Figure 7.24 shows the convergence curve for the Kriging meta-model for the four output parameters from which the performance parameters are derived. It can be seen that the predicted relative error reduces to less than 4% for all the output parameters shown as the refinement process proceeds. The response surface was further verified by comparing the results from the Kriging meta-model with the actual results from the computational fluid dynamics (CFD) simulation as shown in Table 7.5.

Table 7.5: Comparison of results predicted by the response surface with CFD results for a parabolic trough receiver with perforated plate inserts

				Meta-model results		CFD simulation results		% Error	
Re	$\tilde{p}$	$\tilde{\beta}$	$\tilde{d}$	*Nu*	*f*	*Nu*	*f*	*Nu*	*f*
2.18×10^5	0.06	-1	0.30	2956	0.0699	2955	0.0699	-0.01	-0.09
2.18×10^5	0.045	-1	0.91	4564	0.7447	4562	0.7447	0.04	0.00
2.18×10^5	0.045	1	0.91	4147	0.7455	4308	0.7429	-3.72	0.36
2.18×10^5	0.045	0	0.91	4832	1.2329	4706	1.2474	2.67	-1.16
3.20×10^5	0.045	0.5	0.76	5337	0.5492	5358	0.5565	-0.40	-1.31
3.20×10^5	0.045	-1	0.91	6027	0.7409	6177	0.7376	-2.43	0.45

The absolute percentage error was less than 4% in all cases, showing that the meta-model accurately represents the physical model.

Figure 7.25 shows the 3-D response surfaces for the variation in Nusselt numbers, friction factor and absorber tube temperature gradients for a Reynolds number of 4.03×10^5 and T_{inlet} = 650 K. The same trend was obtained with other Reynolds numbers and other values of plate spacing. The figure shows that the Nusselt number increases with plate size. The variation of the Nusselt number with plate orientation is such that at $\tilde{\beta}$ = 1, the Nusselt number has the smallest value. At values of $\tilde{\beta}$ less 0.5, the Nusselt number variation is not very significant.

The friction factor is also shown to increase with an increase plate size. At a given plate size, the friction factor shows minimum values at $\tilde{\beta}$ =1 and $\tilde{\beta}$ = -1 and a maximum at $\tilde{\beta}$ = 0. The trend shown by the absorber tube's circumferential temperature difference is the inverse of the Nusselt number variation. As the Nusselt numbers increase, the absorber tube's circumferential temperature difference reduces due to improved heat transfer performance.

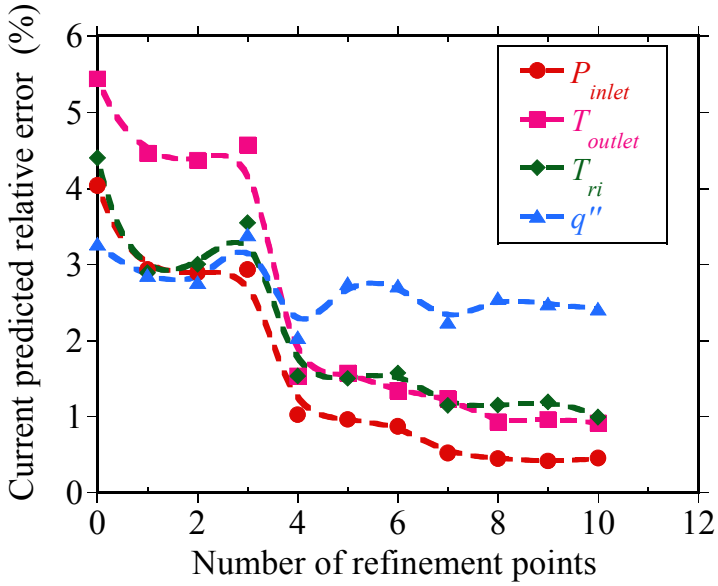

Fig. 7.24: Convergence of inlet pressure (P_{inlet}), outlet temperature (T_{outlet}), absorber tube wall inner temperature (T_{ri}) and absorber tube wall heat flux (q'') in the Kriging-auto refinement procedure for a receiver with perforated plat inserts.

The multi-objective optimisation for a case where two objectives are conflicting, yields a set of solutions in which an improvement in one objective sacrifices the quality of the other. Figure 7.26 (a-c) gives samples of the 3-D Pareto fronts, showing the variation of design variables with the objective functions at a Reynolds number of $Re = 3.36 \times 10^5$ and $T_{inlet} = 650$ K. The figures provide a means for visualising the variation of each variable with the objective function. A number of solutions from which to choose are shown in these figures. From these figures, a 2-D curve showing the Pareto front for friction factor and Nusselt number is derived as shown in Fig. 7.26 (d).

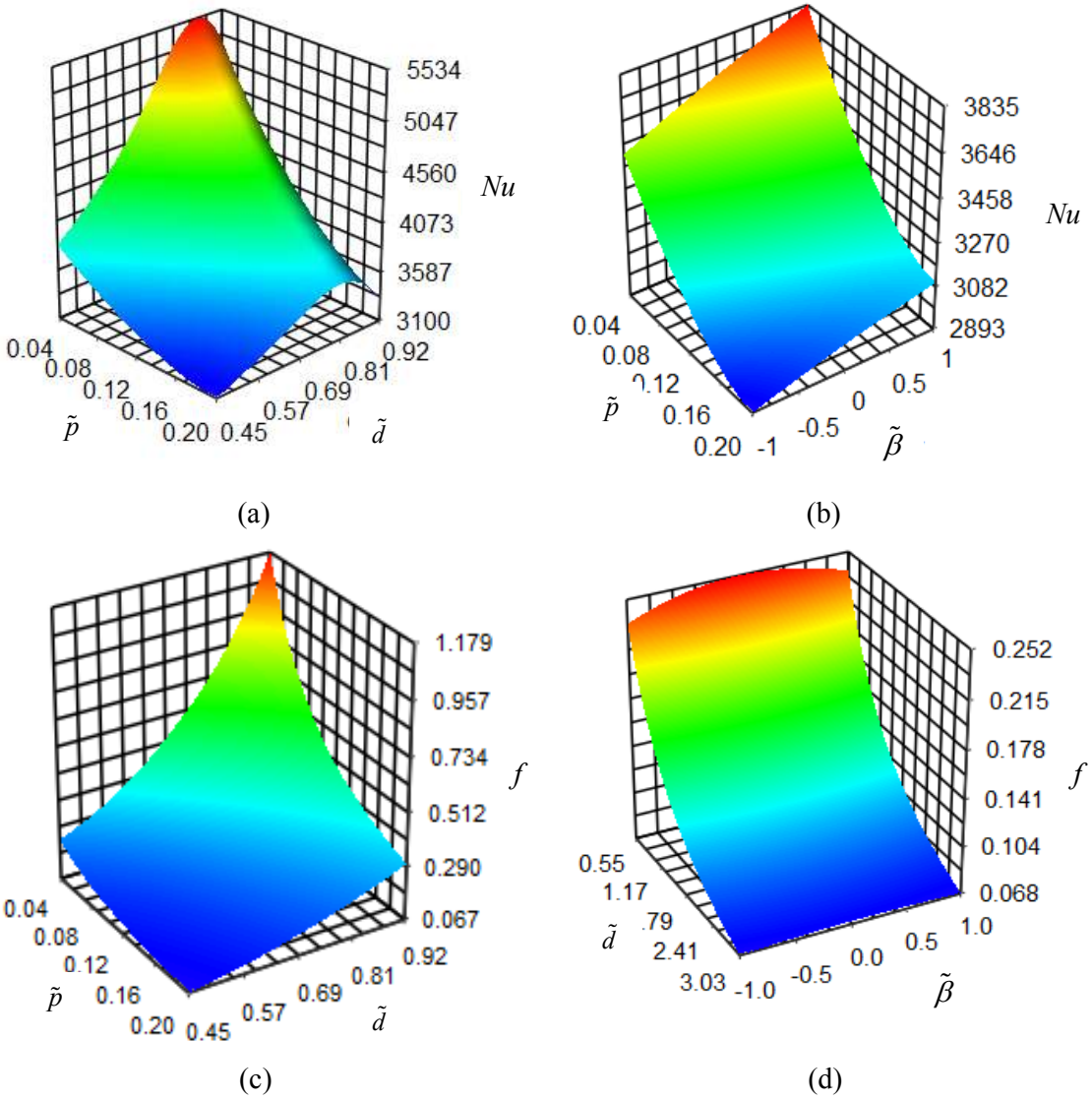

Fig. 7.25: 3-D response surfaces for Nusselt number and friction factor for a receiver with perforated plate inserts for Re = 4.03× 10^5 and an inlet temperature of 650 K: (a) Nusselt number as a function of insert spacing ($\tilde{p}$) and insert size ($\tilde{d}$), (b) Nusselt number as a function of insert spacing ($\tilde{p}$) and insert orientation ($\tilde{\beta}$), (c) friction factor as a function of insert spacing ($\tilde{p}$) and insert size ($\tilde{d}$) and (d) friction factor as a function of insert size ($\tilde{d}$) and insert orientation ($\tilde{\beta}$).

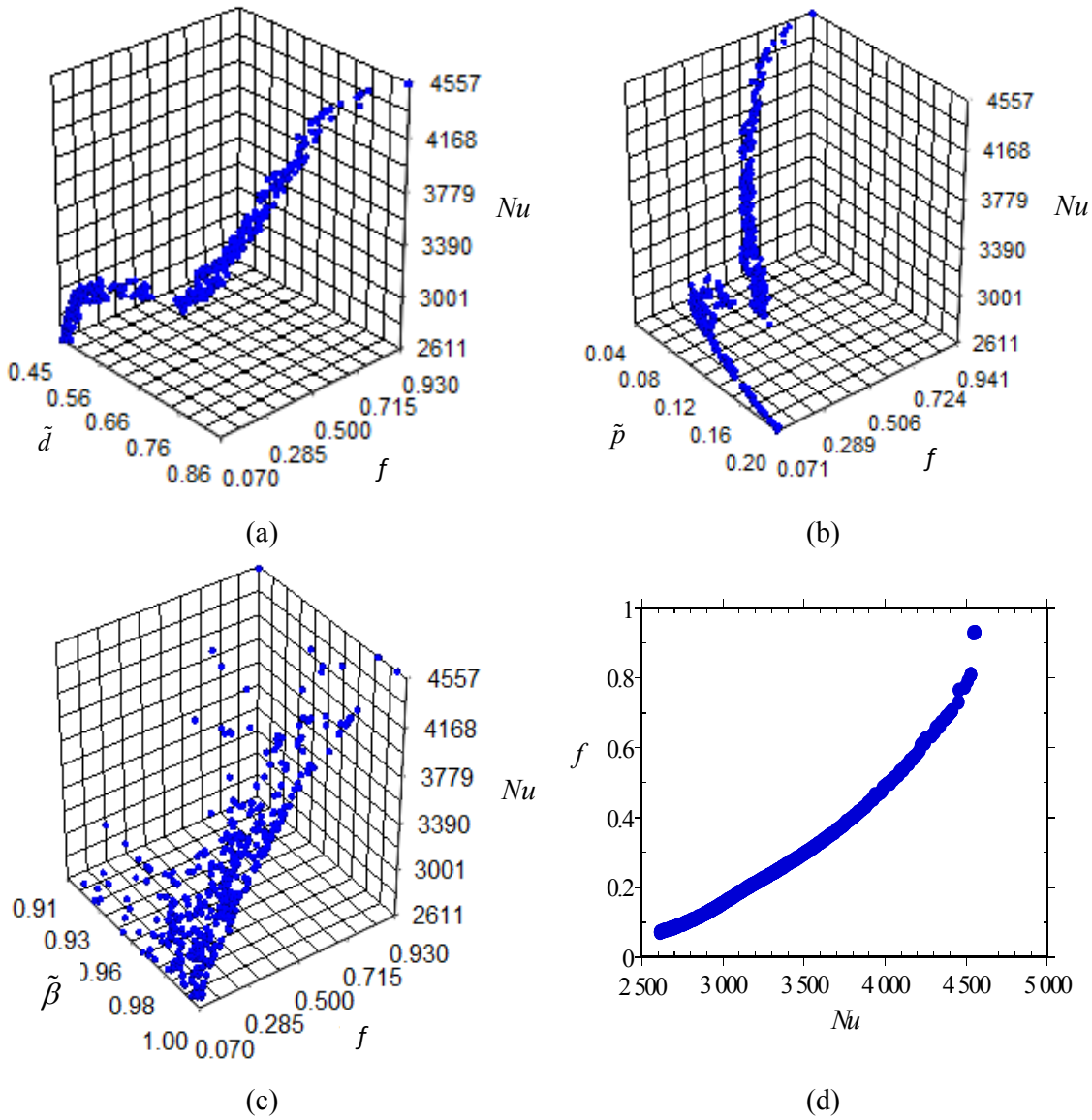

Fig. 7.26: Pareto optimal solutions for a receiver with perforated plate inserts for an inlet temperature of 650 K and $Re = 3.36 \times 10^5$: (a) Nusselt number as a function of insert size ($\tilde{d}$) and friction factor, (b) Nusselt number as a function of insert spacing ($\tilde{p}$) and friction factor, (c) Nusselt number as a function of insert orientation ($\tilde{\beta}$) and friction factor and (d) 2-D Pareto optimal front for friction factor and Nusselt number.

As expected, the variation of friction factor and Nusselt number on the Pareto front is a continuous curve along which selecting any one of the solutions along the curve will improve

one of the objectives while sacrificing the quality of the other objective. Therefore, selecting any one of the solutions along the curve will improve one of the objectives while sacrificing the quality of the other objective. A reduction in perforated plate spacing will give improved heat transfer performance, but it also significantly increases the fluid friction.

Figure 7.27 (a) shows different solution sets of pressure drops (friction factor) and Nusselt numbers at three different Reynolds numbers. As discussed earlier, higher Reynolds numbers give better heat transfer performance, hence at high Reynolds numbers the heat transfer performance is higher as shown. Figure 7.27 (b) shows the optimal solution set at the same flow rate for different fluid temperatures. The same trend is obtained as seen in Figs 7.26 (d) and 7.27 (a). Higher fluid temperatures also show higher Nusselt numbers as discussed earlier.

All the solutions on the Pareto front are optimum solutions for a multi-objective optimisation problem. The final design point can be chosen, depending on the importance of each objective [99].

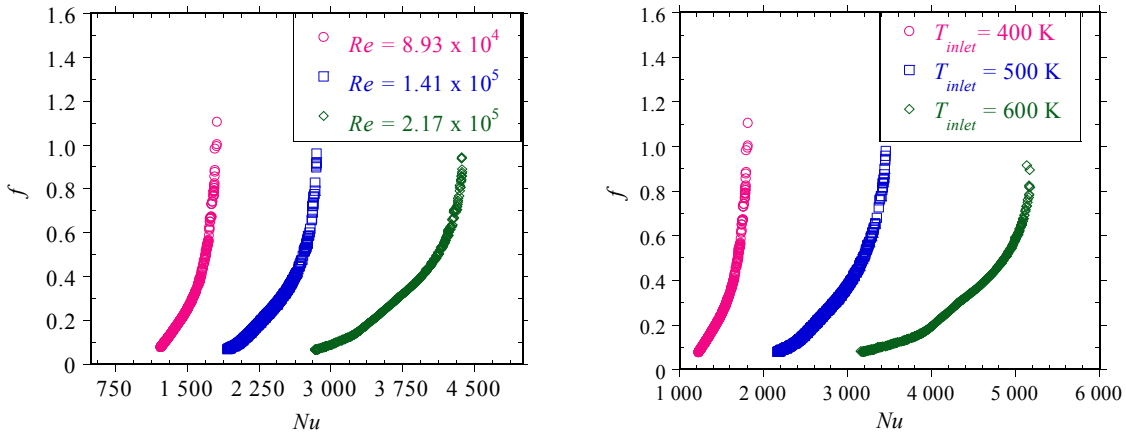

Fig. 7.27: Pareto optimal fronts showing friction factor as a function of Nusselt number and: (a) Reynolds number for an inlet temperature of 400 K and (b) inlet temperature for a flow rate of 43 m^3/h.

Several methods can be used when deciding on a single final design point from the Pareto optimal solution set. In this section, the decision support process discussed in Section 3.8 in Chapter 3 was used. It is a goal-based, weighted, aggregation-based technique [99]. Based on

this ranking method, several design candidates can be identified for each value of Reynolds number in their order of importance. Here a case is considered where all objectives are equally important. Figure 7.28 (a – c) shows the variation of design variables for the case when all objectives are equally important at each fluid temperature and flow rate. Figure 7.28 (a) shows the variation of the optimal plate orientation with flow rate at different values of fluid temperature. In general, the flow rate and fluid temperature do not affect the optimal plate orientation significantly. The value of $\left(\tilde{\beta}\right)_{opt}$ varies between 0.985 – 0.999 as shown in the figure. This is in line with what was discussed in the parametric analysis where maximum heat transfer and minimum fluid friction were shown to exist at $\tilde{\beta}=1$.

Figure 7.28 (b) shows the variation of the optimal plate size with flow rate at different values of fluid temperature. The optimal plate diameter does not vary significantly with the flow rate. The optimal plate size, $\left(\tilde{d}\right)_{opt}$ is about 0.82 , 0.78 and 0.758 at 400 K, 500 K and 600 K respectively. As shown in Fig. 7.28(c), the optimal plate spacing is very small and almost constant, about 0.036 for lower flow rates, then suddenly increases and becomes constant again for flow rates higher than 36 m^3/h at each fluid temperature. It should be noted that these values are merely representative and will vary depending on the weights for each objective and other constraints, as well as the decision support method used. The best way to obtain the design candidates is to consider all the Pareto solutions, as shown in Fig. 7.26 and obtain the most suitable designs according to the designer's needs.

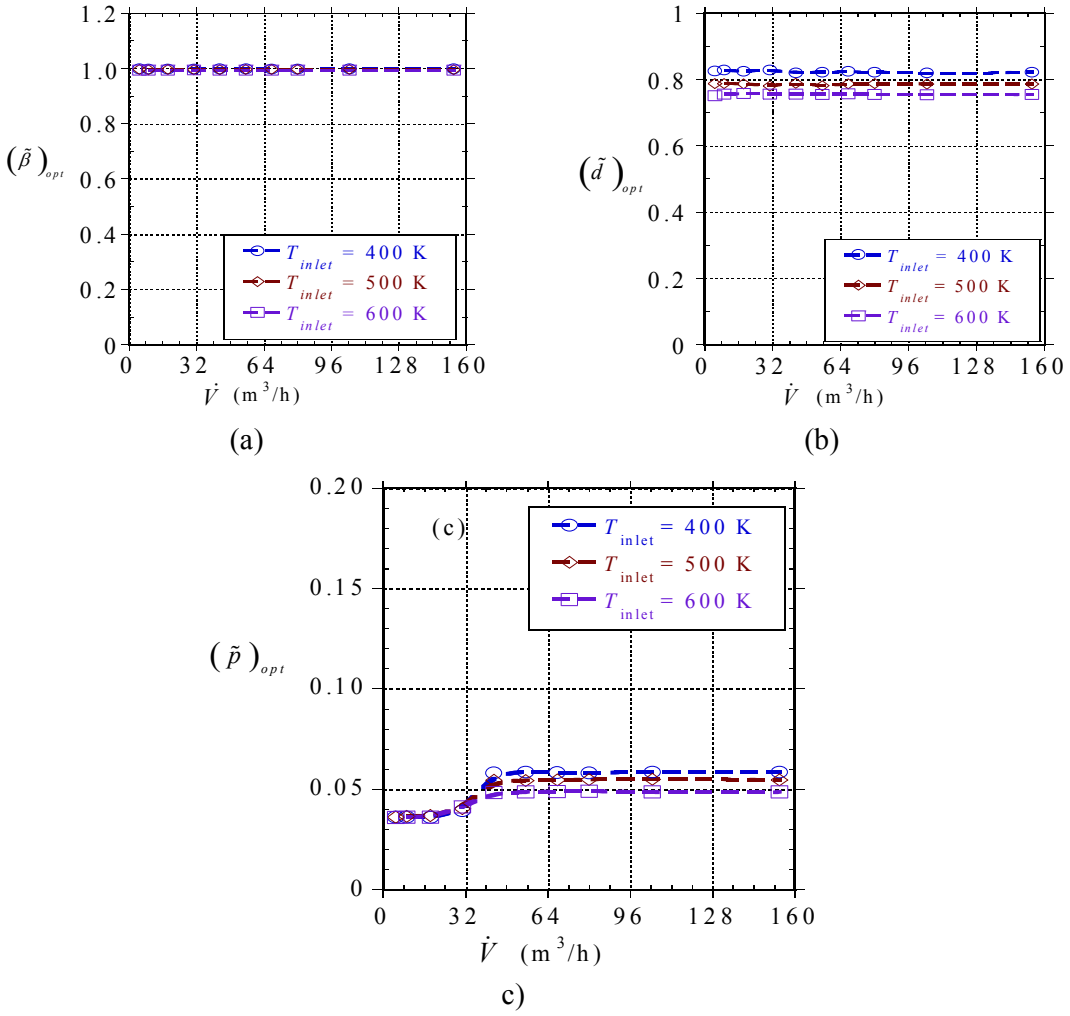

Fig. 7.28: Optimal perforated plate geometry for a receiver with perforated plate inserts as a function of flow rate and inlet temperature: (a) optimal insert orientation $(\tilde{\beta})_{opt}$, (b) optimal insert size $(\tilde{d})_{opt}$ and (c) optimal insert spacing $(\tilde{p})_{opt}$.

At the optimal values of plate size, plate spacing and plate orientation in Fig. 7.28 (a – c), the heat transfer performance is enhanced in the range 1.92 – 2.11 while the fluid friction is in the range 30 – 39 times depending on the flow rate and fluid temperature. For these optimal solutions, the thermal efficiency increases in the range 2% – 6% provided that the flow rate is lower than 18 m^3/h (4.30 kg/s at 400 K, 3.82 kg/s at 500 K, 3.27 kg/s at 600 K and 2.95 kg/s at 650 K)

It can be shown for the optimal configurations in Fig 7.28 that there is also a value of Reynolds number for which the entropy generation is a minimum, as shown in Fig. 7.29 (a). As such, multi-objective optimisation and the entropy generation minimisation method can be used simultaneously to obtain designs that are thermally and thermodynamically optimal. Furthermore, using the enhancement entropy generation ratio, $N_{s,en}$, Reynolds numbers or flow rates can be obtained for which the optimal solutions are thermodynamically better. Figure 7.29 (b) is the plot of the enhancement entropy generation ratio, the Reynolds numbers for which $Ns,en \leq 1$ are clearly shown.

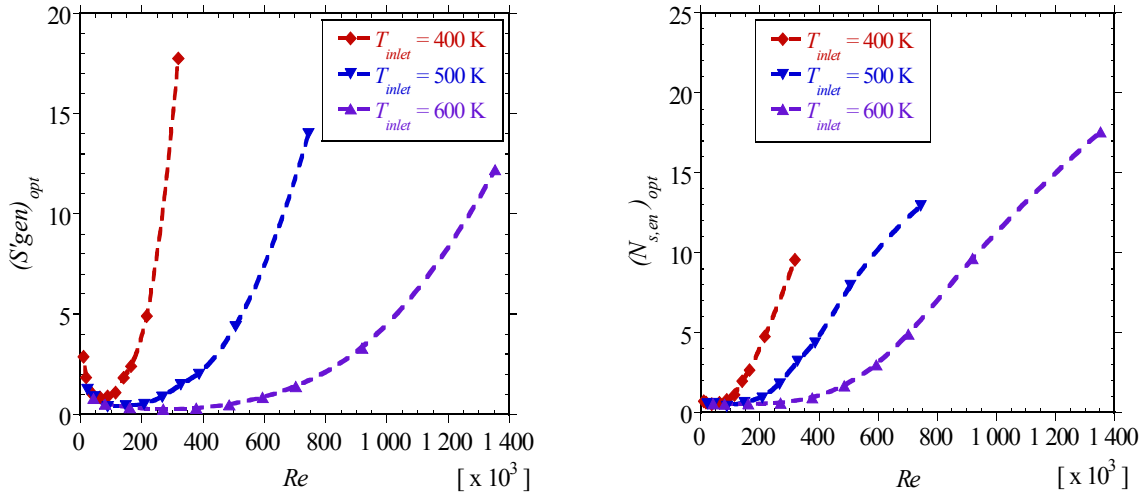

Fig. 7.29: Optimal entropy generation rate and optimal enhancement entropy generation number respectively as functions of Reynolds number and inlet temperatures in a receiver with perforated plate inserts.

7.3 RESULTS AND DISCUSSION – PERFORATED CONICAL INSERTS

7.3.1 FLOW STRUCTURE

The flow behaviour for the perforated conical inserts model is shown in Fig. 7.30 using velocity contours on the symmetry plane in the longitudinal direction.

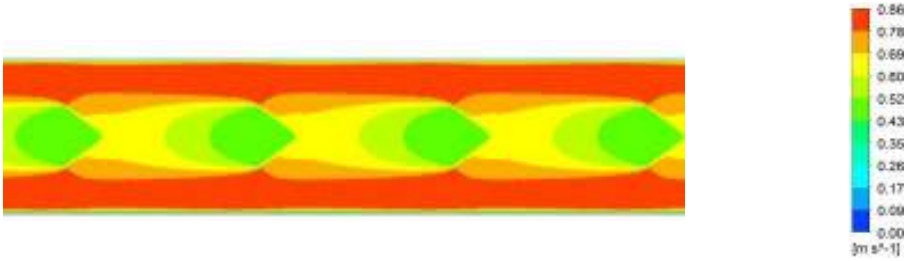

(a) $\tilde{\beta}_c = 0.33$

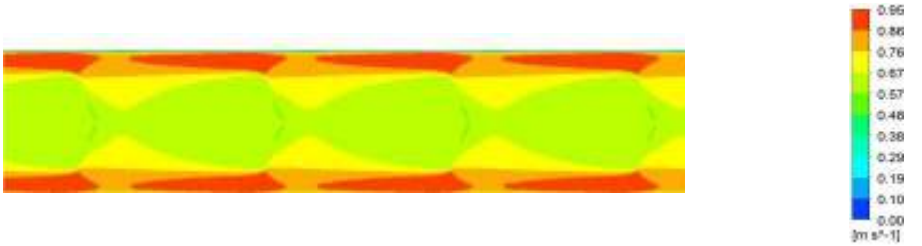

(b) $\tilde{\beta}_c = 0.67$

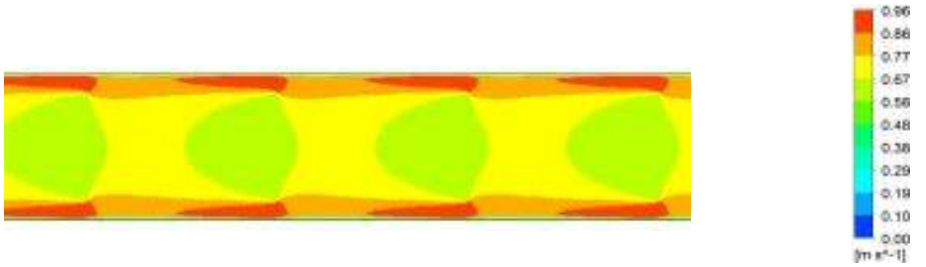

(c) $\tilde{\beta}_c = 0.83$

Fig. 7.30: Velocity contours for a receiver with perforated conical inserts on the symmetry plane of the receiver's absorber tube for insert spacing, $\tilde{p}_c = 0.11$, insert size $\tilde{r}_c = 0.73$, an inlet temperature of 400 K and $Re = 1.94 \times 10^4$ for different values of insert angle $(\tilde{\beta}_c)$.

The flow behaviour presented by the use of centrally placed perforated conical inserts includes mostly flow impingement/tube-side intensification as shown in Fig. 7.30. The heat transfer fluid is displaced from the core flow to cause increased turbulent intensity on the tube side, hence improved heat transfer.

7.3.2 HEAT TRANSFER PERFORMANCE

7.3.2.1 Nusselt numbers

Figure 7.31 shows the variation of Nusselt numbers with the size of the perforated conical insert at different insert cone angles. At a given cone angle, the Nusselt numbers are shown to increase with an increase in insert size. As the insert size increases, the free-flow area reduces, resulting in increased turbulence intensity and flow impingement on the absorber tube's walls. The figure also shows that, at a given size of the insert, the heat transfer performance increases as the cone angle increases. For all Reynolds numbers and insert spacing, the increase in heat transfer performance as the cone angle increases is significant for a cone angle $\tilde{\beta}_c$ greater than 0.70. For angles lower than 0.70, an increase in the insert's cone angle does not result in a significant increase in the receiver's heat transfer performance.

Figure 7.32 (a and b) shows the variation of the Nusselt numbers with Reynolds numbers for different values of insert spacing when $\tilde{r}_c$ = 0.91 for $\tilde{\beta}_c$ = 0.70 and $\tilde{\beta}_c$ = 0.90 respectively, for an inlet of temperature 600 K. Figure 7.32 (c and d) shows the variation of Nusselt numbers with Reynolds numbers for different values of insert spacing when $\tilde{r}_c$ = 0.91 for $\tilde{\beta}_c$ = 0.70 and $\tilde{\beta}_c$ = 0.90 respectively for an inlet temperature of 650 K.

The Nusselt number continues to increase as the Reynolds number increases, due to the thinner boundary layer at higher Reynolds numbers. The Nusselt number is also shown to increase as the insert spacing reduces due to increased flow impingement and turbulent intensity resulting from the use of many inserts per unit metre. For the range of parameters considered, the change in Nusselt numbers as the plate spacing reduces is not very significant as can be seen in Fig. 7.32. The heat transfer rate at higher temperatures is greater than that at lower temperatures. At high temperatures, the Reynolds numbers are higher for the same flow rate, thus thinner boundary layer.

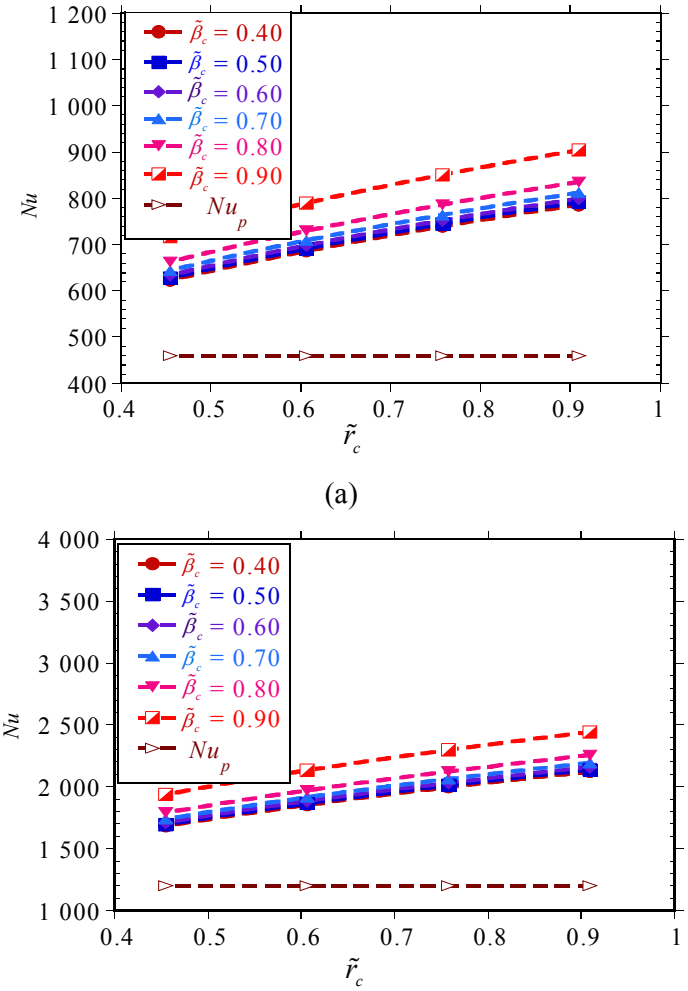

(a)

(b)

Fig. 7.31: Heat transfer performance of a receiver with perforated conical inserts as a function of insert size ($\tilde{r}_c$) and insert cone angle ($\tilde{\beta}_c$) for: (a) inlet temperature of 400 K, Re = 3.91 × 10^4 and insert spacing, $\tilde{p}_c$ = 0.06 and (b) inlet temperature of 650 K, Re = 2.18 × 10^5 and $\tilde{p}_c$ = 0.06.

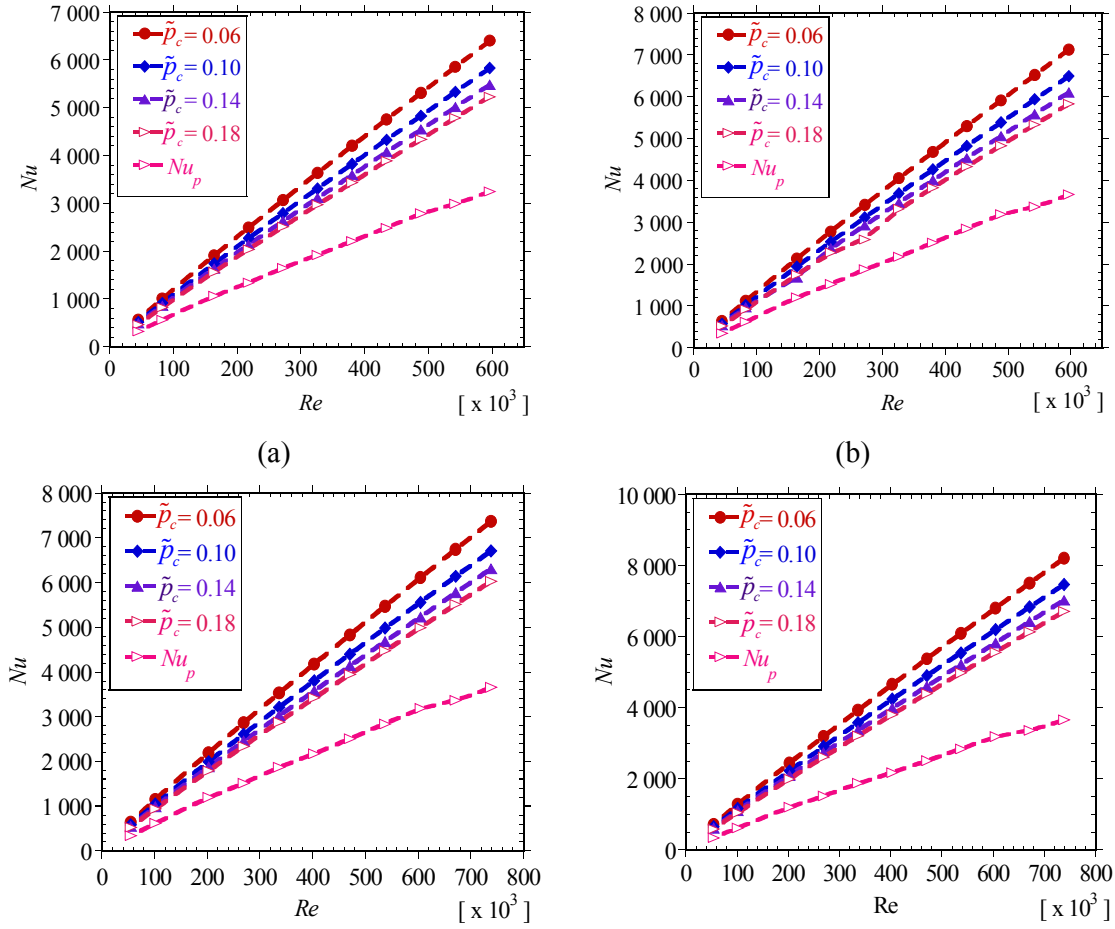

Fig. 7.32: Heat transfer performance of a receiver with perforated conical inserts as a function of Reynolds number and insert spacing, ($\tilde{p}_c$) for: (a) inlet temperature of 600 K, insert cone angle, $\tilde{\beta}_c$ = 0.70 and insert size, $\tilde{r}_c$ = 0.91, (b) inlet temperature of 600 K, $\tilde{\beta}_c$ = 0.90 and $\tilde{r}_c$ = 0.91, (c) inlet temperature of 650 K, $\tilde{\beta}_c$ = 0.70 and $\tilde{r}_c$ = 0.91 and (d) inlet temperature of 650 K, $\tilde{\beta}_c$ = 0.90 and $\tilde{r}_c$ = 0.91.

At a given value of insert cone angle and insert spacing, the heat transfer rate increases as the size of the insert increases. At a given value of the insert's size, the heat transfer rate also increases as the cone angle increases.

7.3.2.2 Heat transfer enhancement factor

The heat transfer enhancement factor by Eq. (7.17) gives the ratio of Nusselt number due to heat transfer enhancement to that in a plain tube. It shows by how much the heat transfer rate has increased. Figure 7.33 shows the variation of the heat transfer enhancement factor with Reynolds numbers for different values of plate spacing.

Generally, the heat transfer enhancement factor is shown to increase as the Reynolds number increases. For the range of parameters considered, the value of Nu^+ was in the range $1.05 \leq Nu^+ \leq 2.24$ for $0.45 \leq \tilde{r}_c \leq 0.91$.

7.3.2.3 Nusselt number correlation

Based on the results of the numerical simulation, a correlation for the Nusselt number was obtained for the range of parameters considered, using regression analysis. The Nusselt number was found to be correlated by

$$Nu = 0.005746\left(\tilde{p}_c\right)^{-0.1840}\left(\tilde{r}_c\right)^{0.3348}(1 + 0.02759\tan\beta_c)\left(Re\right)^{0.9355}\left(Pr\right)^{0.3968} \qquad 7.25$$

The coefficient of determination (R^2) is about 0.991 for this correlation. Figure 7.34 shows the parity plot for the Nusselt number. The correlation is valid within ± 12% for the range of parameters considered (tested for over 552 data points).

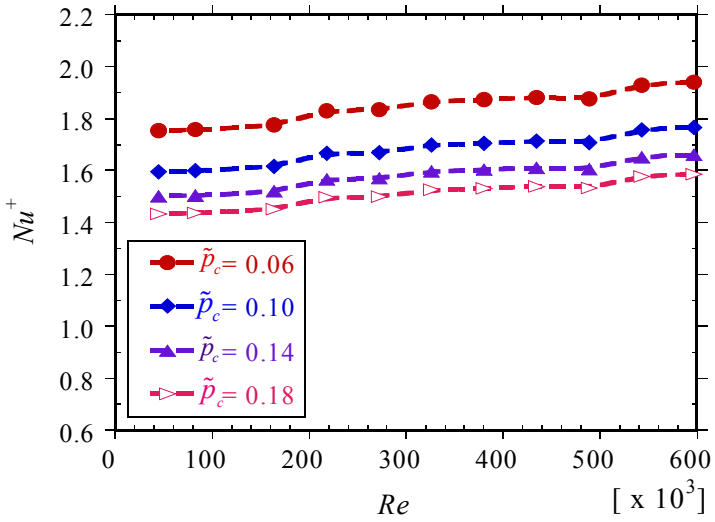

(a)

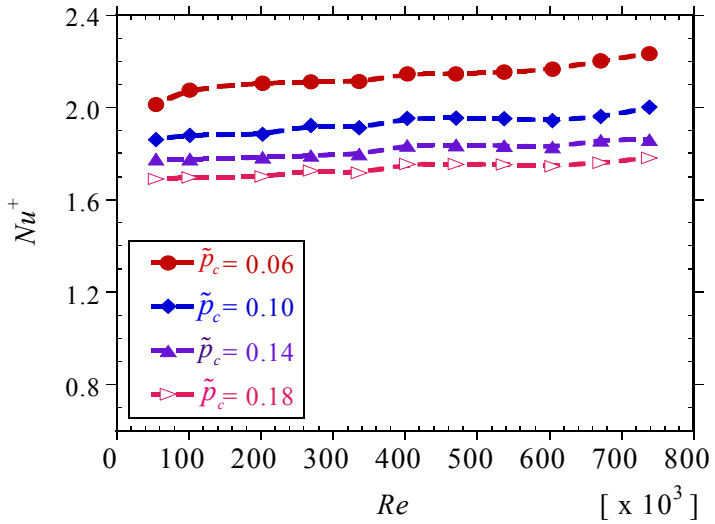

(b)

Fig. 7.33: Heat transfer enhancement factors for a receiver with perforated conical inserts as a function of Reynolds number and insert spacing ($\tilde{p}_c$) for: (a) inlet temperature of 600 K, insert cone angle, $\tilde{\beta}_c$ = 0.60 and insert size, $\tilde{r}_c$ = 0.91 and (b) inlet temperature of 650 K, $\tilde{\beta}_c$ = 0.90 and $\tilde{r}_c$ = 0.91.

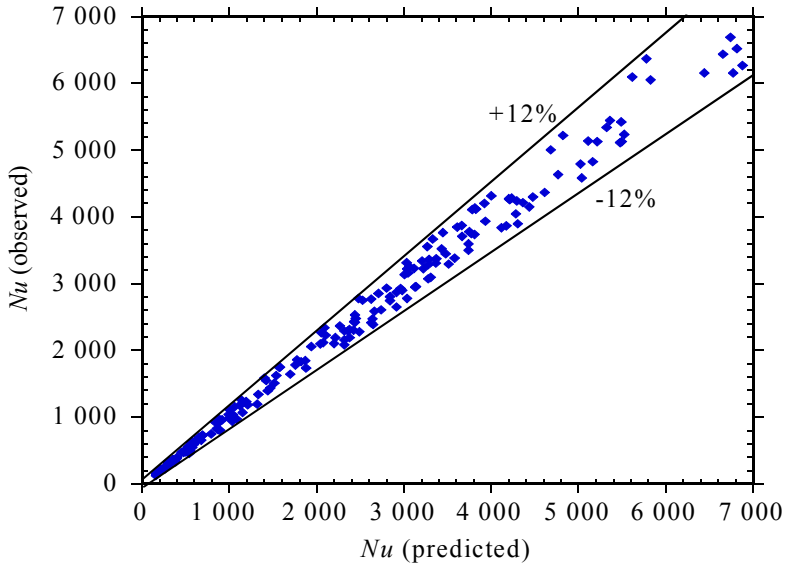

Fig. 7.34: Comparison of present study predicted heat transfer performance with the observed heat transfer performance for a receiver with perforated conical inserts

7.3.3 PRESSURE DROP

7.3.3.1 Friction factors

According to Eq. (7.13), the pressure drop is proportional to the friction factor. An increase in friction factor at a given Reynolds number implies an increase in pressure drop. The variation of friction factors with the perforated conical insert's orientation, spacing and size is presented in this section.

Figure 7.35 (a and b) shows the variation of friction factor with the size of the insert at Re = 3.91 $\times 10^4$ and $\tilde{p}_c$ = 0.06 when the inlet temperature is 400 K and Re = 1.64 $\times 10^5$ and $\tilde{p}_c$ = 0.14 when the inlet temperature is 600 K respectively. As expected, the figures show that the friction factors in the absorber tube with perforated conical inserts are higher than those in the absorber tube with no inserts. Generally, the friction factor increases as the size of the insert increases in all the four cases; this is due to the increased obstruction to flow as the insert size increases.

It can also be seen from the figures that as the insert cone angle increases, the friction factor increases significantly. For a given insert size, an increase of the insert cone angle increases the obstruction to flow, hence greater flow resistance.

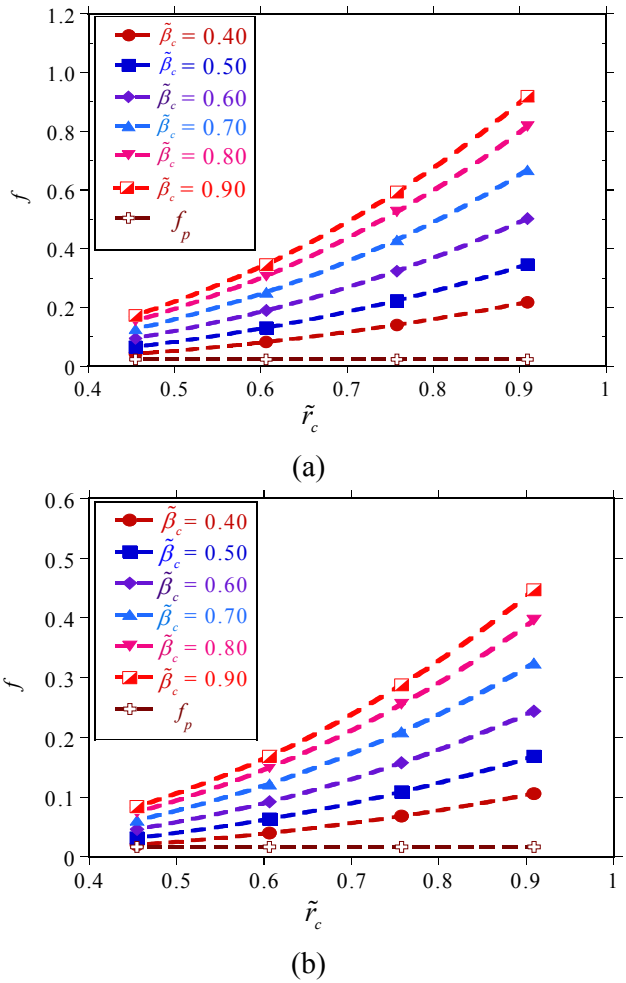

Fig. 7.35: Friction factor for a receiver with perforated conical inserts as a function of insert size ($\tilde{r}_c$) and insert cone angle ($\tilde{\beta}_c$) for: (a) inlet temperature of 400 K, $Re = 3.91 \times 10^4$ and insert spacing, $\tilde{p}_c = 0.06$ and (b) inlet temperature of 600 K, $Re = 1.64 \times 10^5$ and $\tilde{p}_c = 0.14$.

Figure 7.36 (a and b) shows the variation of friction factor with Reynolds numbers at different values of insert spacing for $\tilde{\beta}_c = 0.70$ when $\tilde{r}_c = 0.76$ at an inlet temperature of 650 K and for $\tilde{\beta}_c = 0.90$ when $\tilde{r}_c = 0.61$ at an inlet temperature of 600 K respectively.

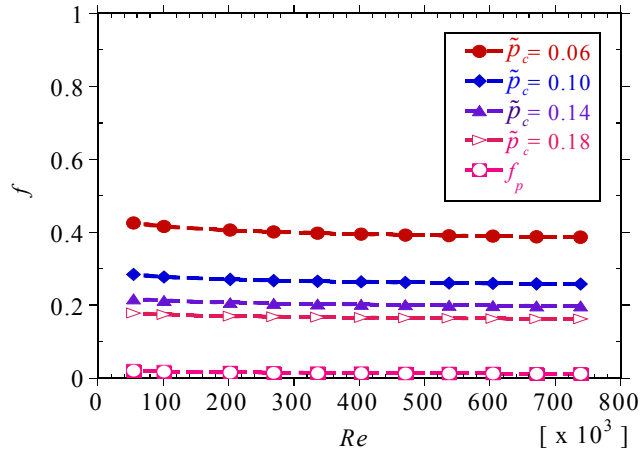

(a)

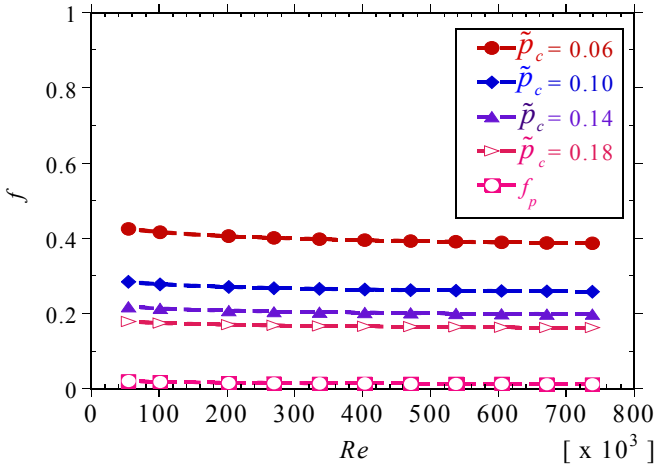

(b)

Fig. 7.36: Friction factor for a receiver with perforated conical inserts as a function of Reynolds number and insert spacing ($\tilde{p}_c$) for: (a) inlet temperature of 650 K, insert cone angle, $\tilde{\beta}_c$ = 0.70 and insert size, $\tilde{r}_c$ = 0.76 and (b) inlet temperature of 600 K, $\tilde{\beta}_c$ = 0.90 and $\tilde{r}_c$ = 0.61.

There is the same trend in the two figures: the friction factor increases as the insert spacing reduces. This is due to the increased number of plates per metre of the absorber tube that offer increased resistance to fluid motion as the spacing reduces.

As indicated above, the friction factor also increases as the cone angle increases and as the size of the insert increases. Increased obstruction to fluid motion as the size of the insert

increases and as the insert cone angle reduces also increases the friction factor. Differing from the heat transfer performance, the friction factor is shown to increase significantly as the insert spacing reduces.

7.3.3.2 Pressure drop penalty factors

The pressure drop of a receiver tube whose absorber tube is fitted with perforated conical inserts is related to that of a receiver with a plain absorber tube using the pressure drop penalty factor given by Eq. (7.18). Figure 7.37 (a) shows the variation of the pressure drop penalty factor with insert size at different angles of orientation for $\tilde{p}_c = 0.14$. The same trend as that obtained for the friction factor is shown. The pressure drop increases as the insert cone angle and insert size increase. This is due to flow blockage at high values of orientation angle and insert sizes, hence high fluid friction. Figure 7.37 (b) shows the variation of the pressure drop penalty factor with Reynolds numbers at different values of insert spacing. Reducing the spacing between consecutive inserts significantly increases the pressure drop. Therefore, the proper selection of the insert geometrical parameters is essential to ensure a sufficient increase in the receiver's heat transfer rates with a moderate increase in fluid friction. Moreover, reducing the spacing between consecutive inserts does not significantly increase the receiver's heat transfer performance.

The same trends can be obtained at other values of insert spacing and fluid temperatures. For the range of parameters considered, the pressure drop penalty factors were in the range $1.36 \leq f/f_p \leq 69$.

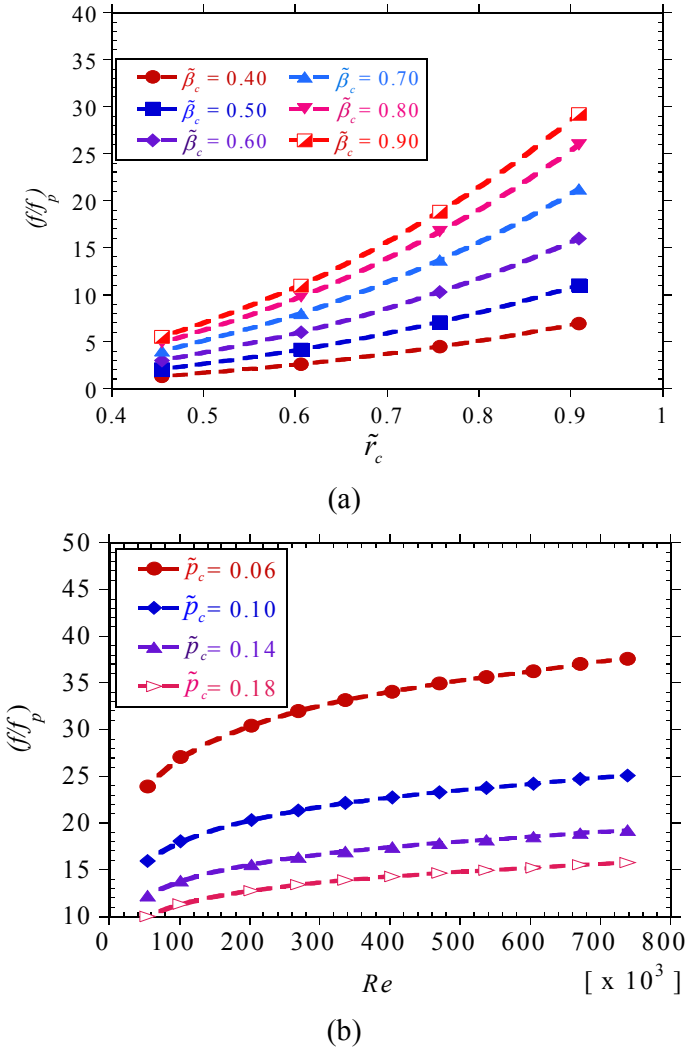

Fig. 7.37: Pressure drop penalty factors for a receiver with perforated conical inserts for an inlet temperature of 600 K: (a) as a function of insert size ($\tilde{r}_c$) and insert cone angle ($\tilde{\beta}_c$) for insert spacing, $\tilde{p}_c = 0.14$ and $Re = 2.18 \times 10^5$ and (b) as a function of Reynolds number and insert spacing ($\tilde{p}_c$) for $\tilde{\beta}_c = 0.60$ and $\tilde{r}_c = 0.91$.

7.3.3.3 Friction factor correlation

The friction factor is correlated according to

$$f = 0.002254\left(\tilde{p}_c\right)^{-0.7912}\left(\tilde{r}_c\right)^{2.4149}\left(1+\sin\beta\right)^{6.4224}\mathrm{Re}^{-0.03731} \qquad 7.26$$

R^2 = 0.988 for this correlation, and f is valid within ± 16% for the range of parameters considered and with $\beta_c \geq 0.60$.

7.3.4 PERFORMANCE EVALUATION

As a preliminary measure of the thermal performance of heat transfer enhancement techniques, Webb [200] developed a performance evaluation criteria based on a constant pumping comparison. For a constant power comparison, the thermal enhancement factor given by Eq. (7.16) should be greater than 1.0 where pumping power is concerned.

As shown in Fig. 7.38 (a), the thermal enhancement factor reduces as the size of the insert increases and as the cone angle increases. This because the increase in friction factor is much more than the increase in heat transfer performance, as the insert size increases or as the insert's cone angle increases. Figure 7.38 (b) shows that, at a given size of the insert and cone angle, the thermal enhancement factor increases with the Reynolds numbers up to some Reynolds numbers and then becomes nearly constant.

The thermal enhancement factor is also shown to be slightly higher at higher values of insert spacing. This was the general trend observed; graphs similar to these can be obtained at other values of inlet temperature. For the range of parameters considered, the thermal enhancement factor was in the range $0.53 \leq \chi \leq 1.14$.

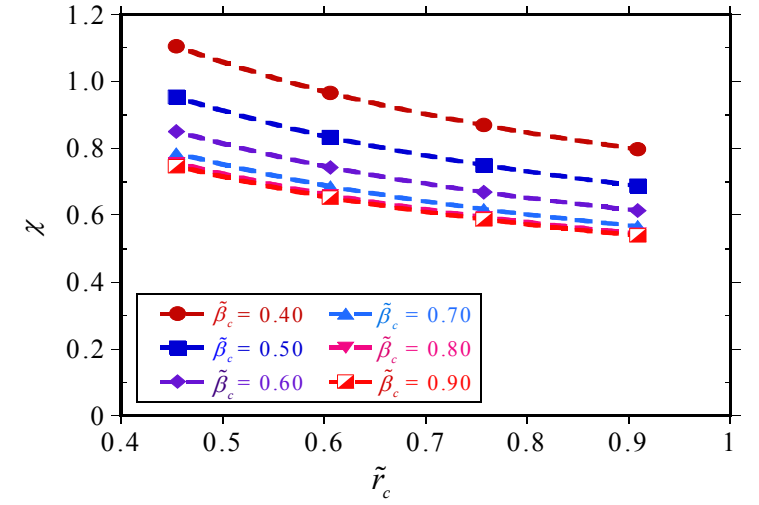

(a)

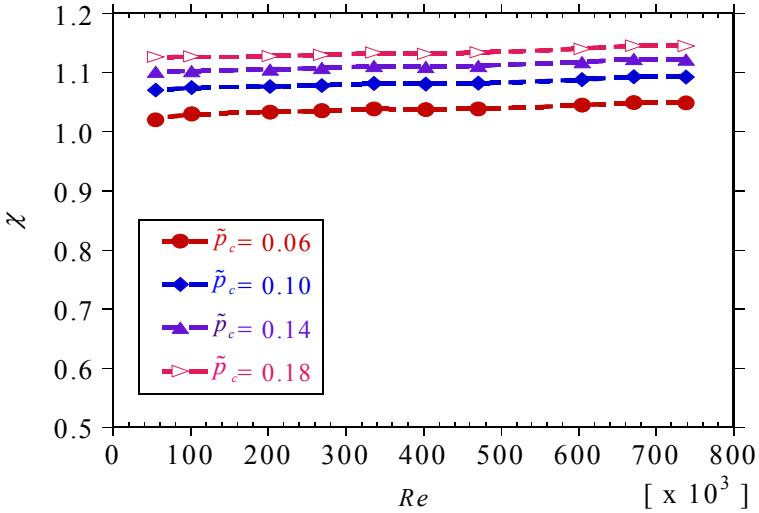

(b)

Fig. 7.38: Thermal enhancement factor for a receiver with perforated conical inserts: (a) as a function of insert size ($\tilde{r}_c$) and insert cone angle ($\tilde{\beta}_c$) for an inlet temperature of 600 K, insert spacing, $\tilde{p}_c$ = 0.14 and Re = 1.64 × 10^5 and (b) as a function of Reynolds number and insert spacing ($\tilde{p}_c$) for an inlet temperature of 650 K, $\tilde{\beta}_c$ = 0.40 and $\tilde{r}_c$ = 0.45.

For a given Reynolds number, values close to 1 were obtained for the smallest value of insert size, smallest cone angle and largest spacing due to the small pressure drops at these values. Despite the value of χ being close to 1, the obtained heat transfer increase was very small.

For solar thermal power plants, it is important to weigh up the increase in performance against the increase in pumping power. The increased heat transfer rate may be more than the increase in pumping power, even when the thermal enhancement factor is less than 1. Moreover, heat transfer enhancement provides additional benefits such as reducing the absorber tube's circumferential temperature difference and reducing the heat transfer irreversibilities at high heat fluxes in parabolic trough systems.

The use of collector thermal efficiency is recommended to show how heat transfer enhancement affects the actual performance of the parabolic trough collector. In this case, the actual gain in performance and the corresponding increase in pumping power are compared with one another as shown in Eq. (6.10). Figure 7.39 (a and b) shows the variation of collector thermal efficiency with insert spacing. Similar trends can be obtained for other inlet temperatures and different combinations of insert orientation and insert size. The reduction in absorber tube temperatures, the resulting reduction in absorber tube emissivity and improved heat transfer rates are the main factors leading to increased thermal efficiency. The thermal efficiency is shown to become lower than that in a collector with a non-enhanced receiver after some Reynolds numbers. This is because at values of Reynolds numbers higher than this, the achieved gain in performance is lower than the increase in pumping power.

The Reynolds number at which the thermal efficiency becomes lower than that in a plain receiver depends on the orientation angle, insert size and insert spacing. In general, increases in efficiency in the range 3% – 8% are obtainable in the range $0.10 \le \tilde{p}_c \le 0.18$, $0.45 \le \tilde{r}_c \le 0.76$ and $0.40 \le \tilde{\beta}_c \le 0.70$ provided the flow rates are lower than 37 m^3/h (about 8.6 kg/s at 400 K, 7.66 kg/s at 500 K, 6.56 kg/s at 600 K and 5.92 kg/s at 650 K). Outside the range mentioned above, an increase in efficiency may be achieved if the flow rate and geometrical parameters are properly matched. For example, at flow rates higher than the one mentioned above, lower insert sizes, lower orientation angles and larger spacings might provide a reasonable increase in thermal efficiency.

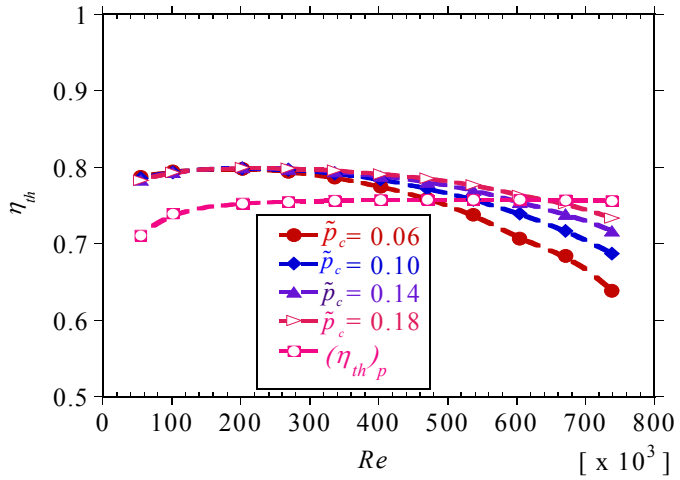

(a)

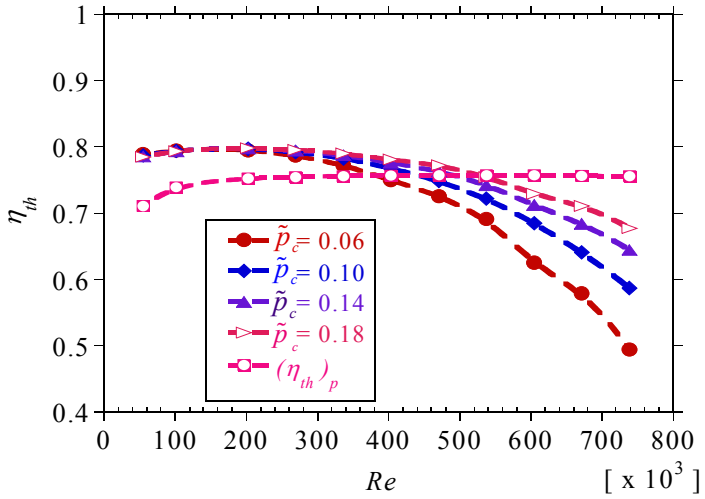

(b)

Fig. 7.39: Thermal efficiency for a receiver with perforated conical inserts as a function of Reynolds number and insert spacing ($\tilde{p}_c$) and an inlet temperature of 650 K: (a) for insert cone angle, $\tilde{\beta}_c = 0.60$ and insert size, $\tilde{r}_c = 0.91$ and (b) for $\tilde{\beta}_c = 0.90$ and $\tilde{r}_c = 0.91$.

7.3.5 ABSORBER TUBE TEMPERATURE DIFFERENCE

The improved heat transfer performance in the receiver's absorber tube is expected to reduce the absorber tube's circumferential temperature difference. Figure 7.40 shows the variation of absorber tube temperature difference with Reynolds numbers at different values of the perforated plate spacing.

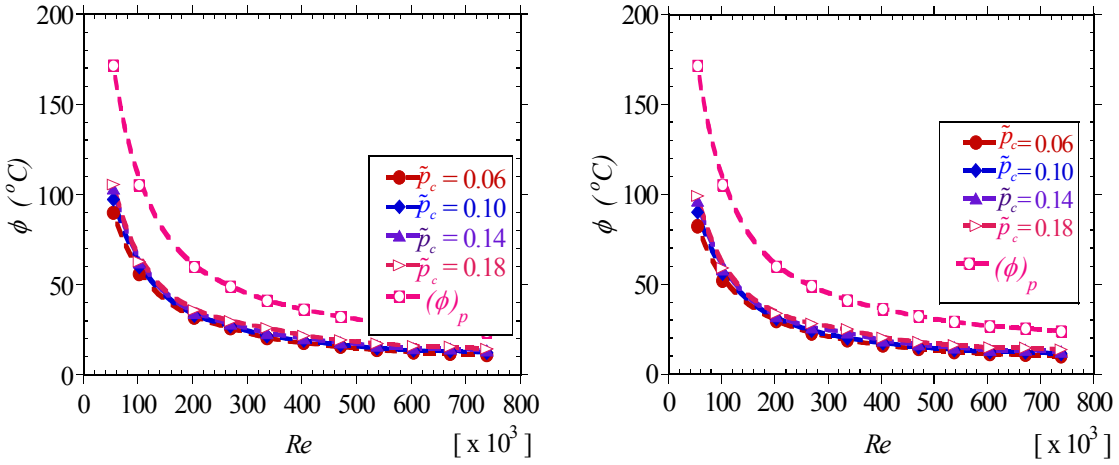

Fig. 7.40: Absorber tube circumferential temperature difference for a receiver with perforated conical inserts as a function of Reynolds number and insert spacing ($\tilde{p}_c$) and an inlet temperature of 650 K: (a) for insert cone angle, $\tilde{\beta}_c = 0.60$ and insert size, $\tilde{r}_c = 0.91$ and (b) for $\tilde{\beta}_c = 0.90$ and $\tilde{r}_c = 0.91$.

The highest reduction corresponds to the configuration with the highest heat transfer enhancement. Generally, the absorber tube's circumferential temperature difference reduces with increasing Reynolds numbers, reducing insert spacing, increasing orientation angle and increasing insert size.

For the range of parameters considered, the absorber tube's circumferential temperature difference was reduced by 3% – 56%. The reduction in absorber tube circumferential difference is beneficial at low Reynolds numbers where temperature differences are higher. However, reductions in the absorber tube's temperatures will still improve performance due to lower radiation loss, even at high Reynolds numbers if the increase in pumping power is lower than the gain in heat transfer performance. Low absorber tube temperatures reduce the radiation temperature and the emissivity of the absorber tube coating since the emissivity is temperature dependent. At lower Reynolds numbers, the absorber tube's circumferential temperature differences are high. For example, at $Re = 5.49 \times 10^4$ (inlet temperature, 650 K) the absorber tube's circumferential temperature difference is 172 °C for a plain absorber tube. With heat transfer enhancement and the same Reynolds number, using the perforated conical

inserts, the circumferential temperature difference reduces to 83 °C for an orientation angle $\tilde{\beta}_c = 0.90$, insert size $\tilde{r}_c = 0.90$ and spacing $\tilde{p}_c = 0.06$. There is the same trend for other inlet temperatures and geometrical parameters. In general, the lower the insert spacing, the larger the insert size.

7.3.6 ENTROPY GENERATION

As discussed above, knowledge of the entropy generation rates is essential for determining whether a given heat transfer enhancement technique makes thermodynamic sense and for determining the configurations that are thermodynamically optimal. Configurations with minimum entropy generation rates are thermodynamically optimal. In general the entropy generation number given by Eq. (7.19) should be less than 1 for better thermodynamic performance of a given heat transfer enhancement techniques when compared with a plain absorber tube. This section presents the entropy generation analysis of a receiver tube whose absorber tube is fitted with perforated conical inserts.

7.3.6.1 Entropy generation distribution

Figure 7.41 (a) shows the variation of entropy generation due to fluid flow irreversibilities with insert size at different cone angles, and Fig. 7.41 (b) shows the variation of entropy generation due to heat transfer irreversibility with insert size at different cone angles, all at $\tilde{p}_c$ = 0.06 and Re = 2.18 × 10^5. The entropy generation due to fluid flow irreversibilities increases as the size of the insert size increases.

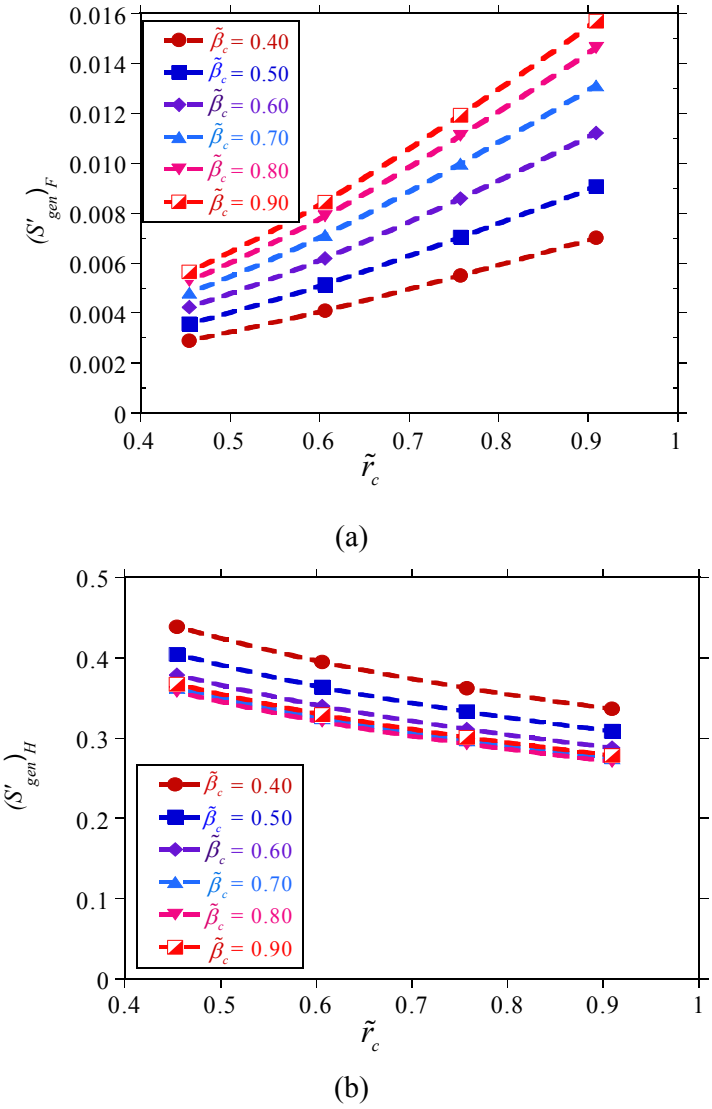

Fig. 7.41: Entropy generation due to fluid friction irreversibility and entropy generation due to heat transfer irreversibility, respectively for a receiver with perforated conical inserts as functions of insert size ($\tilde{r}_c$) and insert cone angle ($\tilde{\beta}_c$) for an inlet temperature of 650 K, $Re = 2.18 \times 10^5$ and insert spacing, $\tilde{p}_c = 0.06$.

By contrast, the entropy generation due to heat transfer irreversibilities reduces as the size of the insert increases. The general trend shown is that the fluid flow irreversibilities continue to increase with an increase in insert size, whereas the heat transfer irreversibilities reduce with an increase in insert size for all Reynolds numbers. The increasing trend of the fluid flow

irreversibilities is due to the increase in fluid resistance as the insert size increases, whereas the reduction in heat transfer irreversibilities as the insert size increases is the result of improved heat transfer that reduces the finite temperature difference.

The variation of fluid flow irreversibility with the insert's cone angle generally follows the same trend as the variation of fluid friction. Fluid flow irreversibilities are shown to increase as the cone angle increases, as shown in Fig. 7.41 (a). Similar to fluid friction, smaller insert cone angles give lower fluid flow irreversibilities than larger angles, because of the obstruction of flow and increased flow impingement rates at larger angles. The variation of the heat transfer irreversibility with cone angle is the inverse of the Nusselt number variation. Smaller angles resulted in low Nusselt numbers, hence higher irreversibilities, whereas larger angles resulted in higher Nusselt numbers, hence reduced irreversibilities as shown in Fig. 7.41 (b). At all inlet temperatures, there are the same trends for the entropy generation due to fluid friction and entropy generation due to heat transfer irreversibility.

The total entropy generation rate is shown to reduce with insert size for the lowest Reynolds number since the fluid flow irreversibility is not significant. As the Reynolds numbers increase, the total entropy generation rate increases with insert size and insert spacing owing to the higher fluid flow irreversibilities.

The entropy generation due to fluid flow irreversibility is shown to increase as the spacing reduces as shown in Fig. 7.42 (a). This is due to increasing fluid friction as the spacing reduces. The variation of the heat transfer irreversibility with insert spacing is not very pronounced as shown in Fig. 7.42 (b). A closer look at Fig. 7.42 (b) shows that the entropy generation due to heat transfer irreversibilities slightly reduces with a reduction in the spacing. As discussed above, the heat transfer performance and absorber tube temperatures are not significantly affected by the reduction in insert spacing.

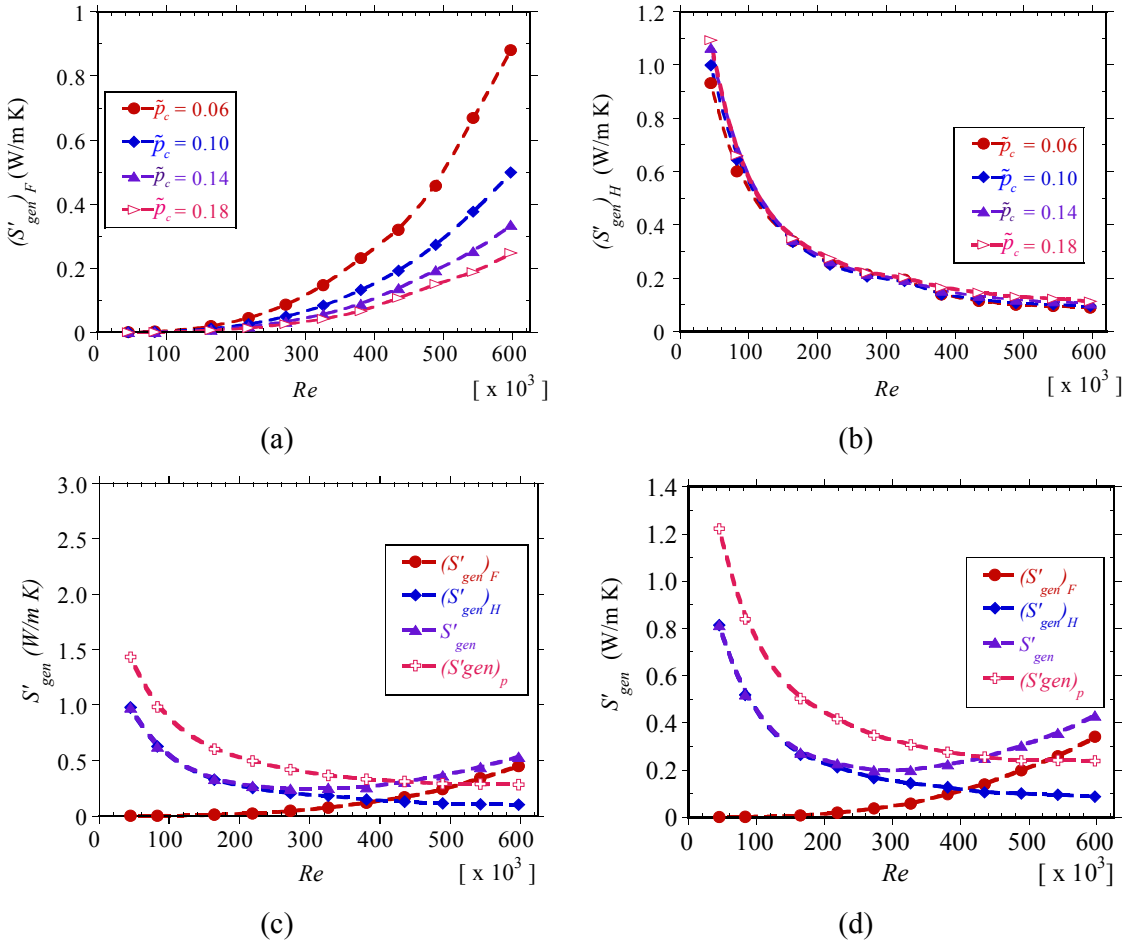

Fig. 7.42: Entropy generation due to fluid friction $(S'_{gen})_F$, entropy generation due to heat transfer irreversibility $(S'_{gen})_H$ and total entropy generation rate, S'_{gen} as functions of Reynolds number for insert cone angle, $\tilde{\beta}_c$ = 0.90 and insert size, $\tilde{r}_c$ = 0.91: (a) $(S'_{gen})_F$ for an inlet temperature of 600 K, (b) $(S'_{gen})_H$ an inlet temperature of 600 K, (c) $(S'_{gen})_F$, $(S'_{gen})_H$ and S'_{gen} for an inlet temperature of 600 K and (d) $(S'_{gen})_F$, $(S'_{gen})_H$ and S'_{gen} for an inlet temperature of 650 K.

The variation of the heat transfer irreversibility and fluid flow irreversibility discussed above results in an optimal Reynolds number at which the total entropy generation rate is minimum, as was obtained for the plain receiver tube (see Chapter 5), for the twisted tape insert (see Chapter 6) and for the perforated plate inserts discussed above. The existence of the optimal Reynolds number is shown in Fig. 7.42 (c and d) for $\tilde{p}_c$ = 0.10 when $\tilde{\beta}_c$ = 0.90 at 600 K and

650 K respectively and a fixed insert size of $\tilde{r}_c = 0.91$. The figures indicate that the entropy generation as well as the optimal Reynolds number for an enhanced receiver is lower than that for a plain receiver.

Figure 7.43 (a – d) shows the variation of Bejan number with Reynolds number at different cone angles, conical insert sizes and conical insert spacings.

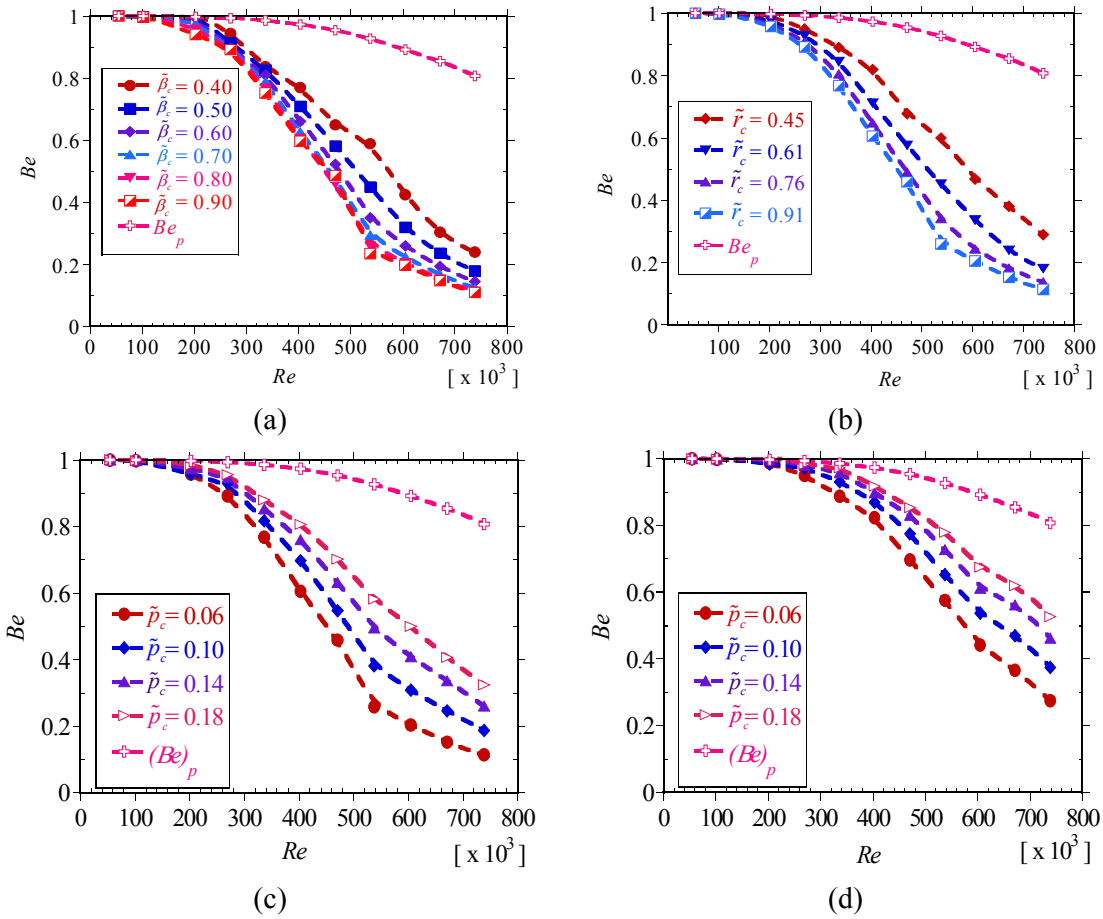

Fig. 7.43: Bejan number for a receiver with perforated conical insets a function of Reynolds number for an inlet temperature of 650 K and: (a) insert cone angle ($\tilde{\beta}_c$), insert spacing, $\tilde{p}_c$ = 0.06 and insert size, $\tilde{r}_c$ = 0.91, (b) insert size ($\tilde{r}_c$), $\tilde{p}_c$ = 0.06 and $\tilde{\beta}_c$ = 0.80, (c) insert spacing ($\tilde{p}_c$), $\tilde{\beta}_c$ = 0.80 and $\tilde{r}_c$ = 0.91 and (d) insert spacing ($\tilde{p}_c$), $\tilde{\beta}_c$ = 0.90 and $\tilde{r}_c$ = 0.45.

It can be seen from the figure that insert size significantly influences the Bejan number

compared to the other parameters. As the insert spacing reduces, the Bejan number reduces. This indicates the reduction in heat transfer irreversibility for low Reynolds numbers and an increase in fluid friction irreversibility as the Reynolds numbers increase.

As shown in Fig. 7.43, the Bejan number is generally significantly less than that for a plain absorber tube for all the Reynolds numbers. Therefore, the use of inserts reduces the heat transfer irreversibilities at all the Reynolds numbers shown in the figure. The Bejan number is shown to depend more on the Reynolds number, plate spacing and insert size than on the angle of orientation.

Figure 7.44 shows the variation of the total entropy generation rate per metre of the receiver tube with perforated conical inserts. The figure shows that for every cone angle, insert size and insert spacing there is a Reynolds number at which the entropy generation is minimum. The figure also shows that at low Reynolds numbers, the entropy generation rates are generally lower than those in a plain absorber tube. As the Reynolds numbers increase beyond the optimal Reynolds number, the entropy generation rates increase substantially, so that heat transfer enhancement becomes undesirable.

It is also shown that using the perforated conical inserts also shifts the optimal Reynolds number to a lower value than is the case for the optimal Reynolds number in a receiver with a plain absorber tube.

For the plain absorber tube, the optimal Reynolds numbers obtained are presented in Chapter 5. The optimal Reynolds number can be determined from the optimal flow rates given in Chapter 5, depending on the concentration ratio. The variation of the optimal Reynolds number with insert spacing is shown in Fig. 7.45.

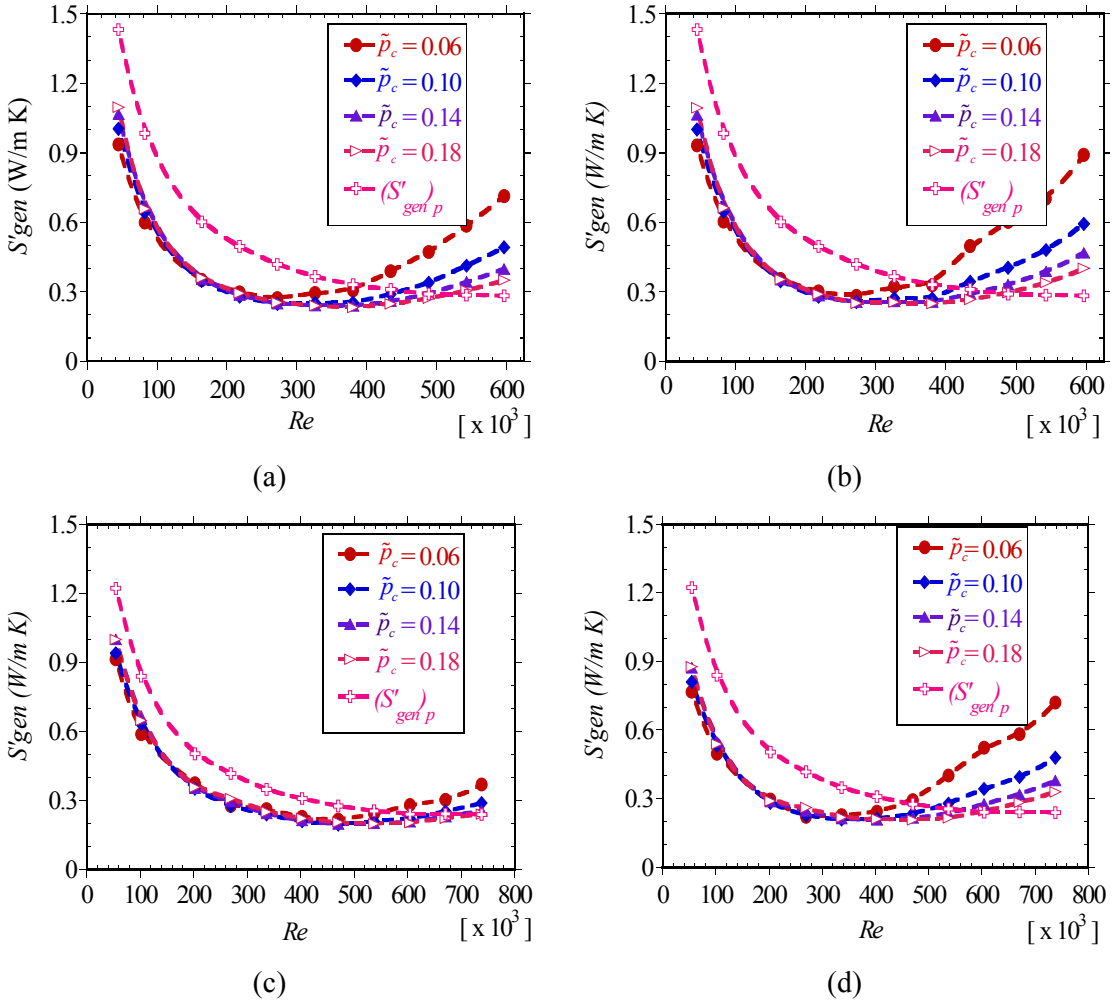

Fig. 7.44: Total entropy generation rate in a receiver with perforated conical insets a function of Reynolds number: (a) for an inlet temperature of 600 K, insert cone angle $\tilde{\beta}_c = 0.60$ and insert size, $\tilde{r}_c = 0.91$, (b) for an inlet temperature of 600 K, $\tilde{\beta}_c = 0.90$ and $\tilde{r}_c = 0.91$, (c) for an inlet temperature of 650 K, $\tilde{\beta}_c = 0.90$ and $\tilde{r}_c = 0.45$ and (d) for an inlet temperature of 650 K, $\tilde{\beta}_c = 0.90$ and $\tilde{r}_c = 0.91$.

Generally, the optimal Reynolds number slightly reduces with a reduction in insert spacing and with an increase in insert size. The optimal Reynolds number also slightly reduces as the insert spacing increases and increases slightly as the cone angle increases. The optimal Reynolds number is in the range $7 \times 10^4 \leq Re_{opt} \leq 1.15 \times 10^5$ for $0.61 \leq \tilde{r}_c \leq 0.91$ for an inlet

temperature of 400 K. The highest Reynolds number corresponds to $\tilde{r}_c = 0.61$ while the lowest Reynolds number corresponds to $\tilde{r}_c = 0.91$.

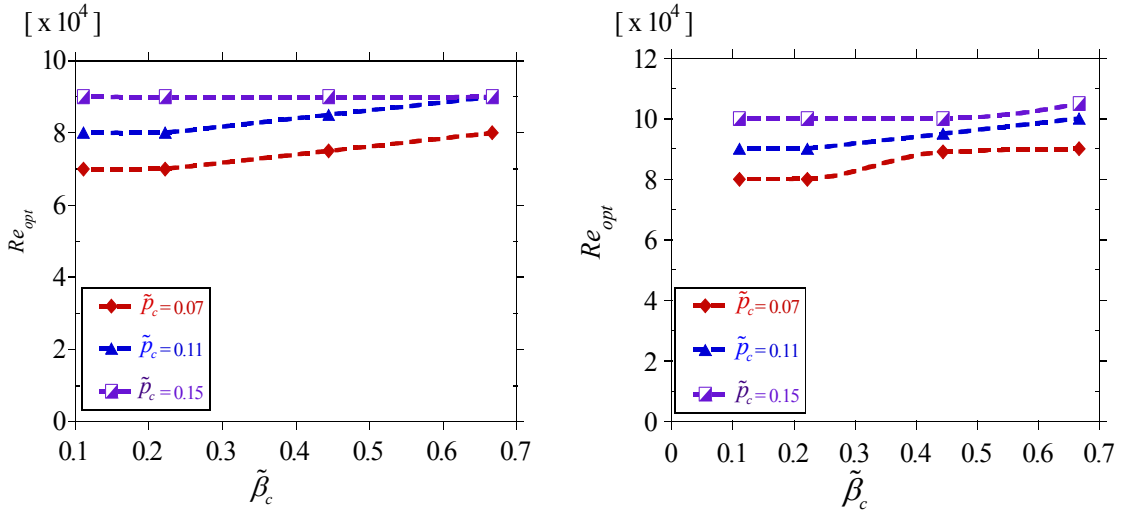

Fig. 7.45: Optimal Reynolds number in a receiver with perforated conical inserts as a function of insert cone angle ($\tilde{\beta}_c$) at an inlet temperature of 400 K: (a) insert size, $\tilde{r}_c = 0.91$ and (b) insert size, $\tilde{r}_c = 0.61$.

7.3.6.2 Thermodynamic evaluation of receiver with perforated plate inserts

The enhancement entropy generation number, $N_{s,en}$ given in Eq. (7.19) was used for evaluating the thermodynamic effectiveness of a given heat transfer enhancement technique. In general, the value of this ratio should be less than 1 for the enhancement technique to be thermodynamically feasible. For ratios less than 1.0, the irreversibilities are reduced when compared to a plain tube and for ratios greater than 1, the enhancement techniques result in more irreversibilities than in a plain tube.

It can be seen from Fig. 7.46 (a – d) that, at Reynolds numbers greater than 9.0 $\times 10^4$, $N_{s,en}$ increases appreciably as the cone angle increases, insert size increases and spacing reduces. For all the values of insert spacing considered, the value of $N_{s,en}$ is greater than 1 for $Re \geq 1.0 \times 10^5$ regardless of the cone angle and insert size. In the range of Reynolds numbers from $1.94 \times 10^4 \leq Re \leq 9.0 \times 10^4$, there are sufficient reductions in entropy generation due to

heat transfer enhancement and $N_{s,en}$ is sufficiently lower than 1.0. Generally, such plots can be obtained at all inlet temperatures and values of flow rates obtained at which $N_{s,en}$ is lower than 1.

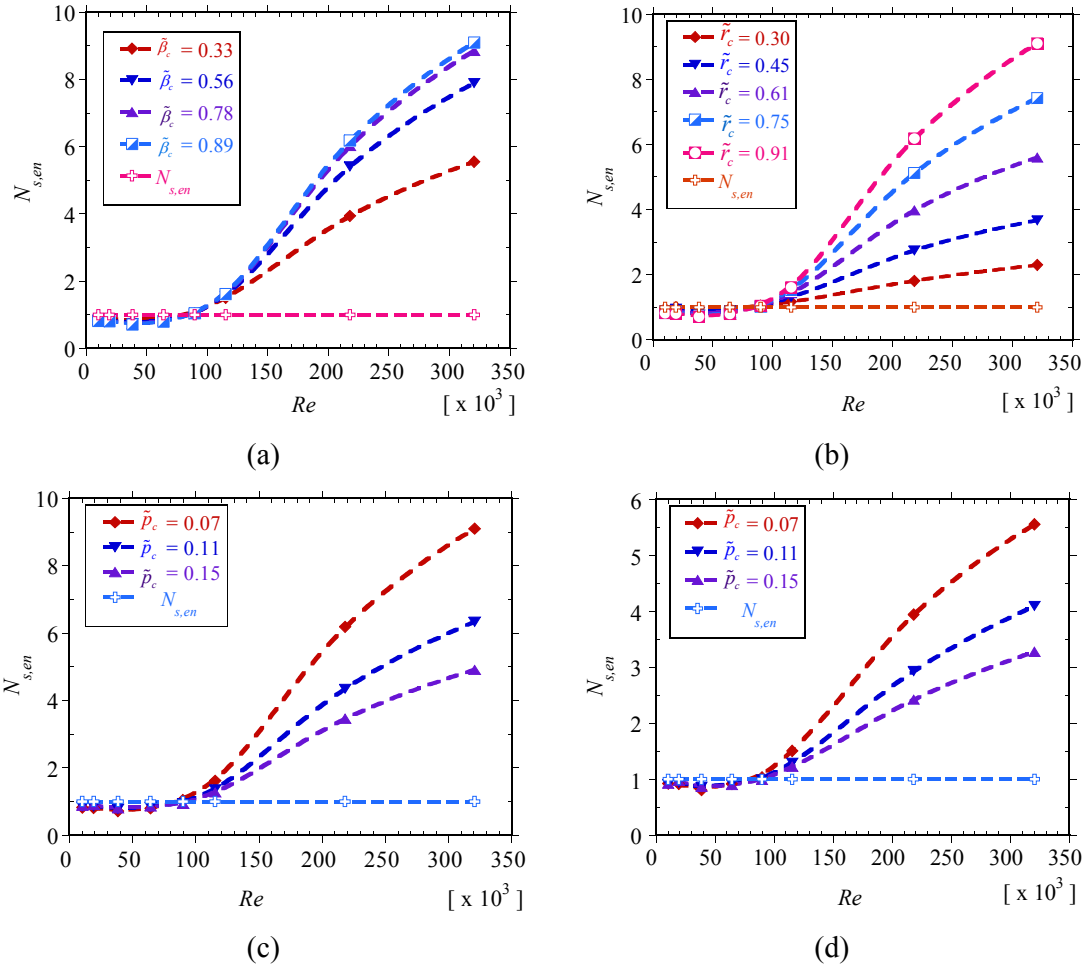

Fig. 7.46: Enhancement entropy generation number for a receiver with perforated conical inserts for an inlet temperature of 400 K as a function of Reynolds number: (a) and insert cone angle ($\tilde{\beta}_c$) for $\tilde{p}_c$ = 0.07 and $\tilde{r}_c$ = 0.91, (b) and insert size ($\tilde{r}_c$) for $\tilde{p}_c$ = 0.07 and $\tilde{\beta}_c$ = 0.11, (c) insert spacing ($\tilde{p}_c$) for $\tilde{\beta}_c$ = 0.11 and $\tilde{r}_c$ = 0.91 and (d) insert spacing ($\tilde{p}_c$) $\tilde{\beta}_c$ = 0.67 and $\tilde{r}_c$ = 0.91.

The value of flow rates at which the entropy generation ratio is less than 1 will generally depend on the insert spacing, insert angle and insert size, and fluid temperature. For all temperatures and

geometrical parameters, flow rates of less than 43 m^3/h (10.18 kg/s at 400 K, 9.05 kg/s at 500 K, 7.75 kg/s at 600 K and 6.69 kg/s at 650 K) ensure entropy generation ratios that are less than 1. For flow rates at which the entropy generation rates are lower than those in a receiver with a plain absorber tube, the entropy generation rates are reduced in the range of 3% – 47%.

7.3.7 MULTI-OBJECTIVE OPTIMISATION

As discussed above, heat transfer enhancement leads to an increase in the heat transfer performance of a given heat exchanger and an increase in pressure drop. As shown in the previous sections, heat transfer and fluid friction both increase as the insert cone angle reduces, insert size increases and as the spacing reduces. For heat transfer problems, the objective is usually to increase the heat transfer performance while keeping fluid friction low. Therefore, a multi-objective optimisation problem arises. As presented in Section 3.4.2, genetic algorithms are suited to such types of problems. Multi-objective genetic algorithms use the concept of dominations to search the decision variable space for a set of solutions that are non-dominated with respect to one another and dominate all other solutions. This set of solutions is known as the Pareto optimal solutions. In the absence of further information, all these solutions are equally important. In this thesis, the hybrid variant of the Non-dominated sorting genetic algorithm II (NSGA II) available in ANSY® release 14 [99] was used to obtain such solutions.

7.3.7.1 Formulation of the optimisation problem

The multi-objective optimisation problem under consideration can be written according to Eq. (3.42) as

$$\text{Maximise } f_1(\mathbf{x}) / \text{ Minimise } f_2(\mathbf{x}) \tag{7.27}$$

The objective functions $f_1(\mathbf{x})$ and $f_2(\mathbf{x})$ are heat transfer performance expressed as the Nusselt number Nu, and the pressure drop expressed as the fluid friction f, respectively.

The numerical simulations and optimisation were carried out for fixed values of Reynolds numbers. The Reynolds numbers were in the range $1.04 \times 10^4 \leq Re \leq 1.36 \times 10^6$ depending on the fluid temperature used. The fluid temperatures were fixed at 400 K, 500 K and 600 K.

The concentration ratio (C_R) was fixed at 86; direct normal irradiance was fixed at 1 000 W/m^2.

The design variable ranges representing the three degrees of freedom in the optimisation problem are given as

$$\begin{aligned} 0.06 \le \tilde{p}_c \le 0.15 \\ 0.30 \le \tilde{r}_c \le 0.91 \\ 0.39 \le \tilde{\beta}_c \le 0.90 \end{aligned} \qquad 7.28$$

7.3.7.2 Optimisation results

The optimisation procedure used was presented in Chapter 3 (Section 3.7). Standard second-order polynomials provided sufficient accuracy for the response surface. The coefficient of determination (R^2) given by Eq. (3.52) and the adjusted coefficient of determination (R^2_{adj}) given by Eq. (3.53) were greater than 0.97. The root mean square error given by Eq. (3.49), the maximum relative residual error given by Eq. (3.50) and the relative average absolute error given by Eq. (3.51) were all less than 2%.

Figure 7.47 shows the 3-D response surfaces for the variation of Nusselt numbers and friction factors with insert size and cone angle (Fig. 7.47 a and b) and with insert spacing and cone angle (Fig. 7.47 (c and d) and a Reynolds number of 2.72×10^5 respectively. The same trend is obtainable with other Reynolds numbers and other values of plate spacing. The figures show the Nusselt number increases as the insert size increases, the cone angle reduces and insert spacing reduces. The friction factor is also shown to increase with an increase in insert size and a reduction in cone angle and insert spacing. The trend shown by the absorber tube temperature gradients is the inverse of the Nusselt number variation. As the Nusselt numbers increase, the absorber tube temperature gradients reduce due to better heat transfer enhancement.

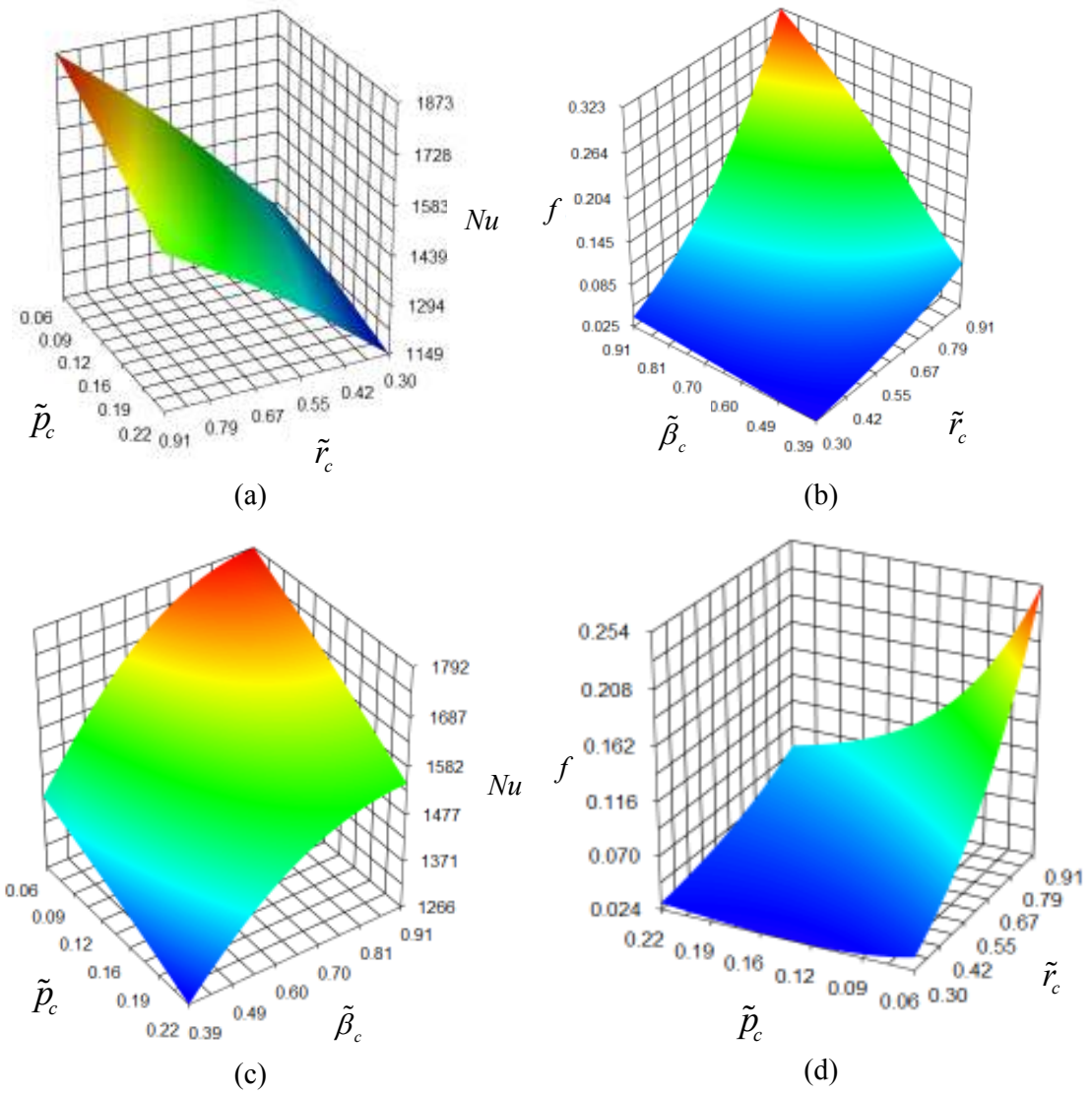

Fig. 7.47: 3-D response surfaces for Nusselt numbers and friction factor for a receiver with perforated conical inserts at Re = 2.72 × 10^5 and inlet temperature of 600 K. (a) Nusselt number as a function of insert spacing, $\tilde{p}_c$ and insert size, $\tilde{r}_c$, (b) friction factor as a function of insert cone angle, $\tilde{\beta}_c$ and insert size, $\tilde{r}_c$, (c) Nusselt number as a function of insert spacing, $\tilde{p}_c$ and insert cone angle, $\tilde{\beta}_c$ and (d) friction factor as a function of insert spacing, $\tilde{p}_c$ and insert size, $\tilde{r}_c$.

As shown above, the multi-objective optimisation for a case where two objectives are conflicting yields a set of solutions in which an improvement in one objective sacrifices the

quality of the other. Figure 7.48 shows such solutions of the multi-objective optimisation at a Reynolds number of 2.18 x 10^5. This is the same variation as was obtained for twisted tape inserts and perforated plate inserts. The same variation is obtainable at other values of Reynolds numbers. The variation of *Nu* and *f* is a smooth and continuous curve for every Reynolds number considered. It is shown from the figure that as *Nu* increases, *f* also increases. Therefore, selecting any one of the solutions along the curve will improve one of the objectives while sacrificing the quality of the other objective. Reducing the perforated insert size and cone angle gives an improved heat transfer performance but significantly increases fluid friction as shown above.

The decision support process described by Eqs. (3.55 – 3.60) in Section 3.8 was used to obtain optimal design candidates. Similar to previous cases of multi-objective optimisation for twisted tape inserts and perforated plate insert, the objectives have the same weights. That is, the maximisation of heat transfer enhancement and the minimisation of fluid friction are equally important.

Figure 7.49 (a – c) shows the effect of Reynolds numbers on optimal parameters for the five cases considered. As shown, no clear trend for the variation of insert spacing, insert size and the insert cone angle. Given that, the optimisation has three degrees of freedom; an increase in insert spacing may be accompanied by either an increase in insert size or a reduction in the insert cone angle for better heat transfer; the opposite is true for lower fluid friction. To show this, one fluid temperature is considered and all the optimal geometrical parameters plotted. The variation of optimal parameters with Reynolds number for T_{inlet} = 650 K is shown in Fig. 7.49 (d). Generally, the optimal spacing slightly reduces with the Reynolds number. The variation of optimal insert size depends on the optimal orientation of the insert. As the insert size increases, the insert orientation reduces. In general, as the plate size increases or reduces, it is shown that the cone angle must increase or reduce accordingly to achieve the desired heat transfer enhancement and fluid friction.

As discussed above, it should be noted that the actual solutions should be selected from the Pareto solutions in Fig. 7.48 and be based on the designer's specified criteria and needs.

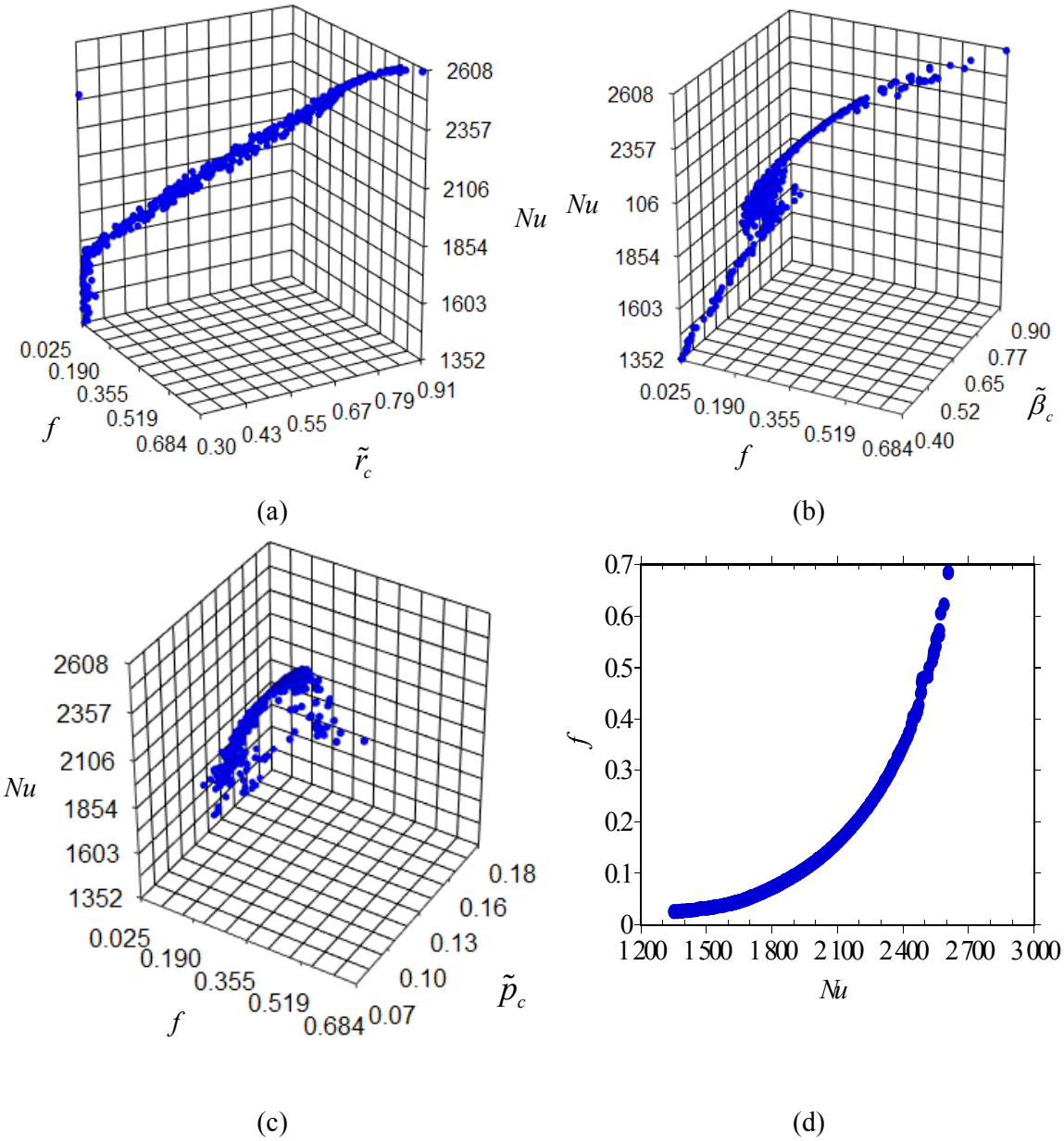

Fig. 7.48: Pareto optimal solutions for a receiver with perforated conical inserts for an inlet temperature of 600 K and $Re = 2.18 \times 10^5$: (a) Nusselt number as a function of friction factor and insert size ($\tilde{r}_c$), (b) Nusselt number as a function of friction factor and insert cone angle ($\tilde{\beta}_c$), (c) Nusselt number as a function of friction factor and insert spacing ($\tilde{p}_c$) and (d) 2-D Pareto optimal front for friction factor and Nusselt number.

Figure 7.50 shows the variation of Nusselt numbers for the optimal cases. For the considered case, it can be shown that the Nusselt number has the same variation as discussed above in the parametric analysis. For the range of parameters considered, the heat transfer enhancement for the optimal configurations is in the range 1.65 to 1.90 depending on the fluid temperature and Reynolds number.

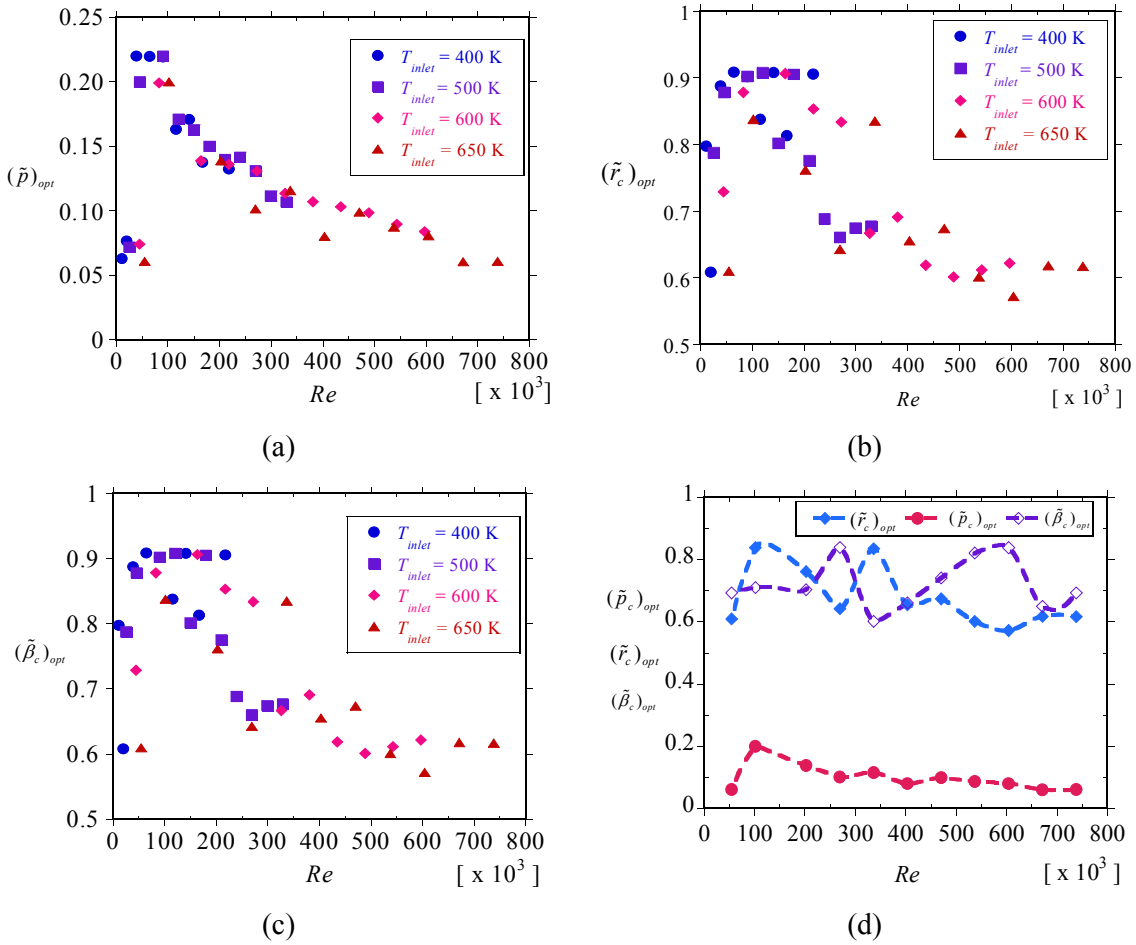

Fig. 7.49: Optimal perforated conical insert geometrical parameters as a functions of Reynolds number: (a) optimal insert spacing $(\tilde{p}_c)_{opt}$, (b) optimal insert size $(\tilde{r}_c)_{opt}$, (c) optimal insert cone angle $(\tilde{\beta}_c)_{opt}$ and (d) $(\tilde{p}_c)_{opt}$, $(\tilde{r}_c)_{opt}$ and $(\tilde{\beta}_c)_{opt}$ for an inlet temperature of 650 K.

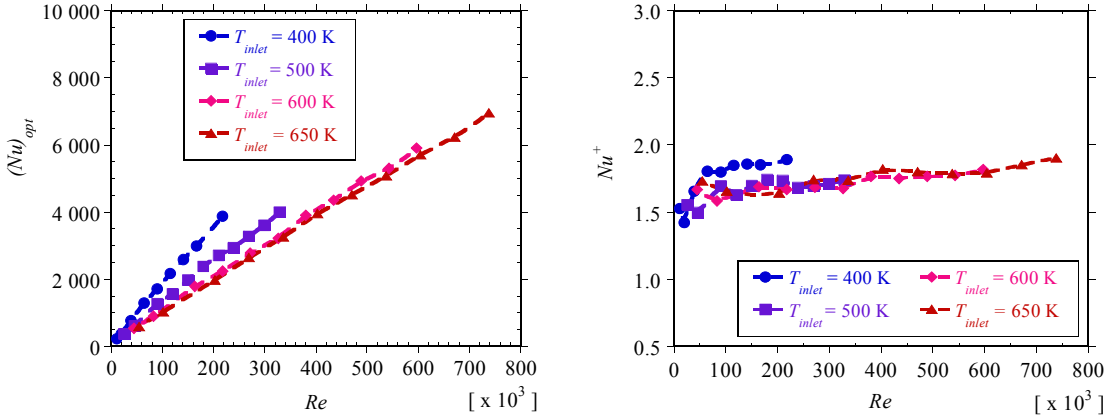

(a) (b)

Fig. 7.50: Optimal heat transfer performance for a receiver with perforated conical inserts as a function of Reynolds number: (a) optimal Nusselt number and (b) optimal heat transfer enhancement factor.

Figure 7.51 depicts the friction factor for the optimal configurations. The same variation is shown as that obtained in the parametric analysis. For the optimal geometrical parameters, the fluid friction increases in the range 11 – 15 times compared to a plain receiver tube.

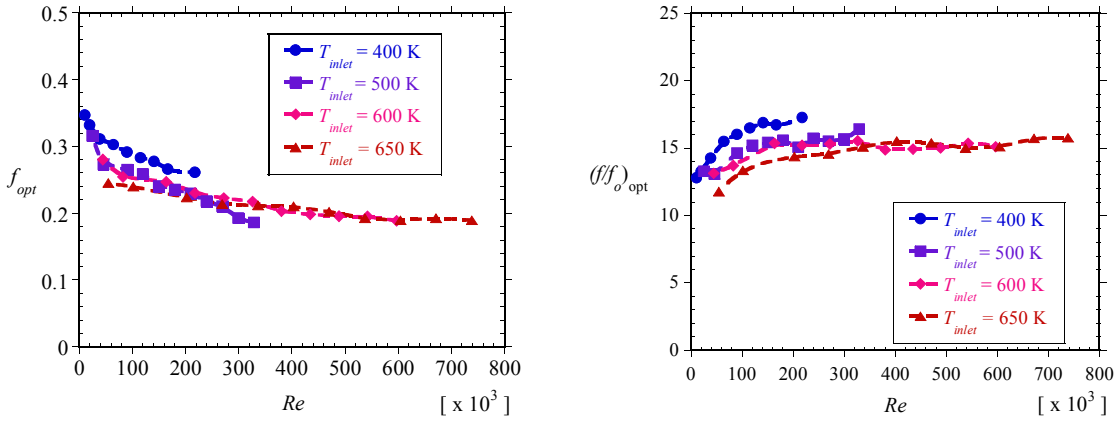

(a) (b)

Fig. 7.51: Optimal friction factor and optimal pressure drop penalty factors respectively for a receiver with perforated conical inserts as a function of Reynolds number and inlet temperature for optimal insert geometries.

For these solutions, by applying the entropy generation minimisation method we can obtain suitable solutions from those obtained in multi-objective optimisation to obtain

thermodynamically optimal solutions. Figure 7.52 shows the variation of entropy generation rate and the entropy generation ratio with Reynolds numbers for the optimal solutions obtained from the multi-objective optimisation. As shown, there is an optimal Reynolds number at which the entropy generation is minimum at any given inlet temperature, as discussed previously. In Fig. 7.52, the entropy generation ratio gives the Reynolds numbers at which heat transfer enhancement makes thermodynamic sense, namely when the entropy generation ratio, $N_{s,en}$ is less than 1. The figure indicates that, even though the solutions are optimal solutions, there are flow rates beyond which the entropy generation ratio exceeds 1. Therefore, multi-objective optimisation alone will not give the best range of operation. The combined use of the entropy generation method and multi-objective optimisation will be beneficial for identifying a design that meets the thermal and thermodynamic performance objectives. For the optimal solutions obtained, significant reductions in entropy generation in the range 18% – 45% are obtainable for flow rates lower than 43 m^3/h (10.05 kg/s at 400 K, 8.94 kg/s at 500 K, 7.65 kg/ s at 600 K and 6.91 kg/s at 650 K).

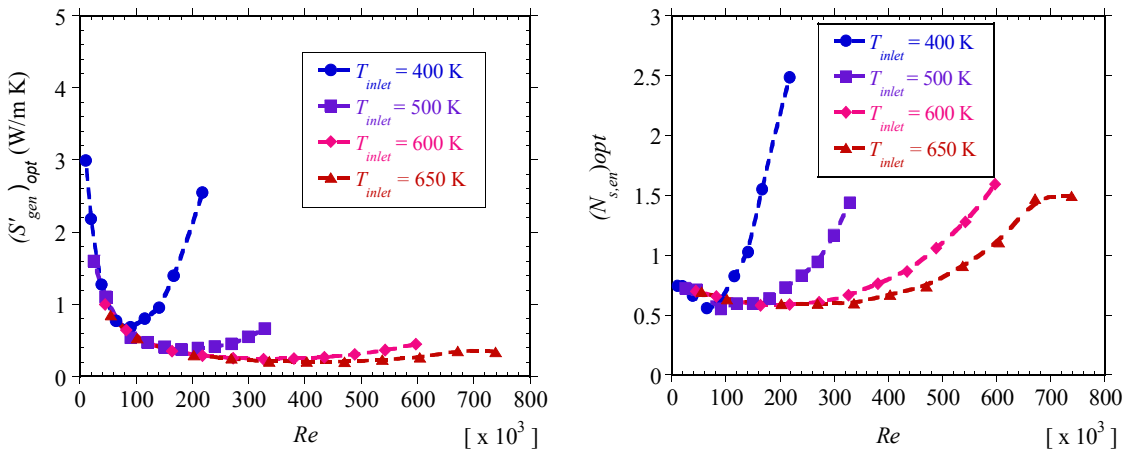

Fig. 7.52: Entropy generation rate and enhancement entropy generation number respectively for a receiver with perforated conical inserts as a function of Reynolds number and inlet temperature for optimal insert geometries

Another method is to consider the thermal efficiency of the receiver in comparison with the plain receiver tube while accounting for increase in pumping power. As shown in Fig. 7.53, it can also be seen that there are solutions among the multi-objective optimisation problems for

which thermal efficiency is lower than that in a plain receiver, making heat transfer enhancement useless in such solutions. For the optimal solutions, the thermal efficiency increases in the range of 3.5% – 6.7% provided the flow rate is lower than 37 m^3/h (8.61 kg/s at 400 K, 7.66 kg/s at 500 K, 6.56 kg/s at 600 K and 5.92 kg/s at 650 K).

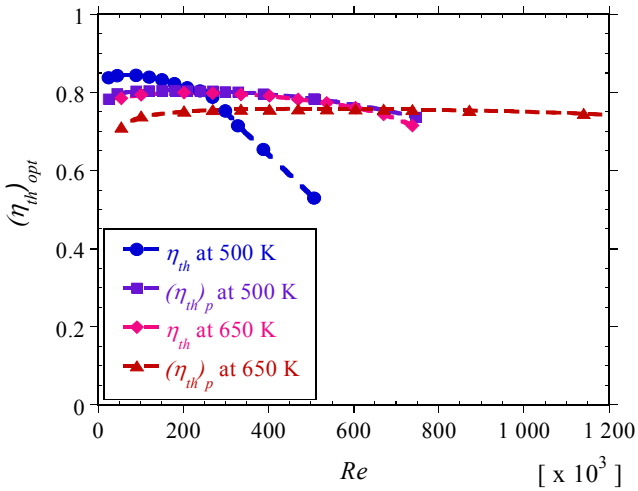

Fig. 7.53: Thermal efficiency of a receiver with perforated conical inserts as a function of Reynolds number for the selected optimal insert geometries.

7.4 CONCLUDING REMARKS

This chapter reports on the numerical investigation of the heat transfer, fluid friction and thermodynamic performance of a parabolic trough receiver with two types of perforated inserts. Furthermore, multi-objective optimisation was used to obtain Pareto optimal solution sets for which heat transfer performance is a maximum and fluid friction is a minimum. From this chapter, the following conclusions can be made.

For heat transfer and fluid friction performance, it has been shown that as plate spacing reduces and as plate size increases, the heat transfer and fluid friction increase for both types of perforated plate inserts. Insert orientation angles were shown to have no significant effect on the heat transfer performance for perforated plate inserts, but significantly affect heat transfer performance for perforated conical inserts. When heat transfer performance improves, the absorber tube circumferential temperature difference is shown to reduce.

Correlations were developed for the Nusselt number and friction factor for the range of parameters considered.

For the perforated plate inserts, thermal efficiency increases in the range 1.2% - 8% depending on the insert spacing, insert size and flow rate. An increase in thermal efficiency of 3% - 8% was obtained for flow rates lower than 38 m^3/h with insert spacing in the range $0.08 \le \tilde{p} \le 0.20$ and insert size in the range $0.45 \le \tilde{d} \le 0.61$. The absorber tube circumferential temperature gradients reduce by about 67% for the maximum heat transfer rate obtained.

For perforated conical inserts, an increase in thermal efficiency in the range 3% - 8% is obtainable for flow rates lower than 37 m^3/h, insert spacing in the range $0.10 \le \tilde{p}_c \le 0.18$, insert size in the range $0.10 \le \tilde{r}_c \le 0.18$ and insert cone angles $0.40 \le \tilde{\beta}_c \le 0.70$. The absorber tube circumferential temperature gradients reduce by up to 56% with perforated conical inserts for the range of parameters considered.

For thermodynamic performance, the study shows that the heat transfer enhancement of the receiver reduces the entropy generation rates. However, the heat transfer enhancement at high Reynolds numbers is undesirable since the entropy generation rates increase significantly. The study shows that the optimal Reynolds number reduces as the insert spacing reduces, and increases as the insert size reduces. Both types of inserts showed there is a flow rate at which heat transfer enhancement makes thermodynamic sense. For the perforated plate inserts and also the perforated conical inserts, flow rates lower than 43 m^3/h give entropy generation ratios of less than 1, hence heat transfer enhancement makes thermodynamic sense. For these flow rates, entropy generation rates can be reduced by up to 53% and up to 45% for perforated plate inserts and perforated conical inserts respectively.

Using multi-objective optimisation, Pareto optimal solutions were obtained and demonstrated for the two types of perforated plate inserts. The combined use of multi-objective optimisation and thermodynamic optimisation gives thermally and thermodynamically optimal solutions.

CHAPTER EIGHT

CHAPTER EIGHT: SUMMARY, CONCLUSIONS AND RECOMMENDATIONS

8.1 SUMMARY

The need to improve access to modern energy services and to reduce the emission of harmful substances into the environment has led to increased research on and the development of new, clean and renewable energy systems. Solar energy is one of the clean and renewable energy resources available today, with an enormous potential to supply a significant portion of the world's energy needs. Several technologies for the conversion of the solar energy resource have been developed and deployed, and others are still in the research and development phase. Compared to photovoltaic systems, concentrating solar power technologies are advantageous for large-scale electricity generation, given that thermal storage can be easily incorporated. It is easier to store heat than electricity on a larger scale.

The parabolic trough systems are one of the most technically and commercially developed systems of the available concentrating solar power technologies. However, several research and development initiatives are still in progress to reduce further the cost of electricity from these systems and to improve their performance. Increasing the optical efficiency and using higher concentration ratio collectors are some of the ways to reduce the cost of electricity generated from parabolic trough systems. Higher concentration ratios mean larger concentrators hence reduced number of drives and controls, resulting in reduced capital costs and operation and maintenance costs. With higher concentration ratios, the main sources of concern are the increase in the absorber tube's circumferential temperature difference and the increase in heat transfer irreversibilities and thus entropy generation rates. The circumferential temperature differences and entropy generation rates will vary with the rim angles, the concentration ratios, inlet temperatures and flow rates. There is potential for improved heat transfer and thermodynamic performance with heat transfer enhancement in parabolic trough receivers as concentration ratios increase.

However, the thermal and thermodynamic performance of parabolic trough receivers at different concentration ratios and rim angles as well as potential of heat transfer enhancement in parabolic trough receivers has not been widely investigated. Therefore, the purpose of this study was to develop an appropriate model for the thermal and thermodynamic analysis of parabolic trough receivers at different rim angles, concentration ratios, Reynolds numbers and inlet temperatures. Moreover, the potential of three heat transfer enhancement techniques i.e. twisted tape inserts, perforated plate inserts and perforated conical inserts in improving the thermal and thermodynamic performance of the receiver was investigated.

In this study, the Monte Carlo ray tracing techniques were used to obtain the actual heat flux distribution on the parabolic trough receiver. The obtained heat flux profiles were then coupled with a general-purpose computational fluid dynamics code for the subsequent numerical investigations. All numerical investigations were also validated with data available in literature. Excellent agreement was obtained in all cases. For the thermodynamic analysis of the receiver, the entropy generation minimisation method was used to develop the receiver thermodynamic model. The potential of three heat transfer enhancement techniques, i.e. twisted tape inserts, perforated plate inserts and perforated conical inserts, to reduce the absorber tube's circumferential temperature differences and minimise entropy generation was investigated numerically using the developed receiver thermal and thermodynamic models. For each heat transfer enhancement techinique, using design exploration tools in ANSYS® and a multi-objective optimisation approach based on the non-dominated sorting genetic algorithms (NSGA-II), optimal solutions for which fluid friction is a minimum and heat transfer is a maximum were obtained. Furthermore, the combined use of multi-objective optimisation and entropy generation minimisation is shown to yield solutions that are optimised for thermal, hydraulic and thermodynamic performance.

8.2 CONCLUSIONS

The specific conclusions are discussed in each of the chapters: Chapter 4, Chapter 5, Chapter 6 and Chapter 7. For parabolic trough thermal model development and validation, entropy generation in parabolic trough receivers at different concentration ratios, heat transfer enhancement in parabolic trough receivers using wall-detached twisted tape inserts and heat

transfer enhancement in parabolic trough receivers using perforated inserts respectively. The major conclusions drawn from this work are summarised below.

8.2.1 PARABOLIC TROUGH RECEIVER THERMAL PERFORMANCE

- The heat flux distribution was shown to be non-uniform around the absorber tube's circumference. Small rim angles gave high heat flux peaks and large rim angles low heat flux peaks. The peak heat flux did not change significantly as the rim angle increased above 80^{o}.

- For rim angles lower than 60^{o}, the thermal performance of the receiver was reduced due to the high temperature peaks at these angles and hence higher heat losses. The thermal efficiency reduced by up to 7.2% as the rim angles decreased from 120^{o} to 40^{o}.

- The absorber tube's circumferential temperature difference increases as the rim angle reduces and as the concentration ratios increase. Accordingly, rim angles lower than 60^{o} should be avoided, especially when flow rates are low and the concentration ratio is larger than 86.

8.2.2 ENTROPY GENERATION IN PARABOLIC TROUGH RECEIVERS AT DIFFERENT CONCENTRATION RATIOS AND RIM ANGLES

Results from this study show the following:

- As the concentration ratios increased, the entropy generation rates in parabolic trough receivers also increased. This is mainly due to the increased heat transfer irreversibilities arising from a large finite temperature difference.

- Low rim angles gave slightly higher entropy generation rates compared to high rim angles because the peak heat flux at low rim angles is higher than the peak heat flux at high rim angles. As the rim angles increased above 80^{o}, the change in entropy generation rates was not very pronounced.

- There was an optimal Reynolds number/flow rate for every combination of rim angle, concentration ratio and inlet temperature for which entropy generation is a minimum. The optimal flow rate is independent of the inlet temperature used, but increases as the concentration ratios increase.

- The volumetric flow rates at the optimal Reynolds numbers were 52.7 m^3/h, 62.4 m^3/h, 70.3 m^3/h, 79.5 m^3/h, 87 m^3/h, 91.2 m^3/h, 95.1 m^3/h at concentration ratios 57, 71, 86, 100, 114, 129 and 143 respectively, regardless of the inlet temperature used.

8.2.3 HEAT TRANSFER ENHANCEMENT WITH WALL-DETACHED TWISTED TAPES IN PARABOLIC TROUGH RECEIVERS

The following are the conclusions drawn from the numerical investigation of heat transfer enhancement in parabolic trough receivers using wall-detached twisted tape inserts:

- Use of twisted tape inserts in the parabolic trough receiver increases the thermal efficiency of the collector system in the range of 5% – 10% for twist ratios greater than 1.0 and all width ratios. This increase in efficiency is achievable if flow rates are lower than 43 m^3/h.

- The increased heat transfer performance reduces the absorber tube's circumferential temperature difference in the range 4% – 68%. Higher reductions are achievable at flow rates lower than 31 m^3/h.

- The use of twisted tape inserts reduced the entropy generation rates by up to 59%. For flow rates greater than 49 m^3/h and most twist ratios and width ratios, the use of twisted tape inserts was shown to be thermodynamically undesirable.

- Using multi-objective and for equally important objectives, the optimal configurations obtained enhance the heat transfer performance in the range of 1.81 – 2.36 with an increase in efficiency of between 4% – 8% if the flow rate is lower than 43 m^3/h. The optimal twist ratio in this study was about 0.42 and an optimal width ratio was about 0.65 at all inlet temperatures and flow rates.

- The combined use of multi-objective optimisation and thermodynamic optimisation was shown to be a useful design tool to give a design that is both thermally and thermodynamically optimised. For the multi-objective solutions, only flow rates lower than 37 m^3/h gave thermodynamically better designs.

8.2.4 HEAT TRANSFER ENHANCEMENT USING PERFORATED INSERTS

The following conclusions were drawn from the numerical investigation of heat transfer enhancement in parabolic trough receivers using perforated inserts:

8.2.4.1 Perforated plate inserts

- The thermal efficiency increased in the range of 3% – 8% for insert spacing ranging from $0.08 \le \tilde{p} \le 0.20$ and insert size in the range $0.45 \le \tilde{d} \le 0.61$ for flow rates lower than 37 m^3/h at all inlet temperatures.

- The absorber tube's circumferential temperature difference was reduced by up to 67% in the range of parameters considered. The highest reduction corresponds to the highest heat transfer enhancement and highest fluid friction for any given Reynolds number.

- The maximum reduction in the entropy generation rates obtained was about 53% and flow rates lower than 44 m^3/h ensured thermodynamically better designs with perforated plate inserts for the range of parameters considered.

- With multi-objective optimisation and when both objectives are equally important, the optimal size of the plate $(\tilde{d})_{opt}$ is shown to be nearly 0.82, 0.78 and 0.76 at 400 K, 500 K and 600 K. The optimal orientation of the plate $(\tilde{\beta})_{opt}$ is about 0.985 – 0.999 whereas the optimal spacing $(\tilde{p})_{opt}$ is about 0.036 at low flow rates, then suddenly increasing to about 0.05 for flow rates above 36 m^3/h.

8.2.4.2 Perforated conical inserts

- An increase in efficiency of about 3% – 8% is obtainable in the range $0.10 \le \tilde{p}_c \le 0.18$, $0.45 \le \tilde{r}_c \le 0.76$ and $0.40 \le \tilde{\beta}_c \le 0.70$ provided that the flow rates are lower than 37 m^3/h.

- The use of perforated conical inserts resulted in a reduction of the absorber tube's circumferential temperature difference of about 3% – 56%.

- The entropy generation variation with Reynolds numbers exhibited the same variation as that in a receiver with a plain absorber tube, twisted tape insert and perforated plate insert. The entropy generation rates reduced by about 45%.

- With multi-objective optimisation, the thermal efficiency increases in the range 4% – 7% for the optimal solutions, if the flow rates are lower than 37 m^3/h.

In general, for better thermal and thermodynamic performance of parabolic trough receivers, rim angles larger than 80^o are necessary. Of all the considered enhancement techniques, the twisted tape inserts provided the best performance regarding heat transfer enhancement, fluid friction, the absorber tube's circumferential temperature reduction and entropy generation reduction. Twisted tape inserts provide better fluid mixing and agitation as well as the longer helical path needed in the absorber tube of the parabolic trough receiver due to the differential heating of the absorber tube wall. Therefore, heat transfer enhancement techniques that provide better fluid mixing will yield high heat transfer enhancement factors in parabolic trough receivers. The perforated plate inserts provided almost similar heat transfer rates as the perforated conical inserts for the range of parameters considered, but the fluid friction was significantly higher for perforated plate inserts than for perforated conical inserts.

This research work has shown that there is the potential for increased performance with heat transfer enhancement in parabolic trough receivers and that heat transfer enhancement reduces the circumferential temperature differences in the receiver's absorber tube as well as reducing the heat transfer irreversibilities. It has been shown that, for all the heat transfer enhancement techniques considered, the optimal Reynolds number is always less than that in a plain absorber tube. Twisted tape inserts showed the lowest optimal Reynolds number of all the heat transfer enhancement techniques studied. Therefore, at higher concentration ratios or heat fluxes, lower flow rates can be used when there is some form of heat transfer enhancement in the receiver's absorber tube, with less concern about the absorber tube's circumferential temperature difference. Moreover, the desired temperatures can be obtained with a shorter collector length, which will likely further reduce the cost of the parabolic trough systems.

8.3 RECOMMENDATIONS

This study considered only three heat transfer enhancement techniques for heat transfer enhancement in parabolic trough receivers. The use of Monte-Carlo ray tracing techniques was explored to determine the actual heat flux distribution on the receiver's absorber tube and therefore the actual temperature reduction due to heat transfer enhancement. The following recommendations are made for future work:

- The investigation of the potential of other passive heat transfer enhancement techniques for heat transfer enhancement in parabolic trough receivers should be pursued.
- An experimental platform should be built to assess the long-term performance of the parabolic trough receiver with and without inserts. In this study, we assumed a perfect reflector with perfect alignment, steady-state conditions giving instantaneous thermal performance of the receiver. An experimental setup would account for the transient nature of the solar radiation as well as any geometrical or alignment errors and the help in evaluating system performance of over a period of time.

REFERENCES

[1] IEA. Measuring progress towards energy for all. In: Priddle R, editor. World energy outlook 2012- special topics, Paris: OECD/IEA; 2012:529-668.

[2] Key world energy statistics. International Energy Agency 2012:1-80.

[3] DINCER I. Energy and environmental impacts: Present and future perspectives. Energy Sources 1998;20:427-53.

[4] Dincer I, Rosen MA. A worldwide perspective on energy, environment and sustainable development. Int J Energy Res 1998;22:1305-21.

[5] Pachauri RK, Reisinger A. Climate change 2007-synthesis report. IPCC 2008:23-71.

[6] IEA. International Energy Agency, World energy outlook 2012 fact sheet. Paris, France: IEA/OECD, 2012.

[7] Bert M, Ogunlade D, Peter B, Rutu D, Leo M. Climate change 2007-Mitigation of climate change. Cambridge University Press 2007:1-841.

[8] Alanne K, Saari A. Distributed energy generation and sustainable development. Renewable and Sustainable Energy Reviews 2006;10:539-58.

[9] IEA. International Energy Agency, World energy outlook 2012-Executive summary. Paris, France: IEA/OECD, 2012.

[10] Kalogirou S. Solar energy engineering: processes and systems. 1st ed. Oxford, UK: Elsevier, Academic Press, 2009.

[11] Knies G, Möller U, Straub M. Clean power from deserts: The DESERTEC concept for energy, water and climate security. WhiteBook 2009;4th ed:2009:1-65.

[12] Philibert C. Barriers to technology diffusion: the case of solar thermal technologies. Paris: OECD/IEA information paper, 2006.

[13] Philibert C, Frankl P. International Energy Agency, Technology roadmap: Concentrating solar power. Paris, France: IEA/OECD, 2010.

[14] Philibert C. International energy technology co-operation case study 1: Concentrating solar power technologies. Paris: OECD/IEA Information Paper, 2004.

[15] Aubrey C, Brakmann G, Aringhoff R. Solar thermal power. ESTIA/Greenpeace 2003: 1-48.

[16] Kalogirou SA. Solar thermal collectors and applications. Prog Energ Combust 2004;30:231-95.

[17] Richter C, Teske S, Short R. Concentrating solar power. Greenpeace/SolarPACES/ESTELA 2009; Global outlook 2009:1-86.

[18] Price H, Kearney D. Reducing the cost of energy from parabolic trough solar power plants. NREL Technical Report, January 2003; NREL/CP-550-33208:1-9.

[19] Wijkman A. We have to move fast towards solar energy. In: Knies G, Möller U, Straub M, editors. Clean power from deserts-The DESERTEC concept for energy, water and

climate security, Hamburg: Trans-Mediterranean Renewable Energy Cooperation; 2009: 10-12.

[20] Breyer C, Knies G. Global energy supply potential of concentrating solar power. SolarPACES September 2009:1-8.

[21] Price H, Lüpfert E, Kearney D, Zarza E, Cohen G, Gee R, Mahoney R. Advances in parabolic trough solar power technology. Sol Energy Eng 2002;124:109-25.

[22] Morin G, Dersch J, Platzer W, Eck M, Häberle A. Comparison of linear Fresnel and parabolic trough collector power plants. Sol Energy 2012;86:1-12.

[23] Price H, Kearney D. Parabolic-trough technology roadmap: A pathway for sustained commercial development and deployment of parabolic trough technology. NREL Technical Report, January, 1999; NREL/TP-550-24748:1-35.

[24] SunShot Initiative available at: http://www1.eere.energy.gov/solar/sunshot/index.html. U S Department of Energy [last accessed 10.06.2014].

[25] Geyer M, Lüpfert E, Osuna R, Esteban A, Schiel W, Schweitzer A, Zarza E, Nava P, Langenkamp J, Madelberg E. EuroTrough - Parabolic trough collector developed for cost efficient solar power generation. 11th SolarPACES international symposium on concentrated solar power and chemical energy technologies, September 4-6, 2002. Zurich, Switzerland.

[26] Lüpfert E, Geyer M, Schiel W, Esteban A, Osuna R, Zarza E, Nava P. Eurotrough design issues and prototype testing at PSA. Proceedings of solar forum 2001 Solar energy: The power to choose, April 21-25, 2001. Washington, D.C.

[27] SunShot Initiative-High-concentration low cost parabolic trough system for baseload CSP, available at: http://www1.eere.energy.gov/solar/sunshot/csp_baseload_skyfuel.html. U S Department of Energy [last accessed 10.10.2013].

[28] Duffie JA, Beckman WA. Solar engineering of thermal processes. 3rd ed. Hoboken, New Jersey: John Wiley and Sons Inc., 2006.

[29] Li J, Wang Z, Lei D, Li J. Hydrogen permeation model of parabolic trough receiver tube. Sol Energy 2012;86:1187-96.

[30] Burkholder F, Kutscher C. Heat loss testing of Schott's 2008 PTR70 parabolic trough receiver. NREL Technical Report, May 2009; NREL/TP - 550-45633:1-58.

[31] Burkholder F, Kutscher C. Heat-loss testing of Solel's UVAC3 parabolic trough receiver. NREL Techical Report, January 2008; NREL/TP - 550-42394:1-19.

[32] Muñoz J, Abánades A. Analysis of internal helically finned tubes for parabolic trough design by CFD tools. Appl Energy 2011;88:4139-49.

[33] Cheng ZD, He YL, Cui FQ, Xu RJ, Tao YB. Numerical simulation of a parabolic trough solar collector with nonuniform solar flux conditions by coupling FVM and MCRT method. Sol Energy 2012;86:1770-84.

[34] He Y, Xiao J, Cheng Z, Tao Y. A MCRT and FVM coupled simulation method for energy conversion process in parabolic trough solar collector. Renew Energ 2011;36:976-85.

[35] Almanza R, Lentz A, Jiménez G. Receiver behavior in direct steam generation with parabolic troughs. Sol Energy 1998;61:275-8.

[36] Lei D, Wang Z, Li J. The calculation and analysis of glass-to-metal sealing stress in solar absorber tube. Renewable Energy 2010;35:405-11.

[37] Gong G, Huang X, Wang J, Hao M. An optimized model and test of the China's first high temperature parabolic trough solar receiver. Sol Energy 2010;84:2230-45.

[38] Daniel P, Joshi Y, Das AK. Numerical investigation of parabolic trough receiver performance with outer vacuum shell. Sol Energy 2011;85:1910-4.

[39] Al-Ansary H, Zeitoun O. Numerical study of conduction and convection heat losses from a half-insulated air-filled annulus of the receiver of a parabolic trough collector. Sol Energy 2011;85:3036-45.

[40] Dudley EV, Kolb JG, Mahoney AR, Mancini T, R., Sloan M, Kearney D. Test results: SEGS LS-2 solar collector. Sandia National Laboratory Technical Report, 1994, SAND94-1884.

[41] Dudley EV, Evans RL, Mathews WC. Test results: Industrial Solar Technology parabolic trough solar collector. Sandia National Laboratory Technical Report, 1995, SAND94-1117.

[42] Liu QB, Wang YL, Gao ZC, Sui J, Jin HG, Li HP. Experimental investigation on a parabolic trough solar collector for thermal power generation. Sci China Ser E-Tech Sci 2010;53:52-6.

[43] Lüpfert E, Riffelmann K, Price H, Burkholder F, Moss T. Experimental analysis of overall thermal properties of parabolic trough receivers. Sol Energy Eng 2008;130:021007.

[44] Price H, Forristall R, Wendelin T, Lewandowski A, Moss T, Gummo C. Field survey of parabolic trough receiver thermal performance, NREL/CP-550-39459, April 2006.

[45] Forristall R. Heat transfer analysis and modeling of a parabolic trough solar receiver implemented in Engineering Equation solver. NREL Technical Report, October 2003, NREL/TP-550-34169:1-145.

[46] Lüpfert E, Pfänder M, Schiricke B, Eck M. Determination of temperature distribution on parabolic trough receivers. 13th International symposium on concentrating solar power and chemical energy technologies, June 20-23, 2006; A1-S6. Seville, Spain.

[47] Roesle M, Coskun V, Steinfeld A. Numerical analysis of heat loss from a parabolic trough absorber tube with active vacuum system. J Sol Energy Eng 2011;133:031015-1,031015-5.

[48] Ravi Kumar K, Reddy KS. Numerical investigation of energy-efficient receiver for solar parabolic trough concentrator. Heat Transfer Eng 2008;29:961-72.

[49] Ravi Kumar K, Reddy KS. Thermal analysis of solar parabolic trough with porous disc receiver. Appl Energy 2009;86:1804-12.

[50] Cheng ZD, He YL, Cui FQ. Numerical study of heat transfer enhancement by unilateral longitudinal vortex generators inside parabolic trough solar receivers. Int J Heat Mass Trans 2012;55:5631-41.

[51] Bergles AE, Webb RL, Junkan GH. Energy conservation via heat transfer enhancement. Energy 1979;4:193-200.

[52] Bergles AE. Techniques to enhance heat transfer. In: Hartnett JP, and Cho YI, editors. Handbook of heat transfer, New York: McGraw-Hill; 1998, p. 11.71-11.76.

[53] Webb R, L. Principles of enhanced heat transfer. New York: John Wiley & Sons, 1994.

[54] Manglik RM. Heat transfer enhancement. In: Bejan A, Kraus AD, editors. Heat transfer handbook, Hoboken, New Jersey: John Wiley & Sons; 2003, p. 1029-1130.

[55] Moens L, Blake DM. Mechanism of hydrogen formation in solar parabolic trough receivers. J Sol Energ-T ASME 2010;132:031006.

[56] Manglik RM, Bergles AE. Swirl flow heat transfer and pressure drop with twisted-tape inserts. In: Hartnett J, P., Irvine TF, Cho Y, I., Greene G, A., editors. Advances in Heat Transfer, San Diego, California: Academic Press; 2002, p. 183-266.

[57] Liu W, Yang K. Mechanisms and numerical analysis of heat transfer enhancement in the core flow along a tube. Sci China Ser E-Tech Sci 2008;51:1195-202.

[58] Liu W, Yang K, Liu ZC, Ming TZ, Fan AW, Yang C. Mechanism of heat transfer enhancement in the core flow of a tube and its numerical simulation. The Open Transport Phenomena Journal 2009;1:1-7.

[59] Huang ZF, Nakayama A, Yang K, Yang C, Liu W. Enhancing heat transfer in the core flow by using porous medium insert in a tube. Int J Heat Mass Trans 2010;53:1164-74.

[60] Ko K, Anand NK. Use of porous baffles to enhance heat transfer in a rectangular channel. Int J Heat Mass Transfer 2003;46:4191-9.

[61] Bejan A. Entropy generation minimization: the method of thermodynamic optimization of finite-size systems and finite-time processes. Boca Raton, Fla.: CRC Press, 1996.

[62] Bejan A. A study of entropy generation in fundamental convective heat transfer. J Heat Transfer 1979;101:718-25.

[63] Deb K. Multi-objective optimization using evolutionary algorithms. New York: Wiley, 2001.

[64] Konak A, Coit DW, Smith AE. Multi-objective optimization using genetic algorithms: A tutorial. Reliab Eng Syst Saf 2006;91:992-1007.

[65] Dipama J, Teyssedou A, Aubé F, Lizon-A-Lugrin L. A grid based multi-objective evolutionary algorithm for the optimization of power plants. Appl Therm Eng 2010;30: 807-16.

[66] Diakaki C, Grigoroudis E, Kabelis N, Kolokotsa D, Kalaitzakis K, Stavrakakis G. A multi-objective decision model for the improvement of energy efficiency in buildings. Energy 2010;35:5483-96.

[67] Molyneaux A, Leyland G, Favrat D. Environomic multi-objective optimisation of a district heating network considering centralized and decentralized heat pumps. Energy 2010;35:751-8.

[68] Giannantoni C, Lazzaretto A, Macor A, Mirandola A, Stoppato A, Tonon S, Ulgiati S. Multicriteria approach for the improvement of energy systems design. Energy 2005;30: 1989-2016.

[69] Burer M, Tanaka K, Favrat D, Yamada K. Multi-criteria optimization of a district cogeneration plant integrating a solid oxide fuel cell–gas turbine combined cycle, heat pumps and chillers. Energy 2003;28:497-518.

[70] Abdollahi G, Meratizaman M. Multi-objective approach in thermoenvironomic optimization of a small-scale distributed CCHP system with risk analysis. Energy Build 2011;43:3144-53.

[71] Besarati SM, Atashkari K, Jamali A, Hajiloo A, Nariman-zadeh N. Multi-objective thermodynamic optimization of combined Brayton and inverse Brayton cycles using genetic algorithms. Energy Conversion and Management 2010;51:212-7.

[72] Atashkari K, Nariman-Zadeh N, Pilechi A, Jamali A, Yao X. Thermodynamic Pareto optimization of turbojet engines using multi-objective genetic algorithms. International Journal of Thermal Sciences 2005;44:1061-71.

[73] Cortes-Quiroz CA, Azarbadegan A, Zangeneh M, Goto A. Analysis and multi-criteria design optimization of geometric characteristics of grooved micromixer. Chem Eng J 2010;160:852-64.

[74] Hajabdollahi H, Tahani M, Shojaee Fard MH. CFD modeling and multi-objective optimization of compact heat exchanger using CAN method. Appl Therm Eng 2011;31:2597-604.

[75] Gholap AK, Khan JA. Design and multi-objective optimization of heat exchangers for refrigerators. Appl Energy 2007;84:1226-39.

[76] Husain A, Kim K. Enhanced multi-objective optimization of a microchannel heat sink through evolutionary algorithm coupled with multiple surrogate models. Appl Therm Eng 2010;30:1683-91.

[77] Kim H, Moon M, Kim K. Multi-objective optimization of a cooling channel with staggered elliptic dimples. Energy 2011;36:3419-28.

[78] Sanaye S, Hajabdollahi H. Multi-objective optimization of shell and tube heat exchangers. Appl Therm Eng 2010;30:1937-45.

[79] Foli K, Okabe T, Olhofer M, Jin Y, Sendhoff B. Optimization of micro heat exchanger: CFD, analytical approach and multi-objective evolutionary algorithms. Int J Heat Mass Transfer 2006;49:1090-9.

[80] Amanifard N, Nariman-Zadeh N, Borji M, Khalkhali A, Habibdoust A. Modelling and Pareto optimization of heat transfer and flow coefficients in microchannels using GMDH type neural networks and genetic algorithms. Energy Conversion and Management 2008;49:311-25.

[81] IEA (2014b). Technology roadmap: Solar thermal electricity, 2014 Edition, OECD/IED, Paris.

[82] Stine BW, Geyer M. Power from the sun - Chapters 4,8,9. Available at: http://www.powerfromthesun.net/book.html [last accessed 12.02. 2013].

[83] Kalogirou SA. A detailed thermal model of a parabolic trough collector receiver. Energy 2012;48:298-306.

[84] Cengel YA. Heat and mass transfer: a practical approach. 3rd ed. Boston: McGraw-Hill, 2007.

[85] Potkay AJ, Sacks DR. A low-power pressure- and temperature-programmable micro gas chromatography column. Microelectromech Syst 2007;16:1071-9.

[86] García-Valladares O, Velázquez N. Numerical simulation of parabolic trough solar collector: Improvement using counter flow concentric circular heat exchangers. Int J Heat Mass Trans 2009;52:597-609.

[87] Versteeg HK, Malalasekera W. An introduction to computational fluid dynamics: the finite volume method. 2nd ed. Harlow, England: Pearson/Prentice Hall, 2007.

[88] ANSYS® Academic research, release 14.5, ANSYS FLUENT, theory guide, ANSYS, Inc.

[89] ANSYS® Academic research, release 14.5, ANSYS FLUENT user's guide, ANSYS, Inc.

[90] ASME Editorial Board. Journal of heat transfer editorial policy statement on numerical accuracy. ASME J Heat Transfer 1994;116:797-8.

[91] Bejan A. Convection heat transfer. 3rd ed. Hoboken, N.J.: Wiley, 2004.

[92] Patankar SV, Spalding DB. A calculation procedure for heat, mass and momentum transfer in three-dimensional parabolic flows. Int J Heat Mass Transfer 1972;15:1787-806.

[93] Kock F, Herwig H. Local entropy production in turbulent shear flows: a high-Reynolds number model with wall functions. Int J Heat Mass Trans 2004;47:2205-15.

[94] Kock F, Herwig H. Entropy production calculation for turbulent shear flows and their implementation in cfd codes. Int J Heat Fluid Fl 2005;26:672-80.

[95] Arora JS. Introduction to optimum design. New York: McGraw-Hill, 1989.

[96] Zitzler E, Deb K, Thiele L. Comparison of multiobjective evolutionary algorithms: Empirical results. Evolutionary Computation 2000;8:173-95.

[97] Deb K, Pratap A, Agarwal S, Meyarivan T. A fast and elitist multi-objective genetic algorithm: NSGA-II. KanGAL Report 2000;200001:1-20.

[98] Deb K, Pratap A, Agarwal S, Meyarivan T. A fast and elitist multiobjective genetic algorithm: NSGA-II. IEEE Transactions on evolutionary computation 2002;6:182-97.

[99] ANSYS® Academic research, release 14.5, ANSYS design exploration user's guide, ANSYS, Inc.

[100] Simpson TW, Poplinski JD, Koch PN, Allen JK. Metamodels for computer-based engineering design: survey and recommendations. Eng Comput 2001;17:129-50.

[101] Myers R, H., Montgomery DC. Response surface methodology: process and product optimization using designed experiments. 2nd ed. Canada: John Wiley and Sons,Inc, 2002.

[102] Khuri AI. Response surface methodology and related topics. Hacenksack, NJ: World Scientific, 2006.

[103] Khuri IA, Mukhopadhyay S. Response surface methodology. Computation Stat 2010;2:128-49.

[104] Li M, Li G, Azarm S. A Kriging metamodel assisted multi-objective genetic algorithm for design optimization. J Mech Des 2008;130:1-10.

[105] Yang B, Zhao J, Xu T, Zhu Q. Calculation of the concentrated flux density distribution in parabolic trough solar concentrators by Monte Carlo ray-trace method. Photonics and Optoelectronic (SOPO) 2010:1-4.

[106] Jeter SM. Analytical determination of the optical performance of practical parabolic trough collectors from design data. Sol Energy 1987;39:11-21.

[107] Jeter SM. Calculation of the concentrated flux density distribution in parabolic trough collectors by a semifinite formulation. Solar Energy 1986;37:335-45.

[108] NREL. SolTrace optical modelling software. SolTrace 2012; v2012.7.9.

[109] Mullick SC, Nanda SK. An improved technique for computing the heat loss factor of a tubular absorber. Solar Energy 1989;42:1-7.

[110] SYLTHERM 800 heat transfer fluid: product techinical data. Available at: http://www.dow.com/heattrans/products/synthetic/syltherm.htm [last accessed 10.10.2013].

[111] Bejan A. Fundamentals of exergy analysis, entropy generation minimization, and the generation of flow architecture. Int J Energy Res 2002;26:0-43.

[112] Ko TH. A numerical study on developing laminar forced convection and entropy generation in half- and double-sine ducts. Int J Therm Sci 2007;46:1275-84.

[113] Tandiroglu A. Effect of flow geometry parameters on transient entropy generation for turbulent flow in circular tube with baffle inserts. Energ Convers Manage 2007;48:898-906.

[114] Zimparov V. Enhancement of heat transfer by a combination of a single-start spirally corrugated tubes with a twisted tape. Exp Therm Fluid Sci 2002;25:535-46.

[115] Ko TH, Ting K. Entropy generation and optimal analysis for laminar forced convection in curved rectangular ducts: A numerical study. Int J Therm Sci 2006;45:138-50.

[116] Jin Y, Chen XD. Entropy production during the drying process of milk droplets in an industrial spray dryer. International Journal of Thermal Sciences 2011;50:615-25.

[117] Ko TH, Wu CP. A numerical study on entropy generation induced by turbulent forced convection in curved rectangular ducts with various aspect ratios. Int Commun Heat Mass Transfer 2009;36:25-31.

[118] Herpe J, Bougeard D, Russeil S, Stanciu M. Numerical investigation of local entropy production rate of a finned oval tube with vortex generators. International Journal of Thermal Sciences 2009;48:922-35.

[119] Ko TH, Cheng CS. Numerical investigation on developing laminar forced convection and entropy generation in a wavy channel. Int Commun Heat Mass 2007;34:924-33.

[120] Ko TH. Numerical investigation on laminar forced convection and entropy generation in a curved rectangular duct with longitudinal ribs mounted on heated wall. Int J Therm Sci 2006;45:390-404.

[121] Bekker J, Aldrich C. The cross-entropy method in multi-objective optimisation: An assessment. Eur J Oper Res 2011;211:112-21.

[122] Guo J, Xu M, Tao Y, Huai X. The effect of temperature-dependent viscosity on entropy generation in curved square microchannel. Chemical Engineering and Processing: Process Intensification 2012;52:85-91.

[123] Satapathy AK. Thermodynamic optimization of a coiled tube heat exchanger under constant wall heat flux condition. Energy 2009;34:1122-6.

[124] Ishioka S, Fuchikami N. Thermodynamics of computing: Entropy of nonergodic systems. Chaos 2001;11:734-46.

[125] Tyagi SK, Wang S, Singhal MK, Kaushik SC, Park SR. Exergy analysis and parametric study of concentrating type solar collectors. Int J Therm Sci 2007;46:1304-10.

[126] Le Roux WG, Bello-Ochende T, Meyer JP. Optimum performance of the small-scale open and direct solar thermal Brayton cycle at various environmental conditions and constraints. Energy 2012;46:42-50.

[127] Şahin AZ. Irreversibilities in various duct geometries with constant wall heat flux and laminar flow. Energy 1998;23:465-73.

[128] Sahin AZ. Entropy generation and pumping power in a turbulent fluid flow through a smooth pipe subjected to constant heat flux. Exergy, An International Journal 2002;2:314-21.

[129] Abu-Nada E. Entropy generation due to heat and fluid flow in backward facing step flow with various expansion ratios. Int J Exergy 2006;3:419-35.

[130] Khan WA, Yovanovich MM, Culham JR. Optimization of microchannel heat sinks using entropy generation minimization method. IEEE Transaction on components and packaging technologies 2009;32:243-51.

[131] Herwig H, Kock F. Direct and indirect methods of calculating entropy generation rates in turbulent convective heat transfer problems. Heat and Mass Transfer 2007;43:207-15.

[132] Sahiti N, Krasniqi F, Fejzullahu X, Bunjaku J, Muriqi A. Entropy generation minimization of a double-pipe pin fin heat exchanger. Appl Therm Eng 2008;28:2337-44.

[133] Esfahani JA, Shahabi PB. Effect of non-uniform heating on entropy generation for the laminar developing pipe flow of a high Prandtl number fluid. Energy Conversion and Management 2010;51:2087-97.

[134] Ozalp A, Alper. Entropy analysis of laminar-forced convection in a pipe with wall roughness. Int J Exergy 2009;6:249-75.

[135] Giangaspero G, Sciubba E. Application of the entropy generation minimization method to a solar heat exchanger: A pseudo-optimization design process based on the analysis of the local entropy generation maps. Energy 2013:58:52-65.

[136] Amani E, Nobari RMH. A Numerical study of entropy generation in the entrance region of curved pipes. Heat Transfer Eng 2010;31:1203-12.

[137] Amani E, Nobari MRH. A numerical investigation of entropy generation in the entrance region of curved pipes at constant wall temperature. Energy 2011;36:4909-18.

[138] Wu S, Li Y, Chen Y, Xiao L. Exergy transfer characteristics of forced convective heat transfer through a duct with constant wall temperature. Energy 2007;32:2385-95.

[139] Ko TH. Thermodynamic analysis of optimal mass flow rate for fully developed laminar forced convection in a helical coiled tube based on minimal entropy generation principle. Energy Conversion and Management 2006;47:3094-104.

[140] Mansour RB, Galanis N, Nguyen CT. Dissipation and entropy generation in fully developed forced and mixed laminar convection. International Journal of Thermal Sciences 2006;45:998-1007.

[141] Ilis GG, Mobedi M, Sunden B. Effect of aspect ratio on entropy generation in a rectangular cavity with differentially heated vertical walls. Int Commun Heat Mass Transfer 2008;35:696-703.

[142] Dagtekin I, Oztop HF, Bahloul A. Entropy generation for natural convection in Γ-shaped enclosures. Int Commun Heat Mass Transfer 2007;34:502-10.

[143] Jankowski TA. Minimizing entropy generation in internal flows by adjusting the shape of the cross-section. Int J Heat Mass Transfer 2009;52:3439-45.

[144] Sciubba E. Entropy generation minimization as a design tool. Part 1: Analysis of different configurations of branched and non-branched laminar isothermal flow through a circular pipe. Int J of Thermodynamics 2011;14:11-20.

[145] Balaji C, Hölling M, Herwig H. Entropy generation minimization in turbulent mixed convection flows. Int Commun Heat Mass Transfer 2007;34:544-52.

[146] Hooman K, Gurgenci H, Merrikh AA. Heat transfer and entropy generation optimization of forced convection in porous-saturated ducts of rectangular cross-section. Int J Heat Mass Transfer 2007;50:2051-9.

[147] Mahmud S FR. Flow, thermal, and entropy generation characteristics inside a porous channel with viscous dissipation. Int J Thermal Sciences 2005;44:21-32.

[148] Mahmud S, Fraser RA. The second law analysis in fundamental convective heat transfer problems. International Journal of Thermal Sciences 2003;42:177-86.

[149] Zhang X, Liu Z, Liu W. Numerical studies on heat transfer and friction factor characteristics of a tube fitted with helical screw-tape without core-rod inserts. Int J Heat Mass Transfer 2013;60:490-8.

[150] Bejan A. The thermodynamic design of heat and mass transfer processes and devices. Int J Heat Fluid Flow 1987;8:258-76.

[151] Bergles AE. ExHFT for fourth generation heat transfer technology. Exp Therm Fluid Sci 2002;26:335-44.

[152] Dewan A, Mahanta P, Raju S,K., Kumar S,P. Review of passive heat transfer augmentation techniques. P I Mech Eng A-J Pow 2004;218:509-27.

[153] Nithiyesh CK, Murugesan P. Review on twisted tapes heat transfer enhancement. IJSER 2012;3:1-9.

[154] Liu S, Sakr M. A comprehensive review on passive heat transfer enhancements in pipe exchangers. Renewable and Sustainable Energy Reviews 2013;19:64-81.

[155] Marner WJ, Bergles AE. Augmentation of highly viscous laminar heat transfer inside tubes with constant wall temperature. Exp Therm Fluid Sci 1989;2:252-67.

[156] Agarwal SK, Raja Rao M. Heat transfer augmentation for the flow of a viscous liquid in circular tubes using twisted tape inserts. Int J Heat Mass Transfer 1996;39:3547-57.

[157] Kumar A, Prasad BN. Investigation of twisted tape inserted solar water heaters—heat transfer, friction factor and thermal performance results. Renewable Energy 2000;19:379-98.

[158] Jaisankar S, Radhakrishnan TK, Sheeba KN. Experimental studies on heat transfer and friction factor characteristics of forced circulation solar water heater system fitted with helical twisted tapes. Solar Energy 2009;83:1943-52.

[159] Jaisankar S, Radhakrishnan TK, Sheeba KN. Studies on heat transfer and friction factor characteristics of thermosyphon solar water heating system with helical twisted tapes. Energy 2009;34:1054-64.

[160] Jaisankar S, Radhakrishnan TK, Sheeba KN. Experimental studies on heat transfer and thermal performance characteristics of thermosyphon solar water heating system with helical and left–right twisted tapes. Energy Conversion and Management 2011;52:2048-55.

[161] Noothong W, Eiamsa-ard S, Promvonge P. Effect of twisted-tape inserts on heat transfer in a tube. The 2nd Joint International Conference on Sustainable Energy and Environment (SEE 2006), November 21-23 2006; A-030(P):1-5. Bangkok Thailand.

[162] Saha SK, Gaitonde UN, Date AW. Heat transfer and pressure drop characteristics of laminar flow in a circular tube fitted with regularly spaced twisted-tape elements. Exp Therm Fluid Sci 1989;2:310-22.

[163] Saha SK, Gaitonde UN, Date AW. Heat transfer and pressure drop characteristics of turbulent flow in a circular tube fitted with regularly spaced twisted-tape elements. Exp Therm Fluid Sci 1990;3:632-40.

[164] Date AW, Saha SK. Numerical prediction of laminar flow and heat transfer characteristics in a tube fitted with regularly spaced twisted-tape elements. Int J Heat Fluid Flow 1990;11:346-54.

[165] Date AW, Gaitonde UN. Development of correlations for predicting characteristics of laminar flow in a tube fitted with regularly spaced twisted-tape elements. Exp Therm Fluid Sci 1990;3:373-82.

[166] Saha SK, Dutta A. Thermohydraulic study of laminar swirl flow through a circular tube fitted with twisted tapes. J Heat Transfer 2001;123:417-27.

[167] Eiamsa-ard S, Thianpong C, Promvonge P. Experimental investigation of heat transfer and flow friction in a circular tube fitted with regularly spaced twisted tape elements. Int Commun Heat Mass Transfer 2006;33:1225-33.

[168] Wang Y, Hou M, Deng X, Li L, Huang C, Huang H, Zhang G, Chen C, Huang W. Configuration optimization of regularly spaced short-length twisted tape in a circular tube to enhance turbulent heat transfer using CFD modeling. Appl Therm Eng 2011;31:1141-9.

[169] Eiamsa-ard S, Thianpong C, Eiamsa-ard P, Promvonge P. Thermal characteristics in a heat exchanger tube fitted with dual twisted tape elements in tandem. Int Commun Heat Mass Transfer 2010;37:39-46.

[170] Jaisankar S, Radhakrishnan TK, Sheeba KN, Suresh S. Experimental investigation of heat transfer and friction factor characteristics of thermosyphon solar water heater system fitted with spacer at the trailing edge of left–right twisted tapes. Energy Conversion and Management 2009;50:2638-49.

[171] Eiamsa-ard S, Seemawute P. Decaying swirl flow in round tubes with short-length twisted tapes. Int Commun Heat Mass Transfer 2012;39:649-56.

[172] Eiamsa-ard S, Thianpong C, Eiamsa-ard P, Promvonge P. Convective heat transfer in a circular tube with short-length twisted tape insert. Int Commun Heat Mass Transfer 2009;36:365-71.

[173] Eiamsa-ard S, Promvonge P. Performance assessment in a heat exchanger tube with alternate clockwise and counter-clockwise twisted-tape inserts. Int J Heat Mass Transfer 2010;53:1364-72.

[174] Eiamsa-ard S, Thianpong C, Eiamsa-ard P. Turbulent heat transfer enhancement by counter/co-swirling flow in a tube fitted with twin twisted tapes. Exp Therm Fluid Sci 2010;34:53-62.

[175] Chiu Y, Jang J. 3D numerical and experimental analysis for thermal–hydraulic characteristics of air flow inside a circular tube with different tube inserts. Appl Therm Eng 2009;29:250-8.

[176] Eiamsa-ard S, Wongcharee K, Eiamsa-ard P, Thianpong C. Thermohydraulic investigation of turbulent flow through a round tube equipped with twisted tapes consisting of centre wings and alternate-axes. Exp Therm Fluid Sci 2010;34:1151-61.

[177] Eiamsa-ard S, Wongcharee K, Eiamsa-ard P, Thianpong C. Heat transfer enhancement in a tube using delta-winglet twisted tape inserts. Appl Therm Eng 2010;30:310-8.

[178] Eiamsa-ard S, Promvonge P. Thermal characteristics in round tube fitted with serrated twisted tape. Appl Therm Eng 2010;30:1673-82.

[179] Chang SW, Yang TL, Liou JS. Heat transfer and pressure drop in tube with broken twisted tape insert. Exp Therm Fluid Sci 2007;32:489-501.

[180] Wongcharee K, Eiamsa-ard S. Heat transfer enhancement by twisted tapes with alternate-axes and triangular, rectangular and trapezoidal wings. Chemical Engineering and Processing: Process Intensification 2011;50:211-9.

[181] Murugesan P, Mayilsamy K, Suresh S. Turbulent heat transfer and pressure drop in tube fitted with square-cut twisted tape. Chin J Chem Eng 2010;18:609-17.

[182] Murugesan P, Mayilsamy K, Suresh S. Heat transfer and friction factor studies in a circular tube fitted with twisted tape consisting of wire-nails. Chin J Chem Eng 2010;18:1038-42.

[183] Hong Y, Deng X, Zhang L. 3D numerical study on compound heat transfer enhancement of converging-diverging tubes equipped with twin twisted tapes. Chin J Chem Eng 2012;20:589-601.

[184] Zimparov V. Enhancement of heat transfer by a combination of three-start spirally corrugated tubes with a twisted tape. Int J Heat Mass Transfer 2001;44:551-74.

[185] Zimparov V. Prediction of friction factors and heat transfer coefficients for turbulent flow in corrugated tubes combined with twisted tape inserts. Part 1: friction factors. Int J Heat Mass Transfer 2004;47:589-99.

[186] Zimparov V. Prediction of friction factors and heat transfer coefficients for turbulent flow in corrugated tubes combined with twisted tape inserts. Part 2: heat transfer coefficients. Int J Heat Mass Transfer 2004;47:385-93.

[187] Thianpong C, Eiamsa-ard P, Wongcharee K, Eiamsa-ard S. Compound heat transfer enhancement of a dimpled tube with a twisted tape swirl generator. Int Commun Heat Mass Transfer 2009;36:698-704.

[188] Eiamsa-ard S, Somkleang P, Nuntadusit C, Thianpong C. Heat transfer enhancement in tube by inserting uniform/non-uniform twisted-tapes with alternate axes: Effect of rotated-axis length. Appl Therm Eng 2013:54:289-309.

[189] Bharadwaj P, Khondge AD, Date AW. Heat transfer and pressure drop in a spirally grooved tube with twisted tape insert. Int J Heat Mass Transfer 2009;52:1938-44.

[190] Promvonge P, Eiamsa-ard S. Heat transfer behaviors in a tube with combined conical-ring and twisted-tape insert. Int Commun Heat Mass Transfer 2007;34:849-59.

[191] Promvonge P, Pethkool S, Pimsarn M, Thianpong C. Heat transfer augmentation in a helical-ribbed tube with double twisted tape inserts. Int Commun Heat Mass Transfer 2012;39:953-9.

[192] Liao Q, Xin MD. Augmentation of convective heat transfer inside tubes with three-dimensional internal extended surfaces and twisted-tape inserts. Chem Eng J 2000;78:95-105.

[193] Ayub ZH, Al-Fahed SF. The effect of gap width between horizontal tube and twisted tape on the pressure drop in turbulent water flow. Int J Heat Fluid Flow 1993;14:64-7.

[194] Al-Fahed S, Chakroun W. Effect of tube-tape clearance on heat transfer for fully developed turbulent flow in a horizontal isothermal tube. Int J Heat Fluid Flow 1996;17: 173-8.

[195] Bas H, Ozceyhan V. Heat transfer enhancement in a tube with twisted tape inserts placed separately from the tube wall. Exp Therm Fluid Sci 2012;41:51-8.

[196] Eiamsa-ard S, Wongcharee K, Sripattanapipat S. 3-D Numerical simulation of swirling flow and convective heat transfer in a circular tube induced by means of loose-fit twisted tapes. Int Commun Heat Mass Transfer 2009;36:947-55.

[197] Guo J, Fan A, Zhang X, Liu W. A numerical study on heat transfer and friction factor characteristics of laminar flow in a circular tube fitted with center-cleared twisted tape. International Journal of Thermal Sciences 2011;50:1263-70.

[198] Zhang X, Liu Z, Liu W. Numerical studies on heat transfer and flow characteristics for laminar flow in a tube with multiple regularly spaced twisted tapes. International Journal of Thermal Sciences 2012;58:157-67.

[199] Mwesigye A, Bello-Ochende T, Meyer JP. Numerical investigation of entropy generation in a parabolic trough receiver at different concentration ratios. Energy 2013;53:114-27.

[200] Webb RL. Performance evaluation criteria for use of enhanced heat transfer surfaces in heat exchanger design. Int J Heat Mass Transfer 1981;24:715-26.

[201] Oullette WR, Bejan A. Conservation of available work (exergy) by using promoters of swirl flow in forced convection heat transfer. Energy 1980;5:587-96.

[202] Zimparov VD, Vulchanov NL. Performance evaluation criteria for enhanced heat transfer surfaces. Int J Heat Mass Transfer 1994;37:1807-16.

[203] Manglik RM, Bergles AE. Heat transfer and pressure drop correlation for twisted-tape inserts in isothermal tubes: Part II - Transition and turbulent flows. J Heat Transfer 1993;115:890-6.

[204] Bergles AE. The implications and challenges of enhanced heat transfer for the chemical process industries. Chem Eng Res Design 2001;79:437-44.

[205] Petitjean E, Aquino B, Polley GT. Observations on the use of tube inserts to suppress fouling in heat exchangers. Hydrocarbon world 2007:47-51.

[206] Ming P, Igor B, Robin S. Exploiting tube inserts to intensify heat transfer for the retrofit of heat exchanger networks considering fouling mitigation. Ind Eng Chem Res 2013;52:2925-43.

[207] Özceyhan V, Altuntop N. Heat transfer and thermal stress analysis in grooved tubes. Sadhana 2005;30:537-53.

[208] Barboy S, Rashkovan A, Ziskind G. Determination of hot spots on a heated wavy wall in channel flow. Int J Heat Mass Transfer 2012;55:3576-81.

[209] Wang L, Sundén B. Performance comparison of some tube inserts. Int Commun Heat Mass Transfer 2002;29:45-56.

[210] Zimparov VD, Penchev PJ. Performance evaluation of some tube inserts as heat transfer enhancement techniques. Heat Transfer Eng 2006;27:39-46.

[211] Kurtbaş İ, Gülçimen F, Akbulut A, Buran D. Heat transfer augmentation by swirl generators inserted into a tube with constant heat flux. Int Commun Heat Mass Transfer 2009;36:865-71.

[212] Fan A, Deng J, Guo J, Liu W. A numerical study on thermo-hydraulic characteristics of turbulent flow in a circular tube fitted with conical strip inserts. Appl Therm Eng 2011;31:2819-28.

[213] You Y, Fan A, Liu W, Huang S. Thermo-hydraulic characteristics of laminar flow in an enhanced tube with conical strip inserts. International Journal of Thermal Sciences 2012;61:28-37.

[214] Kongkaitpaiboon V, Nanan K, Eiamsa-ard S. Experimental investigation of convective heat transfer and pressure loss in a round tube fitted with circular-ring turbulators. Int Commun Heat Mass Transfer 2010;37:568-74.

[215] Kongkaitpaiboon V, Nanan K, Eiamsa-ard S. Experimental investigation of heat transfer and turbulent flow friction in a tube fitted with perforated conical-rings. Int Commun Heat Mass Transfer 2010;37:560-7.

[216] Promvonge P. Heat transfer behaviors in round tube with conical ring inserts. Energy Conversion and Management 2008;49:8-15.

[217] Promvonge P, Eiamsa-ard S. Heat transfer and turbulent flow friction in a circular tube fitted with conical-nozzle turbulators. Int Commun Heat Mass Transfer 2007;34:72-82.

[218] Haque SME, Rasul MG, Khan MMK, Deev AV, Subaschandar N. Flow distribution inside an electrostatic precipitator: Effects of uniform and variable porosity of perforated plate. 5th IASME/WSEAS Int Conference on Heat Transfer, Thermal Engineering and Environment, August 25-27, 2007, 62-7. Athens, Greece

[219] Haque SME, Rasul MG, Khan MMK, Deev AV, Subaschandar N. Numerical modelling for optimizing flow distribution inside an electrostatic precipitator. Math Comput Simulat 2007;1:255-61.

[220] Weber LJ, Cherian MP, Allen ME, Muste M. Headloss characteristics for perforated plates and flat bar screens. IIHR Technical Report March, 2000;411:1-95.

[221] Gan G, Riffat SB. Pressure loss characteristics of orifice and perforated plates. Exp Therm Fluid Sci 1997;14:160-5.

APPENDICES

A. FLOW FIELD AND OPTIMISATION CHARTS FOR TWISTED TAPE INSERT

A.1. Stream lines at $Re = 6.40 \times 10^4$, $\tilde{y} = 0.5$ and $\tilde{w} = 0.91$

A.2. Stream lines at *Re* = 3.84 × 10^4, $\tilde{y} = 0.80$ and $\tilde{w} = 0.76$

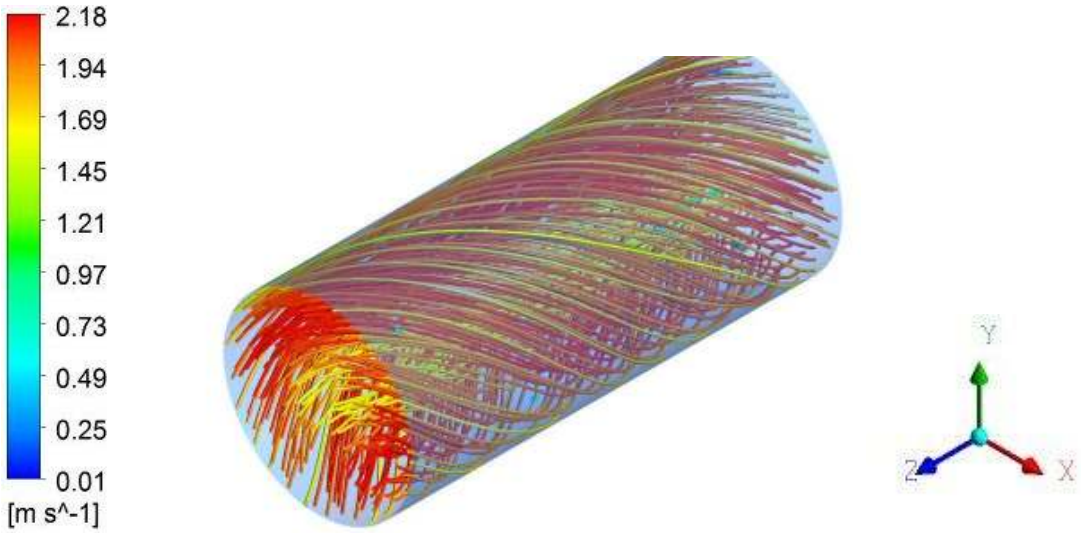

A.3. Velocity contours at *Re* = 6.40 × 10^4, $\tilde{y} = 0.5$ and $\tilde{w} = 0.76$

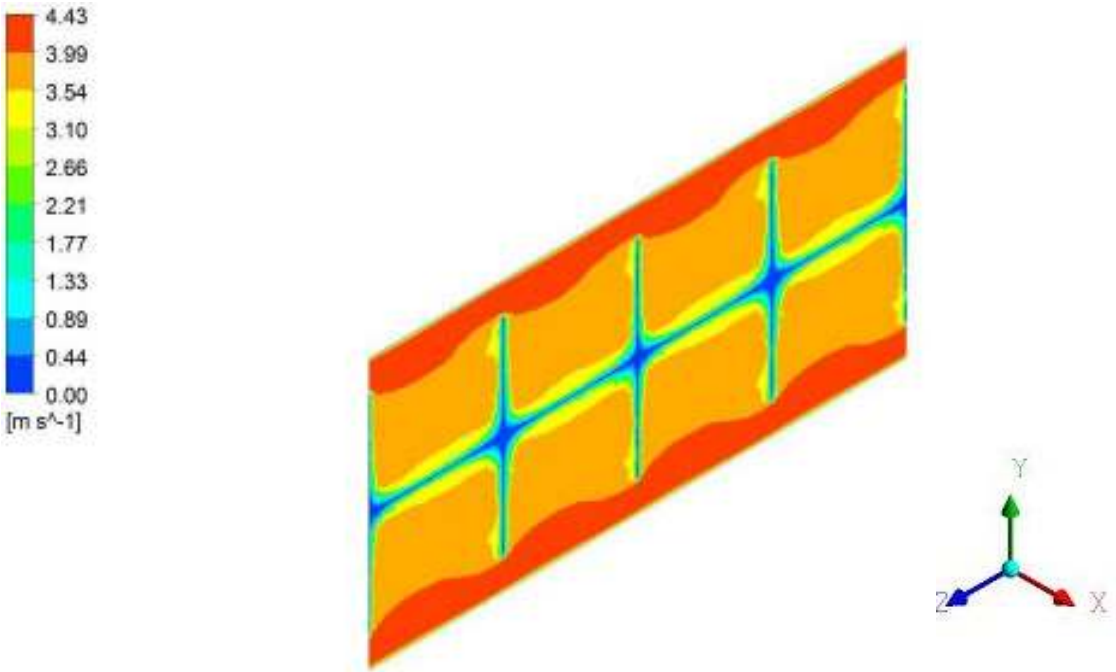

A.4. Temperature contours (periodic boundaries and inner walls) at *Re* = 6.40 × 10^4, $\tilde{y} = 0.33$ and $\tilde{w} = 0.91$

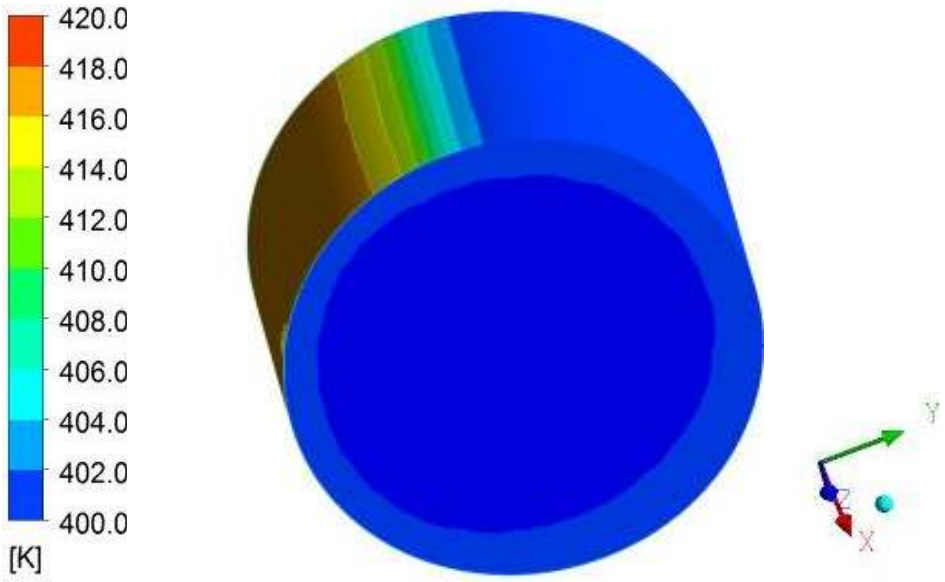

A.5. Sample goodness-of-fit metrics for the twisted tape response surface

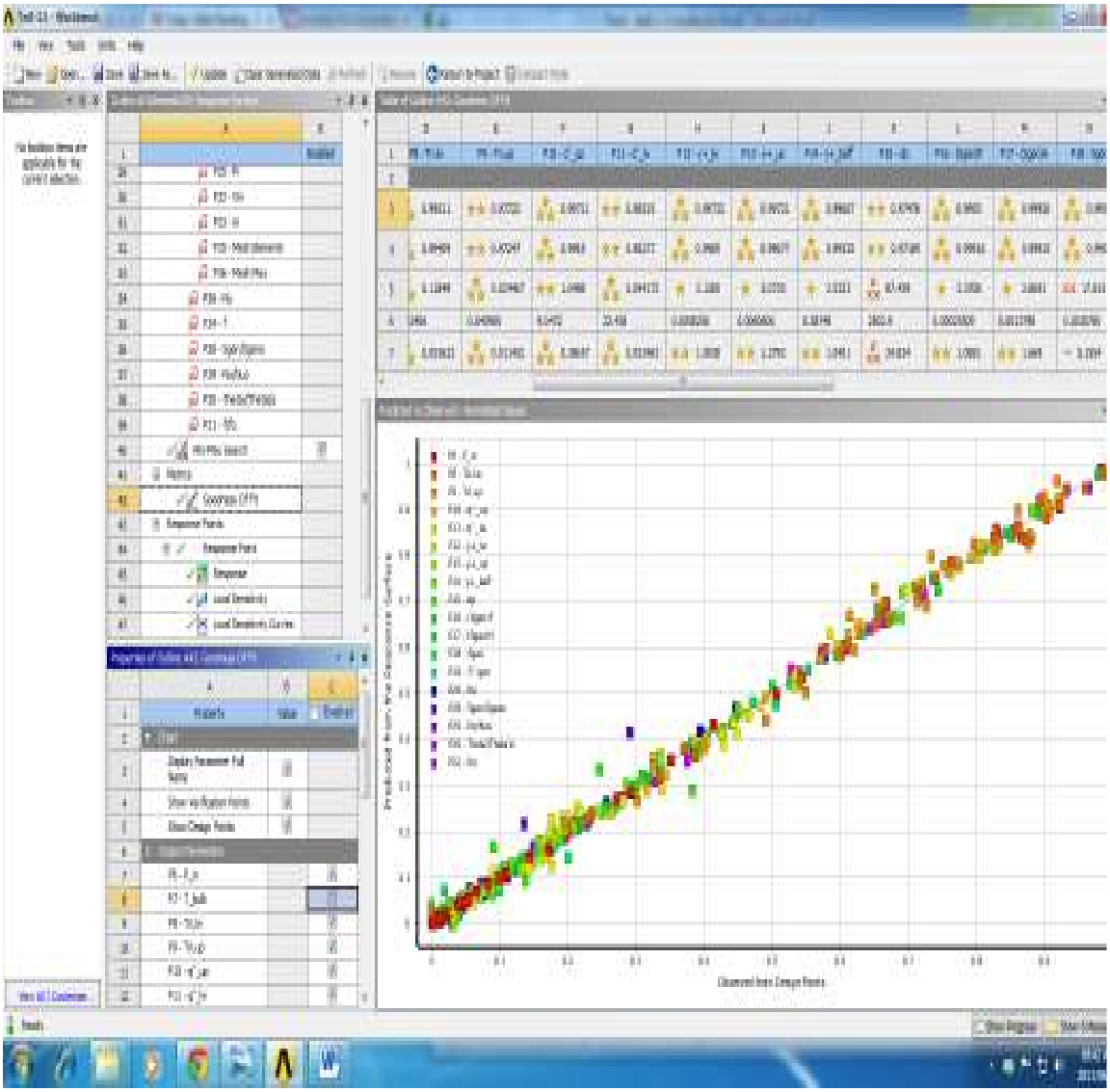

A.6. Sample local sensitivities from the twisted tape response surface

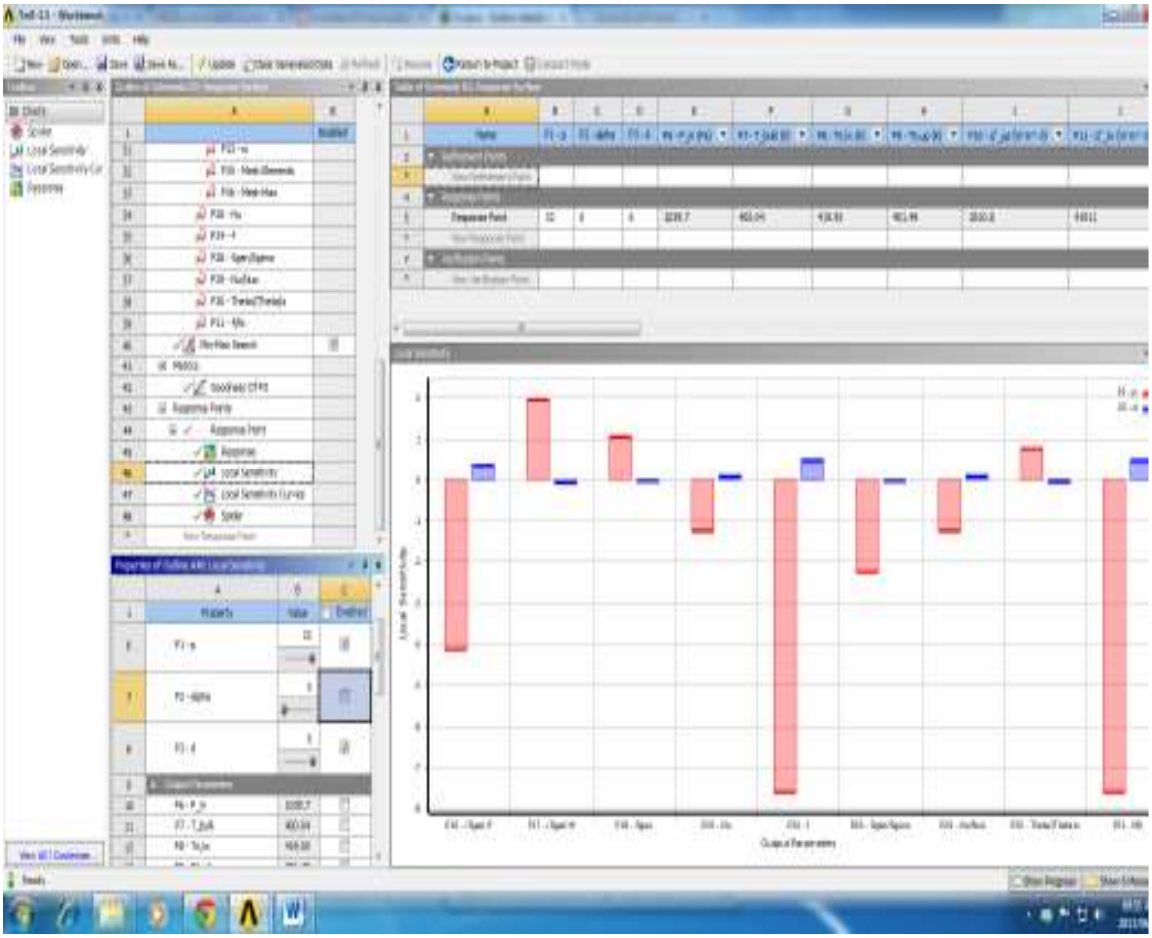

A.7. Sample global sensitivities from the twisted tape multi-objective optimisation

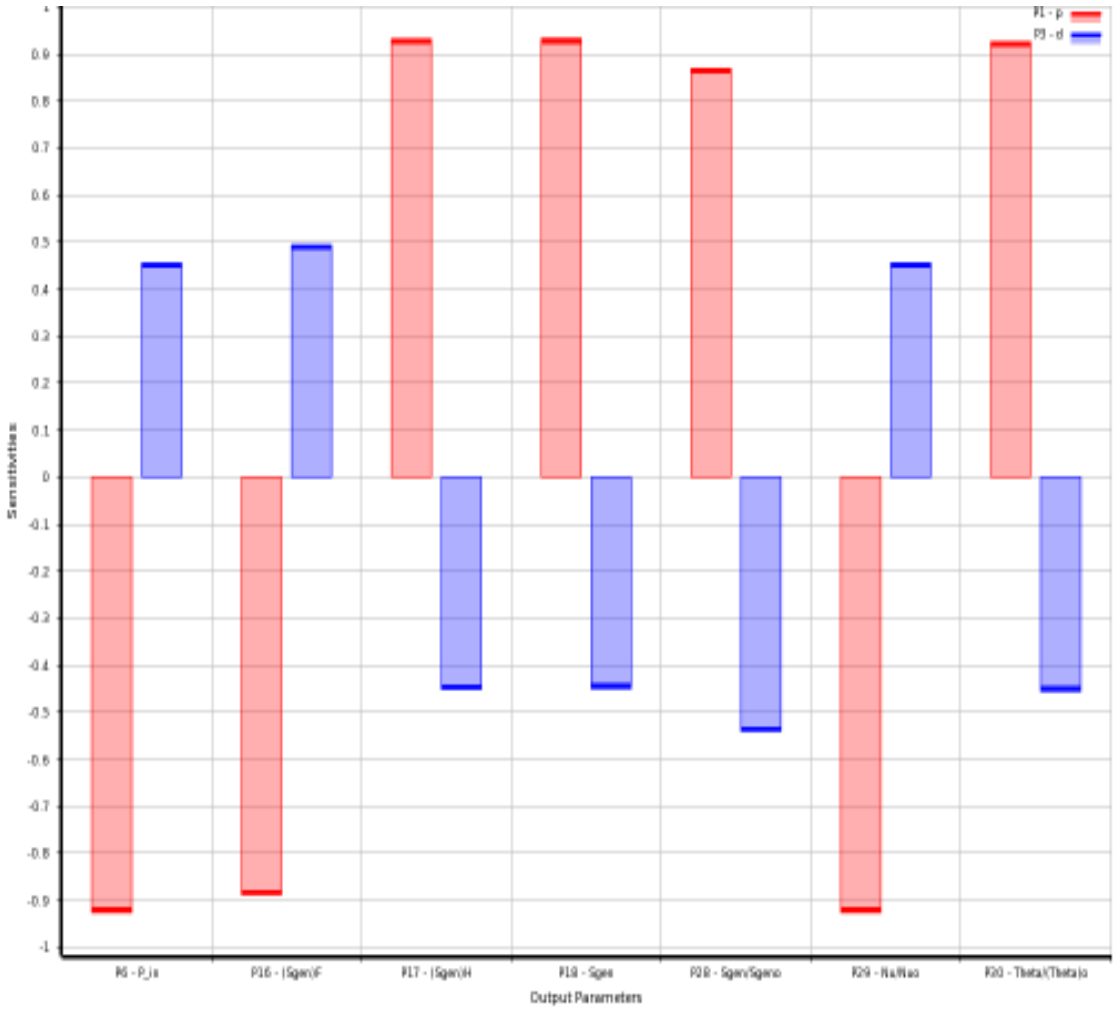

B. PERFORATED PLATE MODEL FLOW FIELD AND OPTIMISATION CHARTS

B.1. Convergence curves

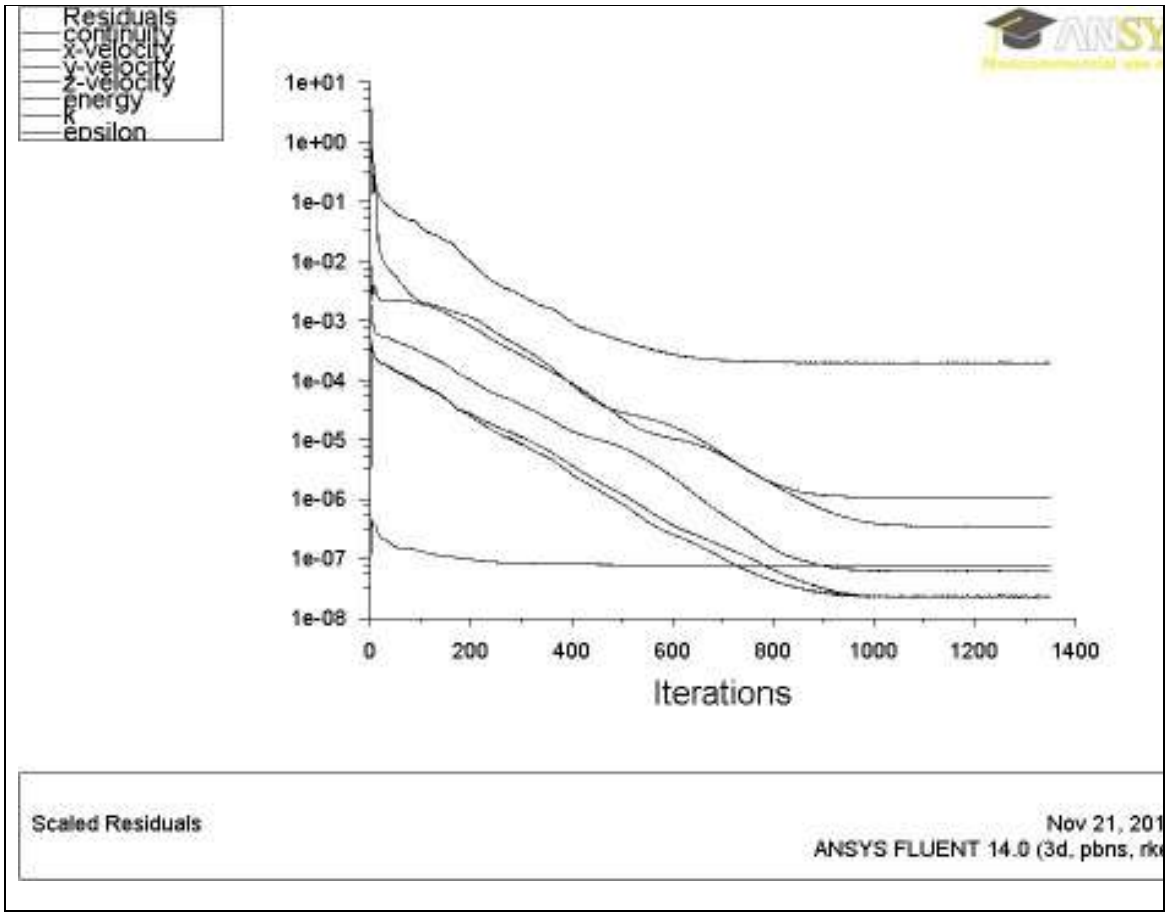

B.2. Temperature contours

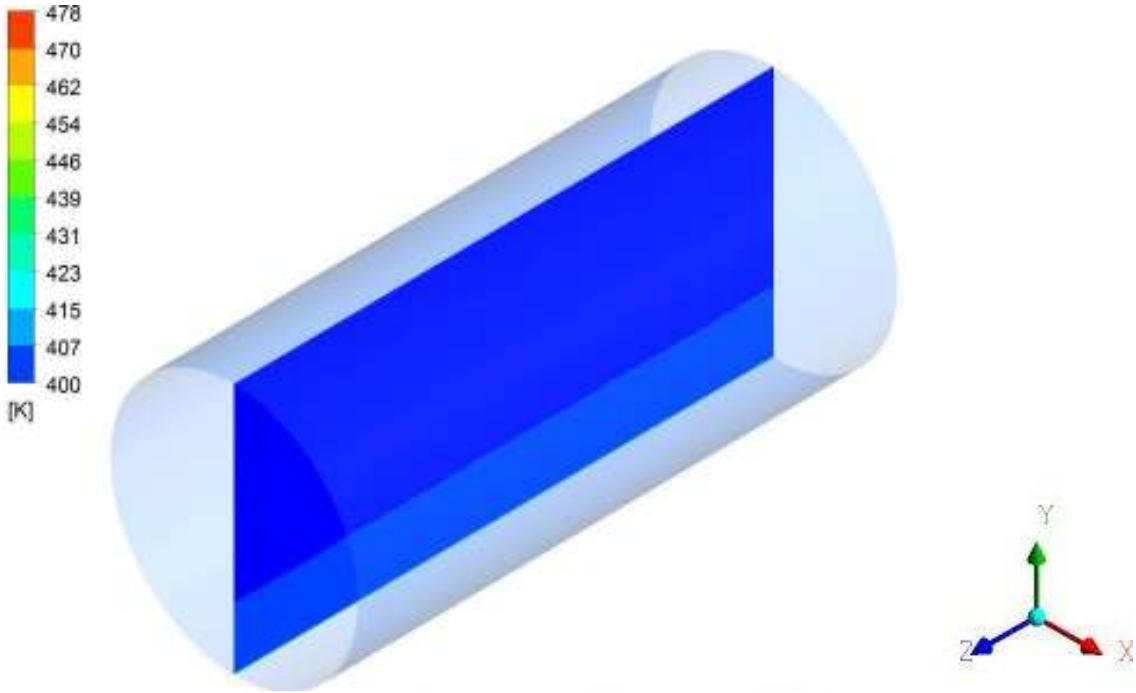

B.3. Goodness of fit with standard response surface for the perforated plate model

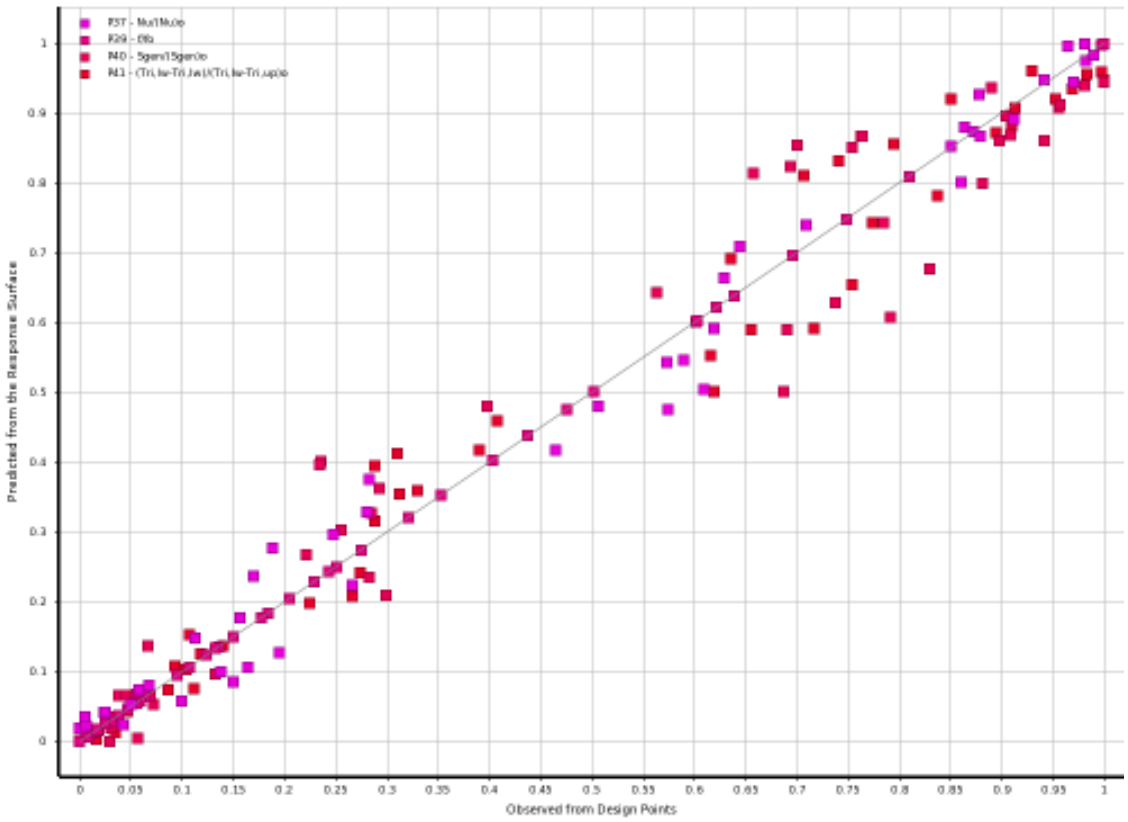

B.4. Goodness of fit after improvement with the Kriging meta-model for the perforated plate model

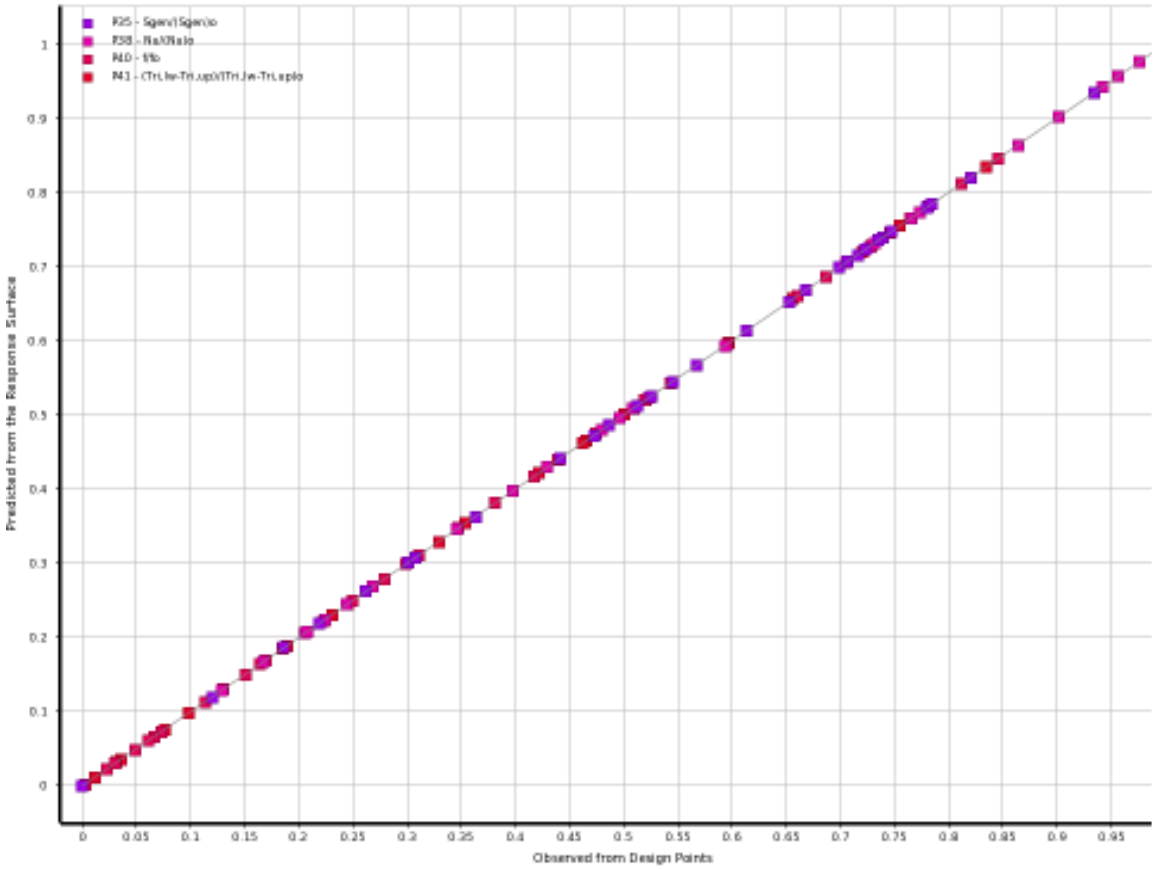

B.5 Sensitivity chart showing the effect of input parameters on output parameters for the perforated plate model

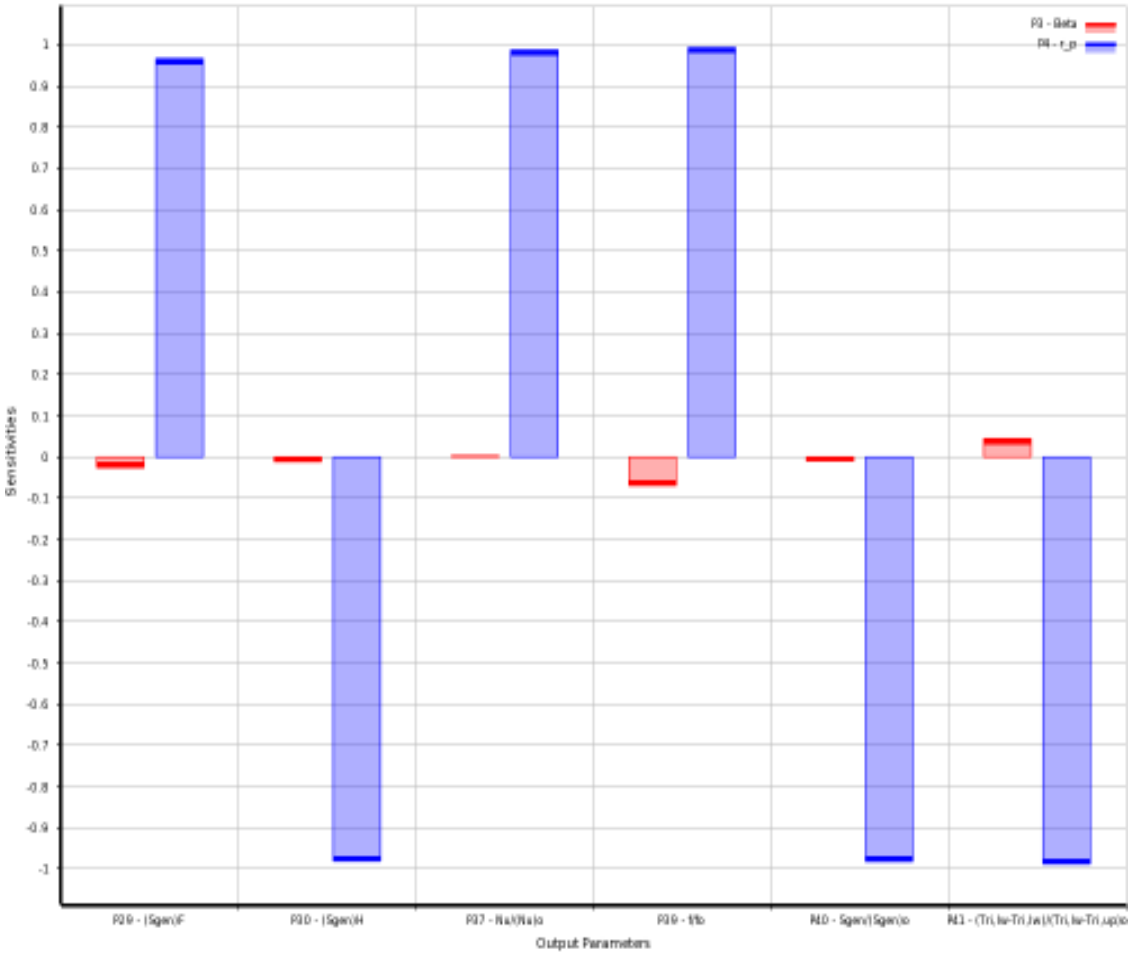

C. PERFORATED CONICAL INSERT MODEL'S FLOW FIELD AND OPTIMISATION CHARTS

C.1. Velocity contours at the periodic boundaries

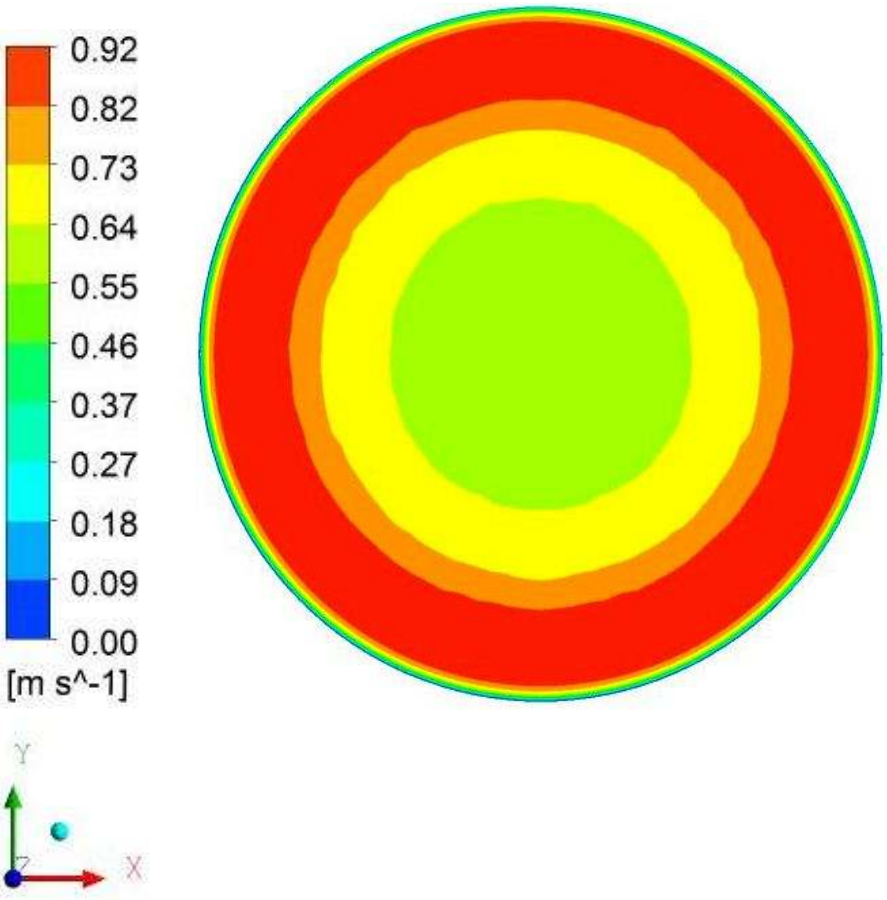

Periodic boundary – $Re = 1.94 \times 10^4$, $\tilde{p}_c = 0.11$, $\tilde{r}_c = 0.73$, $\tilde{\beta}_c = 0.33$

C.2. Temperature contours

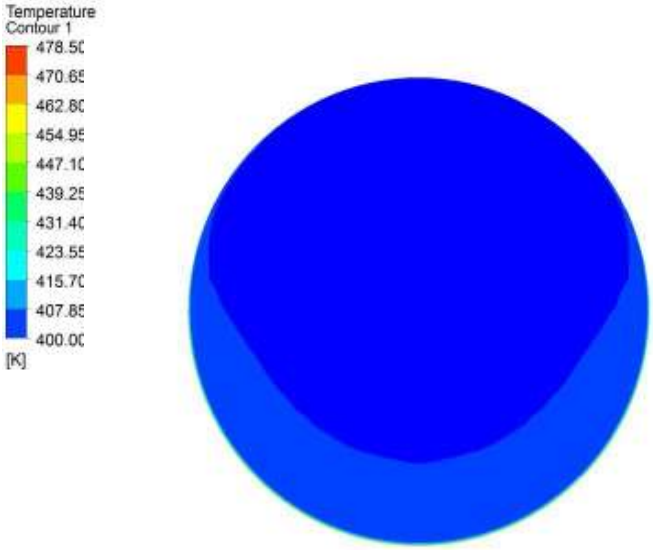

Outlet temperature – $Re = 1.94 \times 10^4$, $\tilde{p}_c = 0.11$, $\tilde{r}_c = 0.73$, $\tilde{\beta}_c = 0.33$

Symmetry plane – $Re = 1.94 \times 10^4$, $\tilde{p}_c = 0.11$, $\tilde{r}_c = 0.73$, $\tilde{\beta}_c = 0.33$

C.3. Sensitivity chart showing the effect of input parameters on output parameters for the perforated conical insert model